Stress-Strain data for metals in bar and sheet form: strain rate, thickness and temperature influences

Sina Roshanaei

A thesis presented for the degree of
Doctor of Philosophy

Mechanical Engineering Department
Brunel University
United Kingdom
March 2017

Stress-Strain data for metals in bar and sheet form: strain rate, thickness and temperature influences

Sina Roshanaei

Abstract

Over the past few decades various models of different formats have been developed to correctly evaluate and predict the strength of materials. However, these models are limited in certain environmental conditions in implementing the effect of material's thickness into their models. As such an there was a need to consider the basics of mechanical engineering and to try and define the trend, thickness has upon the behaviour of materials with respect to environmental conditions. The work consisted of a representation of tensile testing testing of common engineering alloys across a wide range of temperature, strain rate and thickness. Acquisition of high strain rate data and extended strain data (split-hopkinson, bulge forming and plane strain compression). A review of existing graphical techniques and limited applications using strength reduction factors, as well as applying the accepted empirical formulae, Johnson-Cook, Armstrong-Zerrili, Ramberg-Osgood and Hollomon. Later, recognising a need for a new approach as with a universal (quartic) polynomial fit to all plastic flow curves in which coefficients are T, $\dot{\varepsilon}$ and $\bar{t}$ dependant.
Adoptation of a common numerical procedure for strain intercept ε_0 and cut-off instability co-ordinates (σ_i, ε_i)- each as the solution to the roots of a quartic. Therefore, a proposal of the flow curve tables allowing interpolation and extrapolation, a numerical representation of any previous "Atlas of Curves". Subsequently, leading to reconstruction of the full stress-strain curve with the addition of elastic strain calculated from the modulus applicable to the specific test condition by further testing of these data from literature; both improving the existing and producing new empirical and simulation based models to analyse the materials, which will be subjected to dynamic loading as well as temperature and strain rates variations. The main objective of the work, was involved in creating a polynomial fit to describe the three physical conditions in terms of coefficients and to verify the findings in a FEA package, ABAQUS. A new process in reading the stress-strain data. By means of such development an instability study of strain limits based on Considére criteria was developed which illustrated the ways to prolong the instability limit.

A secondary study of this work relates to creating a bridge between the micro-structure and macro-structure of the tested materials. A series of correlations and trends were developed to further signify the shift in micro-structural restructuring, whilst the material is under load.

Another important aspect of the work consists, of carrying out an analytical study on Ramberg-Osgood equation. Ramberg-Osgood equation has been at the forefront of many engineering advancement. However it can yet be improved and reformatted by means of defining a set value for its variable constants. As such a fix

η_t value based on a best-fit approach was developed which was analytically tested.

Dedication

I would like to dedicate this work to my family, whose unwavering support has always been available in my darkest hours.

Special thanks to my friend Milad Beheshti, who has helped make this task easier with his presence, humour and guidance; also a thanks to all of my friends who have helped me on this journey.

I would like to also dedicate this work to my loving partner, who lifted my spirit at my time of need and walked every step of the way hand in hand with me, without her this work might not have had a happy ending, for that I am eternally indebted to her.

Last but not least, Dear Dr. David Rees, for all his guidance and perseverance. He willingly shared his many years of knowledge and experience. His patience, suggestions and encouragements was always available during the years of hard work on this thesis. This work may not have been a success with out his supervision. For all he has done for me I shall forever be thankful.

Declaration

In signing this declaration I am referring to all the tensile testing and all their analyses. Having been transfered to Dr. Rees as first PhD supervisor in my final year he wanted my additional analyses of his previously unpublished bulge forming and plane strain compression data (pp 79-84). The purpose of this was to extend curve fitting and instability analyses to a greater range of strain than is provided by the tensile test. I also declare this work has never been published and/or submitted for any award to any other institution before.

Signed.....

Date.....

Contents

1 Introduction **1**
1.1 Scope of the work . . . 3
1.1.1 Statement of objective . . . 4
1.1.2 Specific objectives . . . 4
1.1.3 Methodology . . . 7
1.1.4 Content of thesis . . . 8

2 Literature Review **10**
2.1 Test Method . . . 11
2.2 Previous Research . . . 12
2.2.1 Reduction factor research . . . 14
2.3 Classification of Strain Rate Regimes . . . 22
2.3.1 Creep rate regime . . . 22
2.3.2 Quasi-static rate regime . . . 23
2.3.3 Intermediate strain rate regime . . . 23
2.3.4 High strain rate regime . . . 24
2.4 Uni-axial Test . . . 25
2.4.1 Tensile machine effect on tensile properties . . . 26
2.4.2 Deformation . . . 27
2.4.3 Ductile fracture . . . 29
2.4.3.1 Brittle cleavage fracture . . . 29
2.4.3.2 Transgranular fracture . . . 30
2.4.4 Deformation prediction . . . 32
2.4.4.1 Elastic-plastic deformation . . . 33
2.4.4.2 Engineering stress-strain . . . 35
2.5 Additional Strain Level . . . 36
2.5.1 Biaxial loading . . . 36
2.5.1.1 Bulge test . . . 38
2.5.2 Plane strain compression test . . . 41
2.6 Numerical Analysis . . . 45
2.6.1 General consideration . . . 45
2.6.2 Validation and verification . . . 46
2.6.3 Meshing analysis . . . 47
2.6.4 Time integration . . . 48
2.6.4.1 Explicit . . . 48
2.6.4.2 Implicit . . . 48
2.6.5 Ductility analysis . . . 49
2.6.5.1 Modes of failure . . . 49

2.6.5.2 Finite element method for recognition of necking . . 57

3 Mechanical Properties 61
3.1 Introduction . . . 61
3.2 Uni-axial Testing . . . 62
3.3 Sample Preparation . . . 65
3.3.1 Materials . . . 65
3.3.1.1 uniaxial tension . . . 65
3.3.1.2 Bi-axial bulging . . . 66
3.3.2 Selection of test specimen . . . 66
3.3.3 Preparation of test specimen . . . 67
3.3.4 Test piece geometry . . . 67
3.4 Testing Apparatus . . . 70
3.4.1 Cross-head movement specification . . . 76
3.4.2 Temperature variation specification . . . 76
3.5 Experimental Sequence . . . 77
3.6 Experimental Results . . . 78
3.6.1 Tensile test results . . . 78
3.6.2 Bulge forming results . . . 79
3.6.3 Plane strain compression testing . . . 82

4 Experimental Investigation 85
4.1 Introduction . . . 85
4.2 Background . . . 86
4.2.1 Existing models . . . 87
4.2.1.1 Johnson-Cook model . . . 89
4.2.1.2 Zerilli-Armstrong model . . . 92
4.3 Varying Temperatures and Strain Rate . . . 96
4.3.1 Yield strength, elastic modulus and ultimate strength . . . 96
4.3.1.1 Yield strength . . . 97
4.3.1.2 Elastic gradient . . . 104
4.3.1.3 Ultimate strength . . . 106
4.3.2 Strain rate study . . . 108
4.3.3 Elongation vs strain rate and temperature . . . 114
4.3.4 Necking formation . . . 120
4.3.4.1 Effect of strain rate based on Considére criterion . . 123
4.3.4.2 Effect of temperature based on Considére criterion . 123
4.3.5 Comparative study . . . 126
4.3.5.1 Comparison of mechanical properties to other design codes . . . 126
4.3.5.2 Comparison of mechanical properties to other researchers . . . 131
4.4 Micro-structural Analysis . . . 133

5 Simulation Process 139
5.1 Introduction . . . 139
5.1.1 Description of intent . . . 139
5.1.2 Theory of finite element analysis . . . 140
5.1.2.1 History of FEA . . . 140

5.1.2.2 FEA sequence . . . 141
5.2 Finite Element Mathematical Modelling . . . 141
5.2.1 Trial solution . . . 142
5.2.2 Nodal displacement . . . 143
5.2.3 Pre-stressing and thermal effect . . . 147
5.2.4 Trial solution optimization . . . 149
5.3 Modelling Variables . . . 150
5.3.1 Elements . . . 150
5.3.2 Meshing . . . 154
5.3.3 Material model . . . 160
5.3.4 Boundary condition . . . 162
5.4 Necking Elongation . . . 165
5.5 Subroutine Modelling . . . 166
5.5.1 Elastic-plastic behaviour . . . 169
5.5.2 Interpolation . . . 172
5.6 Validation . . . 174
5.6.1 Empirical verification . . . 174
5.6.2 Mathematical verification . . . 177
5.7 Conclusion . . . 182

6 Fitting Ramberg-Osgood's Stress-Strain Equation 185
6.1 Introduction . . . 185
6.2 Ramberg-Osgood Equation in Alternative Form . . . 186
6.3 Dimensionless Analysis . . . 186
6.3.1 Error analysis . . . 187
6.4 Best Fit Procedure for Ramberg-Osgood Equation . . . 190
6.5 Variation of Mechanical Properties with Temperature . . . 191
6.6 Evaluation of Exponential Factor in Ramberg-Osgood Correlation . . . 194
6.7 Error Calculation-Propagation Function . . . 197
6.8 Conclusion . . . 199

7 Conclusion 201
7.1 Future Work . . . 203

Appendices 217

A Appendix A 218
A.1 Uni-axial . . . 218
A.2 Bi-axial . . . 255
A.3 Reduction Factor . . . 260

B Appendix B 264
B.1 Source Code . . . 264
B.2 Polynomial Tables . . . 276

List of Figures

1.1 Press-braking process 2
1.2 Roll-forming process 2
1.3 Number of house inflicted with fire 3
1.4 Methodology schematic 7

2.1 Transient state conversion of data to stress-strain, [8]. 13
2.2 Stress-strain curve for steels at elevated temperatures 13
2.3 Reduction factors for mechanical properties of steel at elevated temperatures, [9] 14
2.4 Strength reduction factor based on british standard, [10] 15
2.5 Reduction factor strain levels based on stress-strain curve [6] 17
2.6 Mechanical properties comparison between elevated temperature steel element and after cooling, [8] 18
2.7 Coefficients of proposed equation 2.16 for yield strength, [5] 21
2.8 Dynamic range of strain rates [18] 23
2.9 Electromechanical screw driven testing machine, [20] 24
2.10 Split hopkinson pressure bar apparatus, [21] 25
2.11 Typical engineering stress-strain curve [24] 28
2.12 Localized necking in flat samples [26] 29
2.13 Cup and cone formation [32] 31
2.14 Bulge testing machine during test, [36] 37
2.15 Uni-axial and bi-axial stress states, [37] 37
2.16 Geometry of the bulge test, [36] 39
2.17 The deviatoric plane, [36] 40
2.18 Equivalance between biaxial tension and torsion for brass, [36] 41
2.19 Plane strain compression schematic 42
2.20 Plain strain compression equivalent stress-strain 43
2.21 Computational algorithem process, [42] 45
2.22 Ductile to brittle transition, [31] 49
2.23 Overview of failure criteria with non-proportional loading 50
2.24 FLC for T4 aluminium, [58] 51
2.25 Stress space bi-linear forming path, [61] 53
2.26 Presentation of necking on a stress-strain curve, [31] 58
2.27 Reference stress-strain curve based on Hollomon's law 60

3.1 Reduction factor based on flow curve 62
3.2 Example of test piece for sheets with thickness between 0.1 and 3 mm,[80] 68
3.3 Example of cylindrical test piece 69

3.4 Flat sample configuration . . . 69
3.5 Schematic of split collet, [37] . . . 69
3.6 Circular sample configuration . . . 70
3.7 Furnace & tensile machine . . . 71
3.8 Controller unit . . . 71
3.9 Main controlling panel . . . 71
3.10 The locknut . . . 73
3.11 Furnace controller . . . 74
3.12 Temperature monitor . . . 74
3.13 Data scanner . . . 75
3.14 Temperature designation based on homologous temperature . . . 77
3.15 0.13% C-steel stress-strain family curves at $6.09 \times 10^{-4}s^{-1}$ °C, @ 1mm 79
3.16 0.13% C-steel stress-strain family curves at $6.09 \times 10^{-4}s^{-1}$ °C, @ 2mm 79
3.17 Bulge forming stress-strain plot of AA5754 . . . 80
3.18 Bulge forming stress-strain plot of AA5754 . . . 80
3.19 Bulge forming stress-strain plot of AA6111 . . . 81
3.20 Bulge forming stress-strain plot of stainless steel . . . 81
3.21 Bulge forming stress-strain plot of carbon steel . . . 82
3.22 Compression plate stress-strain plot of AA5754 . . . 83
3.23 Compression plate stress-strain plot of AA6111 . . . 83
3.24 Strain limit of the aluminium alloys based on method of experiment . 84
3.25 Strain limit percentage change of the aluminium alloys based on method of experiment . . . 84

4.1 Example of failed sample . . . 86
4.2 Plot of constant m . . . 92
4.3 Sharp yielding . . . 97
4.4 Smooth yielding . . . 97
4.5 0.6mm 0.13% C-steel at ambient temperature and $6.09 \times 10^{-5}s^{-1}$ . . 98
4.6 0.6mm 0.13% C-steel at $300°C$ temperature and $6.09 \times 10^{-5}s^{-1}$ . . . 98
4.7 0.6mm 0.13% C-steel at $400°C$ temperature and $6.09 \times 10^{-5}s^{-1}$ . . . 99
4.8 0.6mm 0.13% C-steel at $500°C$ temperature and $6.09 \times 10^{-5}s^{-1}$ . . . 99
4.9 Family of stress-strain curves for sheet steel at various temperatures ($\dot{\varepsilon} = 6.09 \times 10^{-5}s^{-1}$) with 0.6 mm flat sample . . . 100
4.10 Yield strength deterioration reduction factor at 0.2% and $\dot{\varepsilon} = 6.09 \times 10^{-5}s^{-1}$ for 0.13 % C-steel . . . 101
4.11 Reduction factor based on strain level of 0.6 mm plate at $\dot{\varepsilon} = 6.09 \times 10^{-5}s^{-1}$ . . . 104
4.12 Elastic gradient reduction factor based on elevated temperature at $\dot{\varepsilon} = 6.09 \times 10^{-5}s^{-1}$ . . . 105
4.13 Percentage change of elasticity based on thickness change . . . 106
4.14 Ultimate strength reduction factor based on elevated temperature . . 107
4.15 Temperature influence upon 0.13% C-steel at 0.6 mm and$\dot{\varepsilon} = 6.09 \times 10^{-5}s^{-1}$ . . . 108
4.16 Strain level evaluation of 18/8 stainless steel based on strain rate variation at $23°C$ and $300°C$ . . . 109
4.17 Strain failure change based on constant temperature at $350°C$ 110

4.18 Strain level evaluation of 0.13% C-steel based on strain rate variation at $300°C$ . . . 110
4.19 Strain level evaluation of Aluminium alloy based on strain rate variation at $100°C$ . . . 111
4.20 Strain level evaluation of Aluminium alloy based on strain rate variation at $23°C$ . . . 112
4.21 Strain level evaluation of 60/40 brass based on strain rate variation at $160°C$ . . . 112
4.22 Strain rate $6.09 \times 10^{-5} s^{-1}$ evaluation of 0.13% C-steel based on thickness variation at $400°C$ . . . 113
4.23 Strain rate $6.09 \times 10^{-5} s^{-1}$ evaluation of 0.13% C-steel based on thickness variation at $23°C$ . . . 113
4.24 Strain rate sensitivity at $23°C$ . . . 114
4.25 Strain rate sensitivity at $600°C$ . . . 115
4.26 Elongation based on strain rate variation at $350°C$ and 1mm thickness of 0.13% C-steel . . . 116
4.27 Elongation based on strain rate variation at $23°C$ of circular samples of 18/8 stainless steel . . . 116
4.28 Elongation based on temperature variation at $6.09 \times 10^{-5} s^{-1}$ of 0.13% C-steel . . . 117
4.29 Influence of strain aging on mild steel [41] . . . 118
4.30 Ultimate strength . . . 118
4.31 Yield strength . . . 118
4.32 Total elongation as a function of temperature at $\dot{\varepsilon} = 6.09 \times 10^{-4} s^{-1}$ . . . 119
4.33 Total elongation as a function of strain rate at $350°C$ . . . 119
4.34 Description of polynomial calculation . . . 121
4.35 Stress vs. Strain with varying strain rate for AISI 6063 at $100°C$ . . . 124
4.36 Effect of displacement rate for AISI 6063 at $23°C$ . . . 124
4.37 Effect of displacement rate for 18/8 stainless steel . . . 125
4.38 Effect of displacement rate for 0.13% C-steel at $300°C$ . . . 125
4.39 Effect of displacement rate for 60/40 brass at $160°C$ . . . 126
4.40 Stress vs. strain with varying temperature on $0.6mm$ 0.13% C-steel . . . 127
4.41 Stress vs. strain with varying temperature on $0.9mm$ 0.13% C-steel . . . 127
4.42 Stress vs. strain with varying temperature on $1.1mm$ 0.13% C-steel . . . 128
4.43 Stress vs. strain with varying temperature on $1.3mm$ 0.13% C-steel . . . 128
4.44 Stress vs. strain with varying temperature on $1.9mm$ 0.13% C-steel . . . 129
4.45 Stress vs. strain with varying temperature on $2.8mm$ 0.13% C-steel . . . 129
4.46 Percentage strain level change of necking formation to failure on varying temperature for 0.13% C-steel . . . 130
4.47 Comparison of yield strength reduction factors based on elevated temperature . . . 131
4.48 Comparison of yield strength reduction factors based on researchers . . . 132
4.49 SEM image of high strain rate vs. low strain rate for 0.13% C-steel . . . 133
4.50 Thickness strain variation to fracture surface of 0.13% C-steel . . . 134
4.51 Void formation rate based on strain rate on 0.13% C-steel for 1.0 mm . . . 135
4.52 Porosity change based on strain rate variation . . . 136
4.53 Ductile fracture of 0.13% C-steel . . . 136
4.54 Presence of Fe and Mn on 0.13% C-steel for 1.0 mm . . . 137

4.55 Area reduction measurement 138

5.1 Sequence of a typical FEA solution 141
5.2 Trial solution method adopted from [111] 142
5.3 Eight node hexahedral element, (a) actual element, (b) parent element 145
5.4 Quadrilateral element arrangement 151
5.5 Triangular element 2^{nd} order 6 noded model 152
5.6 Quadrilateral element 4 noded model 152
5.7 Model created for simulation analysis 155
5.9 Mesh sensitivity 156
5.8 Element mesh comparison 157
5.10 Verifying no difference between quarter model and full model 158
5.11 Seeding of the model based on the sectioning 158
5.12 Total required for initial slacking to be remove for each end 159
5.13 3D and 2D model based on experimental setup 161
5.20 Boundary conditions of the simulated model 162
5.14 Parametric material modelling for 0.13% C-steel at $1mm-3mm/min-350°C$ 163
5.15 Parametric material modelling for 0.13% C-steel at $1mm-90mm/min-350°C$ 163
5.16 Parametric material modelling for 0.13% C-steel at $06mm-0.3mm/min-500°C$ 163
5.17 Parametric material modelling for 0.13% C-steel at $0.9mm-0.3mm/min-23°C$ 164
5.18 Parametric material modelling for 0.13% C-steel at $1.3mm-0.3mm/min-300°C$ 164
5.19 Parametric material modelling for 0.13% C-steel at $2.8mm-0.3mm/min-23°C$ 164
5.21 Effective plastic strain exhibiting necked region deformation 165
5.22 Nominal strain rate against necked strain rate based on numerical simulation 166
5.23 Interpolation algorithm of the user defined code 174
5.24 Comparison between numerical J-C results to experimental results with varying temperature On AA6063 and quasi static strain rate . . 176
5.25 Comparison between numerical J-C results to experimental results with varying temperature on 0.13% C-steel and quasi static strain rate 176
5.26 Comparison between numerical J-C results to experimental results with varying temperature on 18/8 stainless steel 177
5.27 2D FEA Results 179
5.28 3D FEA simulated results 179
5.29 Stress vs. strain comparison of FEA and lab results 180
5.30 FEA verification for environmental condition (a) 181
5.31 FEA verification for environmental condition (b) 181
5.32 FEA verification for environmental condition (c) 182
5.33 FEA verification for environmental condition (d) 182
5.34 Temperature trend based on elastic strain and stress 184

6.1 Variation of error fraction for different test conditions 188

6.2 Variation of error fraction against associated stress at 3mm/min and $300°C$ 189
6.3 Variation of ε against σ for the values of $\eta_t = 3, 4, 5, 6$ 189
6.4 Poh's general stress-strain equation [129] 192
6.5 Variation of yield stress vgainst variation of temperature 193
6.6 Variation of elastic gradient against variation of temperature 193
6.7 Variation of ultimate tensile strength against variation of temperature 194
6.8 Variation of $ln(\pi_1)$ against $ln(\pi_2)$ 195
6.9 Variation of stress against strain for experimental data and calculated values using R-O correlation based on fixed exponential factor 196
6.10 Calculated values of η_t against strain ε by using the average value . . 196
6.11 Applied stress against calculated values of ε from R-O (at $23°C$, 2.8 mm 0.2% C-sheet metal and $6.09 \times 10^{-5}s^{-1}$) 197
6.12 Variation of stress against total strain from R-O correlation (at $23°C$, 2.8 mm 0.2% C sheet metal and $6.09 \times 10^{-5}s^{-1}$) 198
6.13 Error propagation values versus stress determined for original RO correlation and best fit modification 199
6.14 Variation of stress against total strain using experimental data, modified version of R-O correlation and original forms of R-O correlation by using fitting a line and average value technique (at $23°C$, 2.8 mm 0.2% C-sheet metal and $6.09 \times 10^{-5}s^{-1}$) 200

A.1 Stress strain response for 0.13% C-steel, 1mm, 3mm/min and 23C . . 218
A.2 Stress strain response for 0.13% C-steel, 2mm, 3mm/min and 23C . . 219
A.3 Stress strain response for 0.13% C-steel, 1mm, 3mm/min and 300C . 219
A.4 Stress strain response for 0.13% C-steel, 2mm, 3mm/min and 300C . 220
A.5 Stress strain response for 0.13% C-steel, 1mm, 90mm/min and 350C . 220
A.6 Stress strain response for 0.13% C-steel, 1mm, 3mm/min and 350C . 221
A.7 Stress strain response for 0.13% C-steel, 2mm, 3mm/min and 350C . 221
A.8 Stress strain response for 0.13% C-steel, 1mm, 0.3mm/min and 350C 222
A.9 Stress strain response for 0.13% C-steel, 2mm, 0.3mm/min and 350C 222
A.10 Stress strain response for 0.13% C-steel, 1mm, 3mm/min and 400C . 223
A.11 Stress strain response for 0.13% C-steel, 2mm, 3mm/min and 400C . 223
A.12 Stress strain response for 0.13% C-steel, 1mm, 3mm/min and 450C . 224
A.13 Stress strain response for 0.13% C-steel, 2mm, 3mm/min and 450C . 224
A.14 Stress strain response for 0.13% C-steel, 1mm, 3mm/min and 500C . 225
A.15 Stress strain response for 0.13% C-steel, 2mm, 3mm/min and 500C . 225
A.16 Stress strain response for 0.13% C-steel, 0.6mm, 0.3mm/min and 600C226
A.17 Stress strain response for 0.13% C-steel, 0.6mm, 0.3mm/min and 300C226
A.18 Stress strain response for 0.13% C-steel, 0.6mm, 0.3mm/min and 400C227
A.19 Stress strain response for 0.13% C-steel, 0.6mm, 0.3mm/min and 500C227
A.20 Stress strain response for 0.13% C-steel, 0.6mm, 0.3mm/min and 23C 228
A.21 Stress strain response for 0.13% C-steel, 0.9mm, 0.3mm/min and 23C 228
A.22 Stress strain response for 0.13% C-steel, 0.9mm, 0.3mm/min and 600C229
A.23 Stress strain response for 0.13% C-steel, 0.9mm, 0.3mm/min and 300C229
A.24 Stress strain response for 0.13% C-steel, 0.9mm, 0.3mm/min and 400C230
A.25 Stress strain response for 0.13% C-steel, 0.9mm, 0.3mm/min and 500C230
A.26 Stress strain response for 0.13% C-steel, 1.1mm, 0.3mm/min and 500C231

A.27 Stress strain response for 0.13% C-steel, 1.1mm, 0.3mm/min and 600C231
A.28 Stress strain response for 0.13% C-steel, 1.1mm, 0.3mm/min and 300C232
A.29 Stress strain response for 0.13% C-steel, 1.1mm, 0.3mm/min and 400C232
A.30 Stress strain response for 0.13% C-steel, 1.1mm, 0.3mm/min and 23C 233
A.31 Stress strain response for 0.13% C-steel, 1.3mm, 0.3mm/min and 300C233
A.32 Stress strain response for 0.13% C-steel, 1.3mm, 0.3mm/min and 400C234
A.33 Stress strain response for 0.13% C-steel, 1.3mm, 0.3mm/min and 23C 234
A.34 Stress strain response for 0.13% C-steel, 1.3mm, 0.3mm/min and 500C235
A.35 Stress strain response for 0.13% C-steel, 1.3mm, 0.3mm/min and 600C235
A.36 Stress strain response for 0.13% C-steel, 2.8mm, 0.3mm/min and 400C236
A.37 Stress strain response for 0.13% C-steel, 2.8mm, 0.3mm/min and 600C236
A.38 Stress strain response for 0.13% C-steel, 2.8mm, 0.3mm/min and 500C237
A.39 Stress strain response for 0.13% C-steel, 2.8mm, 0.3mm/min and 23C 237
A.40 Stress strain response for 0.13% C-steel, 2.8mm, 0.3mm/min and 300C238
A.41 Stress strain response for 0.13% C-steel, 3mm/min and 150C 238
A.42 Stress strain response for 0.13% C-steel, 0.3mm/min and 300C 239
A.43 Stress strain response for 0.13% C-steel, 30mm/min and 300C 239
A.44 Stress strain response for 0.13% C-steel, 3mm/min and 300C 240
A.45 Stress strain response for 0.13% C-steel, 3mm/min and 450C 240
A.46 Stress strain response for 0.13% C-steel, 3mm/min and 600C 241
A.47 Stress strain response for 0.13% C-steel, 3mm/min and 23C 241
A.48 Stress strain response for 0.13% C-steel, 90mm/min and 300C 242
A.49 Stress strain response for AISI 6063, 3mm/min and 50C 242
A.50 Stress strain response for AISI 6063, 3mm/min and 150C 243
A.51 Stress strain response for AISI 6063, 3mm/min and 100C 243
A.52 Stress strain response for AISI 6063, 0.3mm/min and 100C 244
A.53 Stress strain response for AISI 6063, 30mm/min and 100C 244
A.54 Stress strain response for AISI 6063, 90mm/min and 100C 245
A.55 Stress strain response for AISI 6063, 3mm/min and 200C 245
A.56 Stress strain response for AISI 6063, 3mm/min and 23C 246
A.57 Stress strain response for AISI 6063, 0.3mm/min and 23C 246
A.58 Stress strain response for AISI 6063, 30mm/min and 23C 247
A.59 Stress strain response for AISI 6063, 90mm/min and 23C 247
A.60 Stress strain response for 60/40 brass, 3mm/min and 80C 248
A.61 Stress strain response for 60/40 brass, 3mm/min and 160C 248
A.62 Stress strain response for 60/40 brass, 30mm/min and 160C 249
A.63 Stress strain response for 60/40 brass, 90mm/min and 160C 249
A.64 Stress strain response for 60/40 brass, 3mm/min and 23C 250
A.65 Stress strain response for 18/8 stainless steel, 0.3mm/min and 23C . . 250
A.66 Stress strain response for 18/8 stainless steel, 3mm/min and 23C . . . 251
A.67 Stress strain response for 18/8 stainless steel, 30mm/min and 23C . . 251
A.68 Stress strain response for 18/8 stainless steel, 90mm/min and 23C . . 252
A.69 Stress strain response for 18/8 stainless steel, 3mm/min and 300C . . 252
A.70 Stress strain response for 18/8 stainless steel, 0.3mm/min and 300C . 253
A.71 Stress strain response for 18/8 stainless steel, 3mm/min and 100C . . 253
A.72 Stress strain response for 18/8 stainless steel, 30mm/min and 300C . 254
A.73 Stress strain response for 18/8 stainless steel, 3mm/min and 450C . . 254
A.74 Stress strain response for AA 5754 255

A.75 Stress strain response for AA 6111 255
A.76 Stress strain response for AC 300 256
A.77 Stress strain response for AC 220 256
A.78 Stress strain response for 0.13% C-steel 257
A.79 Stress strain response for 18/8 stainless steel 257
A.80 Stress strain response for AA 5754-18 258
A.81 Stress strain response for AA 5754-30 258
A.82 Stress strain response for AC 300-23 259
A.83 Stress strain response for AC 300-31 259
A.84 Stress strain response for AA 6111 260
A.85 Reduction factor curves for 0.6 mm sheet steel 260
A.86 Reduction factor curves for 0.9 mm sheet steel 261
A.87 Reduction factor curves for 1.1 mm sheet steel 261
A.88 Reduction factor curves for 1.3 mm sheet steel 261
A.89 Reduction factor curves for 1.9 mm sheet steel 262
A.90 Reduction factor curves for 2.8 mm sheet steel 262
A.91 Reduction factor curves for 0.2% strain value of sheet steel 263
A.92 Reduction factor curves for 0.5% strain value of sheet steel 263
A.93 Reduction factor curves for 1.5% strain value of sheet steel 263

List of Tables

3.1 Proposed dimensions for flar test piece (mm), citeiso6892 68
3.2 Modes of cross-head movement 76
3.3 Varying strain rate & minimal thickness variation 77
3.4 Constant strain rate with varying thickness and temperature 77
3.5 Bar samples, experiment arrangements 78

4.1 Yield strength deterioration of flat samples at $\dot{\varepsilon} = 6.09 \times 10^{-5} s^{-1}$ . . 102
4.2 Reduction factors of flat samples at $\dot{\varepsilon} = 6.09 \times 10^{-5} s^{-1}$ 103
4.3 Elastic gradient and elastic reduction factors of 0.13% C-steel at elevated temperatures at $\dot{\varepsilon} = 6.09 \times 10^{-5} s^{-1}$ 105
4.4 Ultimate strength and ultimate strength reduction factor of 0.13% C-steel at elevated temperatures and $\dot{\varepsilon} = 6.09 \times 10^{-5} s^{-1}$ 107

5.1 Element configuration results 153
5.2 Time parameter definition, (a) maximum deflection 155
5.3 Johnson-Cook values for AA6063 at ambient temperature and $6.09 \times 10^{-4} s^{-1}$ 160
5.4 Coefficient values for 0.6mm 0.13% C-steel at $6.09 \times 10^{-5} s^{-1}$ 167
5.5 Coefficient values for 0.9mm 0.13% C-steel at $6.09 \times 10^{-5} s^{-1}$ 167
5.6 Coefficient values for 1.1mm 0.13% C-steel at $6.09 \times 10^{-5} s^{-1}$ 167
5.7 Coefficient values for 1.3mm 0.13% C-steel at $6.09 \times 10^{-5} s^{-1}$ 167
5.8 Coefficient values for 1.9mm 0.13% C-steel at $6.09 \times 10^{-5} s^{-1}$ 168
5.9 Coefficient values for 2.8mm 0.13% C-steel at $6.09 \times 10^{-5} s^{-1}$ 168
5.10 User input variables 173
5.11 Experimental result verification based on simulated results 177
5.12 Modified parameters for verifying FEA interpolation 180

6.1 Error fraction of 0.6 mm 0.13% C-steel sample 188

B.2 2nd stage polynomial coefficients 0.13% C-steel 276
B.1 1st stage poloynomial 0.13% C-steel 277
B.3 Polynomial instability 0.13% C-steel 278
B.4 Polynomial coefficients for aluminium Alloy 279
B.5 Ploynomial instability for aluminium alloy 280
B.6 Polynomial coefficients for brass 281
B.7 Polynomial instability for brass 282
B.8 Polynomial coefficients for carbon steel 283
B.9 Polynomial instability for carbon steel 284
B.10 Polynomial coefficients for stainless steel 285

B.11 Polynomial instability for stainless steel 286
B.12 0.13% C-steel polynomial coefficients 0.6mm 287
B.13 Polynomial instability for 0.13% C-steel 0.6mm 288
B.14 0.13% C-steel polynomial coefficients 0.9mm 289
B.15 Polynomial instability for 0.13% C-steel 0.9mm 290
B.16 0.13% C-steel polynomial coefficients 1.1mm 291
B.17 Polynomial instability for 0.13% C-steel 1.1mm 292
B.18 0.13% C-steel polynomial coefficients 1.3mm 293
B.19 Polynomial instability for 0.13% C-steel 1.3mm 294
B.20 0.13% C-steel polynomial coefficients 1.9mm 295
B.21 Polynomial instability for 0.13% C-steel 1.9mm 296
B.22 0.13% C-steel polynomial coefficients 2.8mm 297
B.23 Polynomial instability for 0.13% C-steel 2.8mm 298

Chapter 1

Introduction

Steels have been widely used in numerous applications within various industries. The two main aspects of steels being cold formed and hot rolled procedures, are routinely being utilized. However, recent research has resulted in hot-rolled steels being uneconomical due to its manufacturing process [1]. Hot rolled steel tends to require more expensive forming stages, when compared to light gauge cold-formed steels; to name a few differences of cold formed steel to hot rolled, whose properties include:

- Homogeneous quality
- Manufacturing simplicity
- Prefabrication quality
- High strength to weight ratio
- Ease of transportation
- Corrosion protection
- Creep resistant at ambient temperatures
- Installation simplicity

In general, due to the stated reasons, a growing trend in utilising use of cold formed metals has been established. As a consequence, cold-formed steel members

are being used within industrial, commercial and residential buildings. Typically the cold-formed metals are formed by means of three methods; press-braking (see Figure 1.1), through roll-forming (see Figure 1.2) or bending break operation. Typically, bending break operation and press braking will be carried out for smaller quantities of material, whilst roll forming will used for larger quantities of the basic sheet material.

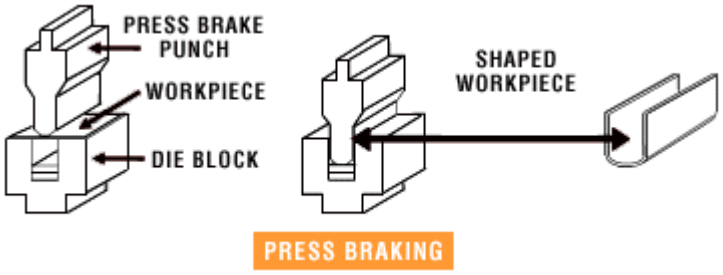

Figure 1.1: Press-braking process

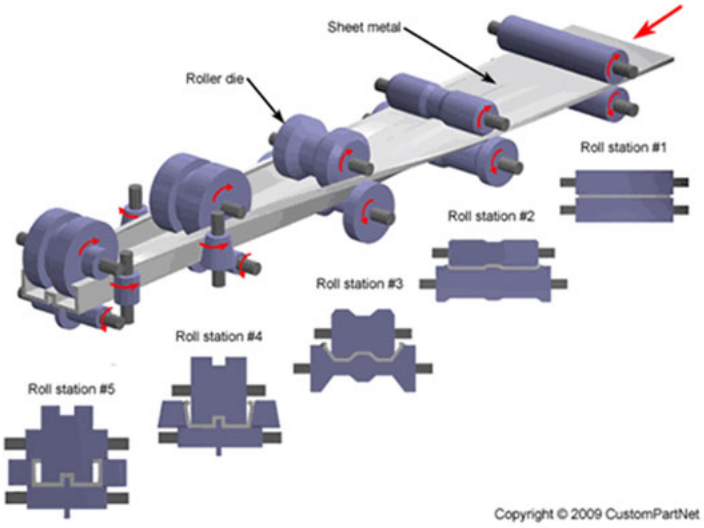

Figure 1.2: Roll-forming process

The use of cold-formed metals came to industry in about 1850s, mainly in the United Kingdom and United States of America. However, their use in commercial and residential building did not begin until 1940s [2]. A trend of utilization of cold formed metals in residential constructions was established by [3] in which it is stated; in USA 500 homes were built by cold formed metals in 1992, 15,000 in 1993 and 75,000 in 1994.

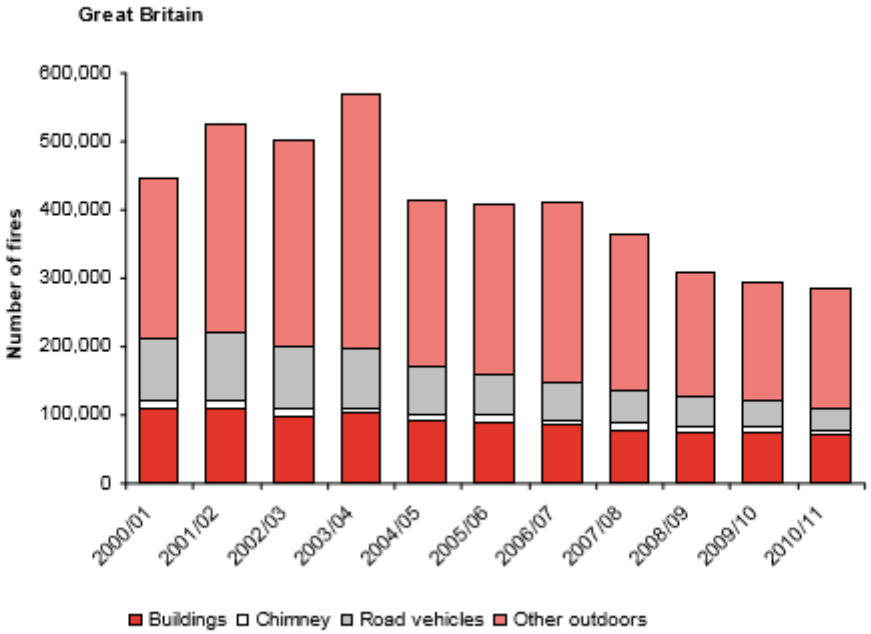

Figure 1.3: Number of house inflicted with fire

With this proven growing trend of using cold formed metals, researchers need to further identify the mechanical properties of such materials. The significance of correctly characterising the mentioned material, grows when considering the number of household fires. Based on a report by National Statistics of UK, 70,000 in 2010/11. Figure 1.3 were involved in house fires which has claimed the life of over 300 people. Out of these numbers 50% of the deaths were due to poor structural analysis. Thankfully, with identifying the importance of research on this topic, since 1946 many institutes as well as as American Iron and Steel Institute (AISI) has created a series of specifications.

1.1 Scope of the work

It is now widely accepted, that most materials have different and defining characteristics in responding to environmental conditions. The characteristics which will not only involve and affect the stress-strain behaviour of the material but also accumulates to mode of failure and damage.

1.1.1 Statement of objective

The main objective of this research is to construct a mathematical model which can identify and predict the behaviour of cold formed metals to assist with modelling of steel behaviour at low strain rates, elevated temperatures and various thicknesses. As such, the model could be used in manufacturing and design tolerance studies. Such a model should enable the user to predict the strength and weaknesses of the material and to also minimise the need for experimental work, while enhancing the reliability of the results. The three parameters were opted in order to gain access to similar studies for the purposes of comparison and parametric study.

The most crucial part of the work enables identifying a relationship which could be generalized for different modes of material behaviour as well as being able to interpolate or in some cases extrapolate its predictions. The model should be constructed in such a way to determine the behaviour under a wide possible array of variables, i.e. strain rates, temperatures and thicknesses.

1.1.2 Specific objectives

1 Conduct a comprehensive study on the experimental tests carried out so far, and to nominate the most suitable empirical model to date; as well as reviewing the mechanical properties and reaction of cold-formed steels at elevated temperatures.

2 Investigate the behavioural trends in the tested materials at elevated temperature. This work involved in measuring the accuracy of the proposed predictive methods.

3 Identifying suitable experimental methods for carrying out the most coherent and comprehensive tests; in order to enable the work to be carried out in variety of strain rate range.

4 Recommission the useable tools and facilities available. In order to increase productivity, reduce time delays and to run the tests in the most economical approach possible.

5 Develop a finite element model capable of simulating the stress-strain behaviour at ambient and elevated temperatures by means of using the ABAQUS package, and to validate the output against experimental results.

6 Introduce a new method of characterising experimental results. In order to define the thickness effects based on set values of coefficients of a polynomial and predict the material characteristics.

7 Construct a new subroutine code, in order to simplify and to minimise the need for experimental work, as well as increasing the accuracy of the stress-strain results.

8 Introduce a modified version of Ramberg-Osgood, which promises to increase accuracy of the prediction.

In general computer simulation can act as a mediator between the theory and the final product. Conducting the experiments to acquire possible prediction of a material behaviour in some cases can prove to be excessively expensive and time consuming and in many a situation it may not be done. Computer simulation will help to bypass the experimentation in many cases and enable the engineer to substantiate the reliability of the product or the structure. Furthermore, in many cases a combination of the experimental, numerical solutions and dynamic material characterisation needs to be proven before being able to execute the FEA model.

Based on the intended use of the mathematical model, the parameters of the equation and the complexity of the model will change. Typical modes of use for this model will be industrial and commercial buildings, forming process, crash worthiness, offshore and aerospace structures. With further investigation on the subject, the aim is to reduce the gap between experimental and the numerical simulation results.

The concept of the mathematical model was derived to ease the operation by simplifying the terms used with acceptable accuracy. This way the engineer using the model can spend time in verifying the results rather than getting in depth with the background theory of the model. Few models will require investigation of the dynamic yield stress and modulus value, whereas others would require a comprehensive description of material behaviour at various conditions. In general, a constitutive model should describe the surrounding boundary conditions of the material as well as the characteristics of the material. Ideally the model has to be mathematically simple, provide accurate final result and not require the user to carry extensive experimental work to obtain input values.

Along with obtaining the appropriate numerical model, an extensive experimental research had to be carried out in order to endorse the constitutive model through means of finding the correct experimental data and determining the constants of the materials. Therefore a relatively simple experimental procedure was generated. The experimental values both helped in verifying the results of the mathematical model and to show existing trends relative to the our experimental variables.

In order to verify the proposed model correctly it was put up against one of the most known mathematical models in this field, established on the basis of power law. In particular the Ramberg-Osgood equation modal was investigated, and a new method of handling its constants was put forth. This investigation lead to second most important aspect of this work, which will be thoroughly discussed in chapter 6.

A third mediatory study was also carried out to establish the trend of stress-strain curves to identify the thickness effect and temperature dependency of the materials through the concept of reduction factors. This study enabled the work to create a similar mathematical model which was in turn examined against the available models.

The explicit finite element method code adopted for this work, comprises of definitions elasticity, plasticity, a strength model, damage criteria, yield criterion, and

modes of failure. In the first instance the model was created to resemble the model used within the experimentation segment, consequently the model was set to be temperature and movement dependent rather than load dependent. The obtained result for each parametric study was then compared to the experimental values in order to verify the simulation. As each section of simulation is confirmed so does the complexity of the model in ABAQUS. The simulation will be further discussed in chapter 5.

1.1.3 Methodology

Given below is schematic of the process based on the methodology. The Schematic represents the way in which the project was carried.

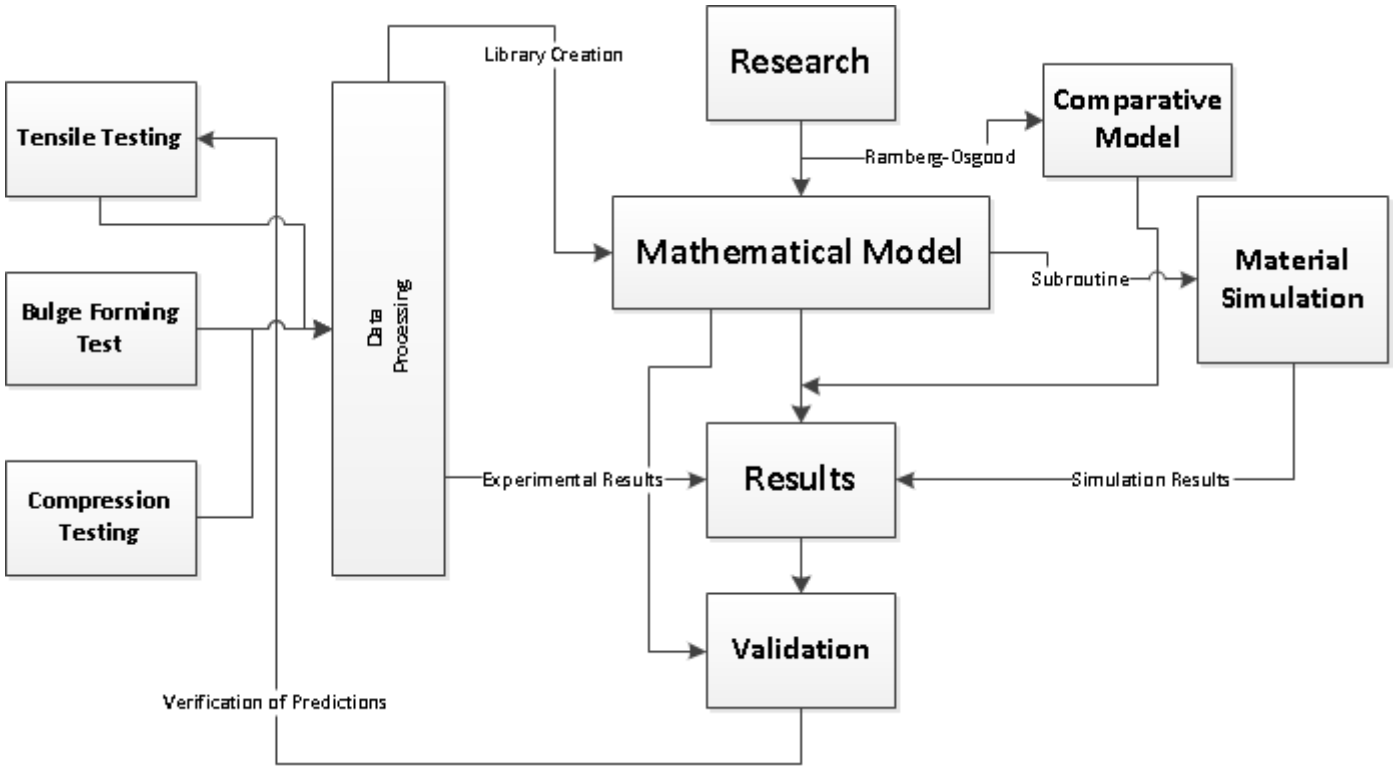

Figure 1.4: Methodology schematic

Upon finalising the background research, experimental work was carried within three categories. Care was taken to gradually increase the limiting strain impact on the specimens tested. These tests were able to provide an accurate set of experimental data, from which it is possible to validate the material model by means of a

computer code. Parallel to this work, the results obtained, were processed by means of code assessment through VBA and MATLAB.

Simultaneously, the preliminary results were assessed against the FEA results, based on a parametric study, for verification purposes; out of which, elastic, elasto-plastic and damage criterion based on minor and major damage limits were evaluated.

Moreover, the mathematical model was constructed at a later stage, which was assisted by creation of a library of coefficients, more on this is explained in chapter 6. The model was written with FORTRAN for communication into FEA. The user inputs were then readily available in ABAQUS.

A model, based on stress as a function of strain in power law format was then considered. The accuracy of two existing models was then evaluated. Subsequently, the rendered results were confirmed by means of repeat test in order to verify the accuracy of the interpolated stress-strain curve.

1.1.4 Content of thesis

The outline of this thesis is as follows:

Chapter 1 Here care was taken to deliver concise and informative preliminary information in format of a general introduction. It describes the problem at hand and the means to solve the issue raised. Finally, the chapter attempts to describe the methodological process and the algorithm used for this problem.

Chapter 2 This chapter aims to accumulate the knowledge of previous works, based on the set objectives within this thesis. Current theories and concepts were investigated; efforts were made to carry the reviews based on the most recent advances in this field.

Chapter 3 This chapter presents the method and means of describing the experimental investigation carried out. As well, concepts related to strain rate influences

upon the behaviour of the material appear.

Chapter 4 Mechanical properties are described and explained, the void in the field related to this research will be presented. Stress-strain plots will be described and explained; as well as a study on reduction factors. The stress dependence to strain rate and thickness as well as temperature will be clarified. New mathematical approach for predicting the behaviour of materials tested. The experimental work carried out will be analysed along with an introductory investigation into the micro-mechanism of the materials.

Chapter 5 The computer based efforts, especially the validation of the experimental results against the FEA results will be justified. The mathematics behind the ABAQUS presentation will be presented as well as means of achieving such FEA model. The parametric study against which the experimental work was weighted will also be present. The polynomial code will be presented and analysed.

Chapter 6 Ramberg-Osgood's mathematical model will be put to test against the proposed model. Additional study will introduce a reformatted version of the Ramberg-Osgood description.

Chapter 7 Presents the conclusion to this work, and outlines the significant findings from the research carried out. Recommendations for future research will be discussed within this chapter.

Chapter 2

Literature Review

It is a proven fact that metals exhibit different characteristics under varied environmental conditions [4]. Due to this fact many researchers all around the world have identified the need to pursue and expand upon their views on this phenomenon.

Within this chapter, the objective is set to identify the progress and background knowledge related to this work. Firstly the understanding of the effect of strain rate upon the material is provided. This is then followed by recognising the effect of temperature as well as a possible means of testing cold formed metals. Typical strain ranges at which the tests are carried out will be examined. Despite, no attempt having been made here to achieve the high strain rates involved, for crash worthiness and penetration, references are provided for the reader to explore this in greater detail.

In general mathematical correlations, will attempt to express the behaviour of the material based upon its dependent and independent values. For this work, in the majority of cases stress will be expressed as a function of strain, temperature, strain rate, damage etc. Such an arrangement is referred to as *constitutive law* or relationship.

The most crucial points to consider whilst constructing such formulae is to consider the class of the material. The best relationship should explain the material behaviour under the widest range of strain rate and temperature. In fact, such an attempt could hardly be made, due to greatly different description of strain classes

at different conditions.

It is worth considering when constructing the relationship, both the stress and strain are point tensors. Therefore, the stress and strain will refer to a single point along the path. In essence, the equation should consider the stress tensor with its three normal and three shear values and the strain tensor including its three normal and three shear values, as well as their time derivatives and additional behavioural defining attributes. The most general form of constitutive law will be expressed by the following:

$$\sigma = f(\varepsilon, \dot{\varepsilon}, T, ...) \tag{2.1}$$

where ε is the strain, $\dot{\varepsilon}$ is the strain rate and T is the temperature.

However these parameters will not be the only derivatives of the constitutive equation; knowing the path dependency and the irreversibility of the plastic deformation, we can conclude the behaviour of every sample will be influenced by its micro-structure response, therefore we have:

$$\sigma = f(\varepsilon, \dot{\varepsilon}, T, microstructure\, response, ...) \tag{2.2}$$

For the sake of simplicity, rather than defining stress and strain in tensor format, scalar components quantities were considered for experiments carried out in one dimensional state of stress and strain.

2.1 Test Method

In order to carry a sound pattern of tests, a sequence of tests were designed to gradually increase the strain level as a means of tackling the constraint imposed according to Considére criterion.

> "Necking begins when the increase in stress due to decrease in the cross-sectional area is greater than the increase in load bearing capacity of the specimen due to work hardening."

$$\frac{d\sigma}{d\varepsilon} = \sigma \quad \Rightarrow \quad \frac{ds}{de} = 0 \tag{2.3}$$

Therefore, the equation 2.3, labels the importance of characterising the onset of the UTS (ultimate tensile stress) in a uniaxial manner and how to extend the strain by offsetting necking instability altogether.

In general there are three ways of carrying a tensile test at elevated temperature.

- Steady State
- Transient State
- ISO test (ISO, 1999)

In steady state testing, the sample is heated to the predetermined temperature and then the load is applied. This process can be applied to both tension and compression, however mechanical properties of the tensile coupon tests does not show great difference [2] initially between the two methods; Therefore, the majority of the researchers tend to adopt tensile tests, if they wish to avoid later buckling or inelastic reserve capacity. There are two means of applying tensile load by this method, either by controlling the strain or controlling the load. In the former the strain rate is kept constant through out, whereas in the load controlled test, the load rate is kept constant. The benefit of the this method arises when upon completion, the stress-strain curve is generated out of the raw data. [5, 6, 7]

In transient state and ISO methods, the test coupon is kept under constant load, and temperature is gradually increased, based on a predetermined temperture rise for the test. This method has been praised by many researchers, as it simulates the situational condition of the metals more realistically, including the effect of creep on the sample [8]. Furthermore figure 2.1 suggests, a transient state method adds an intricacy by requiring the user to convert the temperature states from strain level values to stress.

2.2 Previous Research

Contrary to the hot rolled metals, cold formed metals are shaped at room temperature. The main methods of forming being press braking and roll forming. As a

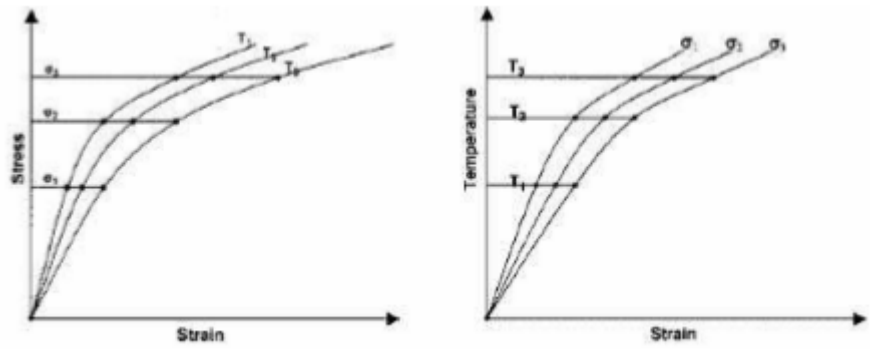

Figure 2.1: Transient state conversion of data to stress-strain, [8].

consequence of this process the yield strength value and to a lesser extent the UTS would tend to get increased. Therefore, elevated temperatures will cause cold formed steels to display mechanical properties different to hot rolled steels. As metals are largely homogeneous material, the properties of each material both in tension and compression would be equal, similar to Figure 2.2.

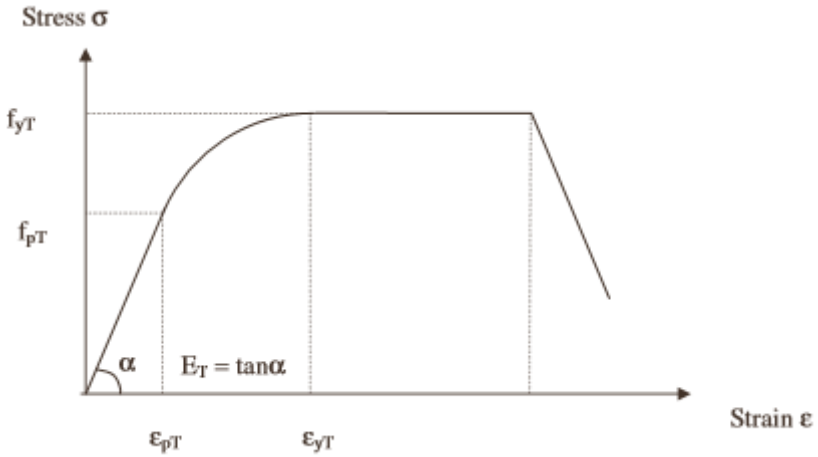

Figure 2.2: Stress-strain curve for steels at elevated temperatures

Where;

- f_{yT}= Effective Yield Strength
- f_{pT}= Proportional Limit
- E_T= Elasticity Modulus
- ε_{pT}= Proportional Limit Strain
- ε_{yT}= Yield Strain

2.2.1 Reduction factor research

Many researchers have attempted to understand and characterise the materials in terms of nominal ratios. One of the most siginifant efforts is the work carried out by Eurocode 3: Part 1.2 [9], which attempts to address the behaviour of material based on temperature elevation. Figure 2.3, nominates the material properties with ambient temperature set as reference. However, an issue with the named figure is the lack of integration between hot rolled steels and cold formed steels, which are inherently different. Further, the figure does not consider the strength of the steel as well as the thickness variation of the gauge length.

Steel temperature θ_a	Reduction factors at temperature θ_a relative to the value of f_y or E_a at 20 °C			
	Reduction factor (relative to f_y) for effective yield strength $k_{y,\theta} = f_{y,\theta}/f_y$	Modified factor (relative to f_y) for satisfying deformation criteria $k_{x,\theta} = f_{x,\theta}/f_y$	Reduction factor (relative to f_y) for proportional limit $k_{p,\theta} = f_{p,\theta}/f_y$	Reduction factor (relative to E_a) for the slope of the linear elastic range $k_{E,\theta} = E_{a,\theta}/E_a$
20 °C	1,000	1,000	1,000	1,000
100 °C	1,000	1,000	1,000	1,000
200 °C	1,000	0,922	0,807	0,900
300 °C	1,000	0,845	0,613	0,800
400 °C	1,000	0,770	0,420	0,700
500 °C	0,780	0,615	0,360	0,600
600 °C	0,470	0,354	0,180	0,310
700 °C	0,230	0,167	0,075	0,130
800 °C	0,110	0,087	0,050	0,090
900 °C	0,060	0,051	0,0375	0,0675
1000 °C	0,040	0,034	0,0250	0,0450
1100 °C	0,020	0,017	0,0125	0,0225
1200 °C	0,000	0,000	0,0000	0,0000

NOTE: For intermediate values of the steel temperature, linear interpolation may be used.

Figure 2.3: Reduction factors for mechanical properties of steel at elevated temperatures, [9]

Based on the Figure 2.2, the reduction factors relative to the ambient temperature can be concluded as below, which will define the reduction factor for the elasticity modulus E_T, proportional limit $f_{p,T}$ and yield strength $f_{y,T}$.

$$k_{ET} = \frac{E_T}{E}$$
$$k_{pT} = \frac{f_{pT}}{f_y} \tag{2.4}$$
$$k_{yT} = \frac{f_{yT}}{f_y}$$

Further to this work British Standard in their 1990 publication [10], created a series of data studying the strength reduction factors of steels. The work conducted the tests within a range of 200°C to 600°C, in which the yield stresses are corresponding to 0.5, 1.5 and 2.0% strain level.

Strain	Strength retention factors at a temperature (in °C) of:								
%	200	250	300	350	400	450	500	550	600
0.5	0.945	0.890	0.834	0.758	0.680	0.575	0.471	0.370	0.269
1.5	1.000	0.985	0.949	0.883	0.815	0.685	0.556	0.453	0.349
2.0	1.000	1.000	1.000	0.935	0.867	0.730	0.590	0.490	0.390
NOTE Intermediate values may be obtained by linear interpolation.									

Figure 2.4: Strength reduction factor based on british standard, [10]

On the basis of these agencies, significant number of research investigations were carried out. Complying with the regulations, teams of researchers conducted various tests with various materials and testing procedures, namely transient states tensile testing and steady state tensile testing (see fig 2.1).

Similar work of Outinen et al. [11], followed the trend of investigating the transient and steady state variable materials, which lead to acquisition of reduction factors of yield stress and elastic stress. Their findings on elastic modulus reduction factors of a 2mm thick zinc coated cold rolled steel, was in good agreement to Eurocode 3 part 1.2, but they could not agree on the values derived for yield stress reduction.

One of the ground breaking works was carried out by Makelainen and Miller in 1983 [12]; in this investigation on galvanized sheet steel Z33, both steady state and transient studies were conducted. The outcome of the investigation was that higher loading rates would yield higher yield stress and ultimate stress values. Moreover, they managed to fit a reduction factor equation to their steady state elastic modulus at temperature T_s:

$$\frac{E_T}{E_{20°C}} = -0.46tanh(\frac{T_s - 550}{250}) + 0.56 \tag{2.5}$$

The work concluded by defining the reduction factor for yield strength and elastic modulus in the transient state method.

$$\frac{\sigma_{y,T}}{\sigma_{y,20°C}} = 1.008 - 0.1314exp(0.0047(T_s) - 148.3°C)) \quad 20 \leq T_s \leq 500°C \tag{2.6a}$$

$$\frac{\sigma_{y,T}}{\sigma_{y,20°C}} = \frac{104°C(1 - T_s/1135°C)}{T_s - 356°C} \quad T_s > 500°C \tag{2.6b}$$

$$\frac{E_T}{E20°C} = 1.01 - 0.139exp(0.007(T_s - 346°C)) \tag{2.6c}$$

Further [13] on the basis of the work by [14] managed to construct a polynomial equation of the reduction factor of yield stress:

$$\frac{F_{y,t}}{F_{y,0}} = 1 - \frac{5.3T}{10^4} + \frac{4.0T^2}{10^6} - \frac{1.9T^3}{10^8} + \frac{1.7T^4}{10^{11}} \tag{2.7}$$

where $F_{y,T}$ is the yield stress (MPa) at temperature T(°C) and $F_{y,0}$ is the yield stress (MPa) at ambient temperature.

The elastic modulus reduction factor is followed as:

$$\frac{E_T}{E_0} = 1 - \frac{3.0T}{10^4} + \frac{3.7T^2}{10^7} - \frac{6.1T^3}{10^9} + \frac{5.4T^4}{10^{11}} \tag{2.8}$$

where E_T is the modulus of elasticity (MPa) at temperature T(°C) and E_0 is the modulus of elasticity (MPa) at ambient temperature.

So far none of the researchers had managed to touch upon sheet thickness effect, nor to relate their proposed equation with this effect in mind. However, in the work carried out by [6]; they managed to develop a set of equations based on range of temperatures although the study was conducted for variation of material thickness, which is incorporated within their equations. Therefore, the thickness parameter is incorporated within the trend line. Both low and high strength materials were investigated, as follows with temperature ranging from 100°C to 800°C with 100°C intervals. The tests were based on steady state method (see fig 2.5)

$$\frac{f_{y,T}}{f_{y,20}} = 1.0 \qquad 20°C \leq T < 500°C \quad (2.9a)$$

$$\frac{f_{y,T}}{f_{y,20}} = 0.964 + 0.00045T - 3.08.10^{-6} + 1.969.10^{-9}T^3 \quad 100°C \leq T \leq 500°C \quad (2.9b)$$

$$\frac{f_{y,T}}{f_{y,20}} = 1.514 - \frac{0.0144T}{f_{y,20}^{\frac{1}{5}} + 4.72} \qquad 400°C \leq T \leq 750°C \quad (2.9c)$$

$$\frac{f_{y,T}}{f_{y,20}} = 0.1 \qquad T = 800°C \quad (2.9d)$$

Equations 2.9 were composed in order to determine the yield strength, based on the reduction factor curves.

In equations 2.10 below we can observe the corresponding reduction factors for the elasticity modulus.

$$\frac{E_T}{E_{20}} = 1.0 \qquad 20°C \leq T \leq 100°C \quad (2.10a)$$

$$\frac{E_T}{E_{20}} = 1 - 0.0014(T - 100) \qquad 100°C < T \leq 500°C \quad (2.10b)$$

$$\frac{E_T}{E_{20}} = \frac{1 - \frac{T}{1200}}{0.00122T + 0.3} - 0.203 \qquad 500°C \leq T \leq 800°C \quad (2.10c)$$

It is worth noting the following analysis was carried out on the basis of figure 2.5.

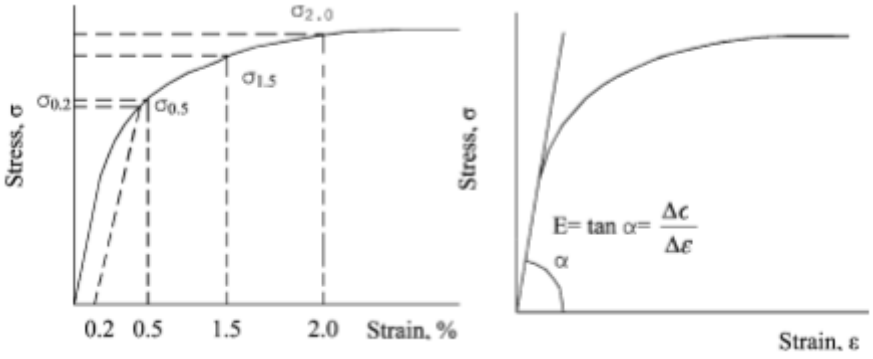

Figure 2.5: Reduction factor strain levels based on stress-strain curve [6]

Most commonly the proof stress of 0.2% as well as the 0.5% total elongation will be subject of defining the proof strength values at ambient temperature. However,

with elevated temperatures additional strain levels will also be investigated for determining the yield strength. The proof stress value is commonly accepted to be considered as the intersection point of the stress strain curve parallel to the proportional line offset at 0.2% strain level as shown. Meanwhile, other yield strength values will correspond to the intersection point of stress-strain curve and to the non-proportional line specified at the designated total strain level, figure 2.5.

An extension to the worked carried out by Lee et al [6], was conducted by Outinen and Makelainen [8], in which the mechanical properties of cold formed steel was studied in both steady state and transient state methods both at elevated temperature and after cooling of the specimen. The work endorsed [11] the findings with respect to steady state at elevated temperature. With respect to the cooling effect on the materials, it was observed that some mechanical properties returned to their original nominal values. The figure below signifies their deduction of cooling effect, based on a Square Hallow Structure (SHS); every test is signified based on the dimension given in mm.

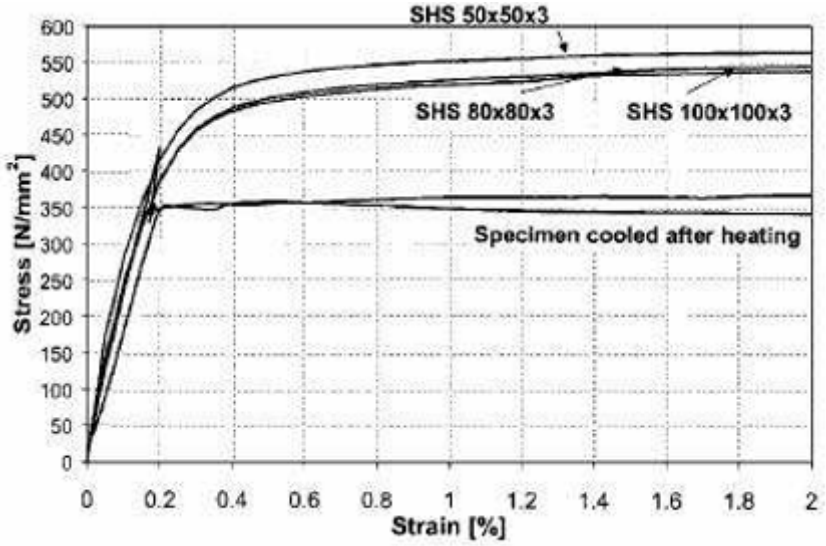

Figure 2.6: Mechanical properties comparison between elevated temperature steel element and after cooling, [8]

Ranawaka and Mahendran [7], sought to follow the same principle for defining the material properties of cold formed steels at elevated temperature. Contrary to the previous works, they proposed a set of empirical equations which would define the reduction factors of yield stress and elasticity modulus for certain ranges of temperature. The significance of their work relies on separating the empirical

equation in sets of low strength and high strength material of various thicknesses with variation in material grade. However, due to an insignificant separation in the results of high strength and low strength in elastic moduli (E_T/E_{20}), a single equation was proposed above $100°C$. In what follows E_T and E_{20} are the elastic moduli at elevated and ambient temperature, respectively. The researh was carried out on G550 and G250. G550 is a hot dipped zinc/aluminium alloy with minimum yield strength of 550 MPa and limited ductility. The chemical properties of G550 is as followed:

Carbon (C) 0.2%

Phosphorous (P) 0.04%

Manganese (Mn) 1.2%

Sulphur (S) 0.03%

Similarly G250 has a minimum yield strength of 250 MPa, with the following chemical composition:

Carbon (C) 0.22%

Phosphorous (P) 0.04%

Manganese (Mn) 1.7%

Sulphur (S) 0.03%

The proposed equation for **G550**:

$$\frac{f_{y,T}}{f_{y,20}} = -0.00016T + 1.0003 \qquad 20°C \leq T \leq 200°C \tag{2.11a}$$

$$\frac{f_{y,T}}{f_{y,20}} = 0.97 - \frac{(T-200)^{1.81}}{58500} \qquad 200°C < T < 600°C \tag{2.11b}$$

$$\frac{f_{y,T}}{f_{y,20}} = -0.00037T + 0.3363 \qquad 600°C \leq T \leq 800°C \tag{2.11c}$$

The proposed empirical equations for **G250**:

$$\frac{f_{y,T}}{f_{y,20}} = -0.0007T + 1.014 \qquad 20°C \leq T \leq 200°C \tag{2.12a}$$

$$\frac{f_{y,T}}{f_{y,20}} = 3.7 - \frac{(T - 74^{0.15}}{0.736} \qquad 200°C < T \leq 800°C \tag{2.12b}$$

$$\tag{2.12c}$$

Elastic Modulus equations for **G550** and **G250**:

$$\frac{E_T}{E_{20}} = 1 \qquad 20°C \leq T \leq 100°C \tag{2.13a}$$

$$\frac{E_T}{E_{20}} = -0.0013T + 1.11297 \qquad 100°C \leq T \leq 800°C \tag{2.13b}$$

In 1943, Ramberg and Osgood [15] defined a simple formula, in order to characterise the stress-strain curve by means of three parametrs; Young's modulus and two secant yield strengths. The equation was endoresed by three metals. Namely, Aluminium alloy, stainless steel and carbon steel. However, since 1943 advances have been carried out to generalise the Ramberg-Osgood equation. One such work was carried out by Ranawaka and Mahendran [7]. In particular an adjustment to the Ramberg-Osgood equation was made. The value η_T (see 2.14) has gone under much speculation within the last few years. Ranawaka, proposed two new equation for a derivation of η_t; in which a fixed value of 0.86 for β, applied both at high and low strengths. The proposed β value was also recommended by Dolamune Kankanamge (2009) [16].

The proposed equation by Ramberg-Osgood:

$$\varepsilon_T = \frac{f_T}{E_T} + \beta \left(\frac{fy, T}{E_T}\right) \left(\frac{f_T}{f_{y,T}}\right)^{\eta_T} \tag{2.14}$$

Applies to the proposal put forth by Ranawaka:

For **G550** Steel:

$$\eta_T = -3.05x10^{-7}T^3 + 0.0005T^2 - 0.2615T + 62.653 \qquad 20°C \leq T \leq 800°C \tag{2.15a}$$

For **G250** Steel:

$$\eta_T = 0.000138T^2 - 0.085468T + 19.212 \qquad 350°C \leq T \leq 800°C \tag{2.15b}$$

Where:

η_T is the found from strain corresponding to a given f_T at temperature T.

E_T is the modulus of elasticity

$f_{y,T}$ is the yield strength at temperature T.

In 2007, Chen and Young [5] carried out an investigation to present mechanical properties of G550 and G450 steels sheet with yield strength, dependent upon thickness. The pair conducted their tests under the two methods of steady state and transient state. A correlation (2.16) given below was proposed along with a figure (2.7) of ranges to suit variation of temperatures. With reference to the work conducted by Ranawaka and Mahendran [7], Chen and Young [5] claimed their proposal predicts non-conservatively when compared with cold formed carbon steel test results, due to them establishing their predictions on hot rolled steel test results [5].

	Eq. (1)			
G550 1.0 mm	Temperature (°C)	$22 \leqslant T < 300$	$300 \leqslant T < 450$	$450 \leqslant T < 1000$
	A	1.0	0.9	0.02
	B	22	300	1000
	C	2.78×10^3	4.8×10^6	9×10^8
	n	1	3	3
G450 1.9 mm	Temperature (°C)	$22 \leqslant T < 300$	$300 \leqslant T < 650$	$650 \leqslant T < 1000$
	a	1.0	0.95	0.105
	b	22	300	650
	c	5.56×10^3	1.45×10^5	5×10^3
	n	1	2	1

Figure 2.7: Coefficients of proposed equation 2.16 for yield strength, [5]

Chen and Young proposed the yield strength:

$$\frac{f_{0.2,T}}{f_{0.2,normal}} = a - \frac{(T-b)^n}{c} \tag{2.16}$$

Where $f_{0.2,normal}$ is the yield strength at ambient temperature and $f_{0.2,T}$ is the yield strength at the temperature T(°C).

A problem evident by the proposed equation 2.15a [16], is the of lack accuracy in predicting stress and strain in cold formed carbon steel for temperatures ranging from 20°C to 650°C. This point was also challenged and discussed by Chen and Young [5] who suggested a more comprehensive strain combination for two regions:

$$\varepsilon_T = \begin{cases} \frac{f_T}{E_T} + 0.002(\frac{f_T}{f_{y,T}})^{\eta_T} & f_T \leq f_{y,T} \\ \frac{f_T - f_{y,T}}{E_{y,T}} + \varepsilon_{u,T}(\frac{f_T - f_{y,T}}{f_{u,T} - f_{y,T}})^{m_T} + \varepsilon_{y,T} & f_T > f_{y,T} \end{cases} \tag{2.17}$$

and in which their data supported three empirical fits:

$$E_{y,T} = \frac{E_T}{1 + 0.002 n_T E_T / f_{y,T}} \tag{2.18a}$$

$$n_T = 20 - 0.6\sqrt{T} \tag{2.18b}$$

$$m_T = 1 + T/350 \tag{2.18c}$$

2.3 Classification of Strain Rate Regimes

In tensile test, metallic material will follow elastic and plastic straining. Plastic deformation is generally considered to be influenced by rate of deformation far more than elasticity. Since deformation behaviour is influenced by the chosen mechanism; identification of dynamic ranges needs to be considered when dealing with strain rate as an influential parameter in its characteristic. The work carried out by Lindholm, 1971 [17] and Zukas,1983 [18], has resulted in the following figure:

2.3.1 Creep rate regime

As illustrated by the figure 2.8, slow strain rates of between 10^{-6} to 10^{-5} s^{-1} represent creep behaviour. Phenomenologically, creep is defined as a process in which work hardening and recovery of the material occurs at similar opossing rates of strain.

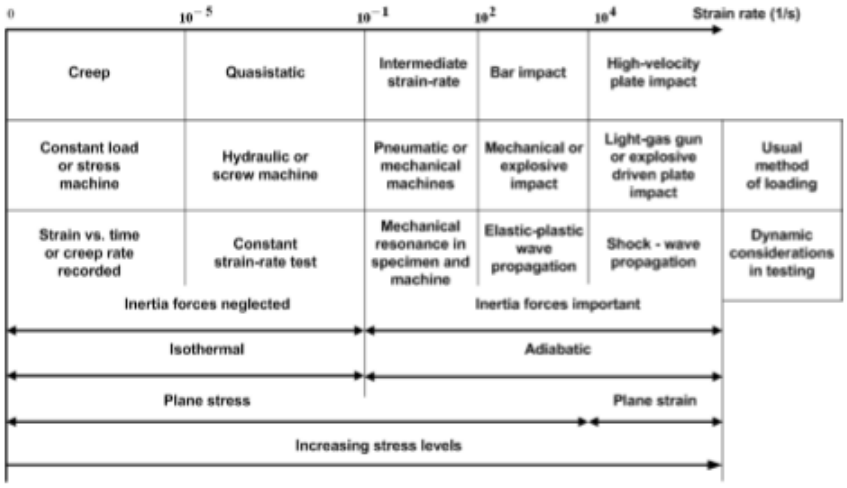

Figure 2.8: Dynamic range of strain rates [18]

It should be noted creep behaviour is usually observed at elevated temperatures, which would exceed 0.3 of the melting point, according to Janghorban, 1991[19].

2.3.2 Quasi-static rate regime

Medium strain rates of the order of 10^{-5} to 10^{-3} s^{-1}, are typically noted as quasi-static. The conventional method of testing at such rate is conducted by means of screw driven machine with pen recorders as the data acquisition device. It should be noted that stress-strain curves in this regime are used as the inherent property of the material providing valid descriptions only at this regime. The capability to test at such strain rate only became available during the first half of the 20th century. During application of load greater precision in flow control for hydraulic systems enabled continuous measurement. It was also made possible to speed up or slow the tests in a hands-off approach. Capability to control the rate of testing was introduced firstly to screw driven machines and later on hydraulic systems, which prohibited yield drops during testing. Provided below is the schematic of a common screw driven tensile machine of the type used for the present experiments.

2.3.3 Intermediate strain rate regime

As with the gradual increase of strain rate, stress-strain properties will subsequently be influenced and changed. At ranges close 10^{-1} to 10^{2} s^{-1}, slightly more specialized techniques of testing will play a part. For such rates, energy storage systems will be

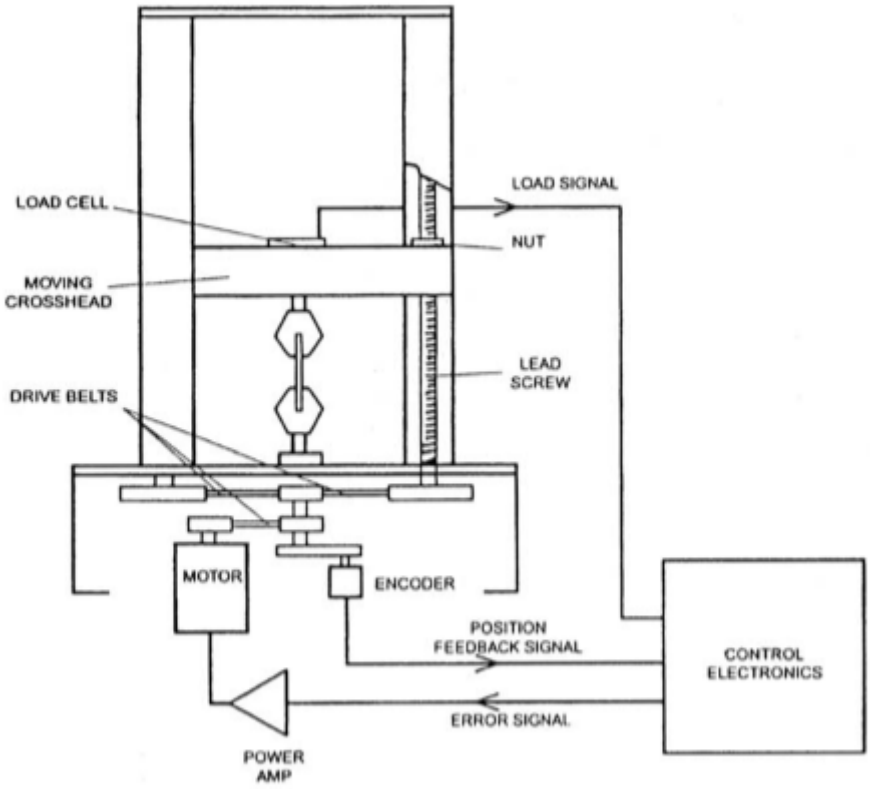

Figure 2.9: Electromechanical screw driven testing machine, [20]

required to supply consistent energy level to the specimen. The most conventional methods of testing would therefore be related to a machine with stored potential energy with a moving mass; such as a pendulum, drop hammer and rotating flywheel. For the purpose of measurement,a speed oscilloscopes and rapid acquisition systems are most commonly used.

2.3.4 High strain rate regime

In engineering sense strain rates above 10^3 s^{-1} are treated as high strain rates, due to the rapid plastic deformation of the specimen. Uniform stress would occur within the sample. It should be noted that the uniformity of the stress will in many cases be related to the method of load application and geometry of the sample itself. In the majority of cases, the deformation is achieved by impact or impulsive methods. The sample is chosen to be as small as possible relative to and perpendicular to the direction of applied load. Adopting a relation to explain the strain rate for this regime will depend greatly on temperature generation due to transition from nominally isothermal conditions to an adiabatic condition; Moreover, inertia, friction and

wave propagation will be important material response.

Split Hopkinson Pressure Bar (SHPB) or Kolsky apparatus is commonly used for high strain experimental investigations. The Hopkinson technique hinders on defining the dynamic stress, strain occurring at the end of the bar by means of observing the experiment. It is worth noting this techniques records the deformation in form of compression rather than tension; however, modifications can be made to load the sample in uniaxial tension or torsion.

As mentioned the most common setup for a Hopkinson test is conducted in compression mode. The apparatus consists of two symmetric bars in the form of pressure bars, alignment fixtures and bearing to enable smooth transition of the pressure bars and to assist with striking the sample with accurate axial alignment. Additionally, a gas gun is utilized as a means of creating kinetic energy and providing acceleration. Strain gauges will also be attached to the two pressure bars for measurement to be taken from the stress wave propagation.

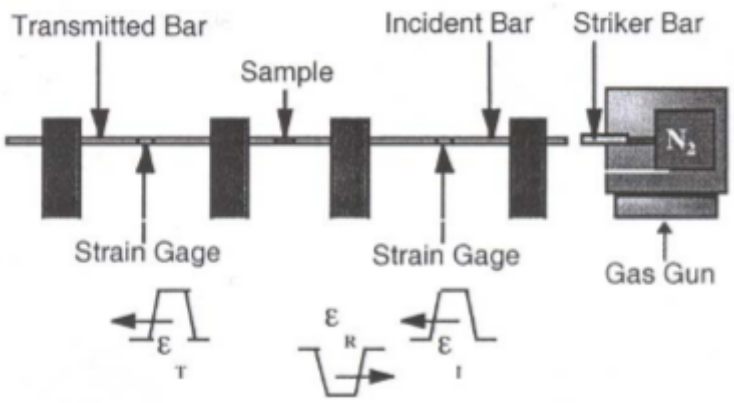

Figure 2.10: Split hopkinson pressure bar apparatus, [21]

2.4 Uni-axial Test

The most widely used test for defining and characterising material behaviour is commonly conducted in a uni-axial mode i.e. tensile test. Tensile tests can be carried out for determining modulus of elasticity, elongation, yield strength and many other behavioural traits. Materials, where a clear yield strength may not be pointed (smooth yielding), a proof stress which is the stress level at an offset strain 0.002 is used.

The samples used for a tensile test are usually machined to standard dimensions based on governing body for sake of consistency with other works and later comparison of the results. Samples could be of flat or circular cross sectional geometry and any other uniform cross section, although round samples are generally utilised for metallics specimens. It should be noted the strength values extracted from a tensile test, may not accurately represent the correct state of the specimen. As environmental conditions, or machining imperfections such as surface toughness and dimensioning errors may arise.

2.4.1 Tensile machine effect on tensile properties

Examinations of testing machines and their limitations have been found to influence the fracture behaviour and stress strain curve. As stated by Dieter 1998 [22] testing machines deflect under load. Therefore, the displaced crosshead of a testing machine may not be an accurate representation of elongation and deformation of the sample. As a result a series of calibrations and corrections are necessary to be carried out. The equation below represents the elastic displacement of the sample [22].

$$\Delta_E = \frac{\sigma L}{E} \tag{2.19}$$

The components of crosshead displacement (Δ_C) could then be summed as elastic displacement (Δ_E) and plastic displacement (Δ_p). However, one needs to account for the deflection of the testing machine Δ_m. Therefore, the total crosshead displacement is:

$$\Delta_c = \Delta_E + \Delta_p + \Delta_m \tag{2.20}$$

$$\Delta_c = \frac{PL}{AE} + E_p L + \frac{P}{K} \tag{2.21}$$

Where K is the machines stiffness and may be represented as [23]:

$$K = \left(\frac{\Delta_c}{P} - \frac{L_0}{A_0 E}^{-1} \right) \tag{2.22}$$

Where L_0 and A_0 are specimen's original length and cross sectional area, respectively. When $\Delta_E + \Delta_m$ are removed from a load vs. displacement plot, there

remains a true measure of the specimen's plasticity. This applies despite an unrealistic modulus arising from the compounded elasticity, a correction adopted for the present study.

2.4.2 Deformation

For a ductile material tensile testing would reveal the elastic, plastic necking and deformation sections [24]. Once a ductile material is displaced below its yield strength, as presented in figure 2.11 , a series of slippage within the system occurs however the atomic bonds remain intact and are not broken. Upon removal of the load, the original state of the sample is restored. The energy gained and lost is referred to as elastic energy W_e. The elastic energy is commonly ignored when describing the total energy of a system W_t [24]. Since proportional limit of a sample is gradually exceeded over the volume of the sample, there are not clearly defined yield point between the elastic and plastic region for the majority of metals.

Upon surpassing the yield strength of a material, the atomic structure of the material will become distorted to an extent that they do not recover their original state; such deformation is refereed to as plasticity. The plastic energy, W_p, is accounted as the dissipitated energy prior to necking, which relates to the bulk material in the gauge length . Commonly, plastic energy plays the bigger role for describing the total energy of a system, as suggested by Mahmudi et al [24], plastic energy may be written as:

$$W_p = W_0 l_0 T_0 w_p \tag{2.23}$$

Where w_p is referred to as plastic energy per unit volume to the limit of ε_u as the true uniform strain.

$$w_p = \int_0^{\varepsilon_u} \sigma d\varepsilon \tag{2.24}$$

The deformation in metals usually occurs by sliding of metal crystallines over slip planes. The deformations within a micro-structure are points of defects which have been created due to a number of reasons. For a plastic deformation the displacement occurs at a higher rate than the rate of stress, as a result cross sectional area reduces

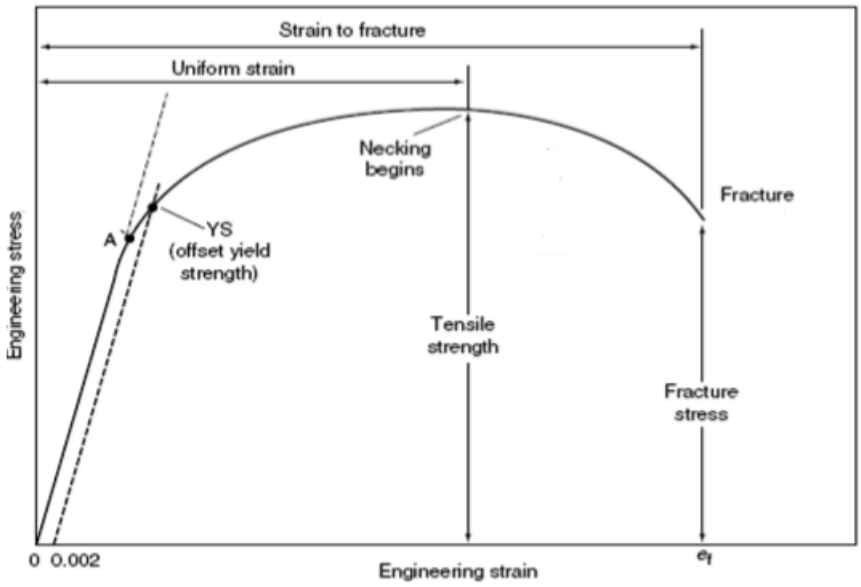

Figure 2.11: Typical engineering stress-strain curve [24]

along the gauge length. For a ductile material, such principle will work along the sustained stress to the sample intensifies gradually by increase of strain as a result of strain hardening, which could lead to necking and failure. Strain hardening or otherwise known as work hardening is caused due dislocation storage and in proportional to dislocation density [25]. The accumulation of the dislocations due to dislocation storage is referred to as statistically stored dislocation. The interconnection between the accumulated dislocation and grain boundaries would further prevent their movement towards the crystal lattice. This impedance will cause dislocation pile up around the crystal lattices, therefore a back stress is developed which would resist the applied stress [22].

Upon exceeding the stress over the ultimate tensile strength, the cross sectional area of the specimen reduces locally in the form of necking. Therefore the concentration of plastic deformation results in a non-uniform deformation. Subsequently, an instability is formed in the flow stress of the material. The diffuse necking could lead to fracture for round samples, however for sheet samples such necking could result in second instability termed as localized necking [26]. The localized necking would be formed at an angle to the specimen, as illustrated in figure 2.12. The formation of diffuse necking is related to plane stress which is caused by increased strain rate and strain [27] which is characterised by thinning of samples thickness as well as contraction in its width; the thinning effect would result in thin sheet fracture which would create a two knife edge fracture [27].

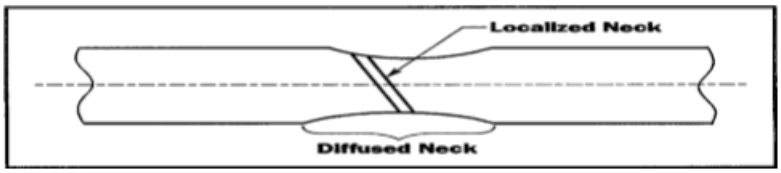

Figure 2.12: Localized necking in flat samples [26]

2.4.3 Ductile fracture

The occurrence of fracture in a homogeneous solid is caused when one or a combination of mechanical stresses, temperature and chemical effects will separate the solid into two or more sections [28]. Fracture energy may then be related to the necked region as well as cross sectional changes. Fracture energy W_f is expressed in terms of tearing energy per unit area:

$$W_f = W_0 T_0 w_f \tag{2.25}$$

Therefore, accumulation of ductile plastic damage will result in ductile failure; which is continued by crack propagation. For ductile failure to occur, significant microscopic mechanisms arise such as void nucleation, shear bond movement and propagation of micro cracks. The initiation of fracture would mean degradation of the material, therefore stiffness and ductility of the material is reduced [29]. Additionally, for a fracture in a material, two modes of failure may occur; namely, brittle cleavage fracture damage and transgranular fracture depending on the temperature of the tests.

2.4.3.1 Brittle cleavage fracture

Brittle fracture is a stress controlled process which is associated with nucleation [30] of separation mechanism lying normal to the stress plane typical of lower temperatures. It occurs when crack propagates rapidly through the cross sectional area without much plastic deformation. The pile up of dislocations along the slip planes would result in shear stress that would would initiate micro-cracks.

2.4.3.2 Transgranular fracture

The more common mode of ductile fracture would initiate with micro-cracks due to elevated temperature along strain planes [30]. Formation of voids by nucleation and coalescence occurs with local plastic flow and therefore they are strain controlled inconstrast to brittle fracture. It should be noted void formation is heavily dependant upon strain and hydrostatic stresses of a system. The void formation is initiated when the applied stress exceeds bonding strength of the atoms around the grain boundaries. The bond strength is associated with the attraction force between atoms per unit area which was expressed by Anderson [31]:

$$\sigma_c \approx \frac{E}{\pi} \tag{2.26}$$

Unlike the former fracture, transgranular fracture would exhibit high degree of plastic deformation around the fractured tip. This type of ductile fracture may be categorised in three sections; shear fracture associated with slow tearing mechanism, cup and cone fracture associated with mildly ductile materials and rupture fracture associated with very ductile materials [22].

Shear fracture occurs with presence of shear stress during the plastic deformation. The cause of such fracture mode is due to extensive slip on slip planes. Since the highest stress builds up at 45° to the stress plane, the shear fracture would occur at the same angle value normal to the gauge length. The stress required to reach shear fracture is known as critical resolved shear stress, and is described as the stress required to break the metallic bond for a slip to take place in a single crystal [32]. An SEM investigation of shear fracture, would result in grey and fibrous surface to be seen, the surface will also show dimples which are elongated parallel to the major principle stress plane.

The cup and cone fracture, is mostly seen with moderately ductile materials, the onset of necking for the grade of material occurs at its ultimate tensile strength. The formation of necking at the ultimate load, causes stress triaxiality to form. As illustrated in figure 2.13a, necking phenomena cause small cavities to form in its centre point, by means of nucleation between the cavities. A crack is formed which

is perpendicular to the applied stress, and would result in a rough flat surface separation. The separation will continue along to the edge of the gauge width, where significant plane stress is present. As mentioned before, voids in high plane stress region will be based on shearing strain, therefore the flat separation propagates into a 45° crack. The SEM investigation on the centre and edge of the fractured tip shows equiaxed dimples and elongated dimples, receptively. Figure 2.13 illustrates this point.

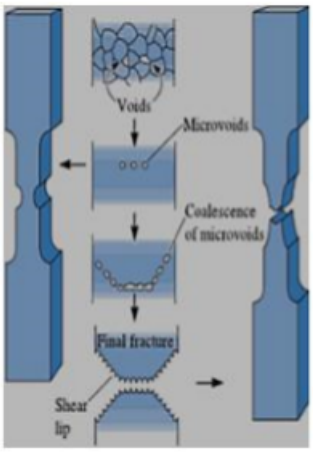

(a) Ductile stages

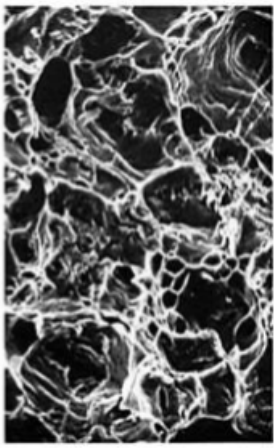

(b) Central section

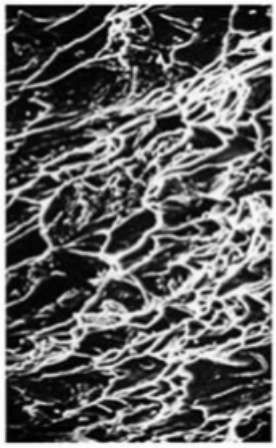

(c) Edge section

Figure 2.13: Cup and cone formation [32]

The third and final mode of transgranular ductile fracture, occurs based on a "tunnelling" crack effect. Crack tunnelling is expressed for cases with faster crack formation in the centre with high triaxiality and slow crack propagation to edges of the sample with low stress biaxiality/triaxiality. It is the difference between high and

low stress zones which causes flat fracture at the centre of the sample and slanted fracture towards the edges.

2.4.4 Deformation prediction

Deformation prediction of a tensile fracture is based on defining the displacement of a point from its initial position to its final position. The mapping of this displacement is expressed by a matrix **F** of deformation gradient:

$$\mathbf{F} = \frac{\partial \mathbf{x}}{\partial \mathbf{X}} \tag{2.27}$$

where x and X are the final and initial positions respectively.

However, matrix **F** may also be expressed in terms of its components, which are the straining component and the rotating component. Straining component is associated with stretch matrix **V**, and the rotating component by the rotation matrix **R**. It is worth noting the rotation matrix is defined on the basis of a rigid body rotation. Therefore:

$$\mathbf{F} = \mathbf{V} \times \mathbf{R} \tag{2.28}$$

The rate of change of the point from its initial position is defind as the velocity ν. It may be calculated as the partial derivative of initial position.

$$\nu = \frac{\partial x}{\partial t} \tag{2.29}$$

As such, strain rate and rate of rotation may be derived as:

$$\dot{\varepsilon} = \frac{1}{2}\left(\left[\frac{\partial \nu}{\partial x}\right] + \left[\frac{\partial \nu}{\partial x}\right]^T\right) \tag{2.30a}$$

$$W = \frac{1}{2}\left(\left[\frac{\partial \nu}{\partial x}\right] - \left[\frac{\partial \nu}{\partial x}\right]^T\right) \tag{2.30b}$$

Therefore the effective Von-Mises stress q is:

$$q = \sqrt{3/2s : s} \tag{2.31}$$

In which s, represents the Cauchy stress deviatoric part:

$$s = PI + \sigma \tag{2.32}$$

P represent the hydrostatic pressure, defined as:

$$p = -1/3\sigma : I \tag{2.33}$$

where σ is the applied uni-axial stress defined as q.

2.4.4.1 Elastic-plastic deformation

Elastic-plastic deformation in its primary form is referred to as incremental plastic theory. Where plastic deformation is concerned with ductile fully plastic fracture with small displacement, stress may be described as total strain. Incremental plastic theory is based on three rate evaluations namely strain rate, hardening and flow rule. Strain rate decomposition is consistent of summation of elastic strain rate and plastic strain rate.

$$\dot{\varepsilon}_T = \dot{\varepsilon}_{el} + \dot{\varepsilon}_{pl} \tag{2.34}$$

Flow rule is defined as a limit with purely elastic response described by yield function f. Yield function is dependent upon true stress σ, temperature θ and hardening parameter H of the material. Additionally, for an isotropic material behaviour the yield function f to equal to the uni-axial Von Mises stress q.

$$f(\sigma, \theta, H) < 0$$
$$f = q = \sqrt{3/2s : s}$$

For the elastic deviators, s and ε_{el}:

$$s = 2G\varepsilon_{el}$$

where G is the shear modulus.

Hardening rate of an isotropic material is defined as the uniform change of yield surface in all principle directions, that is decrease of yield stress will reduce the

stress with plastic straining in x, y, z uniformly. A note to make is isotropic yielding is in independent of pressure stress, except for porous metals.

In situations related to porous metals, Gurson's plasticity theory which is developed on the assumption of yield stress being a function of equivalent plastic strain may be used. The criterion expressed by Gurson and later on modified by Tvergaard may be expressed as [33]:

$$\Phi = \left(\frac{q}{\sigma_y}\right)^2 + 2q_1 f^* cosh\left(-q_2 \frac{3p}{2\sigma_y}\right) - \left(1 + q_3 f^{*2}\right) = 0 \tag{2.36}$$

where hydrostatic pressure p is expressed as:

$$p = -\frac{1}{3}\sigma : I \tag{2.37}$$

For a unit matrix denoted as I. Terms q_1 and q_2 are coefficients of void volume fraction, q_3 denoted as coefficient of pressure. Function f^* expresses the stress carrying capacity that is associated with void coalescence [34]. The stress carrying capacity function is described based on void volume fraction:

$$f^* = \begin{cases} f & if \quad f \leq f_c \\ f_c + \dfrac{\bar{f}_F - f_c}{f_F - f_c}\left(f - f_c\right) & if \quad f_c < f < f_F \\ \bar{f}_F & if \quad f \geq f_F \end{cases} \tag{2.38}$$

where:

$$\bar{f}_F = \frac{q_1 + \sqrt{q_1^2 - q_3}}{q_3} \tag{2.39}$$

Term f_c is the critical value of the void volume fraction at initiation and f_F is the value of void volume fraction, when f^* is reduced to zero. The material is considered as failed when $f \geq f_F$. Contrary to a porous material, for fully dense material ($f = 0$), Gurson's criterion 2.36 will become equal to Von Mises condition. For the condition where $f = 1$ the material has failed, since the stress carrying capability is reduced to zero. Therefore, a plasticity model for a porous metal may be only adaptable for $f < 0.1$.

2.4.4.2 Engineering stress-strain

Engineering or otherwise known as nominal stress strain values are dependent upon geometrical aspects of the specimen tested and do not account for differential change in the dimension of the specimen. As a consequence, making use of nominal values will not accurately describe the characteristics of a material. However, true stress-strain values of a specimen account for instantaneous dimensions of a tensile sample.

$$\sigma = \sigma_{eng}(1 + \varepsilon_{eng}) \tag{2.40a}$$

$$\varepsilon = ln(1 + \varepsilon_{eng}) \tag{2.40b}$$

Although for small values of strain, the difference between true and engineering strain may be neglected. Therefore, true stress may be correlated to true strain; the modulus of elasticity in this case is assumed to be constant both at original state and elongated state.

$$\sigma = E\varepsilon \tag{2.41}$$

At strains over 5%, the most commonly used expression is based on Hollomon's power law, which denotes the logarithmic relation between true stress and strain by proportionality constant K [35].

$$\sigma = K\varepsilon^n \tag{2.42}$$

The term n is the strain hardening component, which signifies the resistance of material to plastic deformation. The value of $n = 1$ denotes the highest degree of strain hardening, the implication of higher n value is a more pronounced work hardening characteristic for the material.

Representation of true stress could also be described by plastic behaviour, such description is known as Swift's power law.

$$\sigma = Y_i(1 + m\varepsilon^n) \tag{2.43}$$

Where Y_i is the initial yield stress.

Additionally, for cases where a smooth transition from elastic to plastic region is present Ramberg-Osgood in its multiaxial stress states may be incorporated for behavioural description of the material. It should be noted, RO model is primarily a non-linear model, however it may be used to describe the plastic response of the material [35].

$$E\varepsilon_T = (1+\nu)\, s - (1-2\nu)\, pI + \frac{3}{2}\alpha \left(\frac{q}{Y_0}\right)^{n-1} s \tag{2.44}$$

Where ε_T is strain tensor, Y_0 is the yield stress, p is the hydrostatic stress, s is stress deviator, ν is Poisson's ratio, I is the identity tensor and α is the yield offset.

2.5 Additional Strain Level

2.5.1 Biaxial loading

The biaxial stress state, as the name suggests nurtures the two principle directions on an infinitesimally small volume. The problem with uni-axial loading tests is the over simplification of the material. In practice the materials which are being used daily in industry are undergoing stress states in more than one axis. The purpose of conducting biaxial testing would be to further eliminate the assumption of isotropic nature of the material; and to investigate the strain limits in a more realistic setting. Bulge forming allows for principle stress states to be imposed on the four sides of a thin sheet plane element, figure 2.14.

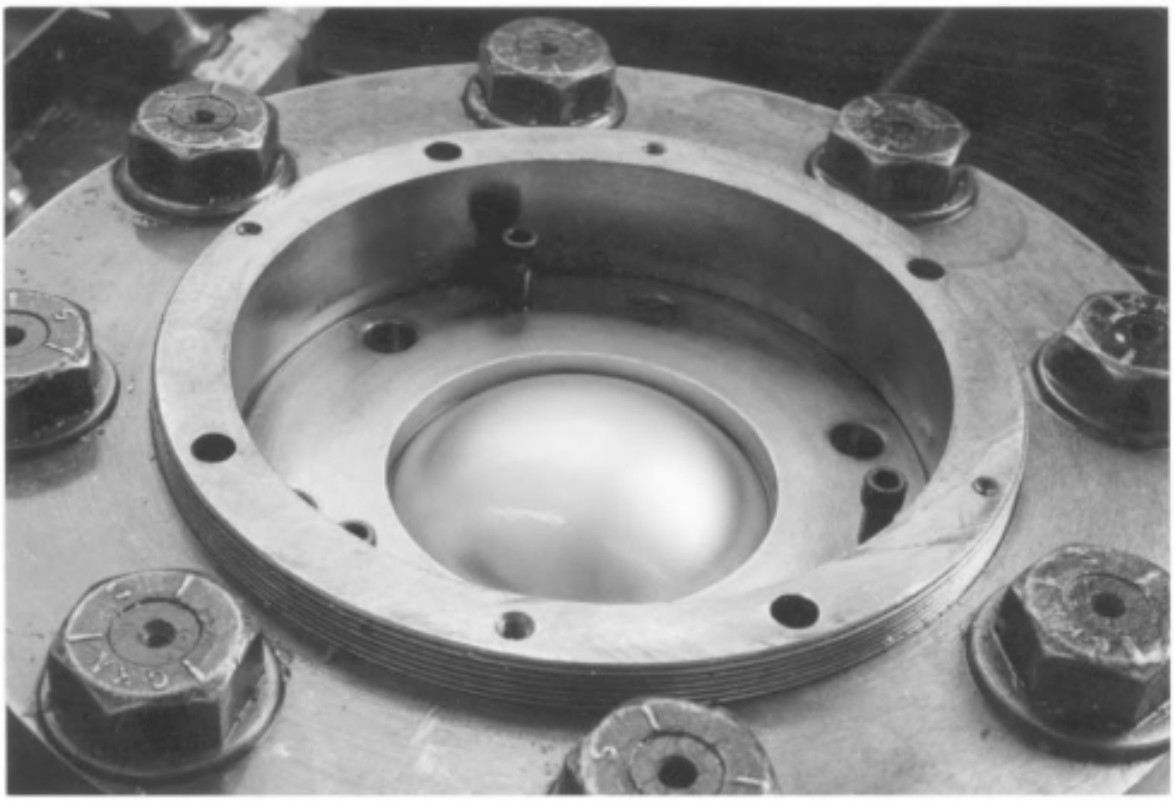

Figure 2.14: Bulge testing machine during test, [36]

The figure 2.16 demonstrates the two biaxial and uni-axial principle directions.

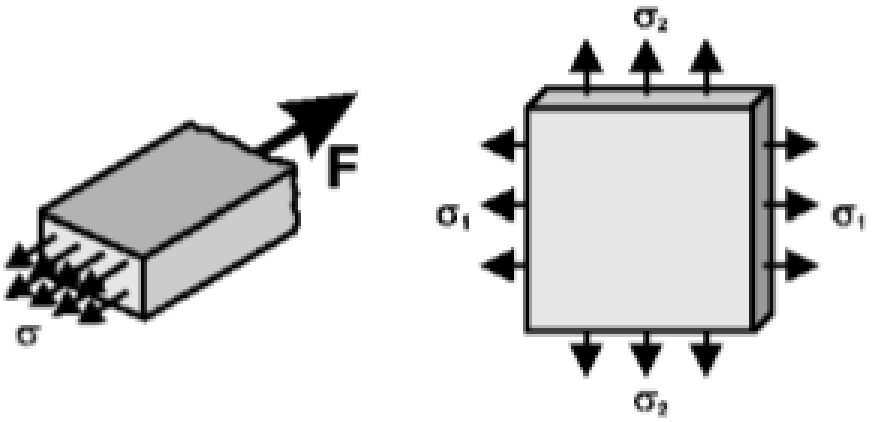

Figure 2.15: Uni-axial and bi-axial stress states, [37]

Based on figure 2.16, the strains are found from the plane stress constitutives below. The stress perpendicular to the plane would therefore be non-existent, $\sigma_z = 0$. The expressions explaining the stress state and strain state of a biaxial element would be sufficient to the point of necking [37]; however as it would be explained later, further work needs to be carried after the localisation in the plastic regime.

$$\varepsilon_1 = \frac{(\sigma_1 - \nu\sigma_2)}{E} \tag{2.45a}$$

$$\varepsilon_2 = \frac{(\sigma_2 - \nu\sigma_1)}{E} \tag{2.45b}$$

$$\varepsilon_3 = \frac{-\nu(\sigma_1 + \sigma_2)}{E} \tag{2.45c}$$

$$\sigma_1 = \frac{E(\varepsilon_1 + \nu\varepsilon_2)}{(1 - \nu^2)} \tag{2.45d}$$

$$\sigma_2 = \frac{E(\varepsilon_2 + \nu\varepsilon_1)}{(1 - \nu^2)} \tag{2.45e}$$

Determining the area which the stresses are acting upon in a biaxial loading, is a more challenging task than it is for uni-axial loading. In the uni-axial loading we know the stress would at all times will be perpendicular to the direction of the load, however such claim can not be made in a biaxial loading.

However, one needs to remember the application of biaxial loading is dependent on the engineer. For this purpose, two possible modes plane investigation has been set-up, namely, out of plane or in-plane.

One issue with out of plane testing would be the bending of the material. However, if bending needs to constrained in the procedure, in-plane testing could be presented. The attribute of in-plane testing is in the constant measure of membrane stress and strain with respect to the thickness of the sheet. One study carried out by Raghavan in 1995[38], showed a 6% difference in forming limit value between the in plane and out of plane tests.

2.5.1.1 Bulge test

Bulge tests are used for a balance biaxial tension tests, in which the latter plastic strain range could be the objective of the experiment. A bulge test machine consist of two main factors, a pressure chamber and a clamping mechanism. A plate with intentionally minimal thickness is used, this practice is done in order to neglect bending of the plat, provided $D/t > 100$. The sample is clamped around its periphery, and pressure is applied to the underside. The pressure is built up by gas, fluid or flowing polymer [36, 39]. The flow behaviour is computed based on the variation of thickness and the travelled height at the centre of circular plate.

The figure below illustrates the geometry of the bugle test.

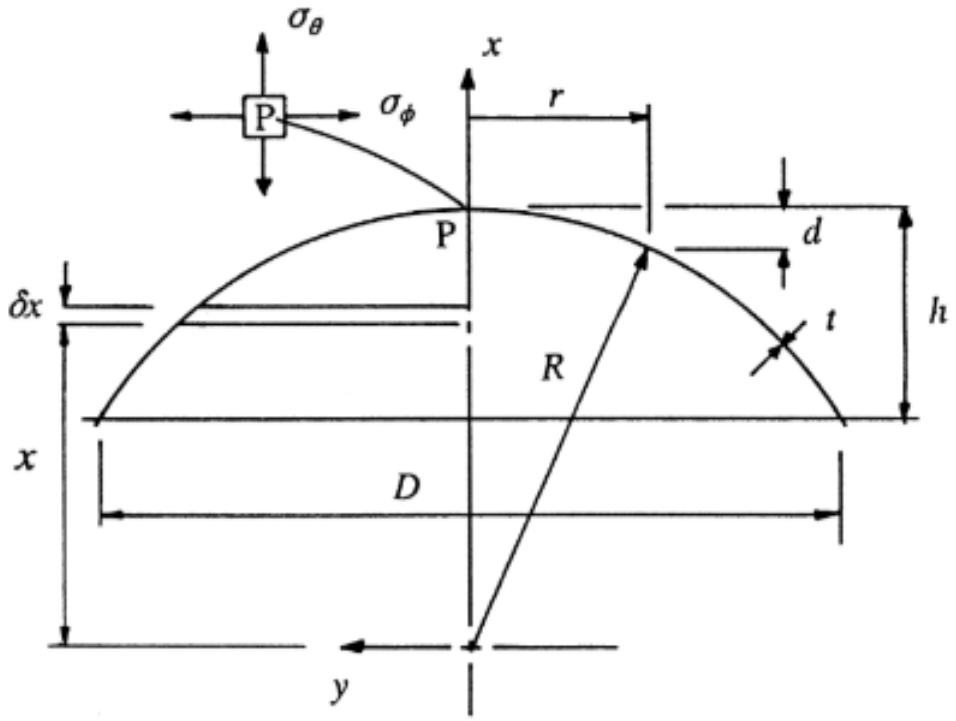

Figure 2.16: Geometry of the bulge test, [36]

In bulge forming, the radial stress σ_r is neglected and only the membrane pressure stresses are considered, σ_θ and σ_ϕ. The meridional stress σ_ϕ may be computed by considering the force equilibrium vertical to the y-plane. Therefore:

$$2\pi Rt\sigma_\phi = p\pi R^2 \qquad \Rightarrow \qquad \sigma_\phi = pR/2t \tag{2.46}$$

Similarly, the same approach can be considered for the other membrane pressure stress σ_θ resulting in $\sigma_\theta = pR/2t$. The fact that $\sigma_\theta = \sigma_\phi$ shows an equi-biaxial stress state could be exhibited everywhere. It should be noted that, for a principal stress system, the shear components are absent, thus the following von Mises expressions can be stated from figure 2.17 as:

$$\bar{\sigma} = \sqrt{\frac{3}{2}(\sigma_1^2 + \sigma_2^2 + \sigma_3^2)} \tag{2.47}$$

$$\bar{\sigma} = \frac{\sqrt{(\sigma_1 - \sigma_2)^2 + (\sigma_2 - \sigma_3)^2 + (\sigma_1 - \sigma_3)^2}}{\sqrt{2}} \tag{2.48}$$

and for Tresca:

$$\bar{\sigma} = \sigma_1 \tag{2.49}$$

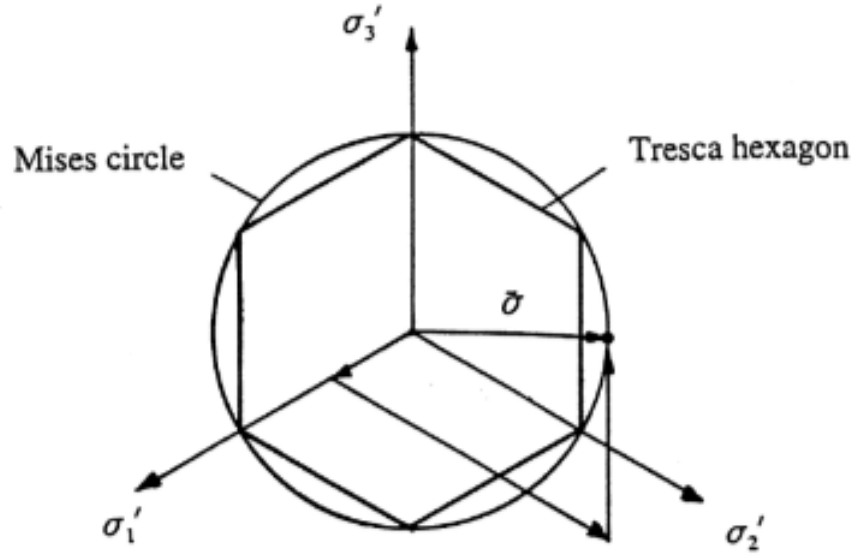

Figure 2.17: The deviatoric plane, [36]

Substituting equation 2.46 into equation 2.48, and considering the perpendicular stress as 0.

$$\begin{aligned} \bar{\sigma}^2 &= \sigma_\theta^2 - \sigma_\theta\sigma_\phi + \sigma_\phi^2 \\ \bar{\sigma} &= \sigma_\phi = \frac{pR}{2t} \end{aligned} \tag{2.50}$$

for both the Mises circle and Tresca's hexagon shown.

Based on Levy-Mises flow rule $d\varepsilon_{ij}^p = d\lambda\sigma_{ij}'$, the plastic strain increments may be calculated.

$$d\varepsilon_{\theta^p} = \frac{1}{3}d\lambda\sigma_\theta \tag{2.51a}$$

$$d\varepsilon_{\phi^p} = \frac{1}{3}d\lambda\sigma_\theta \tag{2.51b}$$

$$d\varepsilon_{r^p} = -\frac{2}{3}d\lambda\sigma_\theta \tag{2.51c}$$

and the radial strain is:

$$\varepsilon_r^p = -ln(t_0/t) \tag{2.52}$$

Subsequently, the thickness may be determined by changes to concentric circles scribed:

$$ln(r/r_0) = \frac{1}{2}ln(t_0/t) \tag{2.53}$$

The figure below shows the flow curves between a bulge test to that of a flat torsional test. As can be see the bulge test can exibit greater fracture strain; as seen here the bulge test extend the strain to 35% at the pole before bursting[36].

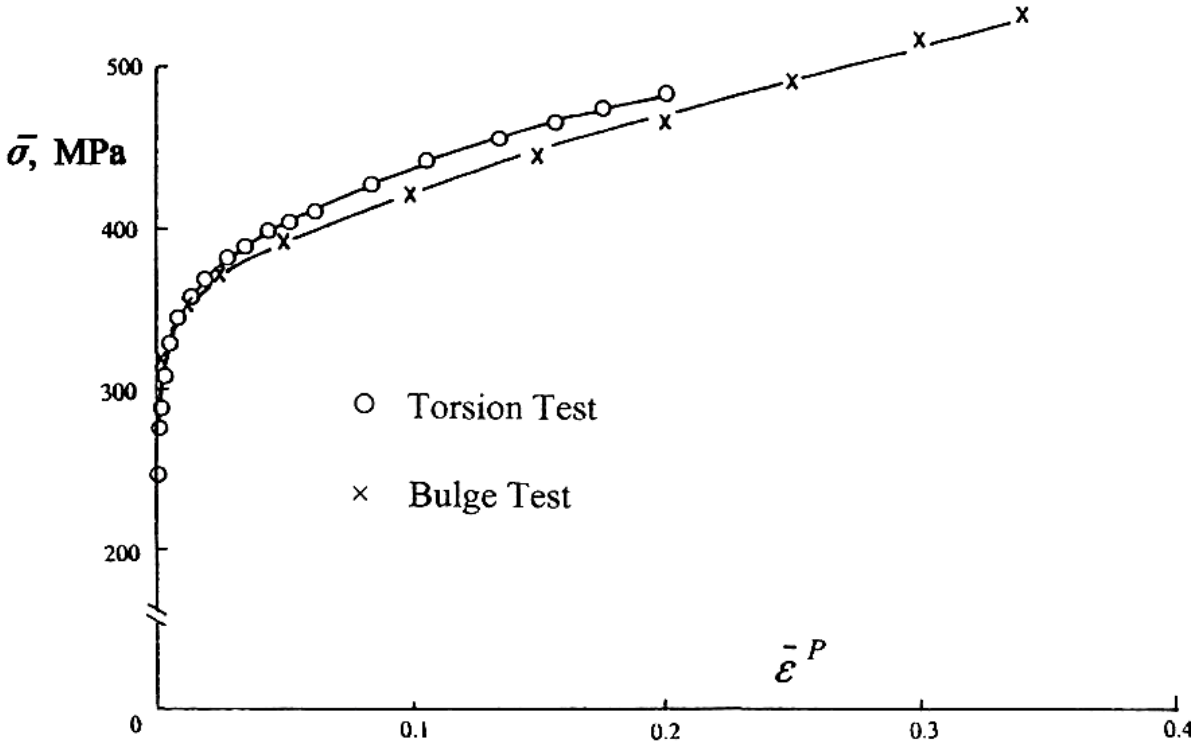

Figure 2.18: Equivalance between biaxial tension and torsion for brass, [36]

Other advantages of bulge forming is the absence of contact in the area under investigation, therefore the FEM can be carried out with few geometrical constraints. However, due the nature of the test, observation of diffuse necking and fracture could be difficult, as it happens very rapidly and making it costly to set-up appropriate tools for observation of rupture.

2.5.2 Plane strain compression test

This type of compression tests is the most effective method of obtaining an extended stress/strain curve. The problems of a normal compression test, that is, a high frictional force at the platens with associated barrelling of the test specimen, are eliminated with this method.

Plane strain means that strain is prevented in the width direction w, as provided in figure 2.19, by the unstressed material on either side of the die breadth b. This condition is established by dies of narrow breadth overlapping the strip width. To

ensure as near frictionless conditions as possible the supporting die faces are highly polished and kept lubricated.

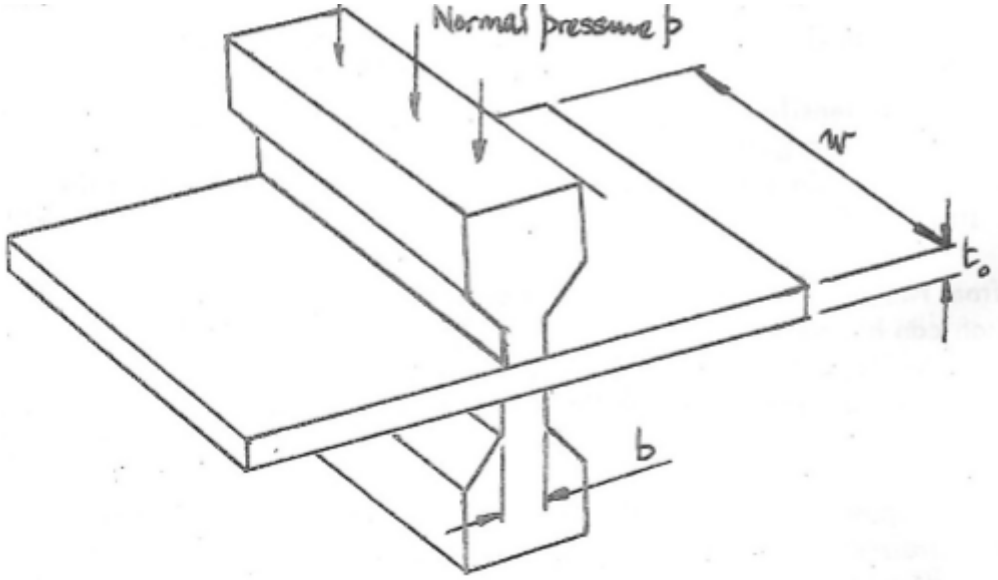

Figure 2.19: Plane strain compression schematic

Plane strain compression test was established in 1950's as a means of acquiring flow curves to large strains [40]. Typically strain of 200% can be reached by conforming to the constraints imposed by the need to attain true material data, i.e. data independent of die geometry. Therefore the most suitable conditions to achieve the valid results are:

$$2 \leq \frac{b}{t} \leq 4 \tag{2.54a}$$

$$5 \leq \frac{w}{b} \leq 12 \tag{2.54b}$$

The first inequality 2.54a, requires a die change to smaller b as the current thickness t decreases progressively under increasing load W. The second inequality 2.54b is fixed at the start of the test. The test is performed incrementaly with successive loading and unloading to greater penetration. Unloading ensures that elastic strain recovers, this allowing the permanent thickness to be found from the a vernier caliper measurment. The stress is not uniaxial- a stress along the width exists, due to the plane constraint, together with the compressive stress in the thickness [41]. Consequently, an equivalent stress and equivalent plastic strain are used to correlate the flow curve with those found under simple tension and bulge forming to lesser strains. The definition of equivalence is currently under review given the number of

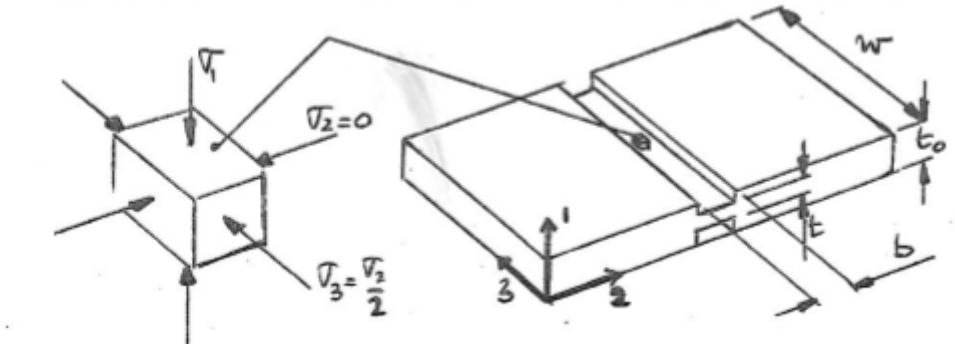

Figure 2.20: Plain strain compression equivalent stress-strain

yield criteria that now claim to account for sheet anisotropy.

In the case of anisotropic sheet during plastic deformation the stress/strain relationships have a similar form to those used from elastic deformation:

$$d\varepsilon_1^p = k\left[\sigma_1 - \frac{1}{2}(\sigma_2 + \sigma_3)\right] \tag{2.55a}$$

$$d\varepsilon_2^p = k\left[\sigma_2 - \frac{1}{2}(\sigma_1 + \sigma_3)\right] \tag{2.55b}$$

$$d\varepsilon_3^p = k\left[\sigma_3 - \frac{1}{2}(\sigma_1 + \sigma_2)\right] \tag{2.55c}$$

Where k is analogous to $1/E$ in the elastic equations and $\nu = \frac{1}{2}$ for plastic deformation. Increments of strain must be used here because the final strained state is path dependent.

For plane strain:

$$d\varepsilon_3^p = 0 = k\left[\sigma_3 - \frac{1}{2}(\sigma_1 + \sigma_2)\right] \tag{2.56a}$$

$$\therefore \qquad \sigma_3 = \frac{1}{2}(\sigma_1 + \sigma_2) \tag{2.56b}$$

$$\therefore \qquad \sigma_3 = \frac{\sigma_1}{2} \tag{2.56c}$$

By means of substituting equation 2.55 into equation 2.56:

$$d\varepsilon_1^p = \frac{3k}{4}\sigma_1$$
$$d\varepsilon_2^p = \frac{-3k}{4}\sigma_1 = -d\varepsilon_1^p$$

Noting σ_1 is a compressive stress.

For a principle stress system $(\sigma_1, \sigma_2, \sigma_3)$ the equivalent stress $\bar{\sigma}$ is defined as:

$$\bar{\sigma} = \frac{1}{\sqrt{2}}\left[(\sigma_1 - \sigma_2)^2 + (\sigma_2 - \sigma_3)^2 + (\sigma_1 - \sigma_3)^2\right]^{\frac{1}{2}} \tag{2.58}$$

which for plane strain compression reduces to:

$$\bar{\sigma} = \frac{\sqrt{3}}{2}\sigma_1 = \frac{\sqrt{2}}{3}\left(\frac{W}{wb}\right) \tag{2.59}$$

Therefore, on the same principal system, the equivalent strain increment $d\bar{\varepsilon}^p$ is defined as:

$$d\bar{\varepsilon}^p = \frac{\sqrt{2}}{3}\left[(d\varepsilon_1^p - d\varepsilon_2^p)^2 + (d\varepsilon_2^p - d\varepsilon_3^p)^2 + (d\varepsilon_1^p - d\varepsilon_3^p)^2\right]^{\frac{1}{2}} \tag{2.60}$$

Similarly, for plane strain compression, equation above reduces to:

$$d\bar{\varepsilon}^p = \frac{2}{\sqrt{3}}\left(d\varepsilon_1^p\right)$$
$$\therefore \qquad \int d\bar{\varepsilon}^p = \frac{2}{\sqrt{3}}\int d\varepsilon_1^p$$

Therefore an equivalent stress/strain curve plot becomes:

$$\bar{\sigma} \qquad vs. \qquad \int d\bar{\varepsilon}^p$$
$$\frac{\sqrt{3}}{2}\sigma_1 \qquad vs. \qquad \frac{2}{\sqrt{3}}\int d\varepsilon_1^p$$
$$\frac{\sqrt{3}}{2}\sigma_1 \qquad vs. \qquad \frac{2}{\sqrt{3}}\int_0^t \frac{dt}{t}$$

That is given w and Δt are measures quantities $\bar{\sigma}$ vs $\bar{\varepsilon}^p$, corresponds to:

$$-\frac{\sqrt{3}}{2}\left(\frac{W}{wb}\right) \qquad vs. \qquad -\frac{2}{\sqrt{3}}\log_e\left(1 - \frac{\Delta t}{t_0}\right) \tag{2.63}$$

For which the minus signs are discarded when compared to flow curves under tension.

2.6 Numerical Analysis

2.6.1 General consideration

In general, the simulation of mechanical models for high accuracy will be attempted in non-linear format, as it is difficult to be solved analytically. All computer codes attempt to solve the differential equations that govern the characteristics of the designed model. These equations will in most cases will be based on equilibrium and compatibility equations of the model, namely stress, strain and rate of movement or the conservation laws, namely energy which is governed by Noether's theorem in that they are associated with a symmetry in their physics and the rate of change is equal to zero $\frac{dX}{dt} = 0$.

> "If a system has a continuous symmetry property, then there are corresponding quantities whose values are conserved in time."

In essence all FEA packages will be sectioned into three interconnected logical units. The figure 2.21, clearly outlines the processes involved. However, codes may be constructed to define all three sections or more commonly separate the processes into more user friendly segments.

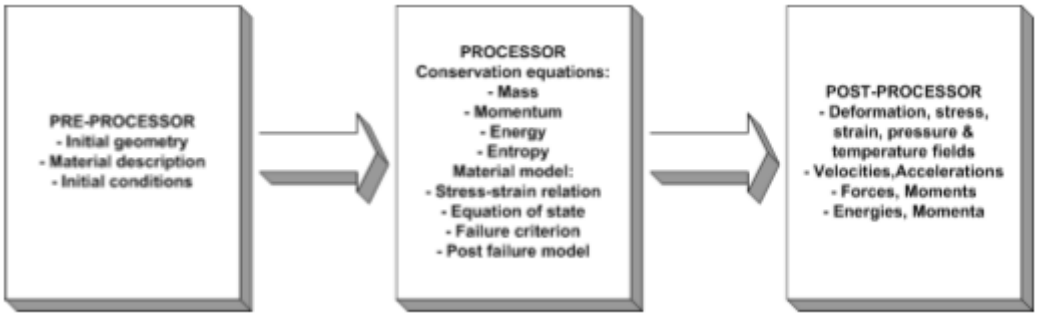

Figure 2.21: Computational algorithem process, [42]

In the preprocessing the user is tasked by defining the geometry of the model from an abbreviated description; after which a computational mesh will be generated based on the user defined limits. This information coupled by the description of

the material as well as the accurate parameters for an equation of state driven from the stress-strain model of the material will be used for constructing the behaviour of the material within the package. Lastly, the environmental description of the model is defined by the user in the shape of boundary conditions.

The most time consuming section of the analysis will be due to processing of the model. Time spent on solving the model will be greatly influenced by hardware limitation, as well as the number of analyses the package is tasked to carry out and the number of nodes defined.

The post processing will output the analysed model in the form of simulated data. The user is given the option to investigate the model within the package or extract the data for other means of processing. The usual available data within the package will be in the form of graphical presentation, for stress, strain, temperature etc. at any given time of the model.

2.6.2 Validation and verification

In simulation analysis, there is always the need to justify the model and results created through it; the need to justify such outputs has grown over the recent years for safety and legal reason. An engineer would be required to ensure the accuracy of the results though means of validating and verifying the findings.

Verification as stated by Oberkampf et al [43], is the process of assessing the software's correctness and numerical accuracy of a given computational model. In essence this process would mean making comparison between the results of a computational modelling to set of known solutions, whether the known solutions are obtained by hand calculations or laboratory tests etc. Through this process the aim is to ensure that the conceptual description of the model created by the developer is correctly assessing the situation.

Validation is described as assessing the physical accuracy correctly; in other words, comparing the computational results with those of experimental results. In

case of this thesis, validation would describe a comparison between stress/strain curves. In essence this process aims to maximise the accuracy of prediction to real world scenarios [43].
By correct review of verification and validation of a simulated model, credibility increases.

2.6.3 Meshing analysis

Arguably one the most crucial aspects of defining a correct model is defining properly the meshing of the model within pre-processing. All codes are fundamentally different in the way in which they arrive at the solution. However, at their core they all follow either Eulerian method of analysis or Langrangian spatial discretisation. Eulerian method makes use of fixed nodes in space in which discretisation will not follow the moving pattern of the material. In Langrangian method however, every node in the deformed model has its root in the reference state of the material.

With the Langrangian method time steps of the model are linked to the smallest element within the model. Therefore as a consequence, the mass of the model remains constant throughout whereas the volume changes with the changes to model. On one hand, a common problem with this method is the possible divergence of the results, in cases where the elements become too distorted. On the other hand, the very same attribute will results in faster processing time. Additionally, the Langrangian method is far simpler when defining the boundary conditions of the model as well as when the user wishes to describe interaction between two parts.

The Eulerian method is usually described for problem with large deformation and distortion. The method assumes an arbitrarily space around the model, in which the mass flow into and out of the designated space is monitored. Due to this fundamental of the Eulerian code, it makes it difficult to design an appropriate space for monitoring the flow in and out of it [42].

2.6.4 Time integration

Adopting the models in FEA packages, are the essence of achieving correct simulation based on the model being static or dynamic. The two forms of establishing time integration are Implicit and Explicit methods. A geometric and/or material analysis will require incremental load defined for it. By the end of each increment of load the geometry of the model might have changed otherwise known as the material yielding. For every change in geometry the model the stiffness matrix for the next increment would need to be updated.

2.6.4.1 Explicit

An explicit FEA code will have evaluated the model and would update the stiffness matrix with the results achieved during the the last increment for implementation of the next increment. One draw back of this method, is compulsive describing of small increments for accurate results. Thus the explicit method would usually result in high computing time. If the increment sizes defined are relatively big, then the outcome solution will differ from correct solution. Therefore, the explicit method is known to be conditionally stable, as the method does not force an equilibrium between the internal forces and the externally applied forces. Also another issue with this method is that it may not be successfully implemented for cyclic loading, or 'snap through' or 'snap back' buckling issues.

2.6.4.2 Implicit

An implicit FEM model, in many aspects work similarly to the explicit method. However, stability is forced into the stiffness matrix. Implicit method, after each executed increment make use of a Newton-Raphson iteration method, which ensures that the internal forces and externally applied forces are in equilibrium. Due to this, larger increment sizes might be considered as each increment will always converge towards the final solution. One problem with this method is the excessive time consumption of the analysis where during each Newton-Raphson iteration, the model must deconstruct and re-construct the stiffness matrix. As a result there are faster versions of Newton-Raphson available, which when applied correctly will see the

solution converge at a quadratic rate.

2.6.5 Ductility analysis

The resistance to ductility of a material is characterised by material fracture toughness, subsequently defined by the measure of deformation in form of plasticity before fracture. Fracture toughness value of materials are extremely dependant on temperature; increasing temperature would result in the material's ability to absorb energy, which in turn increase the ductility. As explained by Anderson [31], Ductile-Brittle Transition Temperature (DBTT) is characterised by small temperature ranges, where the material energy is absorbed, as illustrated in figure 2.22.

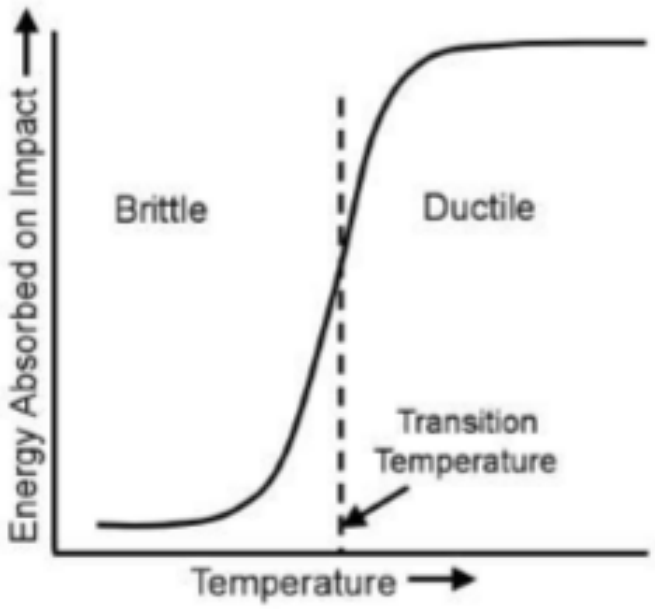

Figure 2.22: Ductile to brittle transition, [31]

In order to understand further the ductility of materials in metal forming the conditions governing the process has to be examined and understood. The forming of metals sheets are highly strain path dependant, which in turn is governed by localised necking. Globally the forming limit curve provides a simple failure criterion to describe these phenomena.

2.6.5.1 Modes of failure

An overview on existing modes of failure will be presented in this section, as well as few failure criteria based on three categories illustrated below.

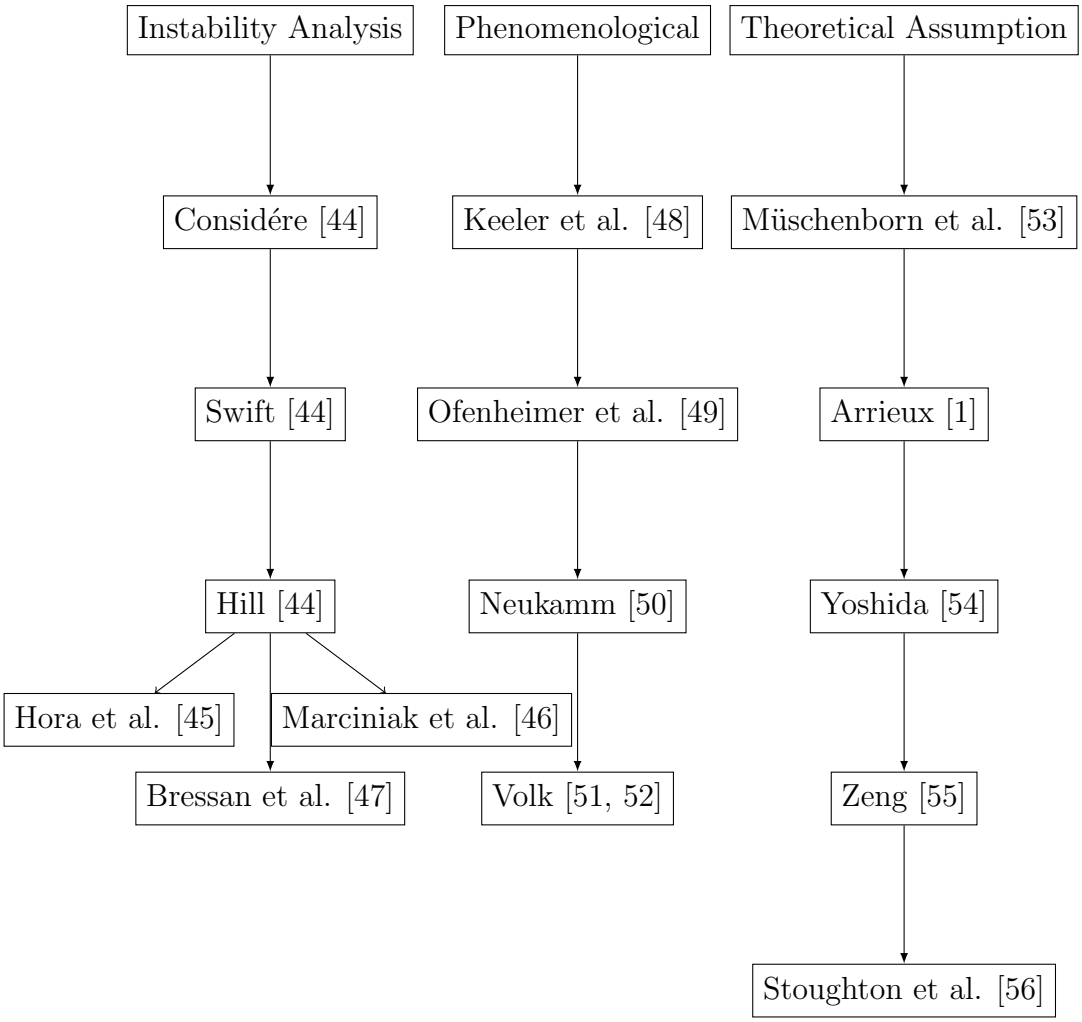

Figure 2.23: Overview of failure criteria with non-proportional loading

Metal sheets are most commonly assessed by using forming limit curve (FLC), in which the onset of localized necking would be described by major and minor engineering stress or true strain[57]. Until 1960's the most reliable FLC's was able to express the formed sheet free of fracture and through-thickness necks. Through-thickness forming is expressed as forming of localized line thinning across the surface of the material. It is worth while to mention the thickness-through necking is preceding factor of fracture in ductile metals. It should be noted the conventional FLC diagrams would be only reliable for linear forming process under proportional in-plane strain, this has been shown from many studies carried out on non-linear strain paths. (see figure 2.23)

The FLD, was originally established and developed by the work Keeler et al [48]. The expression of FLC, based on its shape and location, expresses the limits

between strain states that are not prone to necking and those that are; therefore it describes the characteristic of the material independent of the forming process. In other words, FLC describes the degree of safety before possible failure. As an example, such safety design reported by Graf et al. [58] is present. The material tests in the figure 2.24 applies to T4 aluminium.

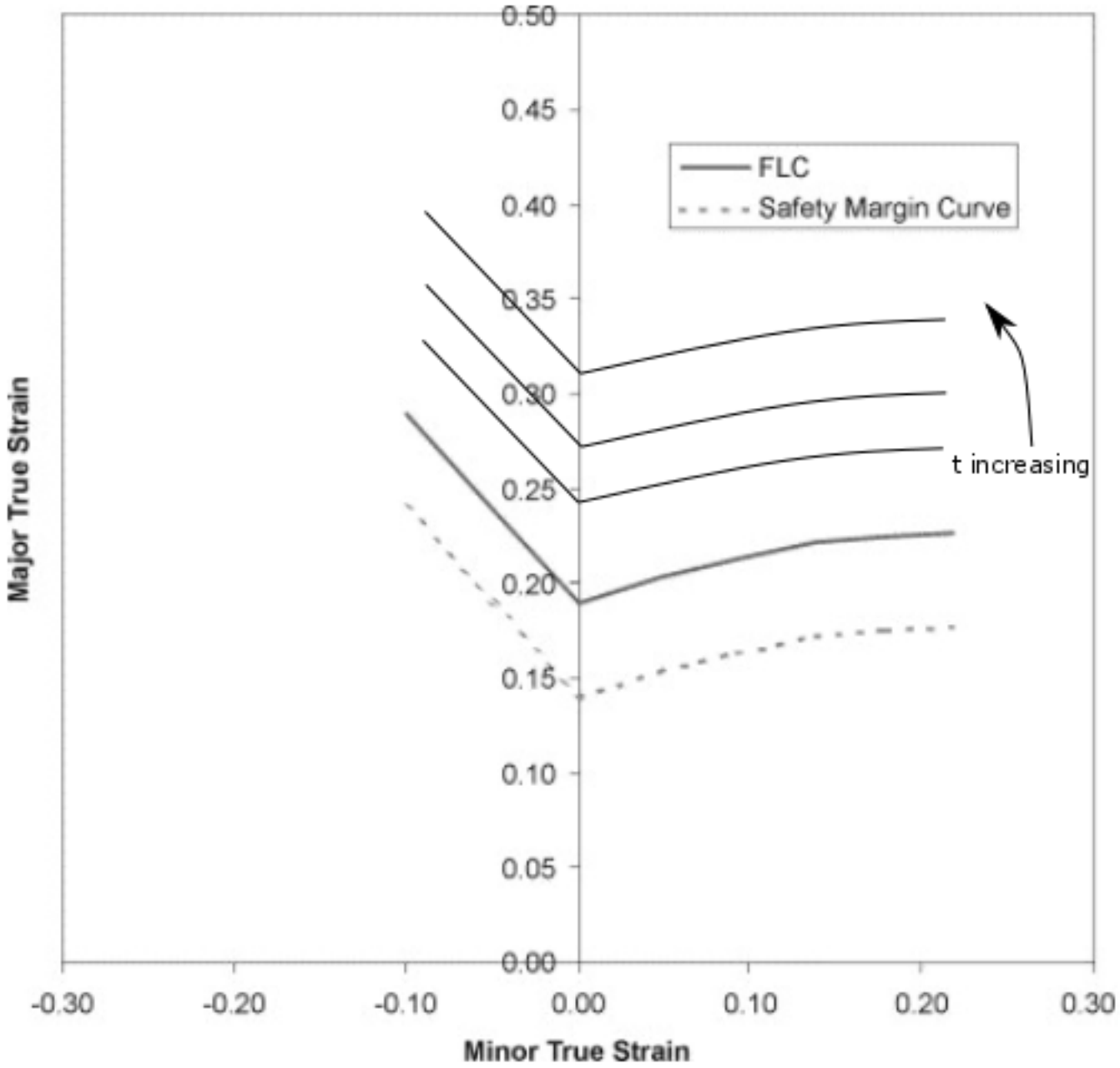

Figure 2.24: FLC for T4 aluminium, [58]

A common discussion is relation of thickness effect upon the limit strains. As such [59] describes the formability of thicker sheets could prove better compared to thinner sheets. The increase of thickness of sheet metals could be related to larger

necking zone and different strain path. Therefore, increasing the tolerance of the sheet against straining and fracture.

One general issue with FLC's, is related to it linear path dependency, meaning the ratio of plastic strain component ε_p would need to be constant for the FLC to be applicable.

In 1885 Considére [44] managed to describe the onset of necking. By his investigation, he concluded diffuse necking would form as the coupon under uniaxial stress reaches its maximum load. Based on this work, Swift in 1952 put forth a more comprehensive version, in which he expressed the Considére criterion in a two dimensional modification. Eventually in 1966 Hora and Tong [45, 46], published their newest addition to the Considére criterion, known as Modified Maximum Force Criterion (MMFC); in which assumption is based upon the current stress for when maximum force is reached.

Due to the MMFC condition, the prediction to the onset of localized necking will be delayed. Further investigation by Bressan et al [47], saw the development of a "through thickness shear stability criterion"; which conditions the failure based on the magnitude and direction of maximum shear.

The problem with strain path effect is that every point and contour in the process is subjected to a different FLC. The problem is amplified when strain path is bi-linear. As a result, the number of required FLC's for mutli formed sheet becomes limited to the number of elements in a FEM analysis. The theoretical failure approach is greatly influenced by the works of Arrieux [1], as he was one of the first people to convert the forming limit strains into stress space. His work was later picked up by Stoughton et al [56], who managed to illustrate the forming limit stress curves were independent of strain path. However a very recent work by Werber et al. [60] proved the statement above is only valid for small strain in which the alloy exhibits isotropic hardening behaviour. The effective proposal by Stoughton is illustrated in figure 2.25.

A work [53] that proved to be a significant contribution showed, forming limit

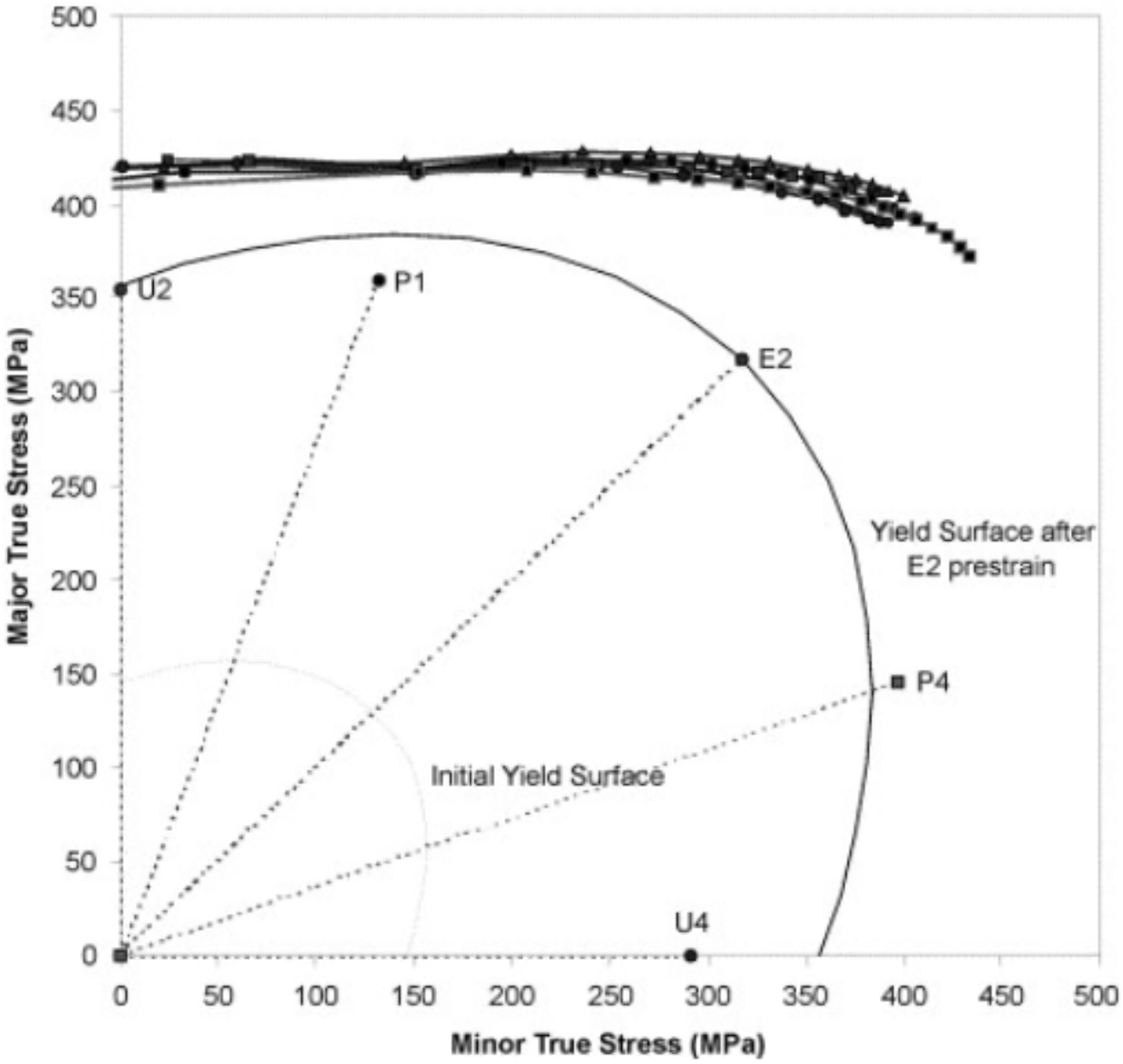

Figure 2.25: Stress space bi-linear forming path, [61]

curves would represent the maximum reachable thickness strain. This work lead to a publication in 2007 by Yoshida et al [54], in which they illustrated the sum of all thickness strains was a function of principle stress.

One question that we will attempt to address below, is why the theories supporting FLC on the basis of strain is more complicated than stress field theories. The strain model is described on the basis of Swift analysis, which defines instability criteria based on minimum strain values qualitatively. Storen in 1975 [62], used a bifurcation analysis for characterising FLC on the basis of a vertex formation in the

yield surface,from enforcing equilibrium between necked and non-necked regions.

However, since the FLC both in terms of strain and stress are identical under proportional loading, the model could be then explained for a strain-based FLC.

In order to evaluate the governing equations of the theories stated above, an assumption has to be made, that the yield function must be treated as an explicit function of the state stress. That is:

$$\overline{\sigma_y} = \overline{\sigma}(\sigma_1, \sigma_2) \tag{2.64}$$

Also the assumption has to made that the effective plastic strain increases, isotropically and is therefore a function of the uniaxial flow stress $\sigma_Y(\bar{\varepsilon}^p)$.

$$\bar{\sigma_y}(\sigma_1, \sigma_2) = \sigma_Y(\bar{\varepsilon_p}) \tag{2.65}$$

Therefore, the rate of change of yield function may be expressed in two ways:

$$\dot{\bar{\sigma}}_y = \frac{\partial \dot{\bar{\sigma}}_y}{\partial \sigma_1}\dot{\sigma_1} + \frac{\partial \dot{\bar{\sigma}}_y}{\partial \sigma_2}\dot{\sigma_2} = \frac{d\sigma_Y}{d\varepsilon_p}\dot{\bar{\varepsilon}}_p \tag{2.66}$$

Also the principal plastic strain rates $\dot{\epsilon}_p (i = 1, 2, 3)$ are given by the flow rule:

$$\dot{\epsilon}_i = \dot{\bar{\varepsilon}}_p \frac{\partial \bar{\sigma_Y}}{\partial \sigma_i} \tag{2.67}$$

Based on linear elasticity assumption of the material, a correlation between stress rate and total strain rate in matrix form may be formed. Based on the elastic component, the following derivation can be computed:

$$\dot{\sigma} = C_e\dot{\epsilon} \equiv \begin{pmatrix} \sigma_1 \\ \sigma_2 \end{pmatrix} = \frac{E}{(1-\nu^2)}) \begin{pmatrix} 1 & \nu \\ \nu & 1 \end{pmatrix} \begin{pmatrix} \dot{\epsilon}_1 \\ \dot{\epsilon}_2 \end{pmatrix} \Rightarrow \begin{cases} \sigma_1 = \frac{E}{1-\nu^2}(\dot{\epsilon}_1 + \nu\dot{\epsilon}_2) \\ \sigma_2 = \frac{E}{1-\nu^2}(\dot{\epsilon_2} + \nu\dot{\epsilon}_1) \end{cases} \tag{2.68}$$

$$\dot{\sigma} = (C_e + C_p)\dot{\epsilon} \tag{2.69}$$

Where C_e is a the elastic matrix refering to Young's modulus and Poisson ratio. Therefore, the equation 2.70 may be rewritten in the following format:

$$C_e = \frac{E}{1-\nu^2} \begin{pmatrix} 1 & \nu \\ \nu & 1 \end{pmatrix} \tag{2.70}$$

Also the C_P for equation 2.70 represents the plastic contribution to strain rate.

$$C_p = \frac{1}{\frac{d\bar{\sigma_Y}}{d\bar{\varepsilon_p}} + p_1 Y_1 + p_2 Y_2} \begin{pmatrix} P_1 Y_1 & P_1 Y_2 \\ P_2 Y_1 & P_2 Y_2 \end{pmatrix} \tag{2.71}$$

Where;

$$P = \begin{pmatrix} P_1 \\ P_2 \end{pmatrix} = C_e p \qquad \text{and} \qquad Y = \begin{pmatrix} Y_1 \\ Y_2 \end{pmatrix} = C_e y \tag{2.72}$$

Also, it was expressed that the stress rate and strain rate have linear elastic relation in this concept, therefore:

$$\dot{\sigma_{ij}} = C_{ij} \dot{e_j} \tag{2.73}$$

Therefore, we can conclude based on the proof above C_{ij} is independent of strain path.

It is important to be able to understand the formation and derivation of the conditions related to necking. It is useful to develop such model based on a much fundamental concepts first. Based on Von Mises the plane principal yield function could be presented by:

$$\bar{\sigma_y} = \sqrt{\sigma_1^2 + \sigma_2^2 - \sigma_1 \sigma_2} \tag{2.74}$$

where we can find the α and β as:

$$\beta = \frac{2\alpha - 1}{2 - \alpha} \tag{2.75}$$

where $\alpha = \frac{\sigma_1}{\sigma_2}$. Based on the power law, we can illustrate the onset of neck formation by:

$$\sigma_Y = K \bar{\varepsilon_p^n} \tag{2.76}$$

With regards to identifying the necking formation Swift [63], managed to present the following expression when the load reaches its maximum along both principal axes.

By means of substitution into equation 2.66 and equation 2.67, therefore:

$$\dot{\bar{\sigma}}_y = \left[(\frac{\partial \bar{\sigma_y}}{\partial \sigma_1})^2 \sigma_1 + (\frac{\partial \bar{\sigma_y}}{\partial \sigma_2})^2 \sigma_2 \right] \dot{\bar{\varepsilon}}_p = \frac{d\sigma_y}{d\bar{\varepsilon_p}} \dot{\bar{\varepsilon}}_p \tag{2.77}$$

The general expression of Swift can be expressed by means of eliminating the common components from the equation above.

$$\frac{d\sigma_y}{d\bar{\varepsilon_p}} = (\frac{\partial \bar{\sigma_y}}{\partial \sigma_1})^2 \sigma_1 + (\frac{\partial \bar{\sigma_y}}{\partial \sigma_2})^2 \sigma_2 \tag{2.78}$$

By means of making use of power law to express stress-strain relation, we may express the above equation with the Von Mises criterion.

$$\frac{d\sigma_y}{d\bar{\varepsilon_p}} = \frac{(4 - 3\alpha - 3\alpha^2 + 4\alpha^3)}{4(1 - \alpha + \alpha + \alpha^2)^{3/2}} \bar{\sigma_y} \tag{2.79a}$$

$$\bar{\varepsilon_p} = 2e \frac{\sqrt{1 - \alpha + \alpha^2}}{2 - \alpha} \tag{2.79b}$$

With proportional loading assumption in mind the flow rule of Von Mises may be expressed as above. Therefore the Swift instability strain co-ordinates can be expressed as follows:

$$\begin{pmatrix} e_1 \\ e_2 \end{pmatrix} = \begin{pmatrix} \frac{2n(2-\alpha)(1-\alpha+\alpha^2)}{4-3\alpha-3\alpha^2+4\alpha^3} \\ -\frac{2n(1-2\alpha)(1-\alpha+\alpha^2)}{4-3\alpha-3\alpha^2+4\alpha^3} \end{pmatrix} \tag{2.80}$$

Also, the Swift instability criterion may also be expressed on the basis of stress. The benefit of such expression that is no assumption on proportional loading needs to be considered. The stress value would merely indicate the maximum stress possible at the onset of necking. The yield stress at the point of instability may be expressed as:

$$\bar{\sigma_y} = K(\frac{4n(1 - \alpha + \alpha^2)^{3/2}}{4 - 3\alpha - 3\alpha^2 = 4\alpha^3})^n \tag{2.81}$$

Therefore, the stress based Swift instability criterion may be expressed by the following stress co-ordinates:

$$\begin{pmatrix} \sigma_1 \\ \sigma_2 \end{pmatrix} = \begin{pmatrix} \frac{K}{\sqrt{1+\alpha^2-\alpha}} (\frac{4n(1-\alpha+\alpha^2)^{3/2}}{4-3\alpha-3\alpha^2+4\alpha^3})^n \\ \frac{\alpha K}{\sqrt{1++\alpha^2-\alpha}} (\frac{4n(1-\alpha+\alpha^2)^{3/2}}{4-3\alpha-3\alpha^2+4\alpha^3})^n \end{pmatrix} \tag{2.82}$$

In a continued attempt an equilibrium between the direction between necking and uniform distrubtion at the onset of necking deformation, Storen and Rice [62], established such equilibrium by developing n_1, n_2 as the units normal to the necking.

$$\begin{aligned} n1[\Delta\dot{\sigma}_1 - \sigma_1 g_1 n_1] + n_2[\Delta\dot{\sigma}_{21} - \sigma_1 g_2 n_1] = 0 \\ n1[\Delta\dot{\sigma}_{12} - \sigma_2 g_1 n_2] + n_2[\Delta\dot{\sigma}_2 - \sigma_2 g_2 n_2] = 0 \end{aligned} \tag{2.83}$$

Where $\Delta\dot{\sigma}$ the stress tensor shows the absolute difference between necked $\dot{\sigma}^n$ and uniform deformation $\dot{\sigma}^u$ at the onset of neck formation. corresponding by the equation below:

$$\Delta\dot{\sigma} = \begin{pmatrix} \Delta\dot{\sigma}_1 \\ \Delta\dot{\sigma}_2 \end{pmatrix} = \begin{pmatrix} \dot{\sigma}_1^n - \dot{\sigma}_1^u \\ \dot{\sigma}_2^n - \dot{\sigma}_2^u \end{pmatrix} = \dot{\sigma}^n - \dot{\sigma}^u \tag{2.84}$$

To better understand the bifurcation constrained analysis proposed by Swift,

2.6.5.2 Finite element method for recognition of necking

Necking is one factor which characterises the behaviour of the material. It is worth noting, necking would usually occur at about the same elongation irrespective of the test coupon; however, the position of the necking can vary.

Based on the statement above, the conclusion is made the necking would relate to either bifurcation or instability problems. Therefore, one needs to understand necking, to recognise the macroscopic behaviour of the material.

According to the past research, FEM may be applied based on different categories in this context. Brünig [64] and Dumoulin et al. [65], conducted their research with a simulation of the whole tensile sample; that is the simulation applied to the coupon as well as the grips used but without any imperfection defined for the sample. In constrast other studies [66, 67, 68, 69], only modelled the rectangular or circular distance of the gauge length constraining the radial displacement, in order to initiate localization.

A concise view of researchers was gathered for a broader perspective upon this topic. Niordson and Redanz [66] studied the necking formation according to plane

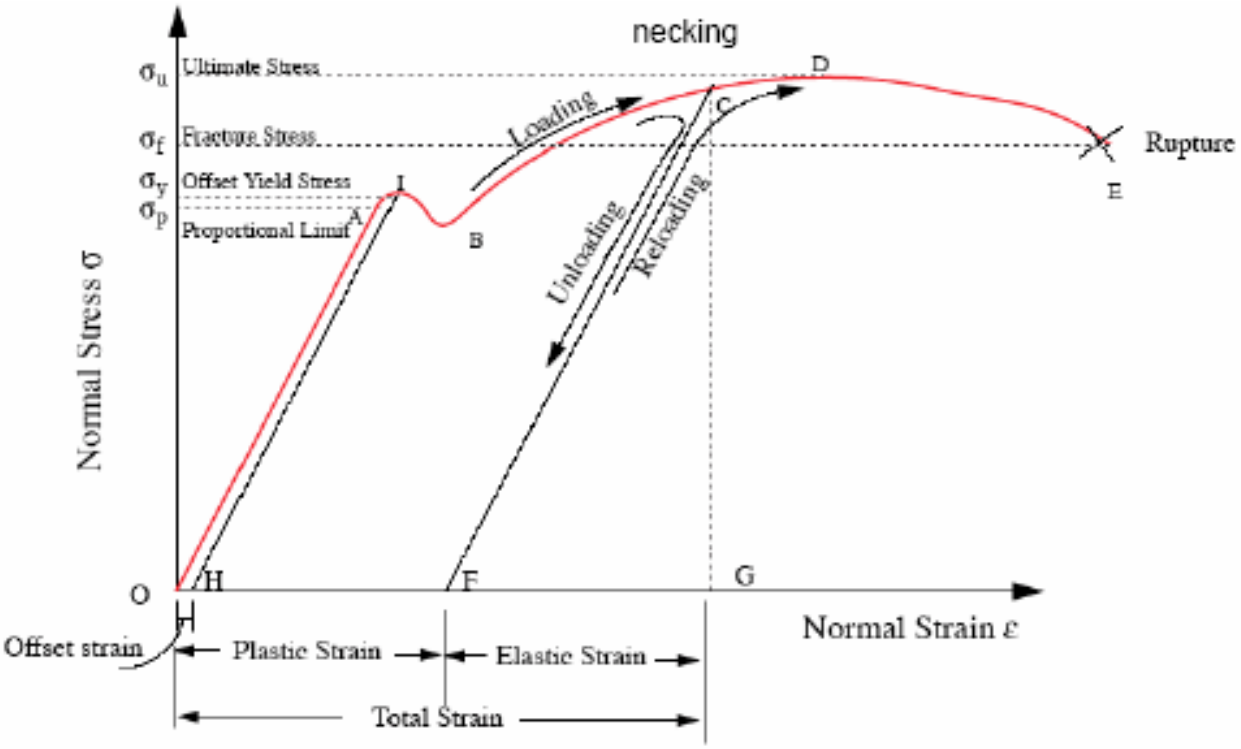

Figure 2.26: Presentation of necking on a stress-strain curve, [31]

strain sheet by means of strain plasticity theory; For their work, they modelled the FEM analysis with an imperfection infused modelled and a shear free grip for a simpler analysis. The outcome of the work designated, with introduction of imperfection to the system the formation of localized necking would occur with a delay as a function of imperfection amplitude. Komori 2002 [67], carried out his research by implementing rigid plastic FEM analysis with an intentional defect. He concluded, through predicting the maximum tensile force, that the material properties of the analysis would match those of the experiment. He later used this finding to predict the fracture of the tensile sample. Brünig [64], endorsed his full analysis method by claiming the cylindrical sample tests with its fix grips would replicate the same sample with shear free ends. Cabezas et al. [70], carried their FEM analysis on both cylindrical and sheet metals with induced imperfection in the model. The finding of this work showed the measured and predicted true strain at the necking would differ by 4.3%. Lee and Joun [71], carried out a full analysis in which it demonstrated the true strain value at the necking is identical to the Hollomon strain hardening exponent, i.e. Considére condition.

The above work have few parameters in common, in the sense that they wish to

address the Considére instability criterion. The work carried out by Dumoulin et al [65], satisfied the criterion. However they failed to explain the difference between results predicted by the model and their experimental results in a quantitative manner. A more recent study by Joun et al. [4], managed to satisfy the Considére criterion as well as the Hollomon's law. In this work, the first model predicts the onset of necking accurately based on the Hollomon's law. Further, they manage to show by means of iteration the non-uniform plastic deformation that occurs after necking.

The analysis of rigid plastic FEM, would depend on determining velocity field ν_i that could satisfy the boundary condition; V as the domain and S as the boundary. In turn the boundary S will be denoted as velocity boundary $S_{\nu i}$, in which the stress vector may be expressed as $t^{(n)} = t^{-(n)}$. Moreover, the constant volume assumption may be denoted as, $\nu_{i,i} = 0$.

The common relationship to identify the true stress σ_t and true strain ε_t with respect to engineering data is expressed below. However, one should mention the following uniaxial equations may be applied under the assumption of negligible volumetric change during uniform plastic deformation. However, multiaxiality of deformation occurs beyond necking.

$$\sigma_t = \sigma_e(1 + \varepsilon_e) \tag{2.85a}$$

$$\varepsilon_t = ln(1 + \varepsilon_e) \tag{2.85b}$$

It is for this reason, prediction of true-stress-strain curve my prove to be more difficult after reaching the point of neck formation. Although a number of possible measuring techniques are available to measure the necking; as such, extensometers or vernier callipers could be used.
The flow stress construction in metal forming simulation will be adopted with Hollomon's law:

$$\sigma = K\varepsilon^n \tag{2.86}$$

Where K is the strength coefficient component and n is the strain hardening

component. Further, the reference strain hardening component n_N, is expressed as the true strain at the onset of necking.

$$n_N = ln(1 + \varepsilon_e^N) \tag{2.87}$$

Where the ε_e^N is the engineering strain at the point of necking. Also, we can express the strength coefficient K, as reference strength coefficient K_N, by forcing the flow stress curve of equation 2.86 to pass through the necking point.

$$K_N = \frac{\sigma_e^N(1 + \varepsilon_e^N)}{[ln(1 + \varepsilon_e^N)]^{ln(1+\varepsilon_e^N)}} \tag{2.88}$$

Therefore, The following reference Hollomon's Law will be achieved:

$$\bar{\sigma} = K_N \bar{\varepsilon}^{n_N} \tag{2.89}$$

With the above equation, the reference stress-strain curve, the necking can be predicted when the true strain equals the reference strain hardening exponent n_N. The figure 2.27 illustrates the utilisation of equation 2.89.

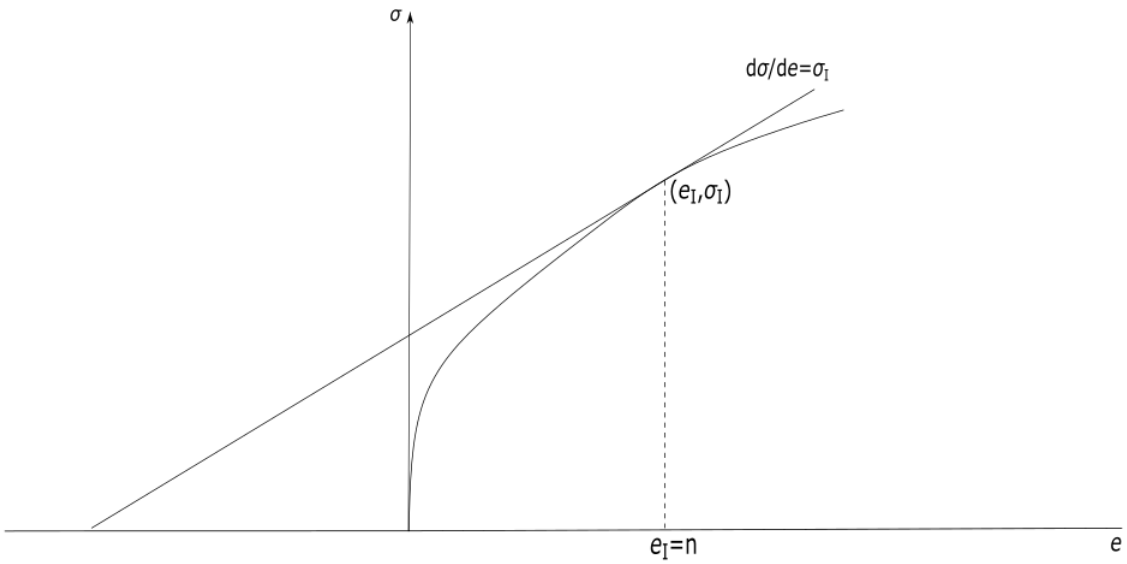

Figure 2.27: Reference stress-strain curve based on Hollomon's law

$$\sigma = ke^n \Rightarrow \qquad \frac{d\sigma}{de} = nke^{n-1} = \frac{n}{e}(ke^n) = \frac{n}{e}\sigma_I$$
$$\therefore \qquad n = e_I$$

Chapter 3

Mechanical Properties

3.1 Introduction

It is widely recognised that the state of the micro-structure and macro-structure of metals will be shaped according to its environmental conditions. Yield strength and elastic modulus are two of the most important aspects of differentiating between metals and their applications. Therefore, the two parameters will need be to be studied in contact with their surrounding.

It is widely accepted, that the strength and stiffness will generally, deteriorate with increase of temperature and vice versa and when plastic strain level is increased. Also, the effect of varying the thickness of the metal sheet has been proved to have some effect on the physical properties of the material. BS5950- part 8[10] and Eurocode-3 part 1.2[9], have managed to provide the stepping stone for characterising the cold-formed metals, by means of introducing the reduction factor investigation of the metals at elevated temperatures. However, the BS5950 merely describes the reduction factors based only on yield strength values which correspond to 0.5%, 1.5% and 2.0% total strain, neglecting the widely used 0.2% proof stress as the initial yield stress value. Moreover, the mentioned study fails to provide stiffness reduction factors based on the elastic modulus (see figure 3.1). On the other hand, EC3 supplies the appropriate data of yield strength and elastic modulus of cold formed steels, but with only two results for hot-rolled metals, the reduction factors of hot-rolled metals remain uncertain. This point becomes more concerning

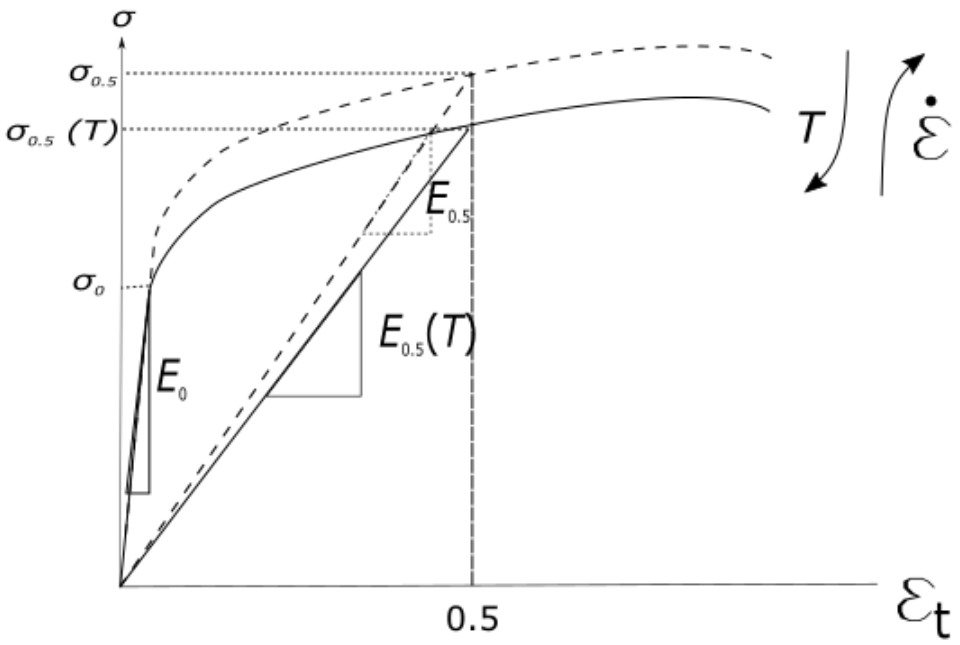

Figure 3.1: Reduction factor based on flow curve

when considering the study by Sidey and Teague [72], in which they claimed the strength reduction of cold-formed metals at raised temperature of upto $800°C$ is around 20.0% higher than those of hot-rolled metals. In the past decade, many researchers have recognised the importance of a thorough study of cold-formed metals, whereas in the past much of the research was focused on reduction factors of hot-rolled metals. The point missing on studying the reduction factors to date, is the effect of thickness variation; in a range for most common cold-formed steels of 0.55mm to 1.95mm.

Further, the correlations developed are not a function of thickness, which mistrust the correlations for thickness other than the tested material.

3.2 Uni-axial Testing

The most widely used means of representing materials for determination of their properties is performing tension and compression tests. As Ranawaka [7] demonstrated there is minimal difference between material properties which have undergone tension test or compression; researchers tend to carry out their tests in tension as it is far easier to investigate. Moreover, tension tests have the flexibility to be conducted in a manner of formats.

Transient state test will be ruled out in this reseach as they are more prone to creep effect, which is a time dependant effect [5]. Moreover, the steady state tests have the advantage of direct generation of stress-strain curves, also the FEM analysis model will have less constraints defined for it. Additionally, based on the work by Lee et al [6], there is minimal discrepancy between the results of a transient method test to that of steady state method.

The purpose of conducting uni-axial testing was to investigate the characteristics of a series of cold-formed metals, namely:

Carbon Steel - AISI 1010, C 0.08-0.13%

Stainless Steel - 304/304L, Ni 8-12%, Cr 17-20%

Brass - Cu 65%, Zn 35%

Aluminium Alloy - 6063, Mg- 0.45-0.9%, Si 0.2-0.6%

The results from the flow curve of these materials will enable the derivation of a mathematical expression, in order to represent similar material grades without the need to rely on experimental work. In contrast to many empirical expressions are still heavily reliant on experimental work.

Plastic regime is tightly related to the thermal signature of the surrounding. Thus, thermally interaction will control the plastic regime. For short distance elements, usually the thermally activated regime can be expressed by Arrhenius description [73].

$$\dot{\varepsilon} = \dot{\varepsilon}_0 exp(\frac{-\Delta G}{kT}) \tag{3.1}$$

In this expression, Arrhenius managed to express strain rate $\dot{\varepsilon}$ as a function of activation energy ΔG and temperature T. Therefore, it shows that temperature T and strain rate $\dot{\varepsilon}$ are interchangeable and have an inverse exponential relation to one another, i.e. as temperature increases the strain rate value would decline. Also another derivation from this expression is that different combination of strain rate and temperature would result in the same thermal activation response.

$$\Delta G = kTln(\frac{\dot{\varepsilon}_0}{\dot{\varepsilon}}) \tag{3.2}$$

On the basis of this theory, the range of strain rate and temperature for conducting the uni-axial tension tests were decided. The tests will fall within the strain rate range of $10^{-6}s^{-1}$ to $10^{-3}s^{-1}$ and temperatures of $23°C$ to $600°C$.

A standard tensile test is conducted by clamping one end and moving the other end, by means of the cross head at a certain speed (mm/min).

In order to interpret the results from a tension test, engineering definitions apply.

$$\sigma_e = P/A_0 \qquad \text{Engineering Stress} \tag{3.3a}$$

$$\varepsilon = \frac{L_1 - L_0}{L_0} \qquad \text{Engineering Strain} \tag{3.3b}$$

The difference between engineering and true stress and strain lies in the change to the cross sectional area. Engineering stress is defined as the applied load over the original cross section of the material; whereas, the true stress will denote the load at the actual cross section at every point during the test. Therefore, following the same concept, the engineering strain refers to the initial length of the gauge length L_d. Thus, the cross-head speed ν will be equal to the extension rate of the material, that the engineering strain rate becomes:

$$\dot{e} = de/dt = \nu/L_d \tag{3.4}$$

Therefore, according to the description of true and engineering stress, true strain refers the deformation to the current length.

$$\varepsilon = \int_{e_t=0}^{e_t} d\varepsilon = \int_{L_0}^{L_f} dl/l = ln(L_f/L_0) \tag{3.5}$$

Moreover, to obtain the true stress, plastic incompressibility needs to be assumed.

In other words, plastic deformation results in constant volume. Therefore:

$$\varepsilon = ln(1+e) \tag{3.6a}$$

$$\sigma_t = \sigma_e(1+e) \tag{3.6b}$$

3.3 Sample Preparation

3.3.1 Materials

The selected materials for this research were chosen as commercially available metal alloys, thus, giving a wider range of database for comparison purposes. However, at different stages of specific experiments, based upon the need and availability of material, alterations were deemed justified.

The decision to chose alloys over pure metals was based on investigating the many engineering applications of alloys, since this research will be heavily involved on comparing the processed data to the works carried out by other researchers.

3.3.1.1 uniaxial tension

The uni-axial tests were conducted on two geometries, reclaimed from sheet and bar.

The sheet formed material **0.13% c-steel** was provided in thicknesses of $0.6mm$, $0.9mm$, $1.1mm$, $1.3mm$, $1.9mm$, $2.0mm$ and $2.8mm$ in the following composition (%): Fe $99.18 - 9.62$, Mn $0.3 - 0.6$, S ≤ 0.05, P ≤ 0.04 and C $0.08 - 0.13$.

The bar Materials were provided in four grades based on American Standard:

AISI 304 was provided with the following composition (%): Carbon $0.08 - 0.03$, Mn 2.0, P 0.045, S 0.03, Si 1, Cr $18 - 20$, Ni $8 - 10.5$.

Commercial Brass alloy **C2600** was provided in the following composition (%): Cu $62.5 - 65.0$, Pb 0.07, Fe 0.07, Zn *Balance*.

0.13% C-steel was provided in the following composition (%):Fe $99.18 - 9.62$, Mn $0.3 - 0.6$, S ≤ 0.05, P ≤ 0.04 and C $0.08 - 0.13$.

AISI 6063 was provided in the following composition (%): Si $02 - 0.6$, Fe $0.0 - 0.35$, Cu 0.1, Mn 0.1, Mg $0.45 - 0.9$, Zn 0.1, Ti 0.1, Cr 0.1, Al *Balance*.

3.3.1.2 Bi-axial bulging

The bi-axial tests were conducted on the basis of a single geometry, with a constant thickness. The materials and data were provided through unpublished work. (see declaration)

AA 5754 was provided in the following composition (%): Mn 0.5, Fe 0.4, Mg $2.6 - 3.6$, Si 0.4, Cr 0.3, Cu 0.1, Al *Balance*.

AA 6111 was provided in the following composition (%): Si $0.7-1.1$,Mg $0.5-1.0$, Fe 0.4, Mn $0.15 - 0.45$, U 0.15, Cr 0.1, Ti 0.1, Al *Balance*.

AC 300 was provided on the following composition (%): Si 0.6, Fe 0.2, Cu 0.13, Mn 0.07, Mg 0.6.

3.3.2 Selection of test specimen

In preperation of each material, care was taken not to alter its properties [74, 75]. For instance, in cutting the sheet metals to form, two methods were available CNC or Plasma cutting. Plasma cutting was ruled out based on the statement that it would harden the edge of the gauge length; thus, influencing the material ductility. Also care was taken to cut the rest pieces aligned with their rolled direction, as it would reduce the influence of sheet anisotropy arising from rolling [76].

For chosen cross-head velocity, temperature was altered for each test to clarify its influence. Here four cross-head speeds were chosen as well as 5 temperature ad-

justments for uni-axial tests.

The number of specimens designated for every test, depended on the validity of the results based on the observed trend. For a test with results other than expected, repeat tests would be carried out and a third test for verification of the previous corrected trend; to ensure the consistency of the presented result.

3.3.3 Preparation of test specimen

The available coupons were assured not to contain any damage prior to the test i.e. unwanted cracks, notches etc. Therefore, any sample with any accidental bend would be disposed of for the sake of consistency, as even slight bending will cause working of the material and alter the properties.

The used piece of the materials was at least 5 mm from shredded side and 5 mm from machined cut side. The final round of checks was carried to ensure all the samples are of the same surface roughness.

3.3.4 Test piece geometry

Uni-axial tests were carried on two stock supplies, either a sheet material is used or a round bar [77, 78, 79].

The gauge length l_0 of the test piece refers to the distance between the visible perpendicular section (refer to figure 3.2). It is this distance that undergoes the deformation and exhibits the yield stress value. The current length should always be absolutely more or less than the original length, depending on the test being tension or compression, respectively.

ISO has proposed a standard geometry for series of flat and round pieces at elevated temperature alloying for thickness variation [80].

However for the purposes of this research, a non standard specimen end geometry was considered and manufactured. The flat sample specimens were cut based on an

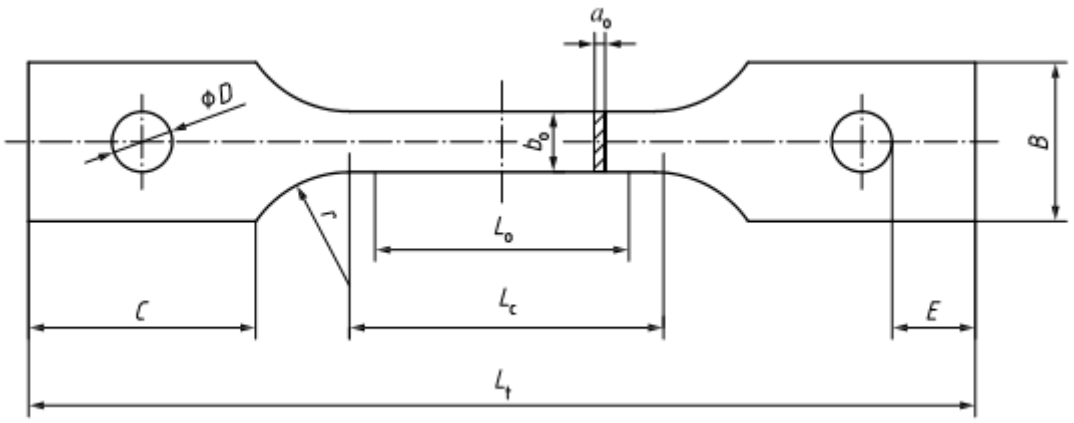

Figure 3.2: Example of test piece for sheets with thickness between 0.1 and 3 mm,[80]

a_0		b_0	L_0	r	B	C	D	E	L_c	L_t
0.1	3.0	12.5	50	25	35	50	15	17	62.5	205

Table 3.1: Proposed dimensions for flar test piece (mm), citeiso6892

improved design. The reason for such action was to extend the strain rate effect based on the screw driven tensile machine available (illustrated in the figure below 3.4). The agreement made is for 80 mm Gauge Length and 180 mm LOA specimens to 0.2% and 0.3% tolerance respectively. The specimen was constructed with two, 2/3 circular holes M8 bolts at each end to assist in securing the specimen in position through the use. The 2/3 circular holes were chosen in order to minimise the build-up of stress concentration factor (SCF) and avoid any unwanted failure along the transverse or longitudinal direction.

The material used on this stage was 0.13% C-steel also known as CR4 with varying thickness. The dimensions provided below are in mm.

Round samples figure 3.6 were chosen in order to apply the study independent of thickness variations. Further, since in this study strain rate characterisation was not as paramount as the previous study; standard specimens were chosen for all four materials. The materials chosen for this investigation are more sensitve to elevated temperatures [77], to ensure load axiality at temperature split collect grips (fig 3.5)were introduced as the holding mechanism.

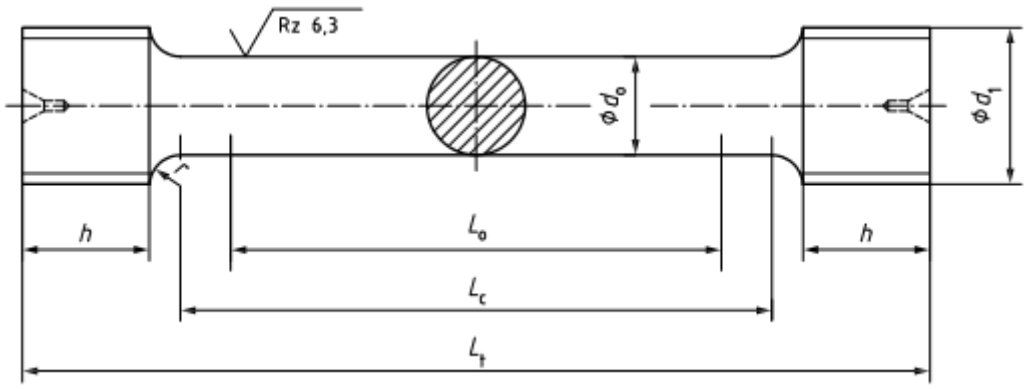

Figure 3.3: Example of cylindrical test piece

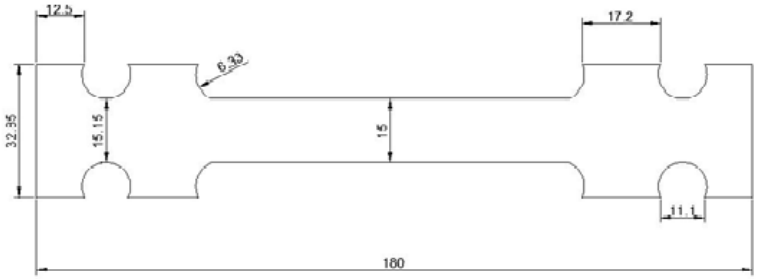

(a) Flat sample schematic

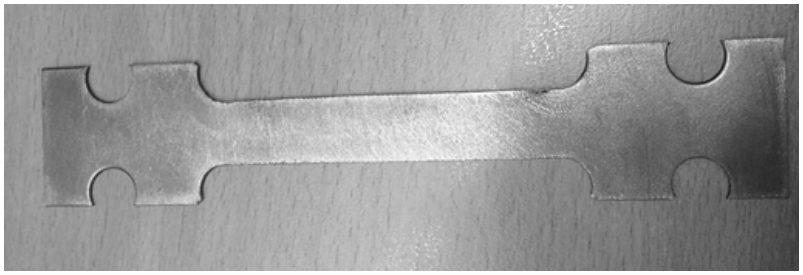

(b) Virgin flat sample

Figure 3.4: Flat sample configuration

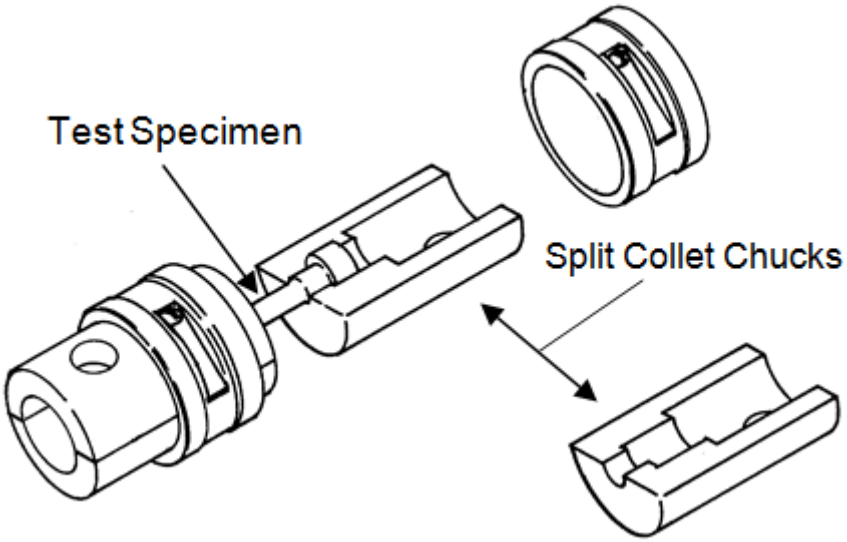

Figure 3.5: Schematic of split collet, [37]

Demonstrated below is the schematic of round samples:

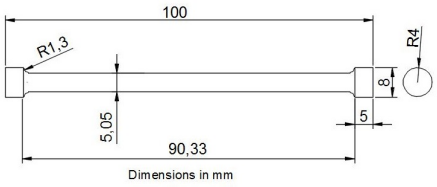

(a) Circular sample schematic

(b) Virgin dumbbell sample

Figure 3.6: Circular sample configuration

3.4 Testing Apparatus

The experimental tests were carried out at the Brunel University, structural and material testing lab. The machine used was out of commission for many years and had to be re-commissioned. The tensile machine system consists of three main components.

- Tension-Compression unit
- Temperature Controlling Unit
- Acquisition System

Dartec limited had provided the machine, the machine weighs 320 kg (710.4 lb.), which is connected to a single phase mains supply (230v 50Hz 2 amp). The straining mechanism consists of a recirculating ball screw attached to a moving cross head. The screw is moved by a servo motor which drives through a reduction gear so as to rotate the nut of the ball screw assembly. The speed of rotation of motor is controlled by reference to tachometer. A manual gear change alters the drive ratio by 10:1.

A servo-motor drives through a reduction box onto a pair of change gears and finally through a second reduction onto a gear wheel fixed to the recirculating ball

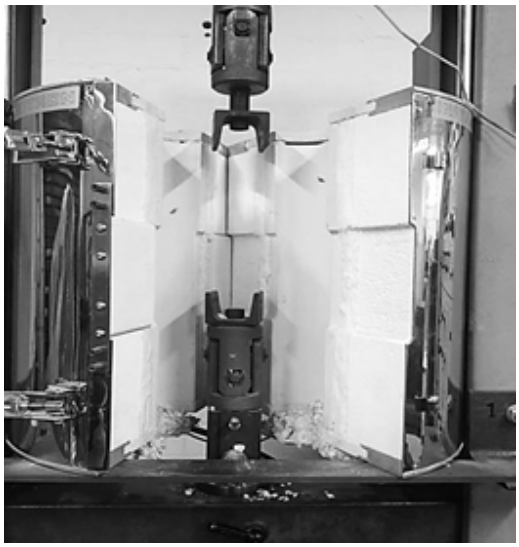

Figure 3.7: Furnace & tensile machine

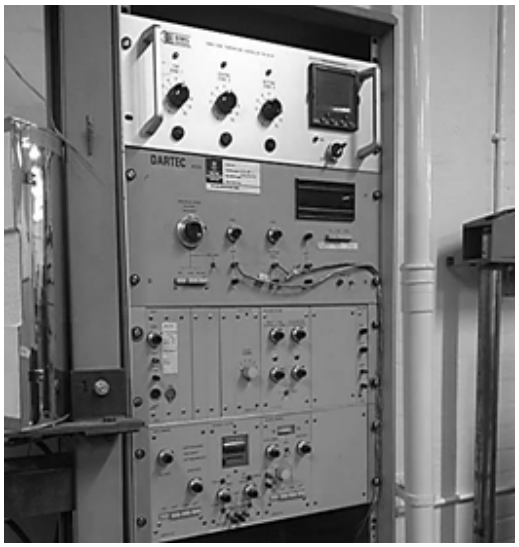

Figure 3.8: Controller unit

nut. Since the screw is prevented from rotating, rotation of the nut causes the crosshead to move.

The speed of the servo motor, which is controlled from the control panel is adjustable over a range of 1000:1. The change gears have a ration of root 10, so that interchanging them produces a straining speed change of 10:1. Therefore speed range will provide the following capacities:

- 0-10mm/min max load 50kN
- 0-100mm/min max load 5kN

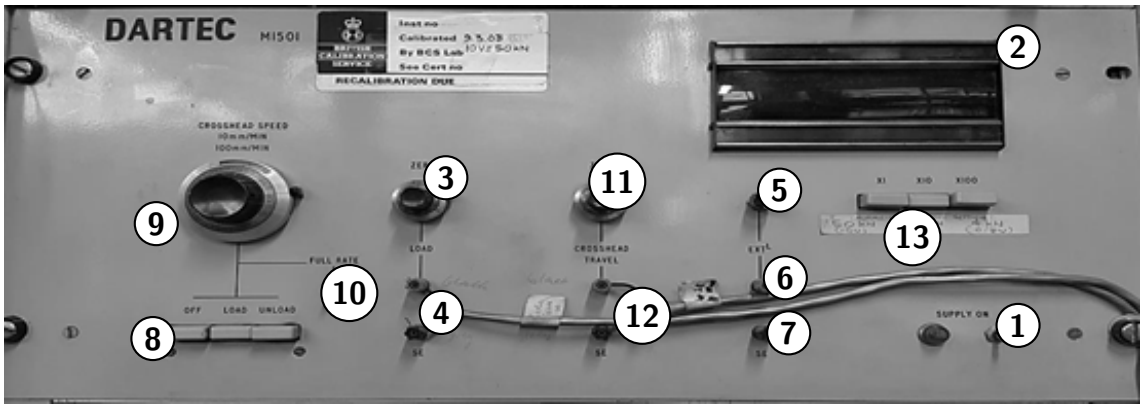

Figure 3.9: Main controlling panel

1. **Main Switch** – Switches on the mains to the indicator and the power drive.
2. **Load Indicator**– digital display shows the load applied to the specimen.

3. **Load Zero Adjustment**– A multi turn potentiometer adjusts the load.

4. **Load Output Signal**– the machine provides a DC analogue signal of load.

5. **Indicator External Button**– when pressed the indicator displays the signal fed to the external socket.

6. **Indicator External Socket**– Accepts signals for display on the indicator.

7. **Signal Earth Socket**– Earth signal socket associated with the external signal to the indicator.

8. **Direction Selection Button**the three buttons will drive the load, unload at the selected speed. Note in "off" position the motor is held to zero speed and some creep may occur.

9. **Rate Setting Potentiometer**– The potentiometer sets the motor drive speed in terms of crosshead rate.

    - Low Gear 100%=10 mm/min
    - High Gear 100%=100 mm/min

10. **Fast Rate Switch**– Sets the drive to operate at full speed.

11. **Cross-head Travel Zero**– A multiturn potentiometer adjusts the cross-head travel to zero.

12. **Cross-head Travel Output Signal**– the machine provides DC analogue signal of travel at this socket.

13. **Load Reading**– the loads can be set to operate within the maximum kN range specified based on the calibration.

x1	50 kN	10 V
x10	40 kN	8 V
x100	4 kN	0.8 V

The load which can be applied at the highest straining speed is limited. The maximum is reached at 50kN; subsequently a 50.5kN (1% overload) the drive cuts.

The specimens are positioned on two precisely vertically aligned rods, of which the top rod is held in place and the bottom rod is the moving part with the motor attached to it, i.e. crosshead.

The centre crosshead slides on four columns which carry the top crosshead. It is moved by the straining screw which is locked to the cross head during a test. The locknut (1) is tightened against the crosshead to remove backlash and the clamp (2) prevents the straining screw from rotating. The travel of the crosshead is therefore limited to a unidirectional motion.

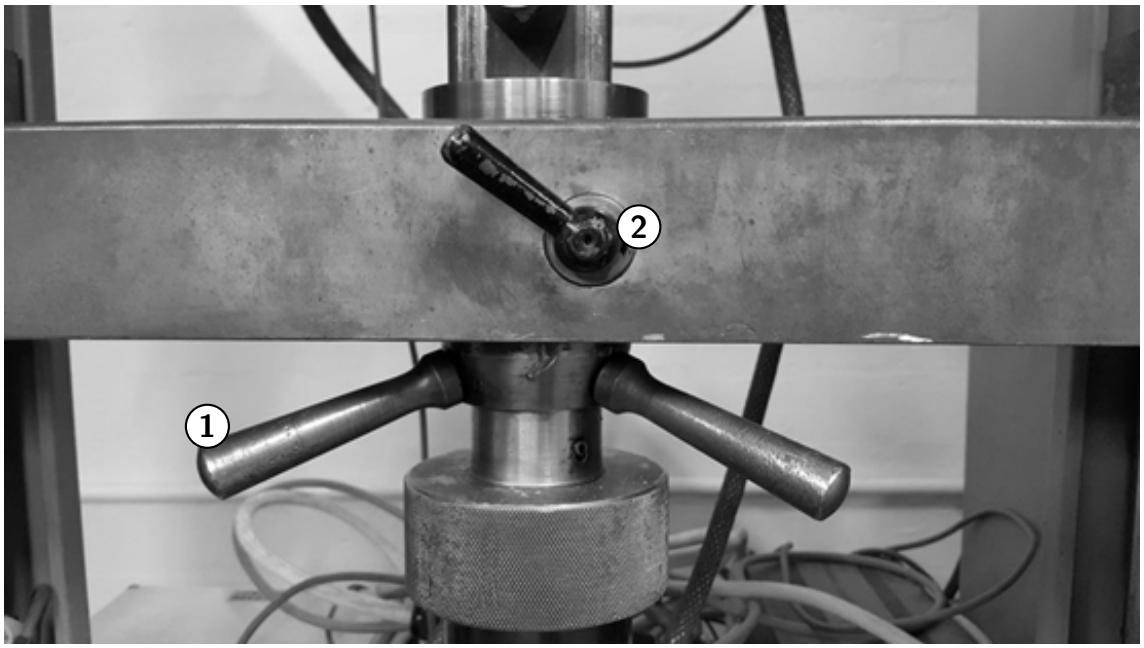

Figure 3.10: The locknut

A strain gauge load cell is mounted in the top crosshead and tests are carried out between gripping tools which are fitted to the load cell and moving crosshead. Additional control and indications were fitted to give control of strain rate, loading rate cycling hold facilities, indication of cross head travel and specimen extension.

In order to carry on the tests, every specimen has to be mounted on to the machine. Therefore, two different fixtures were created to help maintain axiality of the specimen, with the least amount of slacking and controlled degrees of freedom.

The second most important part of the testing is the furnace. The furnace used was supplied from INSTRON; the furnace has a split design that facilitates fast and

easy loading and unloading of specimens. The three zone resistance furnace, encourages reliable, accurate heat loading, based on the temperature demand. Adjustable stainless steel latches help to secure the two splits of the furnace in place whilst in use,figure 3.10(1). The casing of the furnace is fabricated from stainless steel and aluminium with hardened insulation plates to assist the furnace to reduce its heat flux and to feel cool to the touch once under operation.

The furnace is capable of reaching 1050°C at its maximum, however the maximum can only be maintained for short duration. The heating rate of the furnace was chosen to be 10 to 20°C/min. The pre-selected temperature would usually be exceeded by 2% at higher temperatures of 400°C and 7% at lower temperature of 350°C. The overshoot, however would stabilise in short period of time, 1-5 minutes. Subsequently, the specimen was held at the selected temperature to ensure the steady state condition. However, in few cases the temperature of the specimen and the surrounding air would differ, therefore a thermocouple was manually placed in contact with the specimen and the thermometer's temperature was established as the present value.

The temperature inside the heating device is maintained and controlled through 4 thermocouples, which are working on the principle of thermo-electric effect. The furnace is split into three temperature zones, which are controlled by three type K thermocouples located within the insulating panels. The fourth thermocouple (type R) helps by measuring the surface temperature of the specimen and adjusting the power supply accordingly. A Eurotherm temperature controller enables the regulation of the temperature by defining the rate of heating and percentage of the overshoot as well as selecting the required temperature.

Figure 3.11: Furnace controller

Figure 3.12: Temperature monitor

Thermal expansion of the specimen, leading to rise of length in the sample was however recoded during the tests due to increase in temperature; subsequently the thermal expansion could result in compressive loads. Therefore, to account for this effect, a minute tensile load was applied to the sample at time zero, to obviate pre-loading and restrictions for upwards movement of the sample were encouraged.

The third step is to collect the data, for this purpose an analogue measurement processor from MSI model 7321 with 8 channels was employed. All the readings from the tensile machine load cells and thermocouples were recorded in mV and subsequently converted into stress and strain values.

Figure 3.13: Data scanner

All tensile coupons were from the grades of rolled and cold-formed materials with varying grades, thicknesses. In general, the experiments were carried out either at ambient temperature or elevated temperature based on homologous temperatures $\frac{T}{T_m}$ for each individual material. Alternatively, variations in cross head speed were also fundamental in the experiment. For the first set of the experiments, low strength low carbon steel was chosen (0.13% C-steel) with two thicknesses (1mm, 2mm). This chapter aims to describe, discuss and illustrate the selection of the test specimens, procedures involved and the results and the findings. All the tests were conducted with varying temperatures ranging from 20°C to 600°C.

A family of load curves were produced from the experiments, these were later

converted to plots of stress *vs*. strain for post processing. Later, the reduction factors of the samples were produced in order to verify the results obtained against other researchers and international standards along with a comprehensive study based on the constitutive equations. The experiments in the first stage were based on two variables.

- Cross-head movement, and;
- Temperature variation

3.4.1 Cross-head movement specification

The Dartec tensile machine has the capability to alter the cross-head velocity. Due to the capabilities of the tensile machine, four modes of movement from low strain ranges were chosen, and kept constant throughout the experiments.

Mode No.	Rate of Movement
Mode 1	0.3 mm/min
Mode 2	3 mm/min
Mode 3	30 mm/min
Mode 4	90 mm/min

Table 3.2: Modes of cross-head movement

3.4.2 Temperature variation specification

The temperatures were set according to the homologous temperature concept for each individual material; as what constitutes for high temperature is different for different metals. Therefore, by definition the relative temperature of the sample as a fraction of its melting point temperature through the use of Kelvin scale were obtained and subsequently set as the maximum temperature of testing for that material.

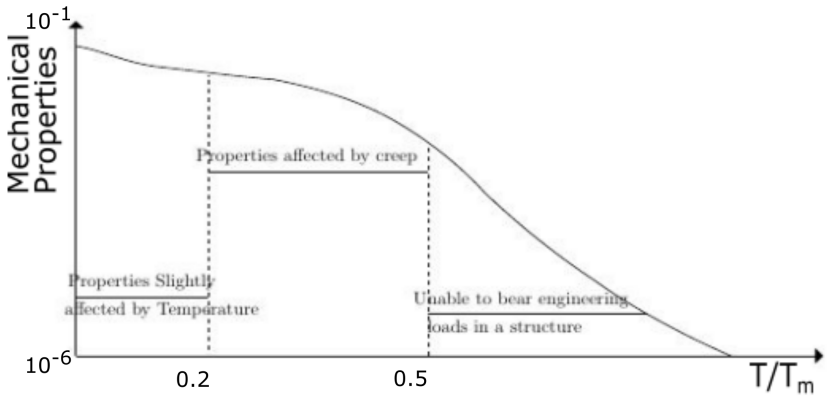

Figure 3.14: Temperature designation based on homologous temperature

3.5 Experimental Sequence

As mentioned in Section 3.3 on page 65, two geometries were decided upon. The first round of sheet experiments were carried out to signify the importance of strain rate variation. As to this, the structure below was composed.

Cross-head Movement (mm/min)	**Temperature (°C)**	**Thickness (mm)**
N/A	23	N/A
0.3	300	N/A
3	450	1.0
30	400	2.0
90	450	N/A
N/A	500	N/A

Table 3.3: Varying strain rate & minimal thickness variation

Subsequently, the processing of the data from table 3.3 suggested and investigation into the trend generated by thickness variation with constant strain rates; Therefore the program below was carried out.

Cross-head Movement (mm/min)	**Temperature (°C)**	**Thickness (mm)**
0.3	23	0.6
↓	300	0.9
↓	400	1.1
↓	500	1.3
↓	600	1.9
↓	N/A	2.8

Table 3.4: Constant strain rate with varying thickness and temperature

Table 3.4, as illustrated will attempt to investigate the effect of thickness. The

correlations achieved will be discussed in chapter 4. As to the chosen value of strain rate; 0.3 mm/min was chosen to have the least rate influence for assessing T and t influences.

Continually, after establishing the structure to carry out the tests on flat samples; similar approach was conducted to form homogeneous sequence for the dumbell samples. The table below represents the behaviour of this round of experiments.

Carbon Steel							Brass						
Crosshead Movement (mm/min)	Temperature (°C)						Temperature (°C)						
		23	150	300	450	500		23	80	160	240	320
	0.3			✓			0.3			✓		
	3	✓	✓	✓	✓	✓	3	✓	✓	✓	✓	✓
	30			✓			30			✓		
	90			✓			90			✓		
Aluminium Alloy							Stainless Steel						
Crosshead Movement (mm/min)	Temperature (°C)						Temperature (°C)						
		23	50	100	150	200		23	100	300	450	600
	0.3			✓			0.3			✓		
	3	✓	✓	✓	✓	✓	3	✓	✓	✓	✓	✓
	30			✓			30			✓		
	90			✓			90			✓		

Table 3.5: Bar samples, experiment arrangements

This chapter aimed to describe, discuss and illustrate the selection of the test specimens, procedures involved, the results and the findings. All the tests were conducted with varying temperatures ranging from 20°C to 700°C.

3.6 Experimental Results

3.6.1 Tensile test results

The figures below represent the uni-axial tension tests upon 1mm sheet at 3 mm/min. As mentioned the tests upon sheet and bar samples were conducted in three segments. The effect of temperature variation and strain effect are clearly present. The thickness variations illustrates changes to material property, however it might be harder to observe; the error analysis of thickness effect will be clarified in the next chapter. A full preview of graphs will be present in the Appendix A.

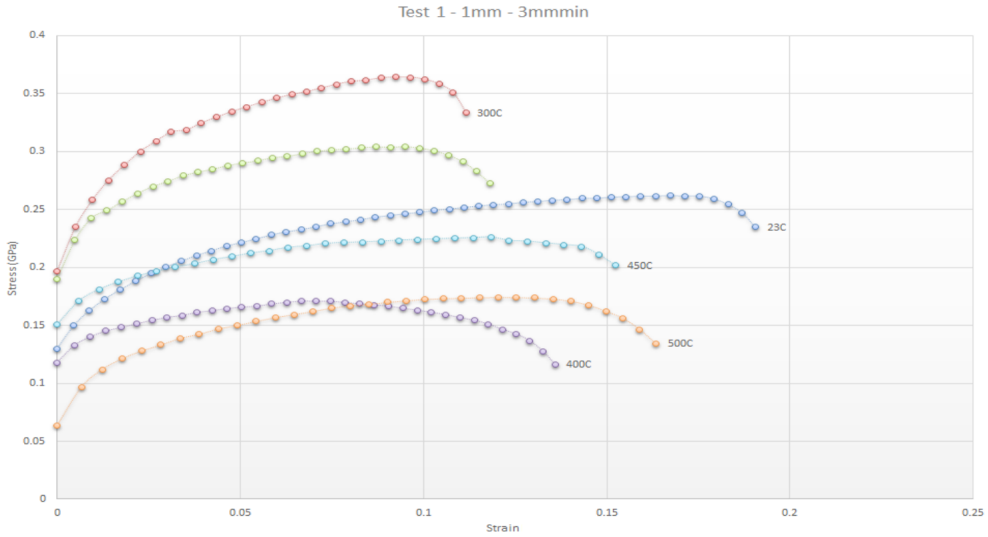

Figure 3.15: 0.13% C-steel stress-strain family curves at $6.09 \times 10^{-4} s^{-1}$ °C, @ 1mm

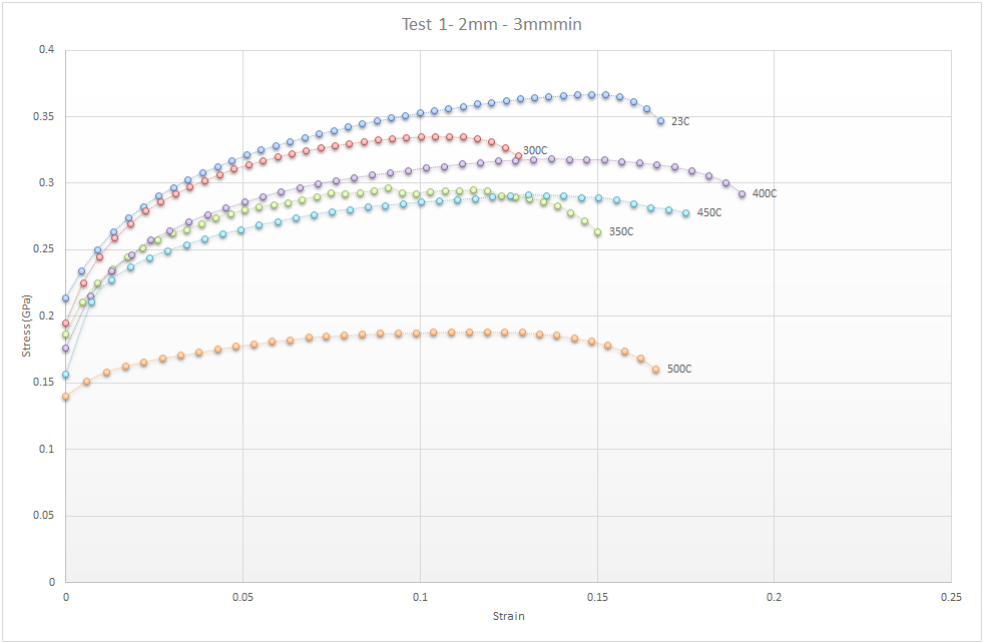

Figure 3.16: 0.13% C-steel stress-strain family curves at $6.09 \times 10^{-4} s^{-1}$ °C, @ 2mm

3.6.2 Bulge forming results

The bulge forming test was carried out in order to increase the strain limit of the tested material. The materials tested are:

Carbon steel 0.13%C

Stainless steel Ni 8-12%, Cr 17-20%

Aluminium (5754)

Aluminium (6111)

Provided below are the plates after bulging has been carried out.

Figure 3.17: Bulge forming stress-strain plot of AA5754

Presented below are the results of the said experiment.

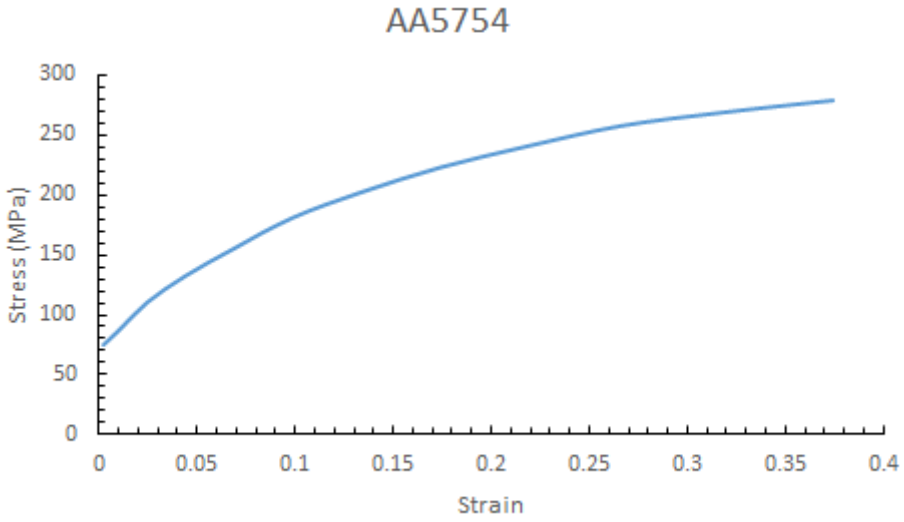

Figure 3.18: Bulge forming stress-strain plot of AA5754

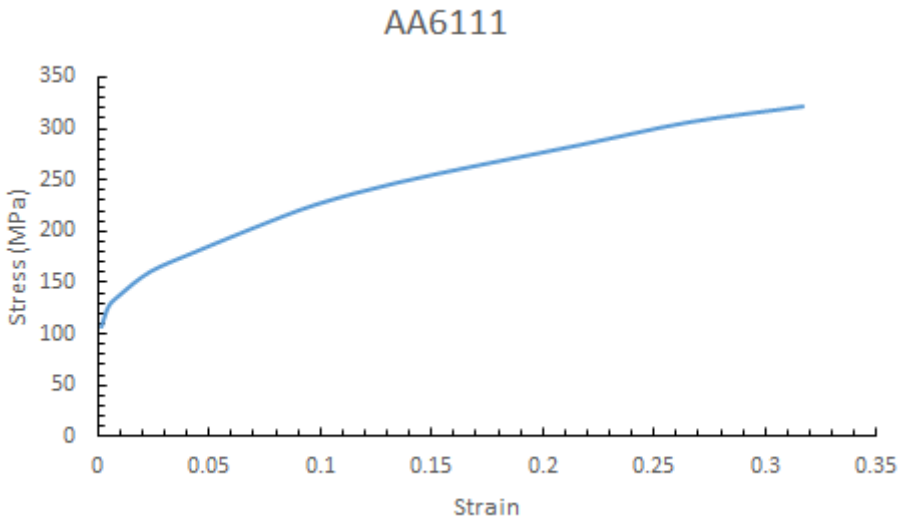

Figure 3.19: Bulge forming stress-strain plot of AA6111

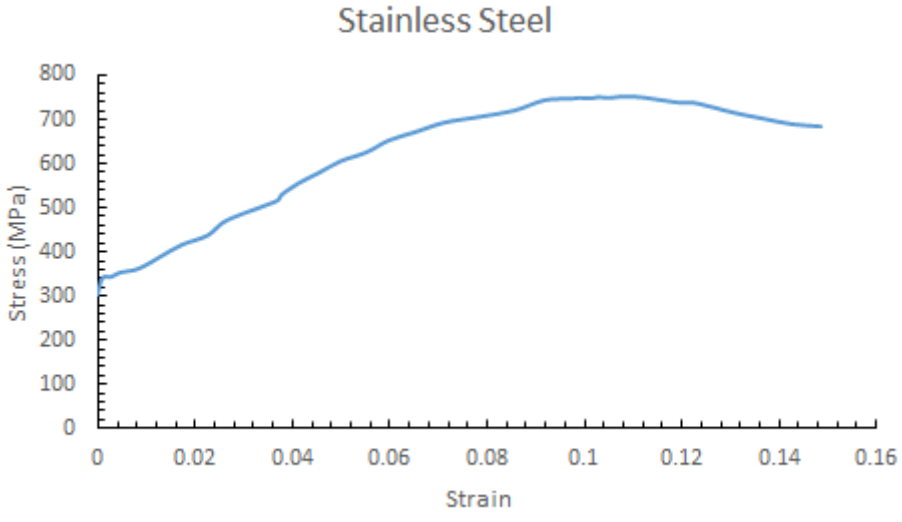

Figure 3.20: Bulge forming stress-strain plot of stainless steel

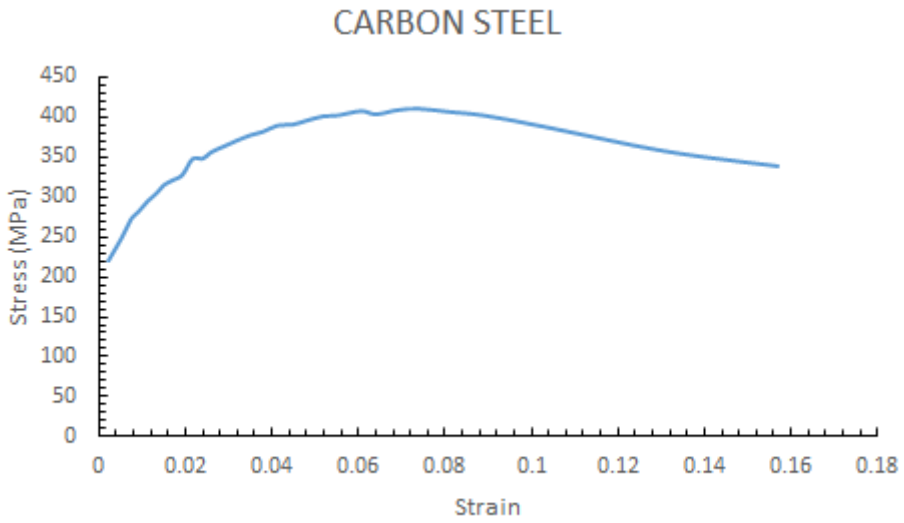

Figure 3.21: Bulge forming stress-strain plot of carbon steel

3.6.3 Plane strain compression testing

In order to further increase the strain level, a series of plate compression testing were conducted. However, since the strain level increase recorded in aluminium alloy showed bigger impact compared to other materials, only AA5754 and AA6111 were chosen for illustrating the strain level increase in this stage.

Provided below are the figures related to this subject.

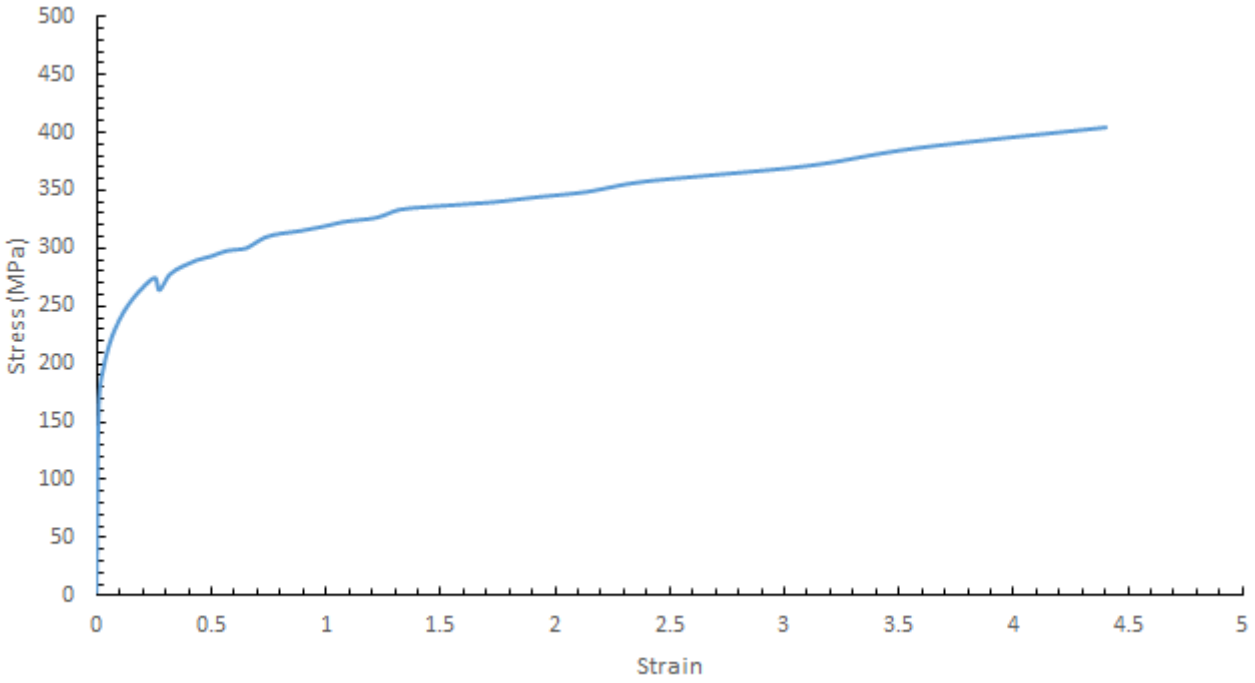

Figure 3.22: Compression plate stress-strain plot of AA5754

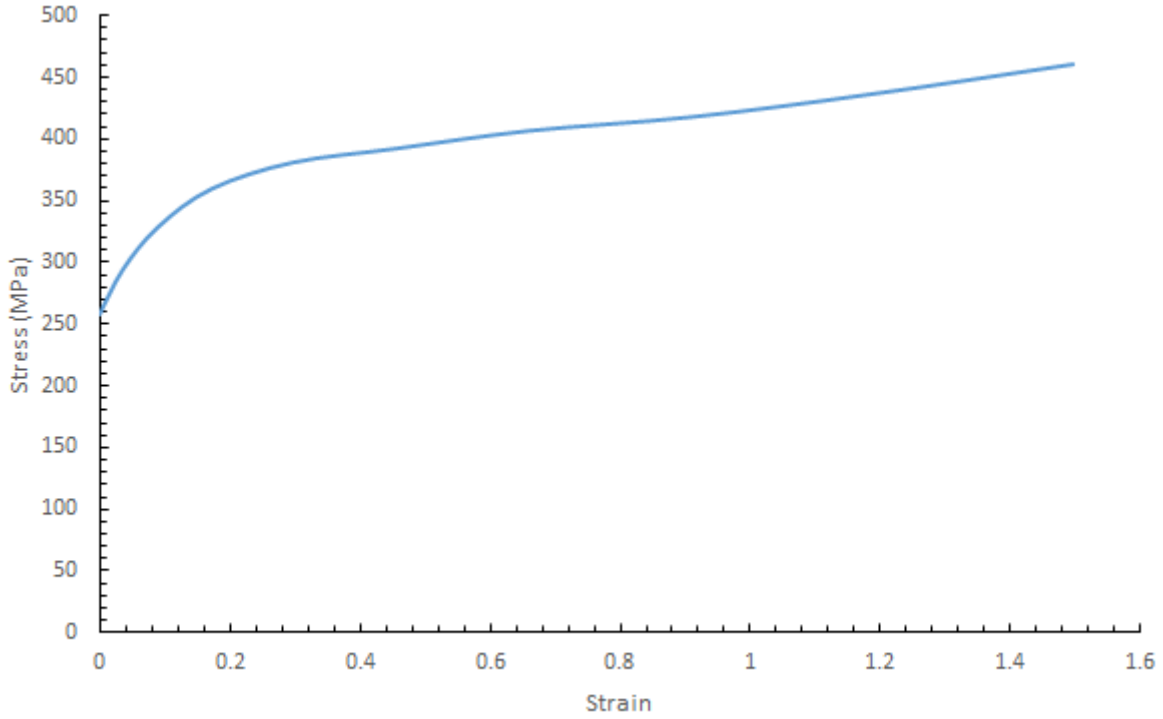

Figure 3.23: Compression plate stress-strain plot of AA6111

To further illustrate the strain limit changes based on method of experiment, figure 3.24 below is provided. As can be seen the figure is adjusted based on the two aluminium alloys tested, the lower limit signifies the smaller strain value of the alloy with less strain limit increase. As shown, with change of test method from tensile

test to bulge forming and later to compression plate testing the limit is exponentially changed.

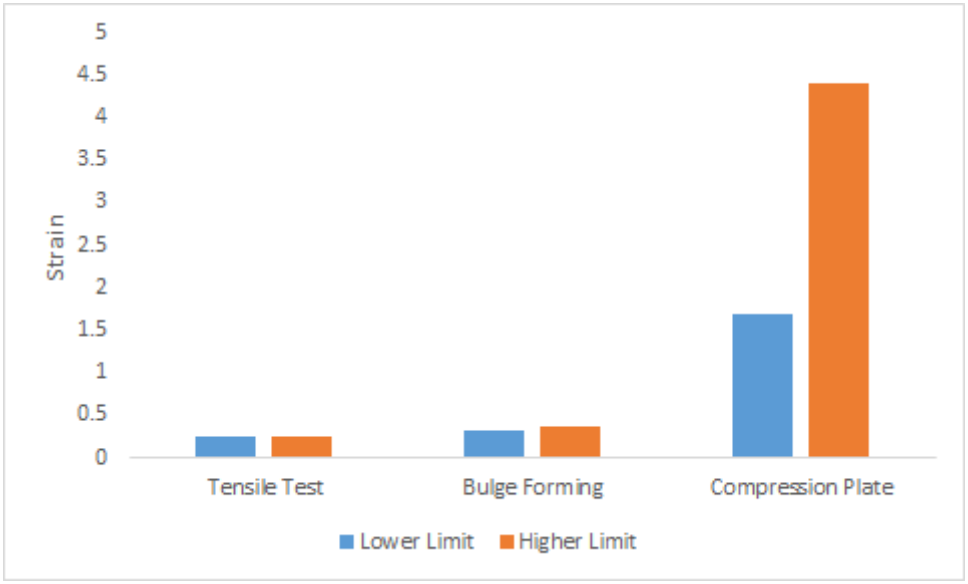

Figure 3.24: Strain limit of the aluminium alloys based on method of experiment

Figure 3.25, shows the percentage difference of every test method with respect to the other two tested methods. The compression plate is seen to increase the strain limit threshold considerably more that the other two methods, 178% compared to tensile test and 169% compared to bulge forming method.

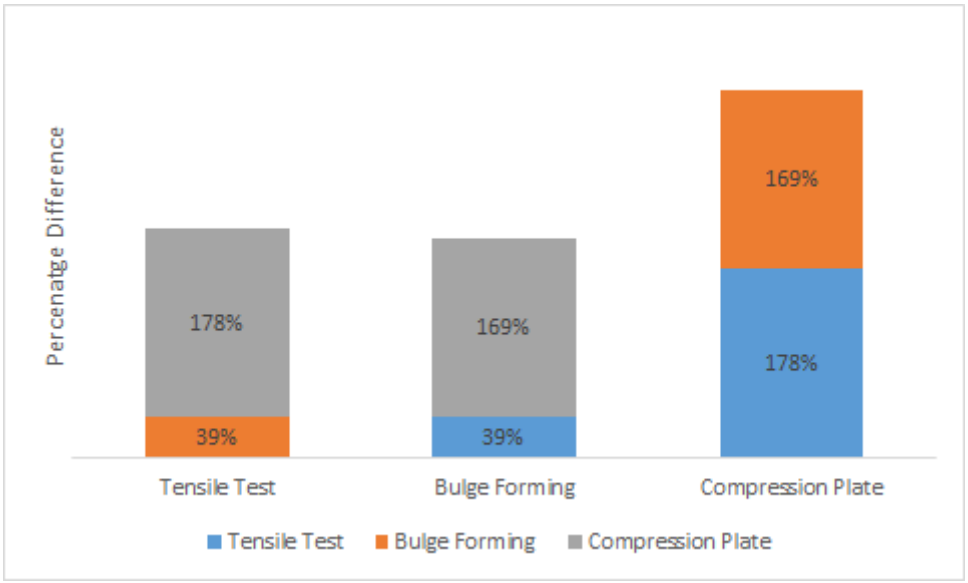

Figure 3.25: Strain limit percentage change of the aluminium alloys based on method of experiment

It should be noted the experimental comparison demonstrated here, was conducted at ambient temperatures.

Chapter 4

Experimental Investigation

4.1 Introduction

As previously discussed a series of High Temperature Tensile Tests (HTTT) were carried out in order to investigate the behaviour of the materials under different conditions.

The experiments were followed based on the fact that under the influence of heat, cold-formed steels will lose their strength faster than hot-rolled steels; due to augmentation of cold-formed steel at room temperature (21° C). Here international guidelines help standardise the developments of information, e.g. British Standard Institution BS5950-part8 [10], the European Committee for standardization part1.2 [9], Standards Australia part 2291[81] and etc.

However, none of them provide a comprehensive study; BSI and ECS both provide the reduction factors based on the mechanical properties of cold-formed steels. For yield strength BSI corresponds to 0.5%, 1.5% and 2.0%, not providing the most crucial corresponding value of 0.2% proof stress; further it does not provide the reduction factors for elastic modulus, ultimate strength and etc. Whereas ECS provides both elastic modulus and yield strength, therefore is assumed that these are similar to hot-rolled values which is a false assumption.

Based on Sidey and Teague [72], showed that cold-formed steels will relinquish a further 10-20% of their strength at elevated temperature compared to the hot-rolled

steels due to their metallurgical composition and molecular surface effects. On the other hand, standards have helped to nominate a few guidelines for steels at elevated temperatures. Many other researchers have tried to carry out their flow curve investigations over the years, despite the significant contributions made by various institutes, our area of interest still needs further investment as it falls in the category of fundamental studies for metallurgy, structural engineering and mechanical engineering.

Figure 4.1: Example of failed sample

4.2 Background

Based on the structure of this project, three primary effects would result in changes of mechanical property. One the most studied effects in defining the mechanical property relates to understanding of strain rates. The mechanical properties of material in relation to strain rate depends greatly on the application and utilisation of the material. As an example in crash-worthiness experiments, in which strain regime would vary between 0.01 s^{-1} to 100 s^{-1}, strain rate effect could not be discarded [18]. Although, this observation is applicable for higher strain rates than tested in this work. The dependence of the material on lower strain rates should not be ignored, as the mathematical model has to be comprehensive in its account of strain rates other than reported.

The most comprehensive mathematical models will describe the trend of the material's yield stress in a function of strain, strain rate and temperature. However, lack of thickness contribution in existing models have been noted as a point of present contribution. The existing models are classified as empirical equations. Holloman's law has been at the core of majority these models connecting them to power law conditions. The latter will signify the log-log plot of stress-strain would travel

in a one to one ratio. However, with today's computational advances more physical explanations can be related to the behaviour of the materials. The advantage of a physically based model is the incorporation of a broader strain rate range, contrary to the older models which would be more accurate over shorter ranges of strain.

A number of models have been greatly relied upon in the past, and many contributions have been derived through their use. In the next section some specific functions will be discussed.

4.2.1 Existing models

In 1980 Steinberg and Guinan [82], described a model based on the shear stress G as a function of yield strength, plastic strain and temperature.

$$G = G_0 \left[1 + (\frac{G'_p}{G_0})\frac{P}{\eta^{1/3}} + (\frac{G'_T}{G_0})(T - 300)\right] \tag{4.1a}$$

$$Y = Y_0[1 + \beta(\varepsilon + \varepsilon_i)]^n \left[1 + (\frac{Y'_P}{Y_0})\frac{P}{\eta^{1/3}} + (\frac{Y'_T}{Y_o})(T - 300)\right] \tag{4.1b}$$

The Steinberg equation 4.1 is constructed upon the assumption that a value of strain rate $\dot{\varepsilon}$ exists above which strain rate would have negligible effect on yield strength of the material. Thus, a limitation of strain rate equal to $10^5\ s^{-1}$ is set for utilising this model. Therefore the limitation could be expressed as:

$$Y_{max} \geq Y_0[1 + \beta(\varepsilon + \varepsilon_i)]^n \tag{4.2}$$

Where β is defined as the compression value i.e. ν_0/ν. The parameters n and ε_i are the work hardening and initial effective plastic strain, respectively. The subscript 0 relates to the reference condition of the material ($P = 0, T = 300K, \varepsilon = 0$).

Continuing on this work, Steinberg and Lund [83] attempted to broaden the spectrum of strain limitation. As a consequence a new model was proposed with strain as low as $10^{-4}s^{-1}$. Thus, the yield stress was given as:

$$\sigma_y = [Y_T f(\dot{\varepsilon}_p, T) + Y_A f(\varepsilon_p)]\frac{G(p,t)}{G_0} \tag{4.3}$$

Where $Y_T f(\dot{\varepsilon})$, describes the yield strength as a function of effective plastic and temperature, there it is commonly known as the thermally activated parameter. The second terms of the equation 4.3 describes the work-hardening $f(\varepsilon_p)$ as:

$$Y_A f(\varepsilon_p) = Y_A[1 + \beta(y_i + \varepsilon_i^p)] \leq Y_{max} \tag{4.4}$$

Where Y_{max} is the maximum yield strength value based on hardening rate and Y_p is the Peierls stress based on the strain rate.

Bodner and Symonds [84] investigation lead to description of a model for a rigid plastic material. Their uni-axial model describes the behaviour based on limitation of strain within the plastic regime, $\varepsilon_y \leq \varepsilon \leq \varepsilon_u$:

$$\frac{\sigma}{\sigma_0} = 1 + \left(\frac{(\varepsilon_u - \varepsilon_y)\dot{\varepsilon}}{(\varepsilon - \varepsilon_y)D_u + (\varepsilon_u - \varepsilon)D_y} \right)^{1/q} \tag{4.5}$$

Where σ_0 is the static flow stress, $\dot{\varepsilon}$ is the strain rate, ε_y is the yield strain, ε_u is the ultimate strain and q is independent of strain. D_u and D_y are the coefficients of strain at or near the ultimate and yield strain, respectively.

For $\varepsilon = \varepsilon_y$:

$$\frac{\sigma}{\sigma_0} = 1 + (\frac{\dot{\sigma}}{D_y})^{1/q} \tag{4.6}$$

For $\varepsilon = \varepsilon_u$:

$$\frac{\sigma}{\sigma_0} = 1 + (\frac{\dot{\sigma}}{D_u})^{1/q} \tag{4.7}$$

Two of the more prominent empirical methods used to verify the results of the experimental work in an analytical approach are the Johnson-Cook and Zerilli-Armstrong models. It should be noted that the two methods mentioned are validated using the materials with more sensitivity to strain rate and temperature.

The most common means of utilising the two models are to verify the experimental results using the numerical simulation, therefore correct approach in defining the constants of the equation has to be established. The disadvantage of the two models compared to the proposed mathematical model, which will will be presented later,

is that the parameters defining the equations need to be computed experimentally. However, since the two models have been around for a long time majority of the parameters are readily available. Moreover, it is widely accepted most metals would reach minute hardening rate at higher strains. However, such a prediction cannot be found in JC or ZA models[85].

4.2.1.1 Johnson-Cook model

Johnson Cook model is an empirical expression of equivalent von Mises stress as a function of temperature, plastic strain and strain rate. Due to its nature the expression, is usually used in high strain rate representation, such as impact or metal forming simulations [86, 87, 88].

A widely used expression to define the metals work hardening behaviour, with low strain rates, is the parabolic hardening rule based on the Ludwick's law:

$$\sigma = \sigma_0 + k\varepsilon^n \tag{4.8}$$

Where k is the strength coefficient, n is the hardening component and σ_0 is the yield stress. However, the effect of thermal softening due adiabatic temperature influence should be considered within the model. Therefore for a given strain the flow stress could be presented as:

$$\sigma = \sigma_r \left[1 - \left(\frac{T - T_r}{T_m - T_r}\right)^m\right] \tag{4.9}$$

Where T_m represent the melting temperature of the material. T_r is the reference temperature at which the test is conducted and m is the homologous exponent.

J-C, based on the fundamentals above, proposed the following expression in five constants.

$$\sigma = [A + B(\varepsilon)^n][1 + Cln(\dot{\varepsilon}^*)][1 - (T^*)^m] \tag{4.10}$$

The material constants A, B, C, n and m may be evaluated by means of experimentation. The $\dot{\varepsilon}^*$ is known as dimensionless strain rate $(\frac{\dot{\varepsilon}}{\dot{\varepsilon}_0})$. As it can be seen

the first bracket defines the stress as a function of strain for $\dot{\varepsilon^*} = 1.0$ and $T^* = 0$, whereas the other two brackets will include the effect of strain rate and temperature into the flow stress. One has to be aware that the J-C model also makes use of the $\sigma \propto ln\dot{\varepsilon}$ for lower strain rates. Further, the term T^* is the homologous temperature, defined from eq.4.9 as:

$$T^* = \frac{T - T_r}{T_m - T_r} \tag{4.11}$$

One of the issues with the J-C model is the presentation of the equation which suggests the temperature and strain rate are independent of one another, which has been ruled out by the behaviour of most metals. One point to note is the J-C model in most cases will be used for damage evaluation. In such cases the J-C model could be regarded as providing strain at point of fracture:

$$\varepsilon_f = [D_1 + D_2 exp(D_3\sigma^*)][1 + D_4 ln(\dot{\varepsilon}^*)][1 - D_5 T^*] \tag{4.12}$$

Where $\sigma^* = p/\bar{\sigma}$ in which $\bar{\sigma}$ is the effective stress. The D's are material damage parameters, where it signifies damage initiates where $D = 1$

$$D = \sum \frac{\Delta\varepsilon}{\varepsilon_f}$$

An attempt to improve the J-C model is reported in [89]. The idea was to increase the strain rate variation. From a better representation of exponential path of stress strain curve. As they suggested the influence of strain rate on strength does not form a linear function of the natural log. Thus the following flow stress representation was suggested.

$$\sigma = [A + B(\varepsilon)^n][(\dot{\varepsilon}^*)^c][1 - (T^*)^m)] \tag{4.13}$$

In order to obtain the constants of the J-C model, a sequence of actions need to be carried since the J-C model is an empirical function. The equation 4.10, shows how three brackets will form the J-C model [90].

The most common method is to define the constant A as representation of yield stress and constants B and n as strain hardening. Based on the assumption of strain rate $\dot{\varepsilon}$ being equal to 1, equation 4.10 may be written for a given temperature as:

$$\sigma = [A + B(\varepsilon)^n] \tag{4.14}$$

Therefore, one can deduce the constant A as stress at start of plastic deformation, which would be readily available from the experimental results [91].

In order to obtain the constants B and n, log-log plot of plastic stress $(\sigma - \sigma_0)$ versus the plastic strain (ε_p) and subsequently defining the trend of least square fit provides the constants.

To obtain the constant C, the J-C model could be presented as below:

$$\sigma = \sigma_a[1 + Cln(\dot{\varepsilon}^*)] \tag{4.15}$$

The expression is valid for ambient temperature and uniform strain. The term σ_a is the stress at the assumed strain rate, $\dot{\varepsilon^*} = 1$. Subsequently, a semi log graph of $\dfrac{\sigma}{\sigma_a}$ versus $\dot{\varepsilon}$ should be constructed. Similar to before the trend of least square fit would identify the constant C.

The third brackets describes the temperature response of the material, therefore at constant strain the J-C model could be represented as:

$$\sigma = \sigma_b[1 - (T^*)^m] \tag{4.16}$$

Where σ_b represents the stress at ambient temperature. Similar to other procedures a graph of $\dfrac{\sigma}{\sigma_b}$ versus T^* would need to be plotted and a least square trend to be applied in the manner of figure 4.2.

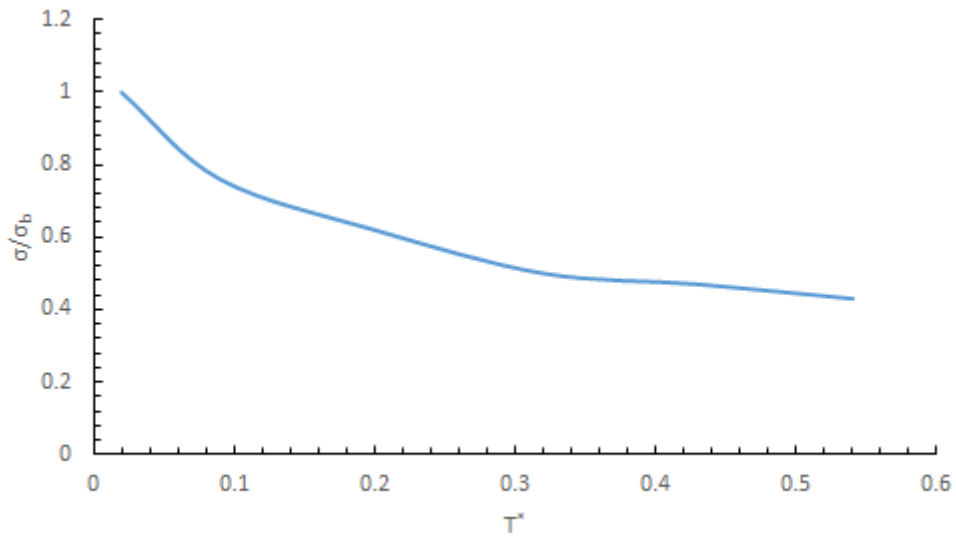

Figure 4.2: Plot of constant m

4.2.1.2 Zerilli-Armstrong model

The Z-A model [92] was originally proposed based on the micro-structural characteristics of materials therefore it is considered as a physical model. The model envisages that thermally activated dislocations within the micro-structure could predict the material behaviour. The model attempts to describe the strain rate and temperature dependency of the material under two known allotropic forms. Since the steels are comprised mainly of iron, depending on the temperature and cooling rate, it can exist in crystalline form either as FCC (Face Centered Cubic) or BCC (Body Centered Cubic). The interactions of the allotropes with other elements of structure, could therefore greatly influence the behavioural properties of the material. Based on the carbon content phase diagram, it may be noted the FCC structure has less sensitivity to temperature compared to a BCC structure.

Their research [92], was based on evaluating an accurate activation volume. The work yielded that FCC structured metals are dependent on strain whereas BCC structures are independent of strain. Thus, the following activation volume equation, based upon activation area A, was stated:

$$V = Ab = l^* \lambda b \tag{4.17}$$

Where b is the Burgers vector magnitude, l^* is the dislocation barrier spacing

and λ is the slip width. In essence for damage to occur the above equation would need to be satisfied, for when slippage of planes occur.

The activation area of FCC structures tends to decrease with increase of strain. Thus spacing of atoms will subsequently shrink which in turn results in an increase of density .

However, for BCC the spacing between the atoms are not reliant upon the plastic strain of the material at any given time, the reason being due to a governing principle of Peierls-Nabarro on the thermal activation of BBC structures. That is P-N refers to the force required to expand a dislocation atoms and is highly related to short range atomic orders. Subsequently as temperature rises, the intermolecular vibration of the structure will increase, resulting in a decrease of yield strength.

The following expresses the relationship between the dislocation spacing and density within the materials structure.

$$l^* = \frac{1}{\sqrt{\rho}} \tag{4.18}$$

Moreover the density may be expressed as ratio of dislocation number N to planar distant l to the dislocation plane.

$$\rho = \frac{N}{l^2} \tag{4.19}$$

With the vibration and consequently the dislocation of atoms, shear strain γ will develop. Therefore the shear strain could be expressed as the sum of dislocations N.

$$\gamma = tan\theta = \frac{Nb}{l} \tag{4.20}$$

Where l expresses the parallel plane to the dislocation plane. Substituting equation 4.19 into equation 4.20, therefore:

$$\gamma = \rho bl \tag{4.21}$$

By introducing Schmid's orientation factor M, the above equation may expressed in terms of applied strain ε:

$$\rho = \frac{M\varepsilon}{lb} \tag{4.22}$$

and subsequently the activation area will be expressed in terms of strain:

$$A = \lambda(\frac{bl}{M})^{1/2}\varepsilon^{-1/2} \tag{4.23}$$

Their work [92], expressed the stress in terms of thermal influence, in the following:

$$\sigma_{th} = \frac{M\Delta G_0}{BA_0}e^{-\beta T} \tag{4.24}$$

in which β is expressed as linear expression to strain rate.

$$\beta = C_3 + C_4 ln\dot{\varepsilon} \tag{4.25}$$

The term ΔG_0, refers to sum of energy at 0 K and A_0 refers to the activation area at the same reference temperature.

However the model could be refined based on the micro-structural reformation, therefore:

For **BCC**:

$$\sigma_{th} = C_1 e^{\{-C_3 T + C_4 T ln\dot{\varepsilon}\}} \tag{4.26}$$

For **FCC**:

$$\sigma_{th} = C_2 \varepsilon^{1/2} e^{\{-C_3 T + C_4 T ln\dot{\varepsilon}\}} \tag{4.27}$$

Moreover, this model incorporates the changes in grain size which describes the flow stress σ_G of the material. Therefore an inverse relation will be established between the yield stress and grain size, the mentioned relation in principle is governed by Hall-Petch equation [93, 94]:

$$\sigma = \sigma_0 + k_1 d_{GB}^{-1/2} + \sigma_{th} \tag{4.28}$$

Where the σ_G is the friction stress, k_1 is a constant and $D_{GB}^{-1/2}$ is the diameter of the grain. Moreover, the plastic strain for BCC structures may be computed by introducing a power law based on strain dependence:

$$\Delta\sigma_G = C_5 \varepsilon^n \tag{4.29}$$

Therefore, the Z-A model could be expressed as:

For **FCC**:

$$\sigma = \sigma_G + C_2\varepsilon^{1/2}e^{\{-C_3T+C_4Tln\dot{\varepsilon}\}} + kD^{-1/2} \tag{4.30}$$

For **BCC**:

$$\sigma = \sigma_G + C_1e^{\{-C_3T+C_4Tln\dot{\varepsilon}\}} + kD^{-1/2} + C_5\varepsilon^n \tag{4.31}$$

Given the Z-A model is a physical model, research was carried out [95, 96] to try and expand the Z-A model and to possibly relate it to the J-C model. Therefore a modified Z-A was constructed to describe the behaviour based on strain rate and plasticity. Thus the following expressions for yield stress were provided:

For **FCC**:

$$\sigma = C_1 + \left\{C_2\varepsilon^{1/2}e^{(-C_3+C_4ln\dot{\varepsilon}^*)T} + C_5\right\}\left(\frac{\mu(T_r)}{\mu(293)}\right) \tag{4.32}$$

For **BCC**:

$$\sigma = C_1 + C_2e^{(-C_3+C_4ln\dot{\varepsilon}^*)T} + \left\{C_5\varepsilon^n + C_6\right\}\left(\frac{\mu(T_r)}{\mu(293)}\right) \tag{4.33}$$

Where ε and $\dot{\varepsilon}^*$ are the effective plastic strain and effective plastic strain rate, respectively. The terms μ could be expressed as below:

$$\frac{\mu(T_r)}{\mu(293)} = B_1 + B_2T + B_3T^2 \tag{4.34}$$

Subsequently a more comprehensive model was generated by relating empirical aspect of J-C to physical behavioural prediction of Z-A.

$$\sigma = [A + B(\varepsilon)^n]e^{-C_3T+C_4Tln\dot{\varepsilon}} \tag{4.35}$$

Integration of the Z-A model based on the explanations above would deduce the following expressions:

For **FCC**:

$$\sigma = \sigma_G + kd^{-1/2} + C_2e^{-C_3T+C_4Tln\dot{\varepsilon}} \tag{4.36}$$

For **BCC**:

$$\sigma = \sigma_G + kd^{-1/2} + C_1 e^{-C_3 T + C_4 ln\dot{\varepsilon}} + C_5 \varepsilon^n \tag{4.37}$$

A concise means of determining the constants of Z-A model would be to categorise the terms with respect to their attributes. In the Z-A models 4.37 and 4.36 two of the terms are irrespective of temperature, strain and strain rate. Additionally, a feature of BCC is having the plastic strain separate from strain rate and temperature, which signifies the major difference of BCC and FCC. Therefore the equation for BCC structure may be altered as below:

$$\sigma_y = C^* + C_1 e^{(-C_3 T + C_4 T ln\dot{\varepsilon})} \tag{4.38}$$

The term C^* is the irrespective term $(\sigma_G + kd_{GB}^{-1/2})$. Similar to the approach with JC, the model may be stated equal to the experimental results for the yield stress for variations of temperature. The experimental result would then be plotted on yield stress and log of strain rate, and thus the constants of the model may be retrieved.

However in the ZA model for BCC model, two additional constants of n and C_5 are present. For obtaining the two constants, an isothermal assumption across the sample has to be maid at the tested strain rates, giving a Ludwick relation.

$$\sigma = \sigma_y + C_5 \varepsilon^n \tag{4.39}$$

4.3 Varying Temperatures and Strain Rate

4.3.1 Yield strength, elastic modulus and ultimate strength

Stress-strain curves will usually follow two path trends, although there are variation of stress-strain curves. The two most observed trends are either a smooth yielding to the point of ultimate strength which would shortly result in necking fracture or a sharp increase of yielding and subsequently a serration period. Metals exhibit a linear relation over their elastic region up to the yield point. However once such point is reached a non-linear relation may be observed. The linear line of the graph identifier is an elastic modulus, i.e. the slope of such line can explain the elastic

behaviour of the material to great extent. Some difficulty may arise when defining the yield point for smooth yielding stress-strain curves. Such complication is not present with the sudden yielding curves, the observation of such point is present in figure 4.3. In cases as figure 4.4 a conventionally acceptable method is to define an arbitrary number of 0.2% proof stress or strengths corresponding to 0.5% of the total strain. It has been proven the two values exhibit similar stress values.

Additionally, for cases of elevated temperature, due to non-linearity of the yield stress further corresponding strain values are extracted from the total strain. With respect to additional strain values figure 4.4, represents the criterion for defining the 0.5%, 1.5%, and 2.0% flow stress. The elastic modulus in this work ($E = tan\alpha$) has been retained at the 0.2% proof stress.

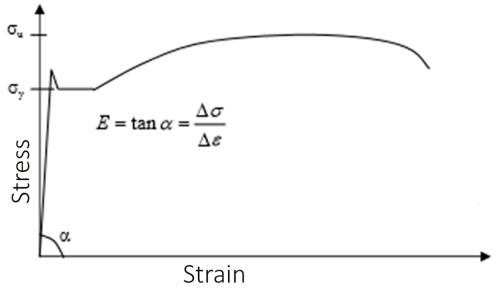

Figure 4.3: Sharp yielding

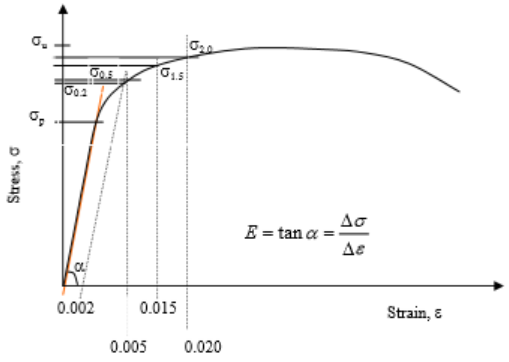

Figure 4.4: Smooth yielding

4.3.1.1 Yield strength

Provided below is the stress strain curves of uni-axial tests carried out for 0.6 mm thickness flat samples. The temperature range was adjusted from ambient to 600°C. The reduction factors are based on the stress strain plots from the uni-axial results. A comprehensive set of results are available in Appendix A.

The static drop(wave format)in few figures, was observed in some of the experiments, such effect was related to the tensile machine rather than the material behaviour. Also as they would not alter the trend of plastic deformation the results were deemed appropriate.

Additionally provided in figure 4.9 is the overall picture of the conducted tests on 0.6 mm sheet steels. As can be seen all the tests are exhibiting a smooth yielding condition. Further, as the temperature increases the stress level is reduced.

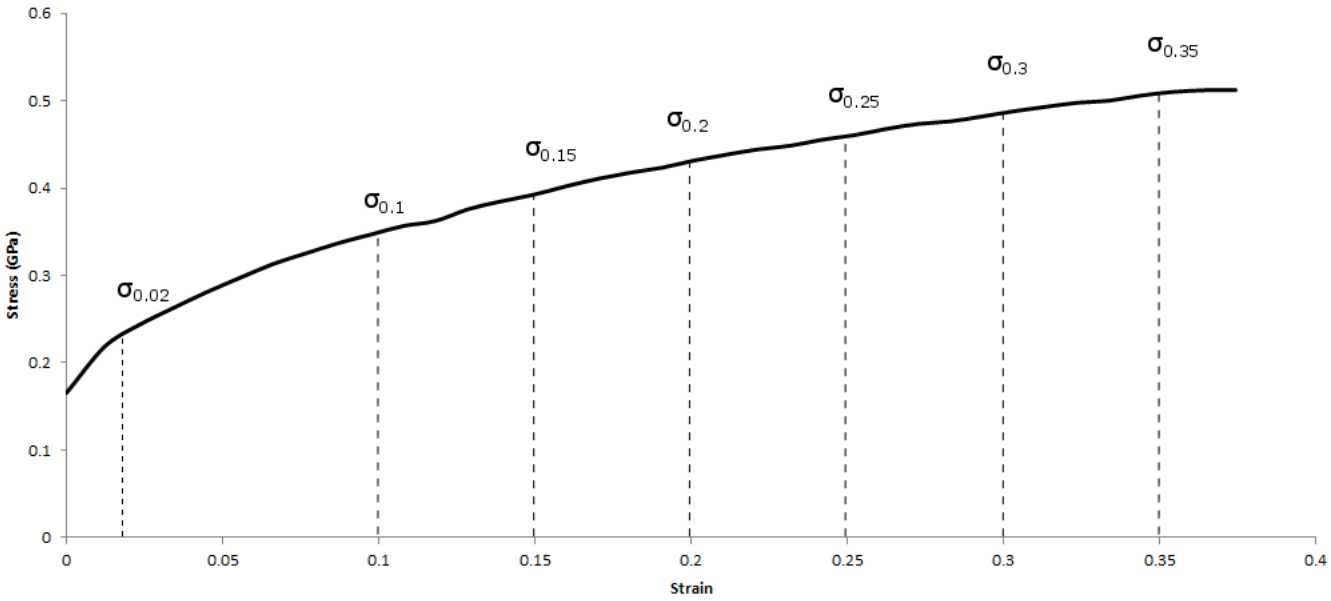

Figure 4.5: 0.6mm 0.13% C-steel at ambient temperature and $6.09 \times 10^{-5} s^{-1}$

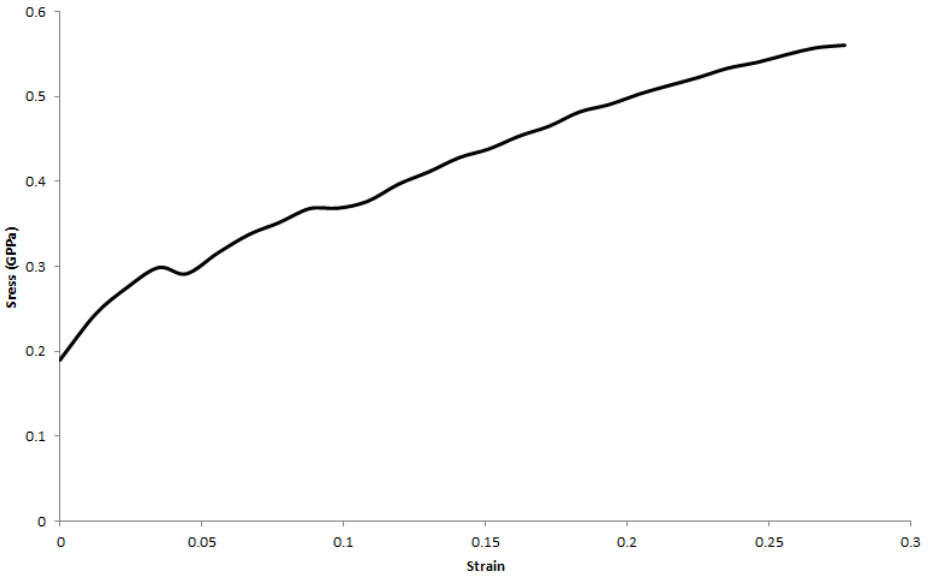

Figure 4.6: 0.6mm 0.13% C-steel at $300°C$ temperature and $6.09 \times 10^{-5} s^{-1}$

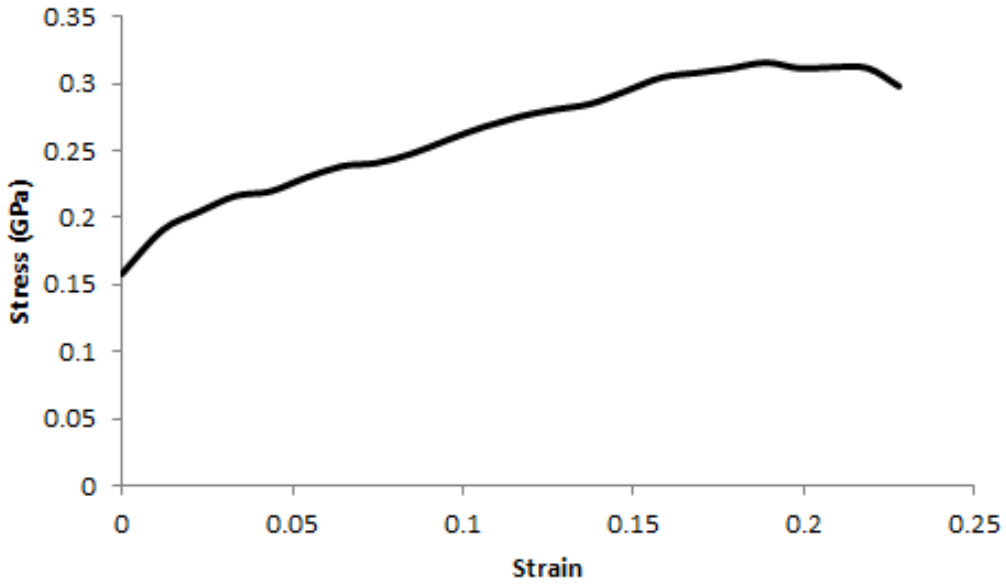

Figure 4.7: 0.6mm 0.13% C-steel at $400°C$ temperature and $6.09 \times 10^{-5} s^{-1}$

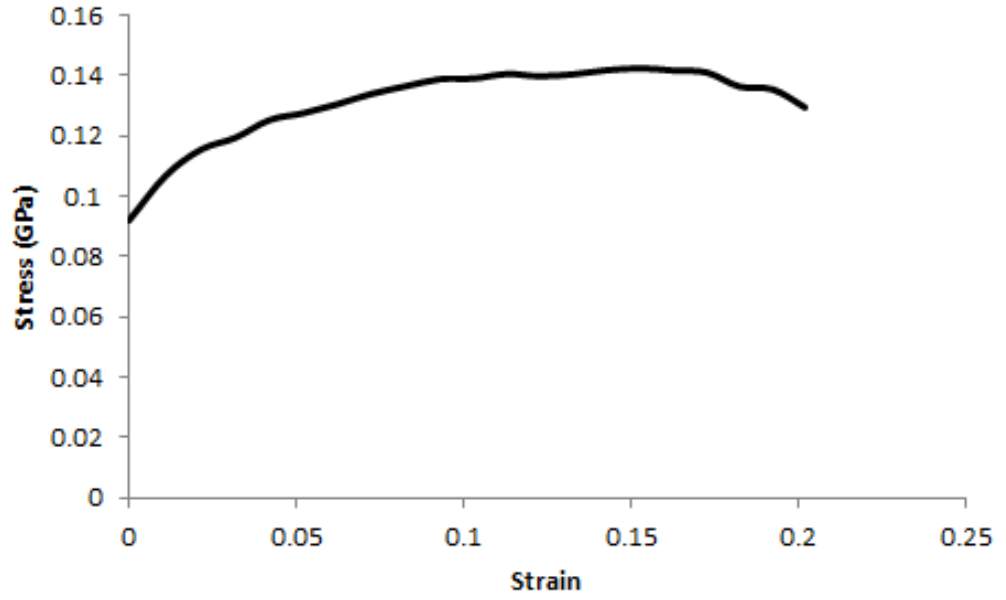

Figure 4.8: 0.6mm 0.13% C-steel at $500°C$ temperature and $6.09 \times 10^{-5} s^{-1}$

However, the exception would be the test conducted at $300°C$; the rise of the stress level is closely related to the micro-structure changes which will be covered later. The instability condition of each stress strain curve can be seen to gradually decrease with increase of temperature. This point can also be observed with necking formation, whilst analysing the results in the simulation package.

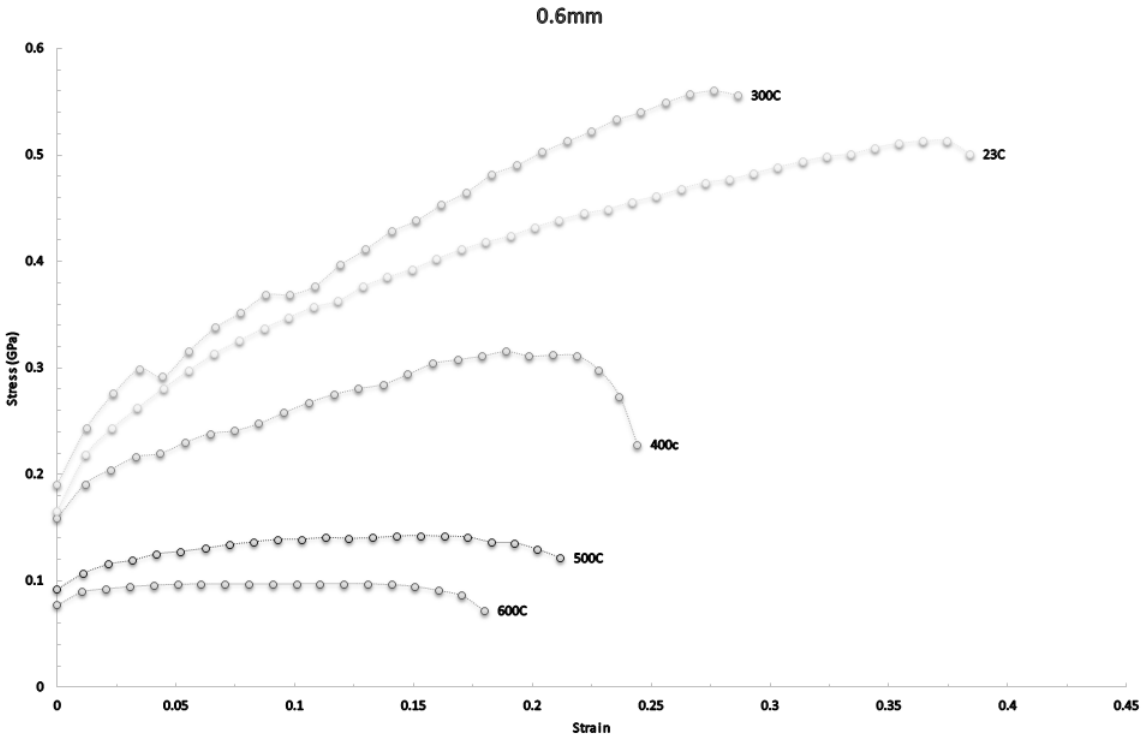

Figure 4.9: Family of stress-strain curves for sheet steel at various temperatures ($\dot{\varepsilon} = 6.09 \times 10^{-5} s^{-1}$) with 0.6 mm flat sample

For cases where double yielding effect is present or fluctuation in the results were present and averaging value was taken over the true strain value. For the cases similar to figures 4.5, 0.2 proof stress was opted for the yield stress as shown. Additionally, values of 0.5,1.5 and 2.0 proof stress level were also chosen as shown.

The reduction factors are designed to provide a single value based on the ratio of stress at elevated temperature $\sigma_{y,T}$ to stress at ambient stress $\sigma_{y,amb}$. The values could also be expressed in terms of percentages. The percentage value has the capability of signifying 100 % as ambient condition in all cases. Provided below in figure 4.10 is the deterioration of the yield strength.

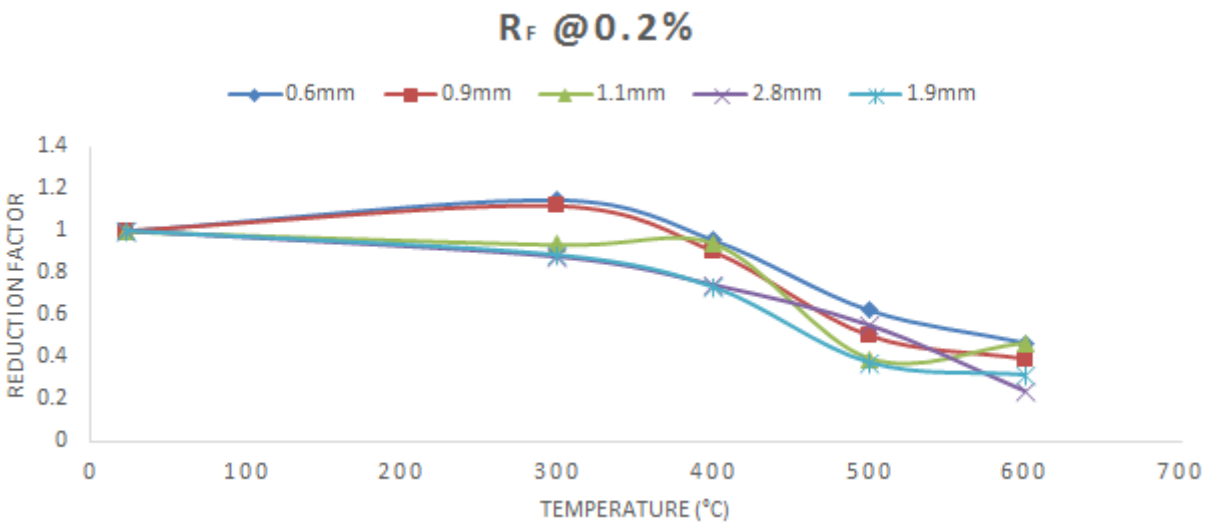

Figure 4.10: Yield strength deterioration reduction factor at 0.2% and $\dot{\varepsilon} = 6.09 \times 10^{-5} s^{-1}$ for 0.13 % C-steel

In figure 4.10, the representation of the reduction factors signifies that in general, with increase of temperature the stress level is reduced. Further, a comprehensive trend can now be established, to describe the change in the material's yield strength based on this graph. One point to note is the rise in stress level over the 300°C, as can be seen the thickness plays an inverse effect over ranges lower that unity thickness. As the thickness is increased the reduction factor beyond 300°C would gradually follow the generally accepted reduction. Additional figures are provided in Appendix A.

Tables below 4.1 and **??** provide the strain value at which the nominal reduction factors for a variety of temperatures and thicknesses.

The reduction factor representation in figure 4.10, presents the thickness to be detrimental at higher temperature. The factors seem to be more reliant on the thickness with higher temperatures and therefore, as a temperature and thickness rise, a lower factor is to be expected. This statement can also be observed in table 4.2. However, lower temperatures ($\geq 300°C$) tend to have similar factors to those of ambient factor value. Another observation is the rate of reduction of yield strength for the high strength material tested. As can be observed the rate of reduction factor for temperature up to 400°C is much lower than it is for temperatures above 400°C. However, other researchers [8] have claimed lower strength materials tend to confront this change of trend at a lower critical temperature of 200°C. The thick-

Temperature °C	0.6 mm				0.9 mm			
	0.2%	0.5%	1.5%	2.0%	0.2%	0.5%	1.5%	2.0%
23	0.1652	0.1936	0.225	0.2632	0.1551	0.1733	0.1937	0.2035
300	0.1898	0.216	0.2518	0.2648	0.1733	0.1924	0.2168	0.2262
400	0.158	0.1758	0.1955	0.2015	0.1396	0.1502	0.1632	0.1671
500	0.1027	0.111	0.113	0.102	0.0777	0.0921	0.0933	0.0972
600	0.077	0.0849	0.0906	0.0921	0.0605	0.0624	0.0664	0.068
Temperature °C	1.1 mm				1.3 mm			
	0.2%	0.5%	1.5%	2.0%	0.2%	0.5%	1.5%	2.0%
23	0.1555	0.1682	0.1861	0.1948	0.1455	0.1615	0.1869	0.187
300	0.1457	0.1672	0.1903	0.1992	0.1596	0.1737	0.1936	0.2012
400	0.147	0.158	0.173	0.178	0.111	0.121	0.136	0.14
500	0.061	0.0654	0.0683	0.0683	0.092	0.0977	0.1121	0.1155
600	0.0726	0.0836	0.0876	0.0908	x	x	x	x
Temperature °C	1.9 mm				2.8 mm			
	0.2%	0.5%	1.5%	2.0%	0.2%	0.5%	1.5%	2.0%
23	0.2213	0.2357	0.2596	0.269	0.2464	0.2554	0.2652	0.2686
300	0.1958	0.2109	0.233	0.238	0.2159	0.2378	0.2654	0.2741
400	0.162	0.174	0.185	0.189	0.183	0.2	0.214	0.216
500	0.0828	0.0924	0.1064	0.1104	0.1362	0.1414	0.1445	0.1425
600	0.0698	0.0766	0.0851	0.0884	0.0591	0.065	0.0686	0.06908

Table 4.1: Yield strength deterioration of flat samples at $\dot{\varepsilon} = 6.09 \times 10^{-5} s^{-1}$

Temperature °C	0.6 mm				0.9 mm			
	0.2%	0.5%	1.5%	2.0%	0.2%	0.5%	1.5%	2.0%
23	1	1	1	1	1	1	1	1
300	1.1489	1.1157	1.1191	1.1210	1.1173	1.1102	1.1192	1.1115
400	0.9564	0.9081	0.8689	0.8531	0.9000	0.8667	0.8425	0.8211
500	0.6216	0.5733	0.5022	0.4318	0.5009	0.5314	0.4816	0.4778
600	0.4661	0.4385	0.4026	0.3899	0.3900	0.3603	0.3427	0.3341
Temperature °C	1.1 mm				1.3 mm			
	0.2%	0.5%	1.5%	2.0%	0.2%	0.5%	1.5%	2.0%
23	1	1	1	1	1	1	1	1
300	0.9369	0.9940	1.0225	1.0225	1.0969	1.0755	1.035	1.0759
400	0.943	0.94	0.93	0.915	0.76	0.752	0.726	0.75
500	0.3922	0.3889	0.3672	0.3506	0.6323	0.6049	0.5997	0.6176
600	0.4668	0.4971	0.4709	0.4661	x	x	x	x
Temperature °C	1.9 mm				2.8 mm			
	0.2%	0.5%	1.5%	2.0%	0.2%	0.5%	1.5%	2.0%
23	1	1	1	1	1	1	1	1
300	0.8847	0.8947	0.8975	0.8847	0.8762	0.9310	0.9958	0.9947
400	0.732	0.739	0.711	0.704	0.743	0.782	0.808	0.803
500	0.3741	0.3920	0.4098	0.4104	0.5527	0.5536	0.5448	0.5305
600	0.3154	0.3249	0.3278	0.3286	0.2398	0.2545	0.2586	0.2571

Table 4.2: Reduction factors of flat samples at $\dot{\varepsilon} = 6.09 \times 10^{-5} s^{-1}$

ness effect in terms of reduction factor around 300°C provides a difference of 16% for lower than $1mm$ thickness and 9% for thicknesses above $1mm$.

Figure below (4.11) represents the reduction factor on the basis of strain levels for 0.6 mm 0.13% C-steel. It should be noted the yeild strength reduction factors tend to be tighly close to one another upto 300°C, with 0.2% and 0.5% following an exceptionally similar trend. This was also observed by other researchers [2] for high strength metals. However similarities in the factors tend to fade slightly as the critical temperature of 400°C is reached. Additionally, the yield strength reduction factor, shows a sequential deterioration in the yield strength value as strain level is increased. Therefore, a recommendation is to use the lower levels of strain when calculating for yield strength, as using higher strain levels such as 2.0% tends to under predict the value.

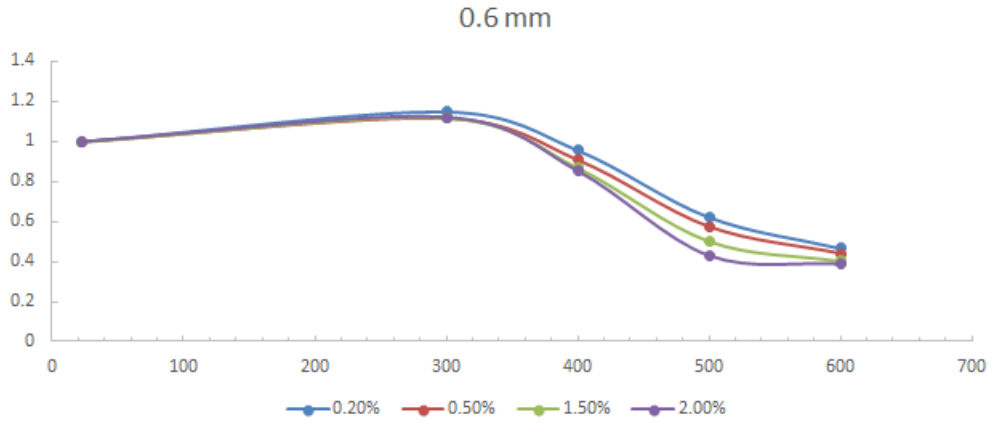

Figure 4.11: Reduction factor based on strain level of 0.6 mm plate at $\dot{\varepsilon} = 6.09 \times 10^{-5} s^{-1}$

4.3.1.2 Elastic gradient

Describing the correct trend of elastic modulus could greatly describe the stiffness behaviour and application possibilities of the materials. Similar to yield strength values elastic modulus tends to deteriorate with increase of temperature. In essence the modulus of elasticity could be calculated by measuring the slope of elastic region of the stress strain curve as presented in figure 4.4, denoted by E. Calculating the elastic modulus factor, follows the similar method; that is, the ratio between tested temperature to the ambient ratio, $\frac{E_T}{E_{amb}}$. Provided in table 4.3, are the values for elastic gradients which provides the ratio.

As can be noticed with increase of thickness the absolute value of gradient at ambient and elevated temperature gradually induces non-linearity of elastic modulus. However, the nominal ratio based on the ambient ratio stays coarsely the same. An important concept to note is utilising the elastic gradient instead of elastic modulus for the best approximation to the ratio $E\dfrac{E_T}{E_{amb}}$.

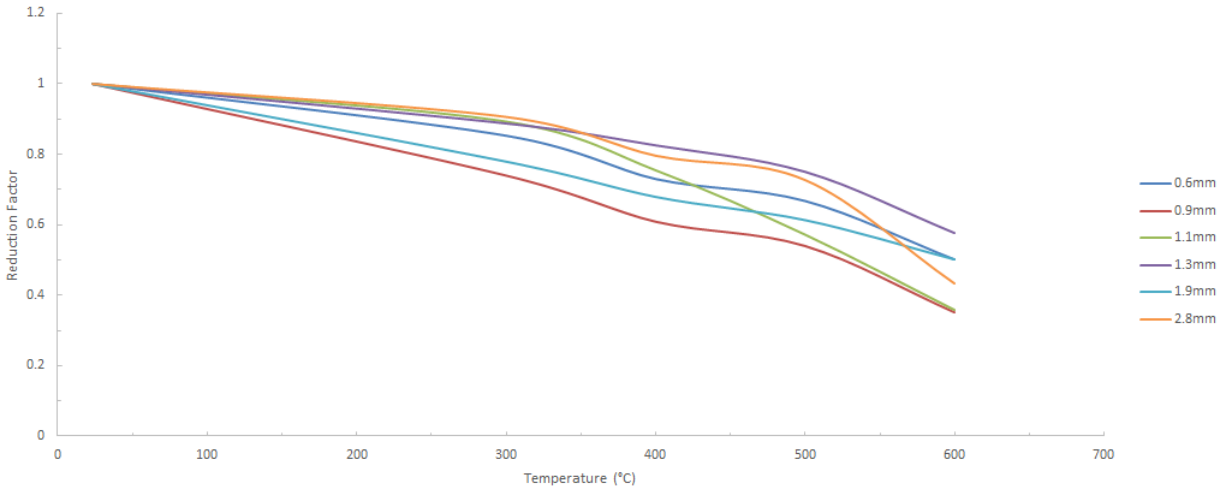

Figure 4.12: Elastic gradient reduction factor based on elevated temperature at $\dot{\varepsilon} = 6.09 \times 10^{-5} s^{-1}$

Temperature°C	*Elastic Gradient*					
	0.6 mm	0.9 mm	1.1 mm	1.3 mm	1.9 mm	2.8 mm
23	24	20	14	13.14	7.89	8
300	20.46	14.78	12.5	11.66	6.15	7.25
400	17.5	12.16	10.56	10.84	5.36	6.37
500	16	10.78	8	9.85	4.84	5.82
600	12	7	5	7.56	3.96	3.47
Temperature°C	E_T/E_{amb}					
	0.6 mm	0.9 mm	1.1 mm	1.3 mm	1.9 mm	2.8 mm
23	1	1	1	1	1	1
300	0.8525	0.739	0.8928	0.8873	0.7794	0.9062
400	0.7292	0.608	0.754	0.825	0.679	0.796
500	0.6667	0.539	0.5714	0.7496	0.6134	0.7275
600	0.5	0.35	0.3571	0.5753	0.5019	0.4337

Table 4.3: Elastic gradient and elastic reduction factors of 0.13% C-steel at elevated temperatures at $\dot{\varepsilon} = 6.09 \times 10^{-5} s^{-1}$

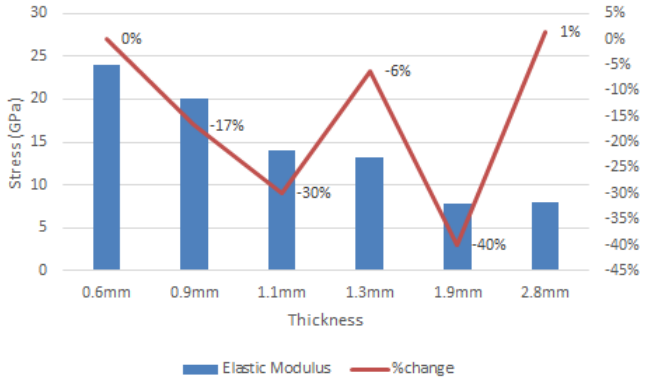

Figure 4.13: Percentage change of elasticity based on thickness change

The trend of the elastic gradient stress level, presents a steady decline by increase of temperature, independent of the thickness variation. Although few minor discrepancies are present in the result, they account for negligible deviation. Therefore, the finalised mathematical model is composed with the assumption of such deviation as negligible.

The observation of change in elastic modulus based on thickness variation, shows an overall reduction in stress level by 90% as thickness is varied from 0.6 mm to 2.8 mm. However towards the end, a slight increase is noted which could be presentation of a plateau. Nonetheless, what is certain is the change in stress levels with a change in thickness of the material (see figure 4.13). Therefore it can be suggested further tests to be carried out to fully understand the behavior of the line as thickness is increased.

4.3.1.3 Ultimate strength

Defining the appropriate limits before reaching ultimate strength value, could prevent damage to structure, which in turn could both save lives and save unnecessary expenses. The ultimate behavior of a material is described as the maximum stress or strain it could withstand before leading to fracture. Similar to elastic gradient analysis, the ultimate strength was calculated based on the ratio of ultimate strength at the tested temperature ($\sigma_{u,T}$) to that of the ambient temperature ($\sigma_{u,amb}$).

The most notable phenomenon in reviewing figure 4.14 is the region related to temperatures between 200°C and 300°C, where an increase in stress levels is present.

Temperature°C	$\sigma_{u,T}(GPa)$					
	0.6 mm	0.9 mm	1.1 mm	1.3 mm	1.9 mm	2.8 mm
23	0.5146	0.3586	0.378	0.397	0.4044	0.394
300	0.5609	0.3625	0.3256	0.329	0.4351	0.382
400	0.32	0.2318	0.247	0.245	0.2415	0.281
500	0.1437	0.0994	0.1256	0.151	0.1512	0.165
600	0.0791	0.0798	0.105	0.0897	0.1073	0.072
Temperature°C	$\sigma_{u,T}/\sigma_{u,amb}$					
	0.6 mm	0.9 mm	1.1 mm	1.3 mm	1.9 mm	2.8 mm
23	1	1	1	1	1	1
300	1.0899	1.0108	0.8613	0.8287	1.0759	0.9695
400	0.6218	0.6464	0.6534	0.6171	0.5971	0.7131
500	0.2792	0.2771	0.3322	0.3803	0.3738	0.4187
600	0.1537	0.2225	0.2777	02259	0.2653	0.1827

Table 4.4: Ultimate strength and ultimate strength reduction factor of 0.13% C-steel at elevated temperatures and $\dot{\varepsilon} = 6.09 \times 10^{-5} s^{-1}$

The effect is related to the composition of the materials, in which material's structural transformation at lower temperatures is more predominate as it is in higher temperatures. However, the effect of reduction of ultimate strength due to increase in temperature, suppresses the structural changes of the material. Therefore, a decline of strength factor is clearly present for temperatures above 300°C.

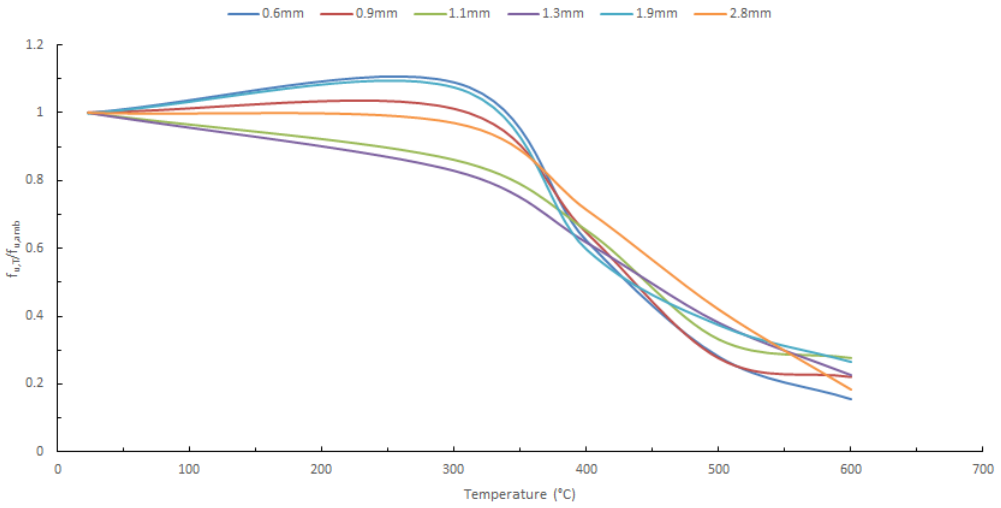

Figure 4.14: Ultimate strength reduction factor based on elevated temperature

4.3.2 Strain rate study

Considering the ultimate strain in figure 4.15, a trend can be established; that is, with increase of temperature the ultimate strain achieved is reduced. Additonnaly, a point of instability trend is established which indicates the instability condition of the tested material at the mentioned condition would gradually decrease with increase of temperature. Similar effect was observed by other researchers, however they have mostly studied the effect of strain rate on limited variation of temperature[97]. Studying strain rate sensitivity would therefore be crucial in better understanding the phenomenon taking place especially at lower strain rates where global necking plays an important role.

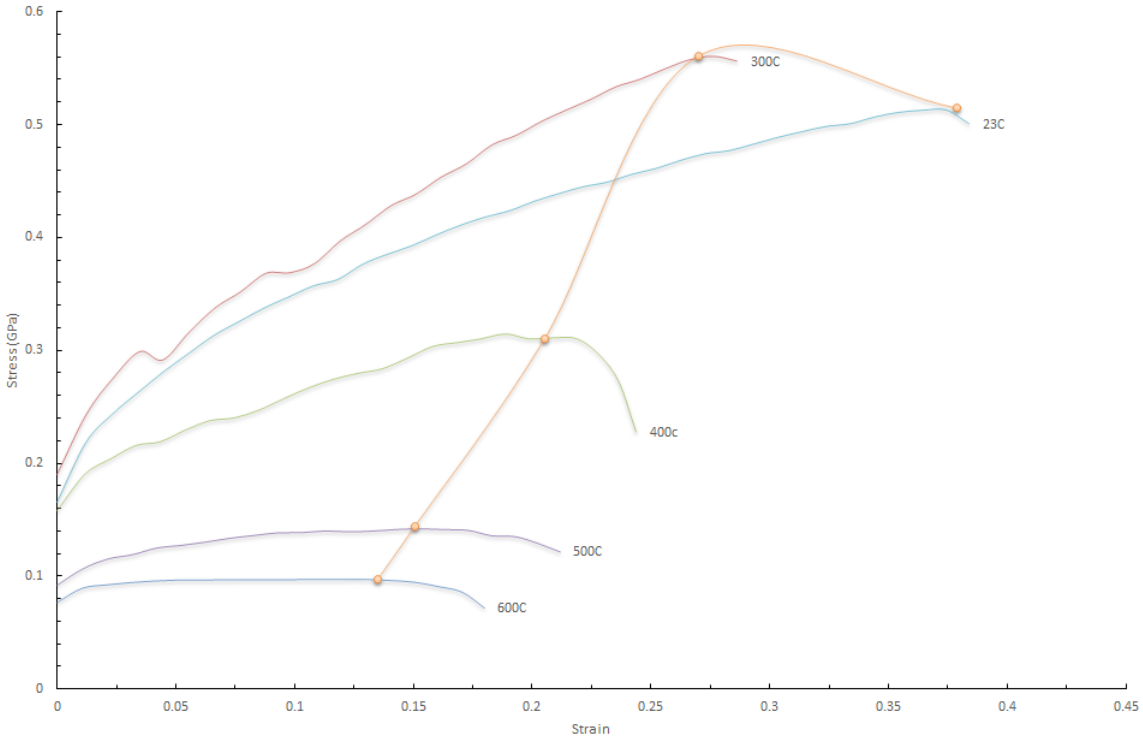

Figure 4.15: Temperature influence upon 0.13% C-steel at 0.6 mm and$\dot{\varepsilon} = 6.09 \times 10^{-5} s^{-1}$

Based on the work carried out, an increase of hardening rate was observed by in figure 4.15 and increasing the strain rate or by decreasing temperature. The finding was in line with the known effect of thermal activation on strain. One note to consider is the margin for shifting the strain rate sensitivity from positive rate to negative which was observed to be for temperatures below 300°C comparatively. Additionally as provided in Appendix A, a serrated stress strain curve can be observed (see figure A.47), during yielding and preliminary stage of the plastic region,

which signifies the dynamic strain aging for lower strain rates.

Figures 4.16 to 4.21, demonstrate the implications of varying strain rate based on possible variations in temperature. Figure 4.16 shows the stainless steel alloy. As can be seen consistently in the following figures; strain rate increases the strain at fracture. However as figure 4.16 suggests elevated temperature, although suppressing the elongation significantly, will also affect the strain rate sensitivity and in turn will affect the hardening of the material. As an example, strain at fracture in test 0.3mm/min ($5.714 \times 10^{-5} s^{-1}$) and $23°C$ will occur at a strain 0.2864, whereas at the same strain rate at $300°C$ same fracture will occur at a strain 0.309, which will signify a percentage difference of of 7.5%. Out of this observation similar trend could be identified further which resulted in figure 4.17, As can be seen the percentage difference of strain rate at constant temperature has a more profound presence at higher magnitudes of strain rate. However, the same percentage difference growth slows down by increase of strain rate magnitude.

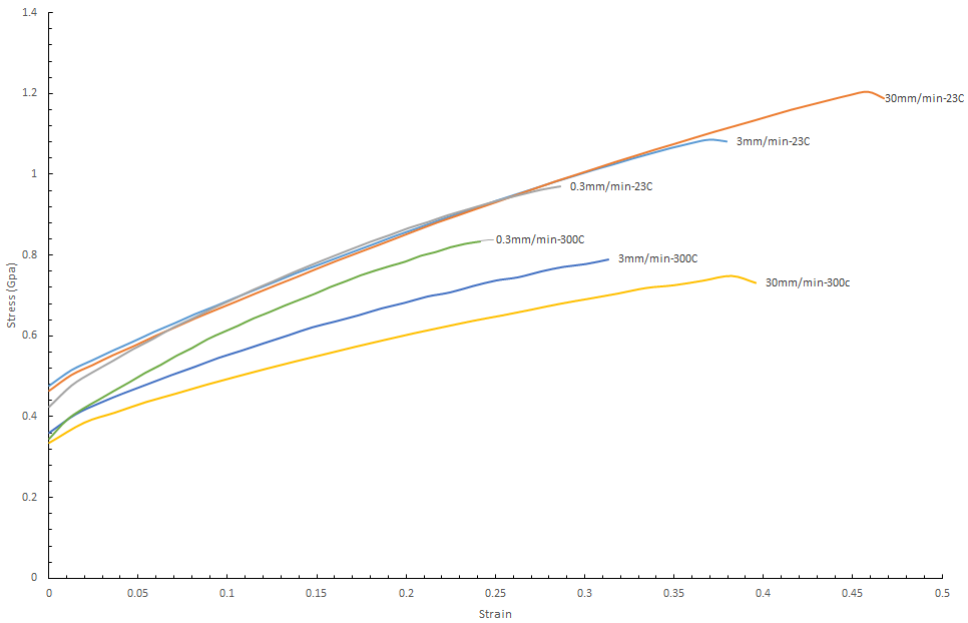

Figure 4.16: Strain level evaluation of 18/8 stainless steel based on strain rate variation at $23°C$ and $300°C$

Aluminium alloy strain evaluation in figure 4.19 similar to brass strain evaluation figure 4.21, signifies the strain level increase by increase in strain rate. Additionally, the same behaviour can be seen for flow stress. Further, this effect was observed

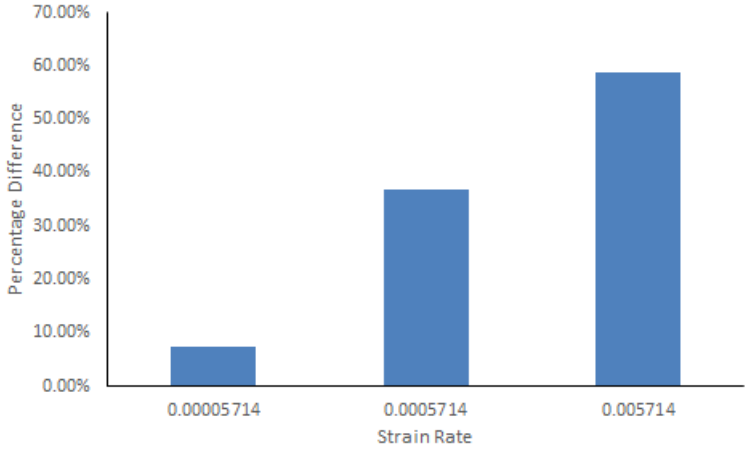

Figure 4.17: Strain failure change based on constant temperature at 350°C

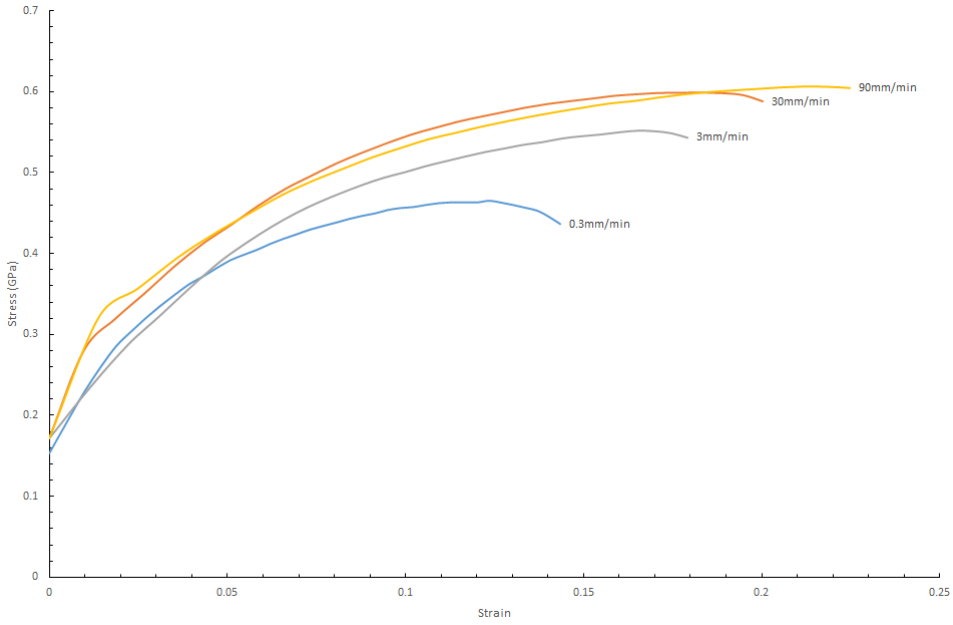

Figure 4.18: Strain level evaluation of 0.13% C-steel based on strain rate variation at 300°C

with other researchers [17][98], where a logarithmic relation between flow stress and strain rate was detected. Although, this effect could also be contributed to different mechanical alterations experienced by each sample.

Additionally figure 4.21, suggests brass to be the most strain rate insensitive material within the strain rate range tested. As can be seen, 60/40 brass exhibits the least flow stress change and hardly any change in hardening rate of the material. The same effect was observed by Hamouda [99].

Theseries of figures below, represent the strain rate in term of cross head movement.

- 0.3mm/min=$\dot{\varepsilon} = 6.09 \times 10^{-5} s^{-1}$
- 3mm/min=$\dot{\varepsilon} = 6.09 \times 10^{-4} s^{-1}$
- 30mm/min=$\dot{\varepsilon} = 6.09 \times 10^{-3} s^{-1}$
- 90mm/min=$\dot{\varepsilon} = 0.01829 s^{-1}$

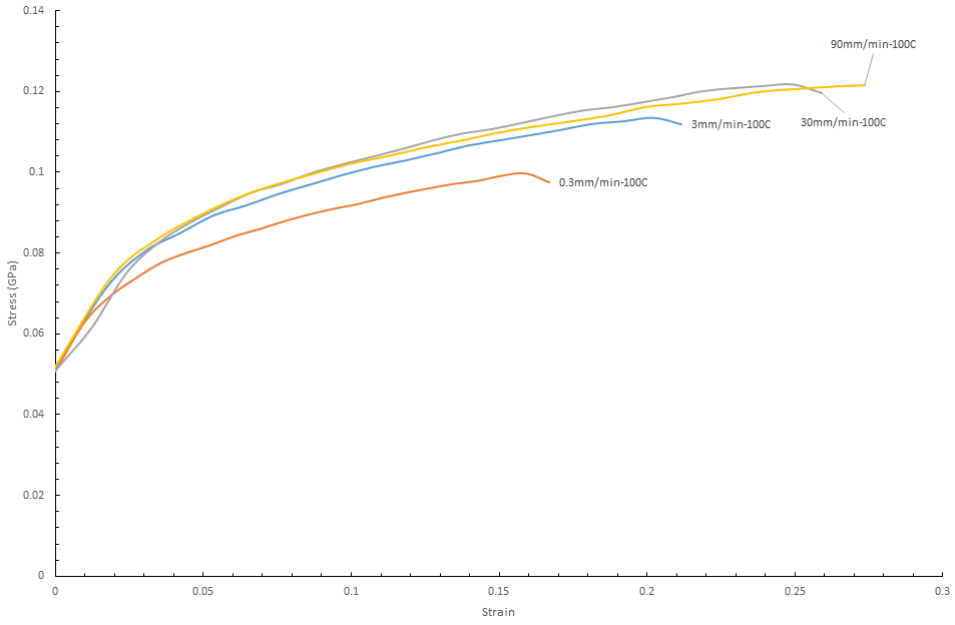

Figure 4.19: Strain level evaluation of Aluminium alloy based on strain rate variation at $100°C$

A point to note as the thickness of a material increases the flow stress has less effect, which can be attributed to additional cold rolling effects present in lower

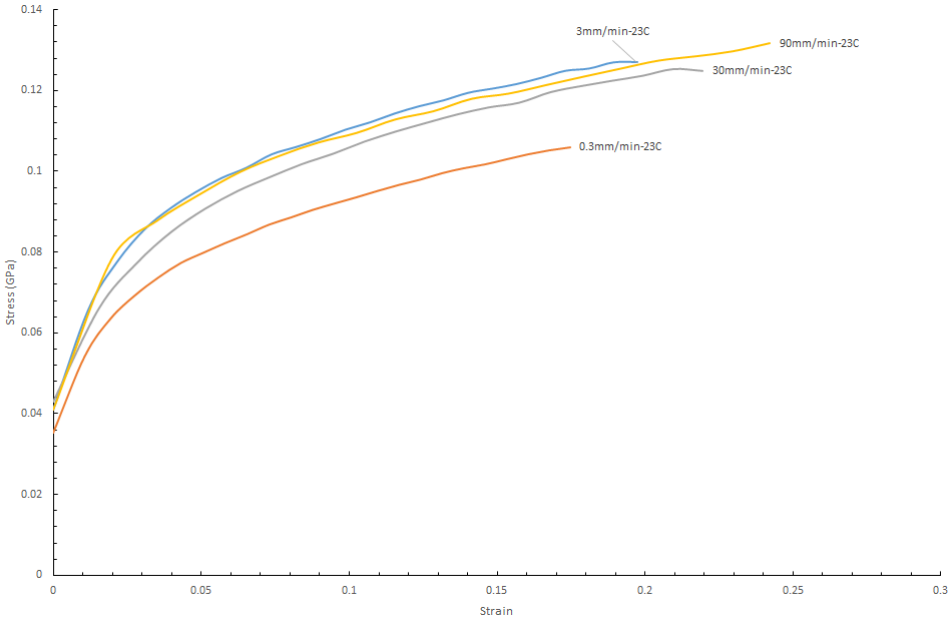

Figure 4.20: Strain level evaluation of Aluminium alloy based on strain rate variation at $23°C$

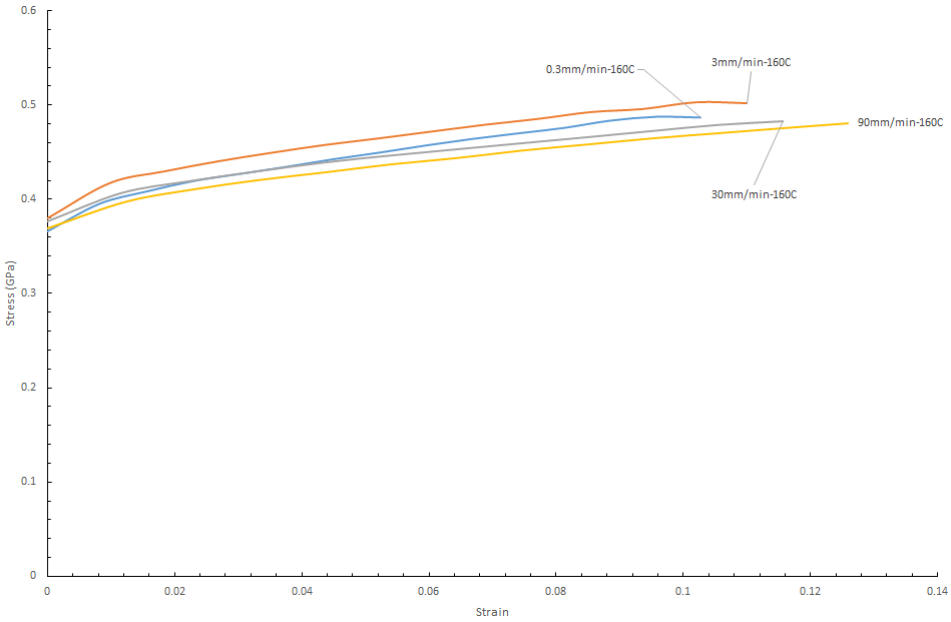

Figure 4.21: Strain level evaluation of 60/40 brass based on strain rate variation at $160°C$

thickness material. The figures 4.23 and 4.22, demonstrate the behaviour of such effects. Figure 4.23, exhibits the thinnest sample to contain the highest stress flow. Additionally the two figures show that the effect of elevated temperature on uniform strain rate, will result in a lower strain at failure. Further, elevated temperature will cause separation of flow stresses; this phenomena could be related to micro-structural changes of the samples by means of void formation. As the manufacturing procedure could differ sample to sample that could lead to small separation of flow stresses, the changes based on micro-structure effects will be discussed later.

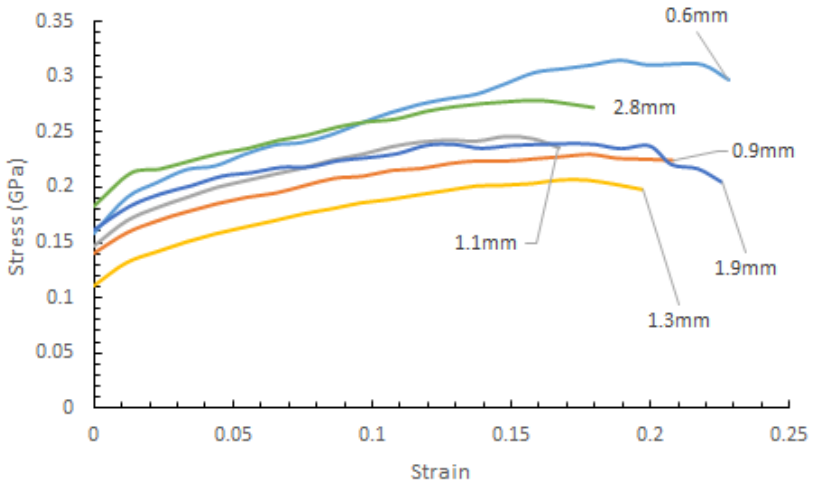

Figure 4.22: Strain rate $6.09 \times 10^{-5} s^{-1}$ evaluation of 0.13% C-steel based on thickness variation at $400°C$

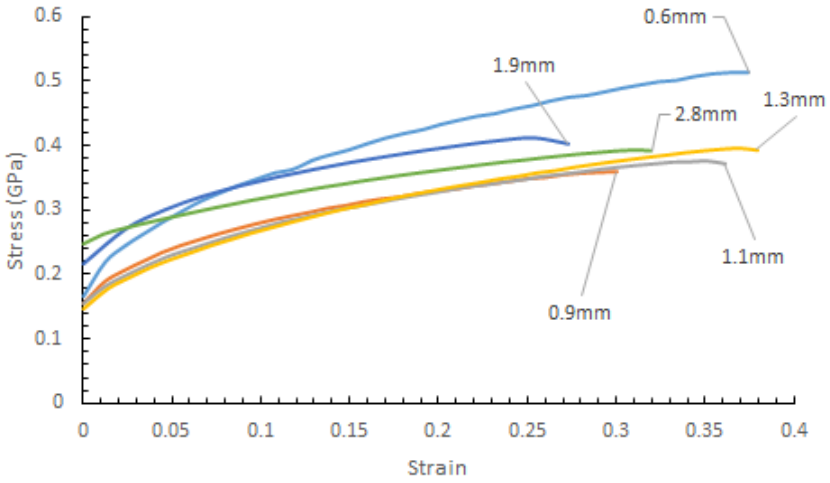

Figure 4.23: Strain rate $6.09 \times 10^{-5} s^{-1}$ evaluation of 0.13% C-steel based on thickness variation at $23°C$

In order to better comprehend the strain rate sensitivity based on environmental

conditions and its effect on flow stress, a series of true stress versus logarithmic strain was computed. In general the strain rate sensitivity is observed to reduce by increase of temperature at uniform strain rates. This phenomenon can be illustrated in figures 4.24 and 4.25. At lower temperatures figure 4.24, shows every cycle increase of strain rate results in an increase of stress. However, as temperature is increased in figure 4.25 strain rate cycles will not affect the flow stress. A dip is visible at the higher end of strain rate, which suggests a negligible drop in flow stress by increasing the strain rate. Additionally for figure 4.24, straight line approximation proves and exponential law power.

$$\sigma = c(t)e^{D(T)\dot{\varepsilon}} \tag{4.40}$$

Similar straight line approximation could be formed for figure 4.25:

$$\sigma = Ae^{B\dot{\varepsilon}} \tag{4.41}$$

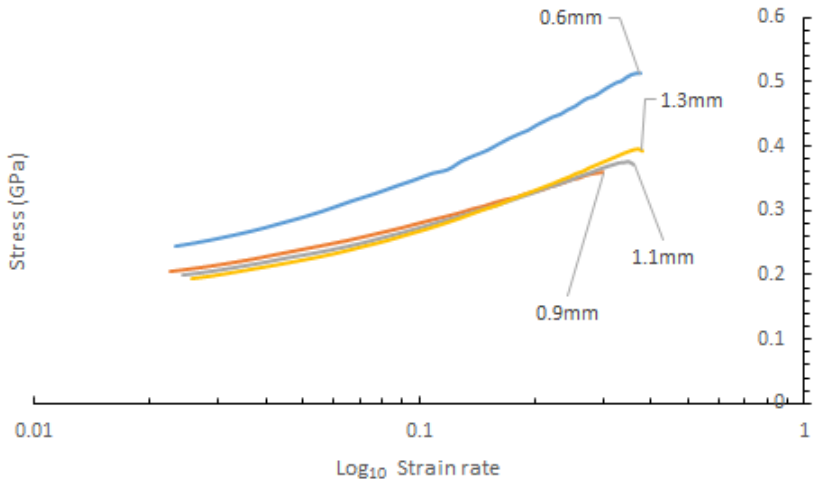

Figure 4.24: Strain rate sensitivity at $23°C$

4.3.3 Elongation vs strain rate and temperature

The elongation of the sample is best computed by physical measurement of the failed samples rather than relying on its final strain value. The decision to physically measure the elongation was to avoid the slacking effect within the tensile machine grips.

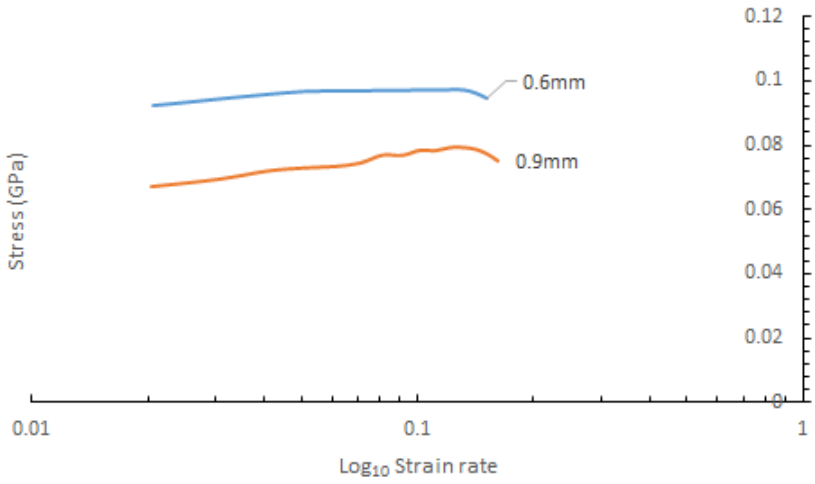

Figure 4.25: Strain rate sensitivity at $600°C$

Different materials within this study yielded similar trends when considering strain rate effect upon elongation. In general within uniform temperature , increase of strain rate would result in further elongation of the material. However, the degree to which the specimen was elongated was reliant upon the alloy and thickness of the sample, in case of dog bone samples. Thinner flat samples will provide greater elongation with increase of strain rate. In case of $1mm$ sample, elongation to failure changed from 12.07% to 24.4% when strain rate was changed from $6.09 \times 10^{-5}s^{-1}$ to $0.01829s^{-1}$; meanwhile the same strain rates resulted in change of elongation to failure from 13.8% to 22.13% for the 2 mm dog bone samples.

As can be seen in figure 4.26, maximum deflection of the gague length at uniform temperature increases with strain rate. However, the maximum elongation increase slows down by increase of strain rate. To this end other researchers have reported less elongation at bar impact and high velocity plate impact strain regimes [100].

Additionally, the same trend was illustrated with other material alloys. Figure 4.27 presents the elongation variation of Stainless steel specimen, carried out with dumbbell samples. As it can be seen the rate of change gradually slows by increase of strain rate.

Furthermore, a similar investigation is carried out in order to isolate the effect of temperature upon elongation. The elongation to failure tends to decrease with elevation of temperature; however as figure 4.29 suggests the rate of change reduces

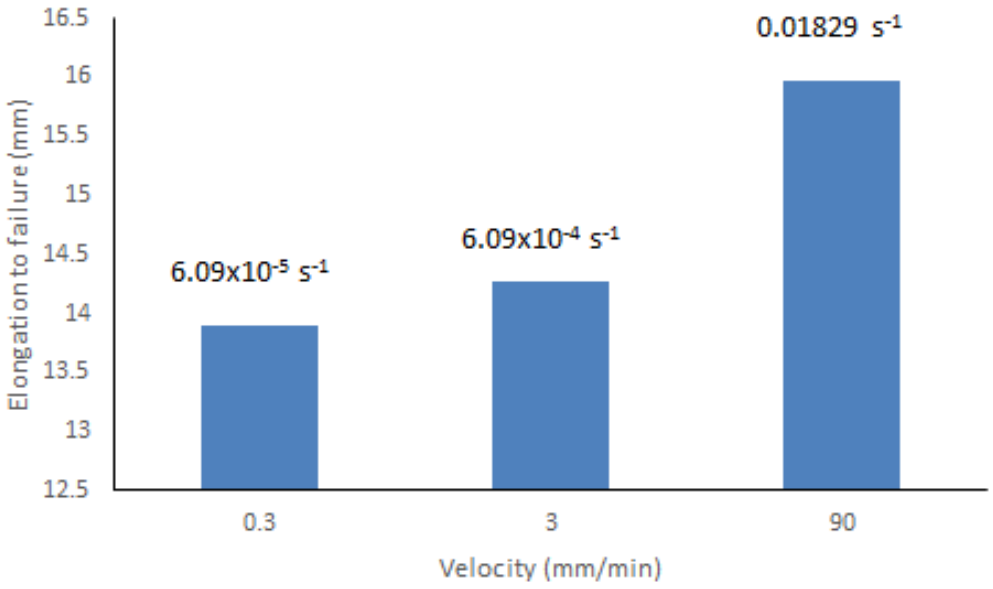

Figure 4.26: Elongation based on strain rate variation at $350°C$ and 1mm thickness of 0.13% C-steel

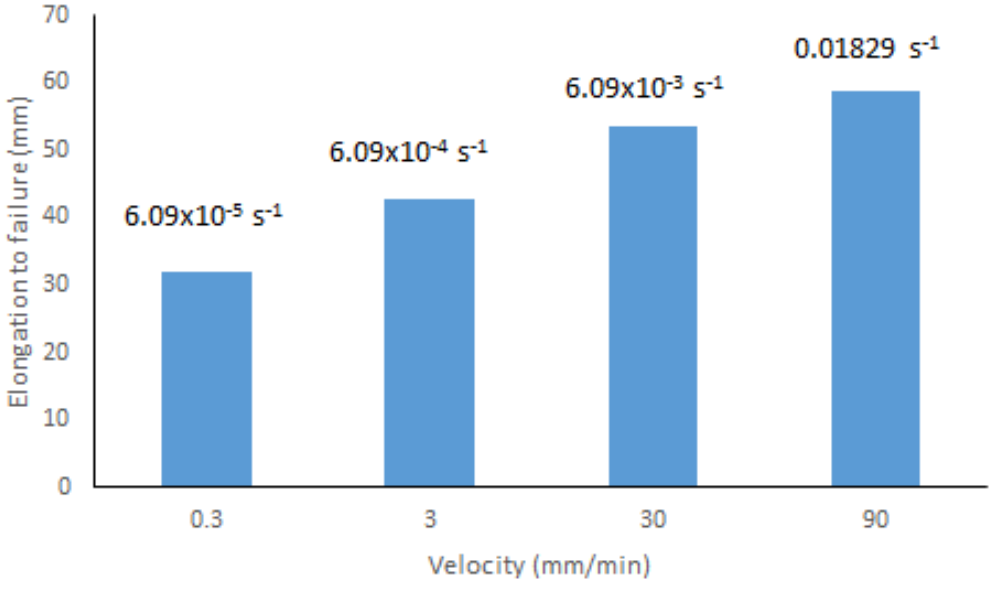

Figure 4.27: Elongation based on strain rate variation at $23°C$ of circular samples of 18/8 stainless steel

significantly at higher temperatures. Additionally, the thinner samples tend to be more resilient towards the rate change of elongation. Both of these phenomena could be related to void formation within the material. In the thinner material void formation plays smaller role whereas the thicker material will be adversely effected with the formations of voids at elevated temperature. It is worth noting the rate of change of failure to elongation briefly intensifies around the $300°C$ margin, the significance of which, has already been covered with a reduction factor explanation. The elongation to failure with respect to temperature suggested the elongation variation with non-uniform strain rate will not be significantly affected; e.g. at a temperature of $300°C$ the $1mm$ thick sample exhibited an elongation of 13.5% for strain rate of $6.09 \times 10^{-5}s^{-1}$, where the same $1mm$ sample at $6.09 \times 10^{-4}s^{-1}$ and $6.09 \times 10^{-3}s^{-1}$ strain rate showed elongations of 14.8% and 14.2%, respectively.
However it should be noted, among the tested samples few discrepancies were observed which have been recalled due to calibration error of the tensile machine and the acquisition system.

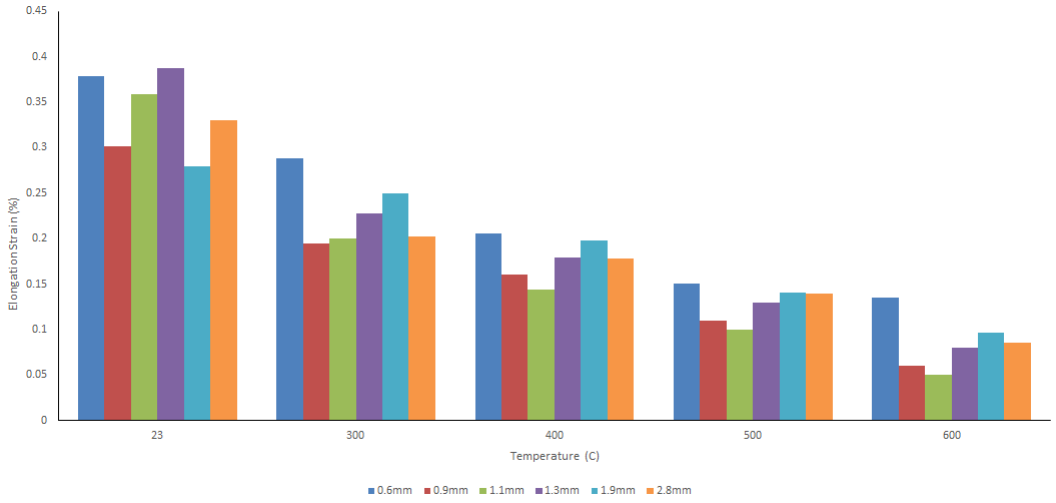

Figure 4.28: Elongation based on temperature variation at $6.09 \times 10^{-5}s^{-1}$ of 0.13% C-steel

Generally, the effect of strain aging is more prominent at yield strength as it is for ultimate strength. In broad terms, strain aging occurs when steel has been strained and allowed to rest for a period of time. This process alloys fo rmaximum load carrying capacity to be raised. The figure below expresses the stress-strain curve of a mild steel before and after strain aging; the yield strength and tensile strength were raised by ΔY and ΔU respectively, whereas the elongation Δe is shown to have decreased.

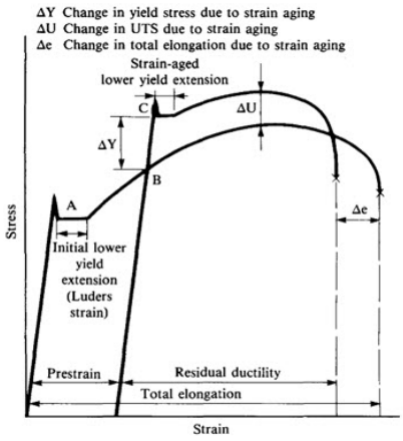

Figure 4.29: Influence of strain aging on mild steel [41]

However, in order to better understand the effect, the study was carried out at ultimate strength as proof of strain aging at yield strength. The comparison between yield strength and ultimate strength strain hardening are present in figure 4.30. The strain hardening components R_m and $R_{0.2}$, is shown to decrease by temperature and increase by strain rate.

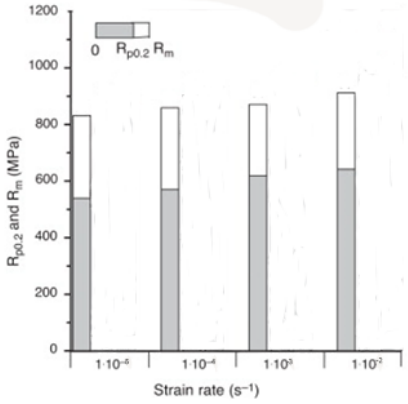

Figure 4.30: Ultimate strength

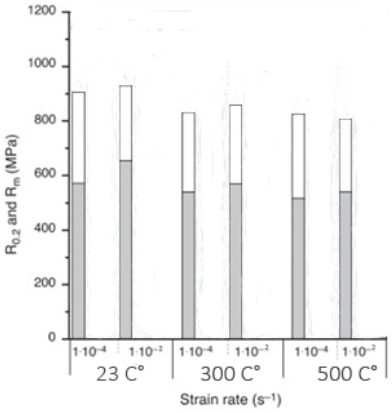

Figure 4.31: Yield strength

With reference to gradual shift of strain sensitivity from positive to negative, it may be correlated to the formation of slip planes and dislocations at elevated temperature and high strains. The slip plane will be introduced as nucleation sites within the micro-structure, and subsequently introducing the formation of carbide precipitates which in general would lead to a secondary hardening of the material. The time dependant nature of the effect and increase of strain hardening as after fact, causes the effect to be less visible at higher strain rates. Therefore, one may observe higher stress levels at lower strain rates caused by dynamic precipitation[97].

Presented in figures 4.32 and 4.33 is the elongation expressed as a function of temperature and strain rate for the samples of 1 mm and 2 mm thickness.

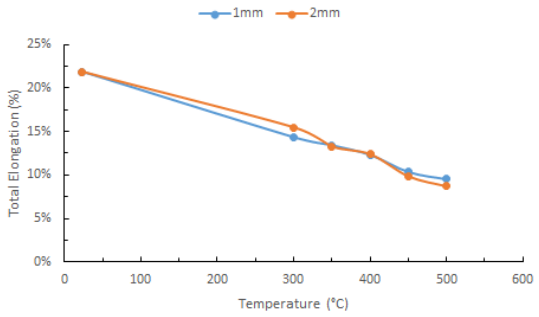

Figure 4.32: Total elongation as a function of temperature at $\dot{\varepsilon} = 6.09 \times 10^{-4} s^{-1}$

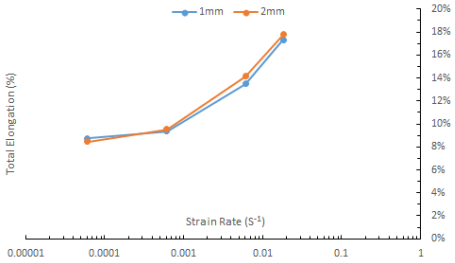

Figure 4.33: Total elongation as a function of strain rate at $350°C$

The sensitivity of strain to failure is clearly illustrated in the figures above. Therefore the temperature effect in figure 4.15, is clearly expressed in figure 4.32. In general increasing the strain rate is shown to increases the elongation and increase of temperature decreases elongation. Micro-structurally, this effect can be referred to the degree of transformation of martensite. Transformation can never be completely comprehensive, that is small pockets of austenite remain in their original state. In theory the austenite is stable and would no longer change its state any further. However the tendency remains for them to migrate into martensite by means of straining the material. As a result of this effect, ductility and hardening of the material is improved. However, a critical temperature range was observed by Sachdev [101], in which it was observed that temperatures ranging from -53°C to 187°C would introduce stability to the metastable austenite. It should be noted martensite formation is highly relient upon the strain rate, as it was reported [102] at moderate strain rate the formation of martensite is repressed, due to generated heat.

Contrary to total elongation, uniform elongation of the gauge length is limited by local neck formation. As strain rate is dependant upon the dimensions of the gauge length, the formation of neck would increase the local strain rate within the vicinity of the neck region, causing a descrepency between the starting strain rate and the local strain rate. Continually, this phenomenon would lead to increase of strain hardening ability, and would even increase further by higher initial strain

rates. Thus, enforcing greater neck formation which results in increase of total elongation to failure.

Temperatures functionality to total elongation is an inverse relation. Generally the elongation is reduced by increase of temperature. The effect becomes more visible with lower strain rates, which is reliant upon improvement of ductility and formation of carbides at increased temperatures. It should be noted from the Hall-Petch [103] condition that grain size would greatly influence and increase the strength the material at ambient temperatures. However, as temperature is raised grain growth of the material would adversely affect the material. Further, with elevated temperature the slip planes will contribute to Hall-Petch relation .

An observation made from figure 4.15, at higher temperatures yield strength and ultimate strength tend to be closely following one another. The reason for such behaviour could be deduced to dynamic recovery of the material. Dynamic recovery would subsequently be a leading role of strain softening at higher temperatures.

Recovery of a structure is one in which the deformed grains reduce the amount of stored energy, by doing so the arrangement of the crystal structure is shifted to its original state. However, for a dynamic recovery the energy introduced to the crystal structure is present as the recovery process attempts to restore the original state of the structure. Additionally, strain softening effect refers to the shear resistance being gradually reduced with continued plastic shear strains. As a result, only the strain path tests could be studied rather than the stress paths.

4.3.4 Necking formation

Due to the reasons stated above, it is clear an investigation on formation of necking is crucial. According to Considére criterion at the onset of necking formation, an instability in the tension test would occur. The onset is described by rate hardness becoming equal to the stress. Therefore for a given strain [104]:

$$\sigma = \frac{d\sigma}{d\varepsilon} \tag{4.42}$$

A "take-up" error in the elastic response resulted from grip and bar connections, resulted in investigating equation 4.42 within the plastic region only. The effect of strain rate on the strain were plotted against the hardening parameter and stress. That a best fit polynomial tends itself most conviniently to a considére instability analysis compared to J-C, Z-A and etc. As a result 4^{th} and 5^{th} order polynomial were created on the experimental data. The outcome of the polynomial fitting procedure was subsequently used for differentiation and interpolation. The polynomials, generated coefficients which were later used for assisting the mathematical FEA code.

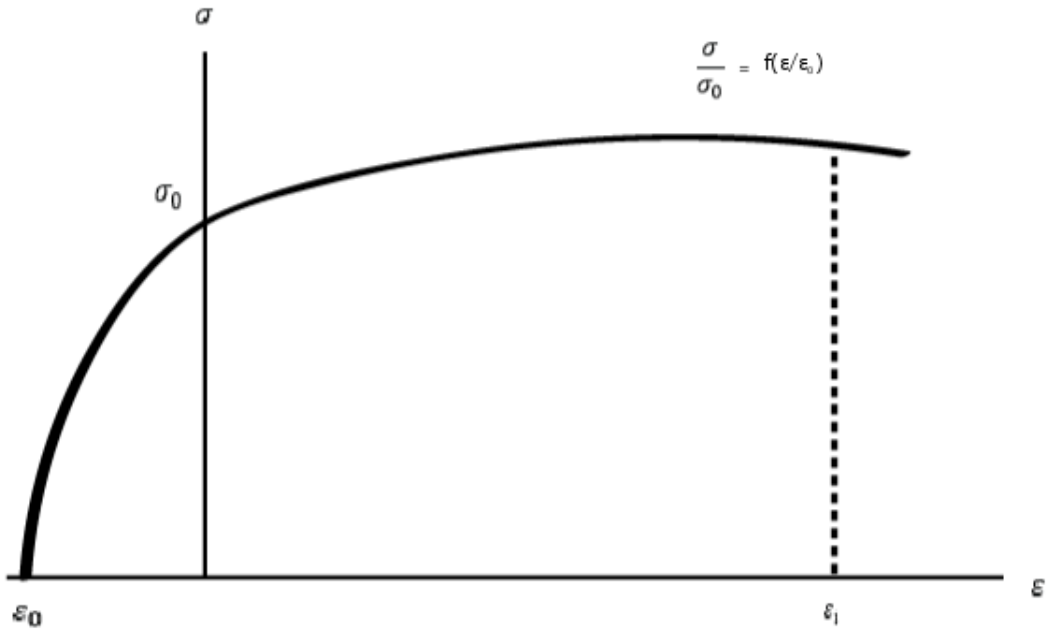

Figure 4.34: Description of polynomial calculation

On the basis of figure 4.34, which was derived from merging of Swift analysis and Considére criterion, the following calculations were computed.
The polynomial of each stress-strain curve was computed with σ as the unknown parameter and the path of the curve being dependant upon the value of strain at four points along the curve. This method enables the user to compute an accurate value of yield strength, stated as σ_0. By considering the two sides of Considére criterion separately, LHS may be written as:

$$\sigma = \sigma_0 + a_1\varepsilon_0 + a_2\varepsilon_0^2 + a_3\varepsilon_0^3 + a_4\varepsilon_0^4 \tag{4.43}$$

Therefore by means of normalising the yield stress:

$$\frac{\sigma}{\sigma_0} = 1 + \frac{a_1}{\sigma_0}\varepsilon_0 \left(\frac{\varepsilon}{\varepsilon_0}\right) + \frac{a_2}{\sigma_0}\varepsilon_0^2 \left(\frac{\varepsilon}{\varepsilon_0}\right)^2 + \frac{a_3}{\sigma_0}\varepsilon_0^3 \left(\frac{\varepsilon}{\varepsilon_0}\right)^3 + \frac{a_4}{\sigma_0}\varepsilon_0^4 \left(\frac{\varepsilon}{\varepsilon_0}\right)^4 \tag{4.44a}$$

$$\frac{\sigma}{\sigma_0} = 1 + {a_1}' \left(\frac{\varepsilon}{\varepsilon_0}\right) + {a_2}' \left(\frac{\varepsilon}{\varepsilon_2}\right)^2 + {a_3}' \left(\frac{\varepsilon}{\varepsilon_0}\right)^3 + {a_4}' \left(\frac{\varepsilon}{\varepsilon_0}\right)^4 \tag{4.44b}$$

In order to calculate for ε_0, Newton Raphson approximation was used. Iteration of NR is an integral element for better accuracy, therefore MATLAB coding was adopted for better accuracy. Subsequently, RHS of Considére criterion was computed for defining the instability of polynomial.

$$\frac{d\sigma_i}{d\varepsilon_i} = a_1 + 2a_2\varepsilon_i + 3a_3\varepsilon_i^2 + 4a_4\varepsilon_i^3 \tag{4.45}$$

By means of equating RHS to LHS, we may derive the instability quartic.

$${a_4}'\varepsilon_i^4 + \left({a_3}'\varepsilon_0 - 4{a_4}'\right)\varepsilon_i^3 + \left[\left({a_2}'\varepsilon_0 - 3{a_3}'\right)\varepsilon_0\right]\varepsilon_i^2 + \left[\left({a_1}'\varepsilon_0 - 2{a_2}'\right)\varepsilon_0^2\right]\varepsilon_i + \left(1 - \frac{{a_1}'}{\varepsilon_0}\right)\varepsilon_0^4 = 0 \tag{4.46}$$

Additionally the same procedure was carried out for describing a fifth order instability equation;where:

$${a_1}' = \frac{a_1}{\bar{\sigma}_0}\bar{\varepsilon}_0 \tag{4.47a}$$

$${a_2}' = \frac{a_2}{\bar{\sigma}_0}\bar{\varepsilon}_0^2 \tag{4.47b}$$

$${a_3}' = \frac{a_3}{\bar{\sigma}_0}\bar{\varepsilon}_0^3 \tag{4.47c}$$

$${a_4}' = \frac{a_4}{\bar{\sigma}_0}\bar{\varepsilon}_0^4 \tag{4.47d}$$

Therefore a new fifth order instability quadratic was derived:

$${a_4}'\left(\varepsilon_i^p\right)^5 + \left(11{a_3}'\bar{\varepsilon}_0 - 4a'\right)\left(\bar{\varepsilon}_i^p\right)^4 + \left(11{a_2}'\bar{\varepsilon}_0^2 - 16{a_4}' - 4{a_3}'\bar{\varepsilon}_0\right)\left(\bar{\varepsilon}_i^p\right)^3$$
$$+ \left(11a'\bar{\varepsilon}_0^2 - 12{a_3}' - 4{a_2}'\bar{\varepsilon}_0\right)\bar{\varepsilon}_0\left(\varepsilon_i^p\right)^2 + \left(11\bar{\varepsilon}_0^2 - 8{a_2}' - 4{a_1}'\bar{\varepsilon}_0\right)\bar{\varepsilon}_0^2\bar{\varepsilon}_i^p - 4\left({a_1}' + \bar{\varepsilon}_0\right)\bar{\varepsilon}_0^3 = 0 \tag{4.48}$$

By means of establishing the instability quartic, the coefficients could be stated in a matrix format, according to their environmental conditions.

$$\underset{\sim}{\sigma} = \underset{\sim\sim}{\varepsilon a} \tag{4.49}$$

$$\begin{bmatrix} \sigma_1 \\ \sigma_2 \\ \sigma_3 \\ \vdots \end{bmatrix} = \begin{bmatrix} \varepsilon_1 & \varepsilon_1^2 & \varepsilon_1^3 & \dots \\ \varepsilon_2 & \varepsilon_2^2 & \varepsilon_2^3 & \dots \\ \varepsilon_3 & \varepsilon_3^2 & \varepsilon_3^3 & \dots \\ \vdots & \vdots & \vdots & \vdots \end{bmatrix} \begin{bmatrix} a_1 \\ a_2 \\ a_3 \\ \vdots \end{bmatrix} \tag{4.50}$$

4.3.4.1 Effect of strain rate based on Considére criterion

Figures 4.35 to 4.39, predicts that increasing displacement (strain) rate delays the onset of necking according to the Considére criterion. Therefore, the increase of strain hardening rate of the material complements the ductility of the material by means of increasing the strain rate for a given temperature. The finding here, confirms the observation made earlier in which increasing the rate of straining increases the elongation to fracture (see section 4.3.3).

A point to consider from figure 4.38, where in comparison carbon steel shows that the Considére effect is met earlier than for other materials. This can be related to the change in ductility of carbon steel as well as its micro-structural change. Additionally the fracture strain value decline can be correlated to the increase of temperature for this figure; the investigation of temperature on necking formation will be discussed next.

4.3.4.2 Effect of temperature based on Considére criterion

Prior to discussion of polynomial and matrix formation of the coefficients, the effect of temperature upon formation will be investigated. The onset of necking was found to be heavily reliant upon test temperature. At lower temperatures the necking was formed at later stages of strain levels. However, as figure 4.40-4.45 show, with elevation of temperature, necking occurs at lower strain levels. This finding was both observed experimentally and mathematically through Considére criterion. Additionally, this finding further cements the findings in section 4.3.3 in which elongation was observed to decrease with temperatures above $300°C$. The elevated temperature is shown to reduce the strain hardening rate, as a consequence lowering the prediction

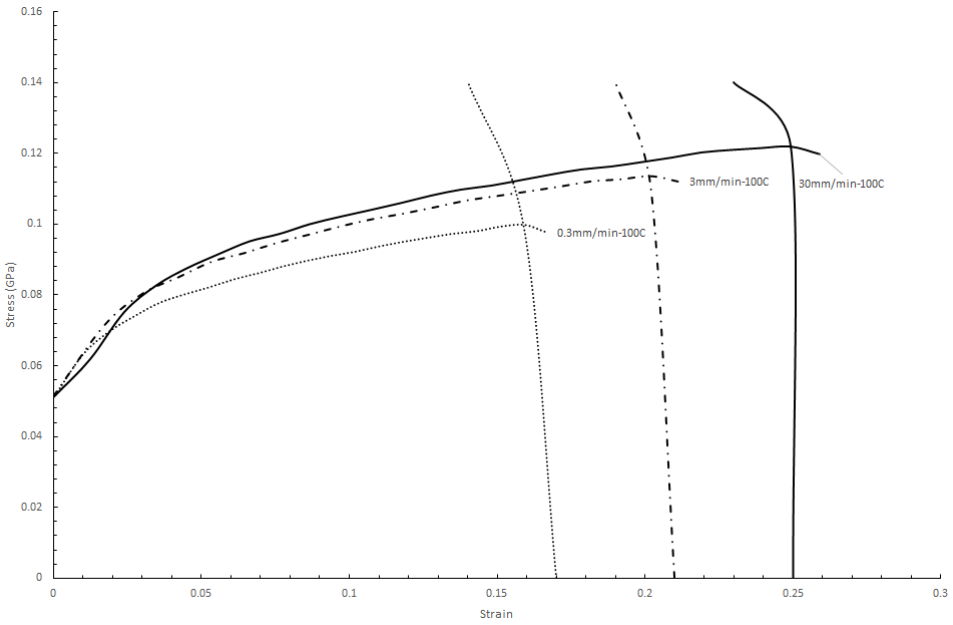

Figure 4.35: Stress vs. Strain with varying strain rate for AISI 6063 at 100°C

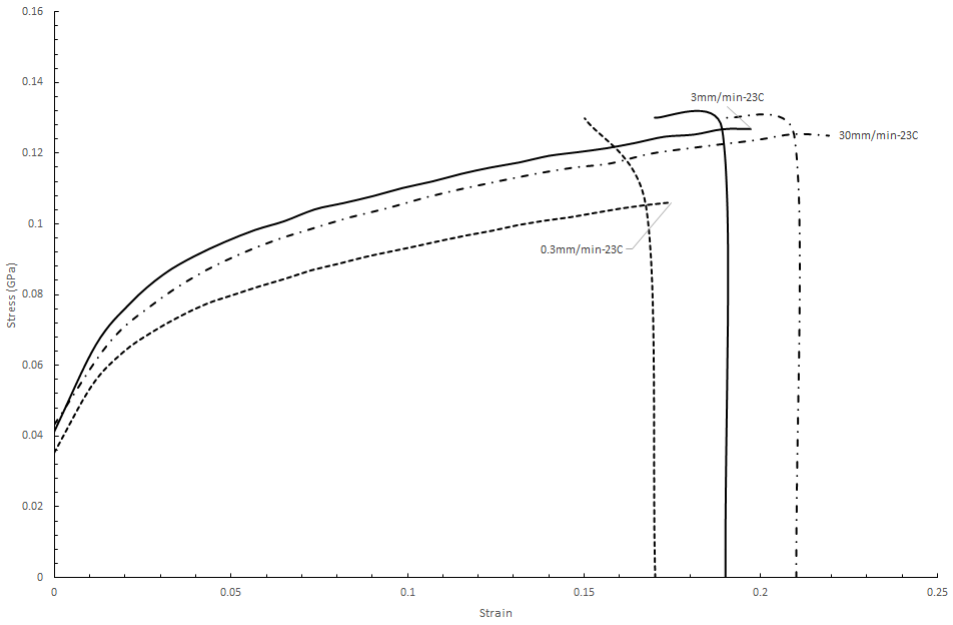

Figure 4.36: Effect of displacement rate for AISI 6063 at 23°C

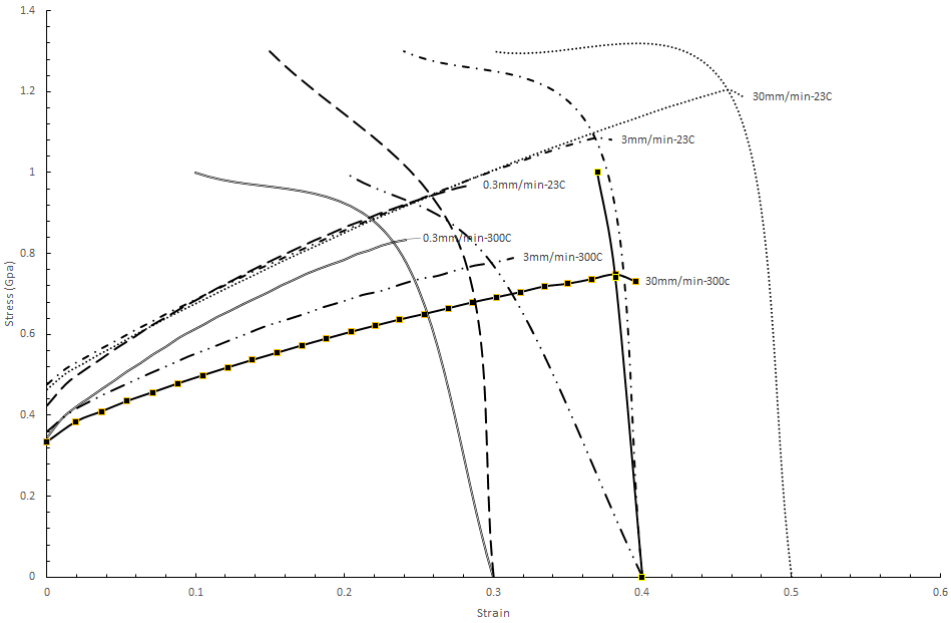

Figure 4.37: Effect of displacement rate for 18/8 stainless steel

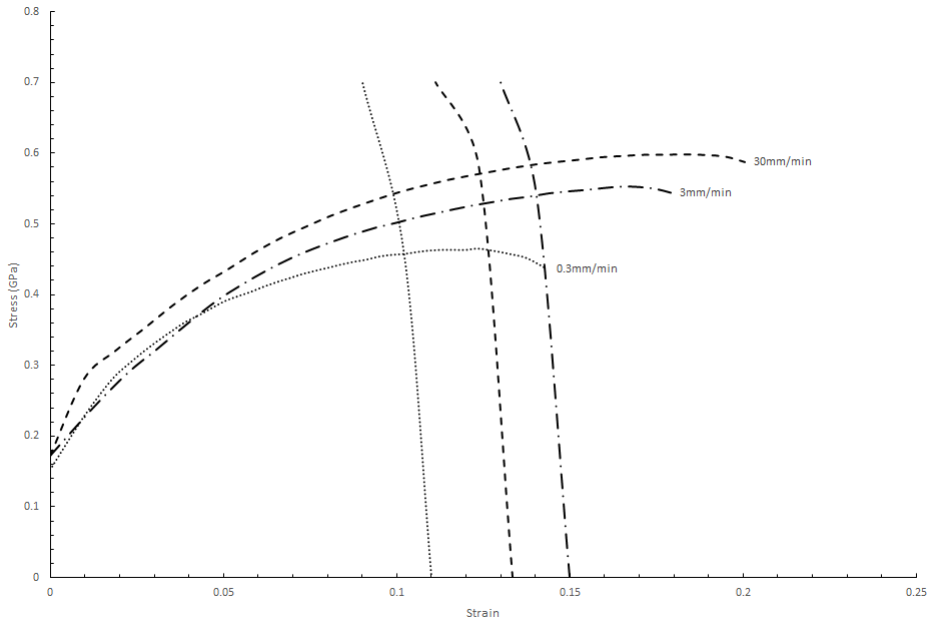

Figure 4.38: Effect of displacement rate for 0.13% C-steel at $300°C$

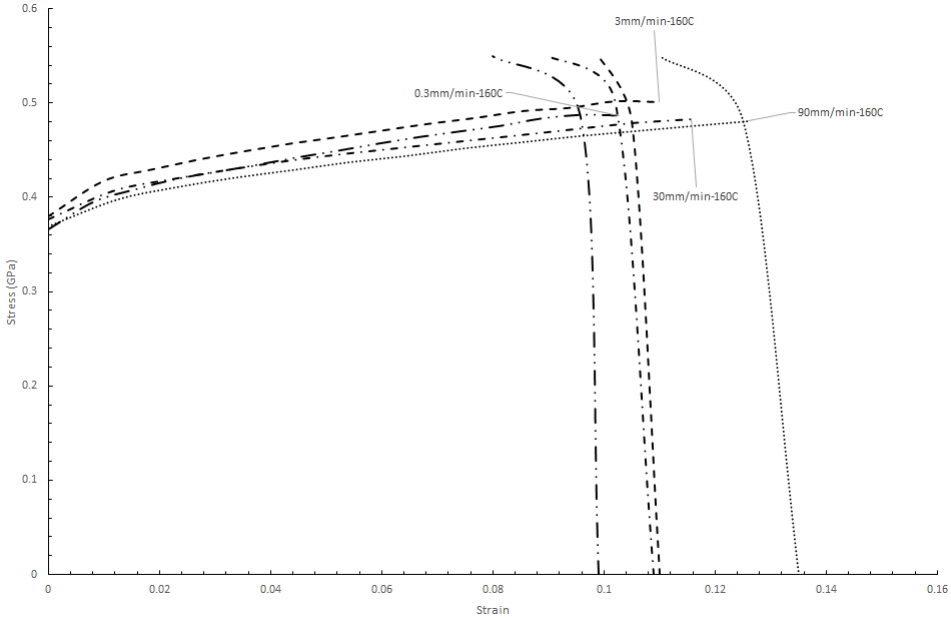

Figure 4.39: Effect of displacement rate for 60/40 brass at $160°C$

of instability point. In the series of figures presented here, the vertical line would illustrate the calculated point of instability based on the Considere criterion.
In order to illustrate the point clearly a series of figures with uniform strain rate at $6.09 \times 10^{-5} s^{-1}$ are provided below.

As evident by figures 4.40 to 4.45, the prediction of necking is heavily dependent on thickness of the sample. It appears that instability for thinner materials are less influenced by elevation of temperature. However, as the thickness increases the influence of temperature becomes more substantial. Figure 4.46, shows this effect; it can be concluded as thickness of a material increase along with temperature the onset of necking forms a linear relation to the strain value at failure.
Thickness of $0.6mm$ is relatively unchanged with temperature elevation, and only at about $400°C$ a percentage difference increase is observed; same effect can be seen for $0.9mm$ samples, only the temperature affected zone is lowered to $300°C$.

4.3.5 Comparative study

4.3.5.1 Comparison of mechanical properties to other design codes

Previously it was mentioned a set of codes of conduct were proposed by a number of institutes. Therefore, in order to further examine the reduction factor values

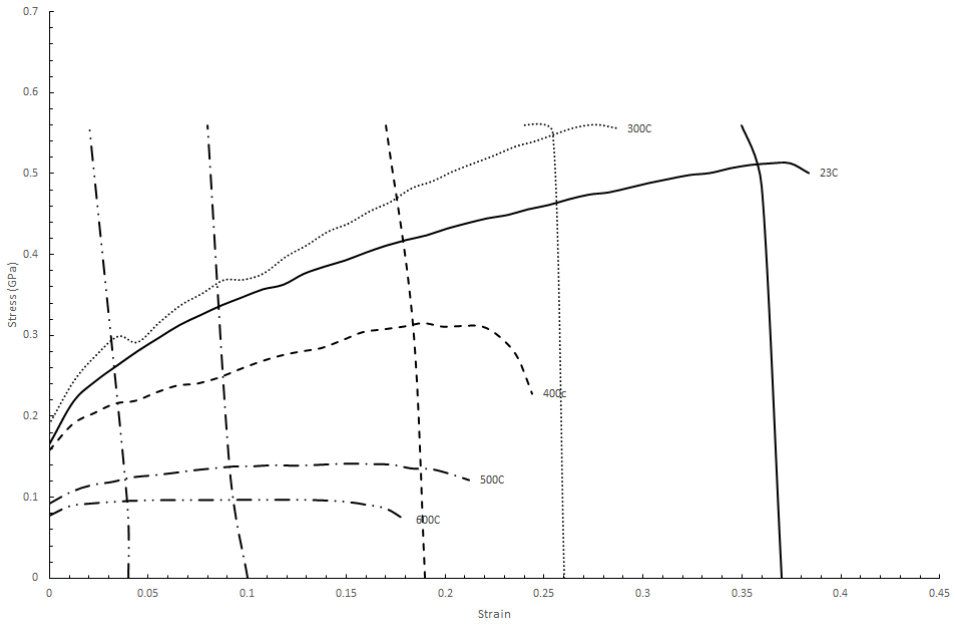

Figure 4.40: Stress vs. strain with varying temperature on 0.6mm 0.13% C-steel

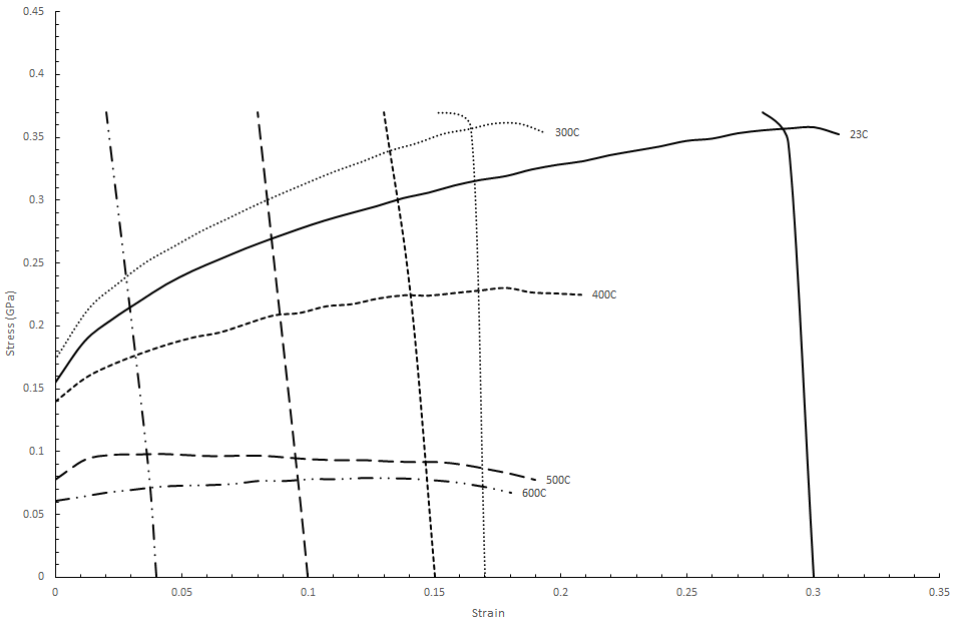

Figure 4.41: Stress vs. strain with varying temperature on 0.9mm 0.13% C-steel

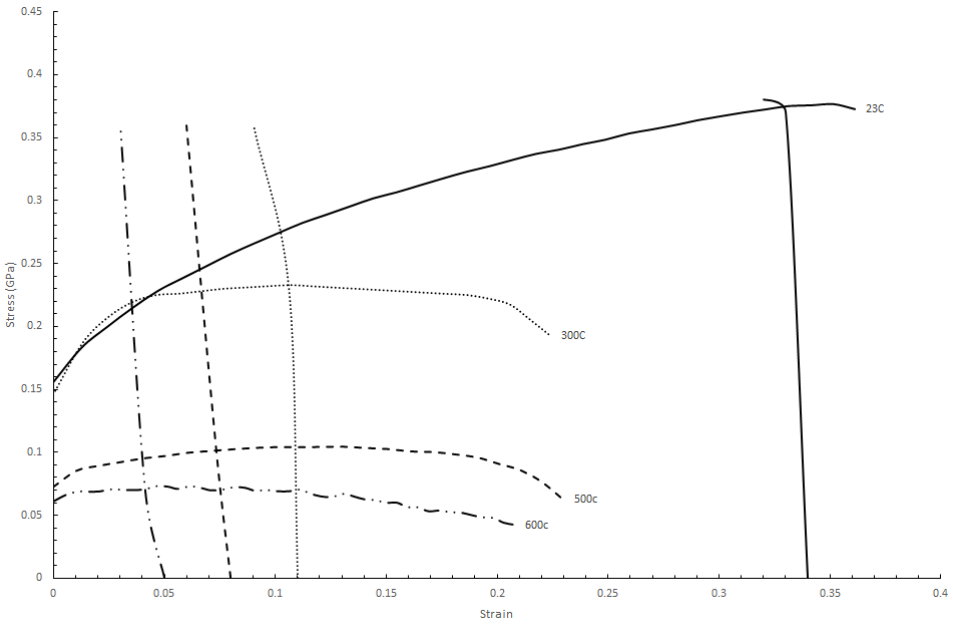

Figure 4.42: Stress vs. strain with varying temperature on 1.1mm 0.13% C-steel

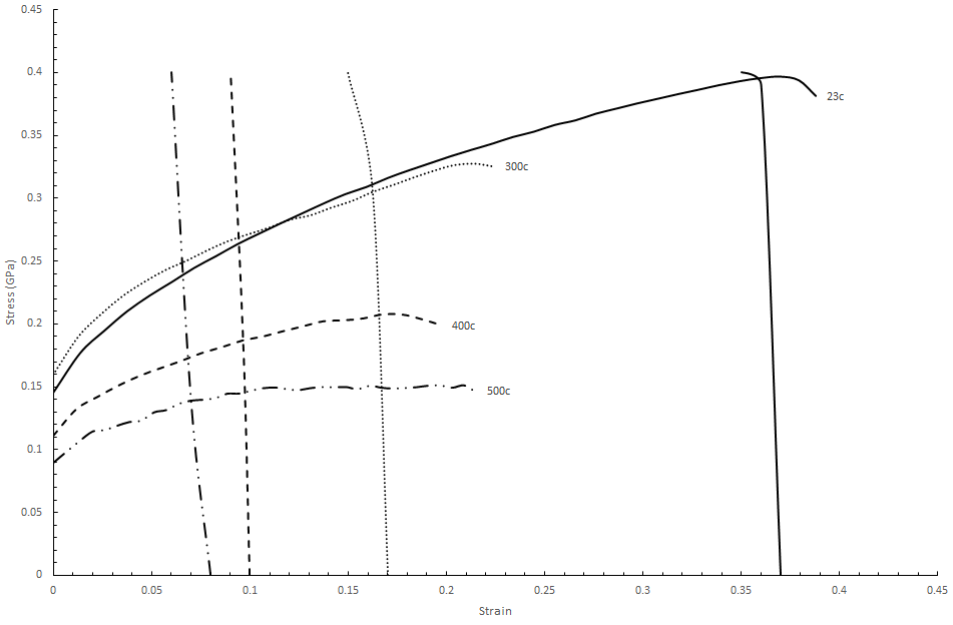

Figure 4.43: Stress vs. strain with varying temperature on 1.3mm 0.13% C-steel

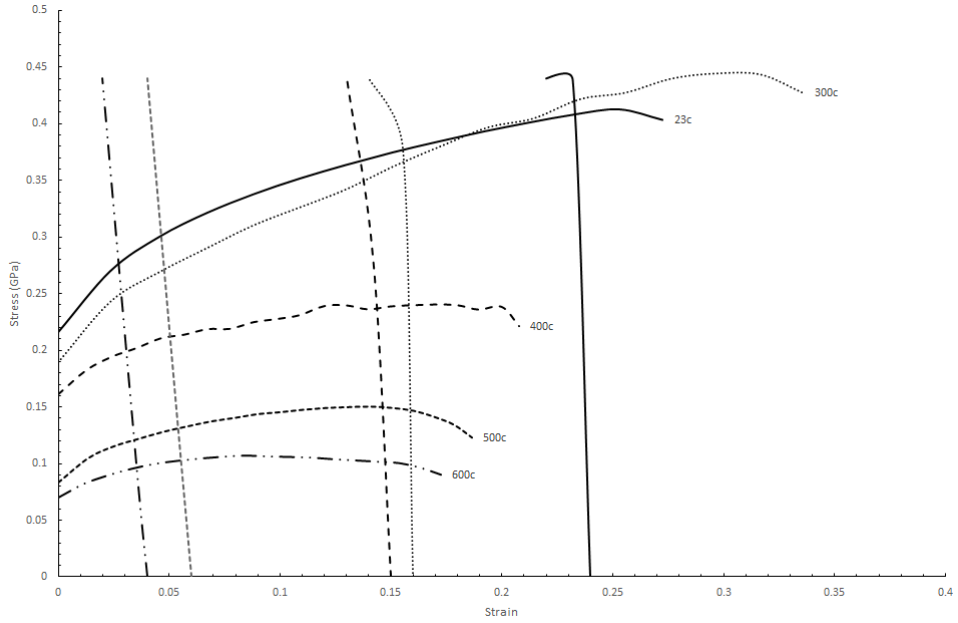

Figure 4.44: Stress vs. strain with varying temperature on 1.9mm 0.13% C-steel

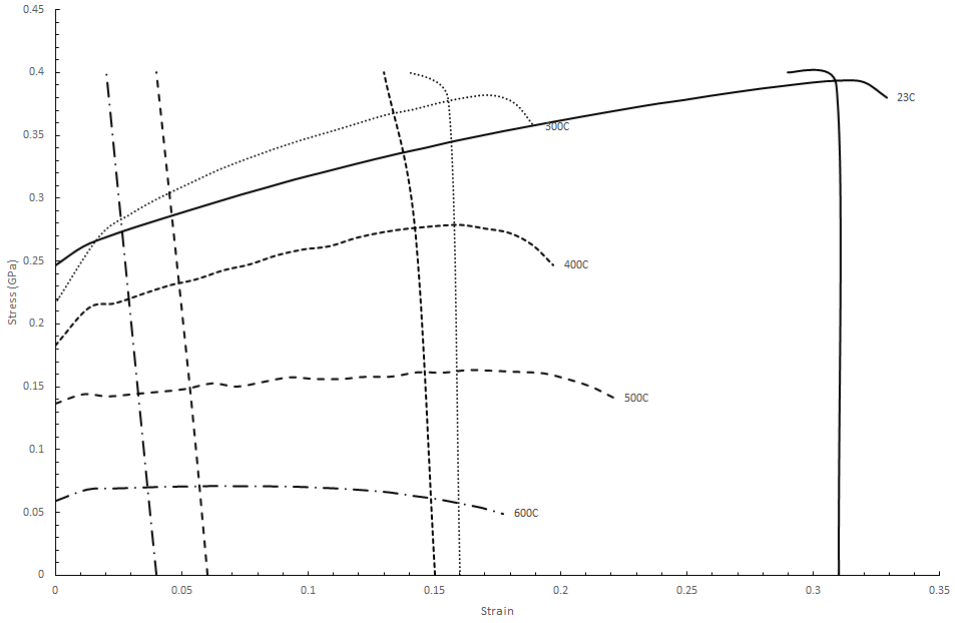

Figure 4.45: Stress vs. strain with varying temperature on 2.8mm 0.13% C-steel

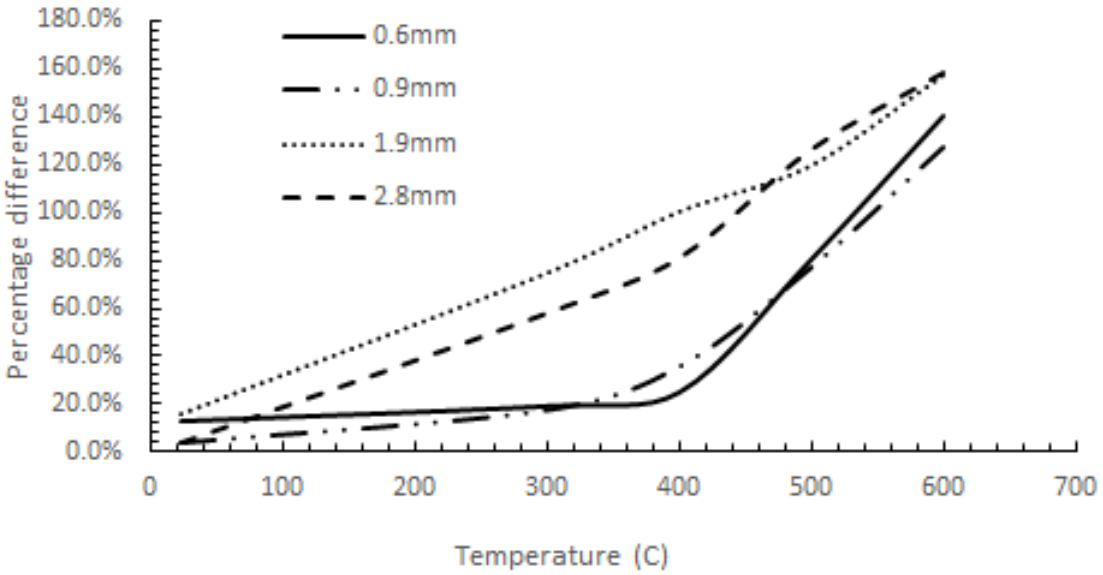

Figure 4.46: Percentage strain level change of necking formation to failure on varying temperature for 0.13% C-steel

recommended a comparison of the results was carried out. BS5950 [10] and Eurocode 3 [9] were the two cores for comparison, the former standard calculates the reduction factors at four strain levels, whereas the Eurocode applies to proof stress only. Figure 4.47 compares the yield strength reduction factor values to those of the standards for the 0.6mm thickness material.

As observed by figure 4.47, the general trend of the tested samples comply with findings of BS and EC3. However, a discrepancy arises around 300°C; where the calculated Reduction Factor (RF) values are over estimated compared to BS and EC3. That is due to the thickness effect discussed previously. The work carried out the by the two institutes have not accounted for thickness effect. The thicknesses used for their calculation are over the unity value of $1mm$. Therefore, a decline in RF is observed; the discrepancy mentioned reduces as the effect of temperature is increased across all thicknesses. It is worthwhile to mention the results presented by BS and EC3 tend to be very tolerant of temperature and physical changes. The discrepancies observed over the 300°C is thought to be due to under-predicting of the RF values by the two institutes. The RF values presented in this work are highly dependent on the thickness and strain rate of each test. However neither BS or EC3 have made any recommendations related to the aspects mentioned. This compari-

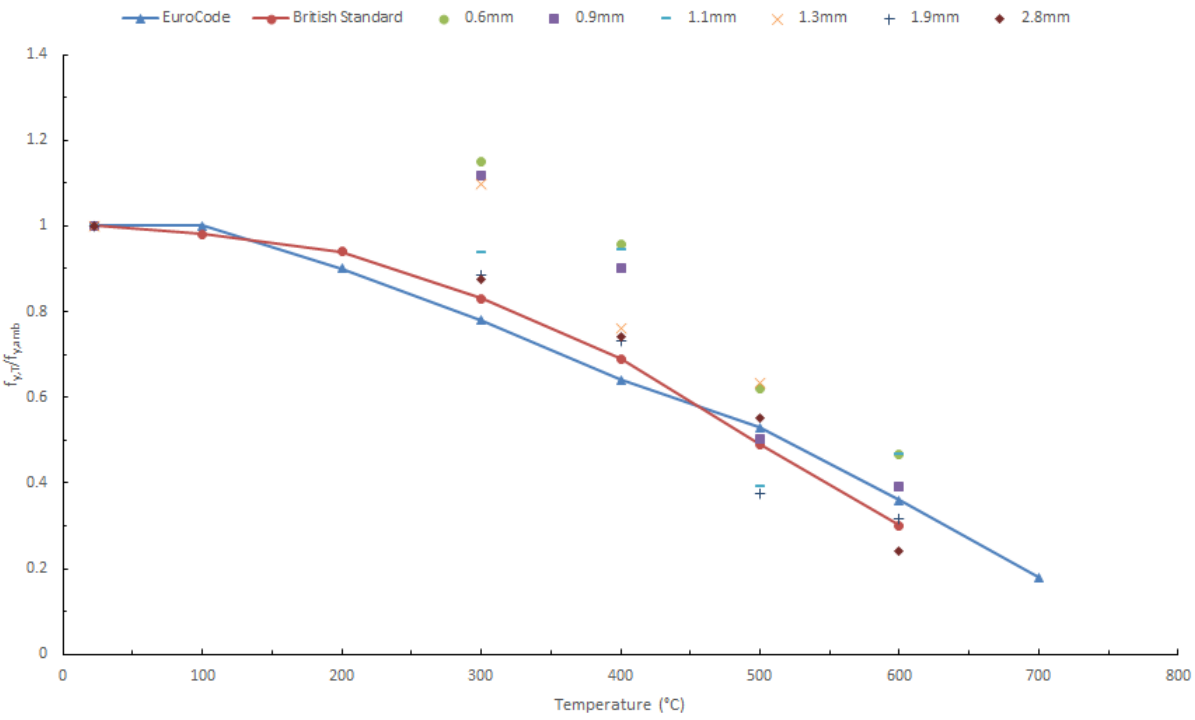

Figure 4.47: Comparison of yield strength reduction factors based on elevated temperature

son between yield strength RF's, justifies experimental RF values for compiling the mathematical model for use in finite element analyses.

4.3.5.2 Comparison of mechanical properties to other researchers

Over the past 50 years substantial amount work has been carried out to try and describe the plastic behaviour of metals under various conditions. In this an section attempt was made to try to make a broad comparison between the works carried so far.

One of the more prominent works was carried out by Outinen [8], in which $2mm$ thick sheet metals coated in zinc was tested, the RF values were calculated and provided for both the yield strength and elastic modulus. Contrary to Outinen where the tests were conducted in steady state format, Mecozzi [105] carried similar study where the work was based on both transient and steady state format. Mecozzi conducted his tests on a number of flat sheets with ranging thickness. Additionally to these works Ranawaka et al [7] carried steady state tests in which attempt was made to cover a larger range of plate thickness in their uni-axial tests. In one of the latest presentations of RF values Chen [5], studied the behaviour of stainless steels

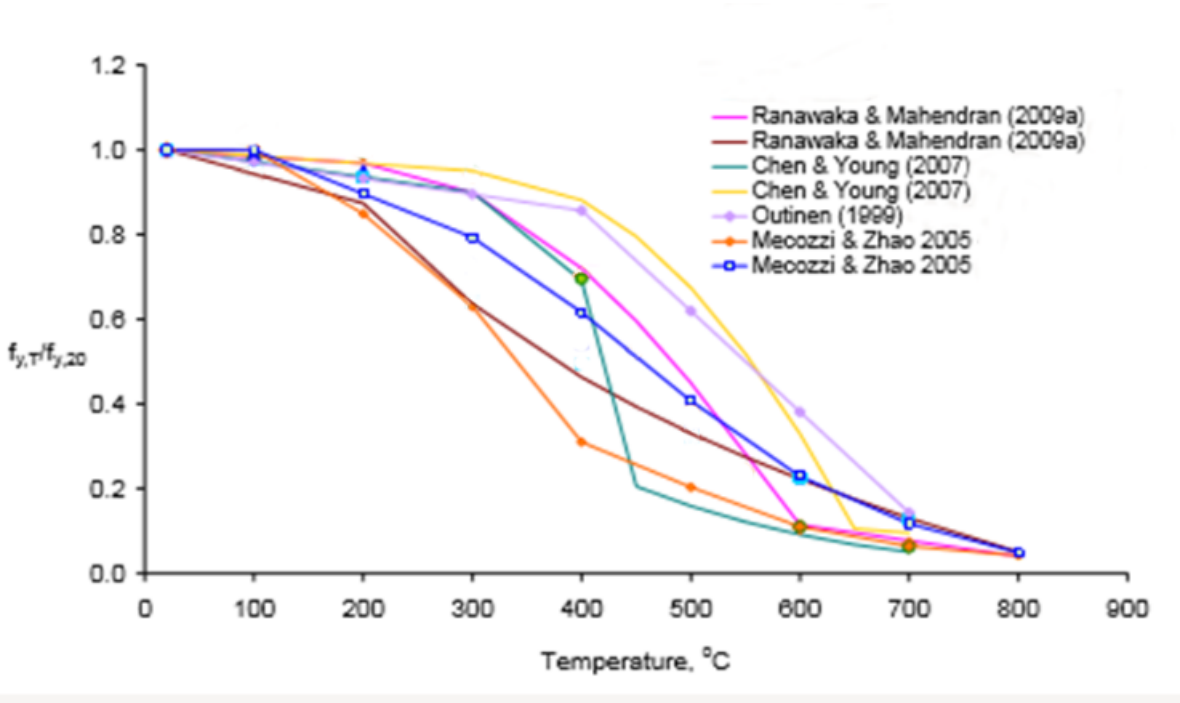

Figure 4.48: Comparison of yield strength reduction factors based on researchers

at elevated temperature. The work made a recommendation for predicting stress strain and in smaller part estimating yield strength and elastic modulus. However, the proposed correlations for yield strength was based on steady state format and transient state for elastic modulus. Presented in figure 4.48 is the combination of the works mentioned based on yield strength evaluation.

The majority of materials tested in this comparison were steel grades G250 and G450. As can be seen in figure 4.48, Mecozzi under-predicted the RF value for the yield strength. Also, what is suggested and confirmed by Ranawaka and Chen is the discrepancy between the RF values based on steel grades. The outcome of the tests verified the RF values are higher when put against high strength materials than for low strength materials. The most amount of discrepancy was observed in Chen's work at 400°C where over 30% difference was noted between the high and low strength material.

It appears that the proposal put forth by all researchers have failed to observe the effect of thickness completely as presented by this work. The values RF presented by Meccozi for the S280 and S380 materials tend to be over-conservative over a range of temperature. The RF values given by Chen, for a steel plate of $1.9mm$ thickness differs from the results presented in this work. Therefore, the correlations described by previous research would not be adequate for adaptation to a suitable

the mathematical model completely.

4.4 Micro-structural Analysis

A SEM (Scanning electron microscope) was used, in order to further study the microstructural changes of the samples based on variation of environmental conditions. The optical pictures were taken from the necked and fractured region of some of the more defining samples. Ductile shear fracture tends to be the leading cause of failure among the samples. A point discovered was the increase in strain rate accelerates the necking and damage; resulting from void nucleation, growth and coalescence of the voids in the necked region. Their sites are inherently the position of second phase particles where the plastic strain and hydrostatic stress are most prominent.

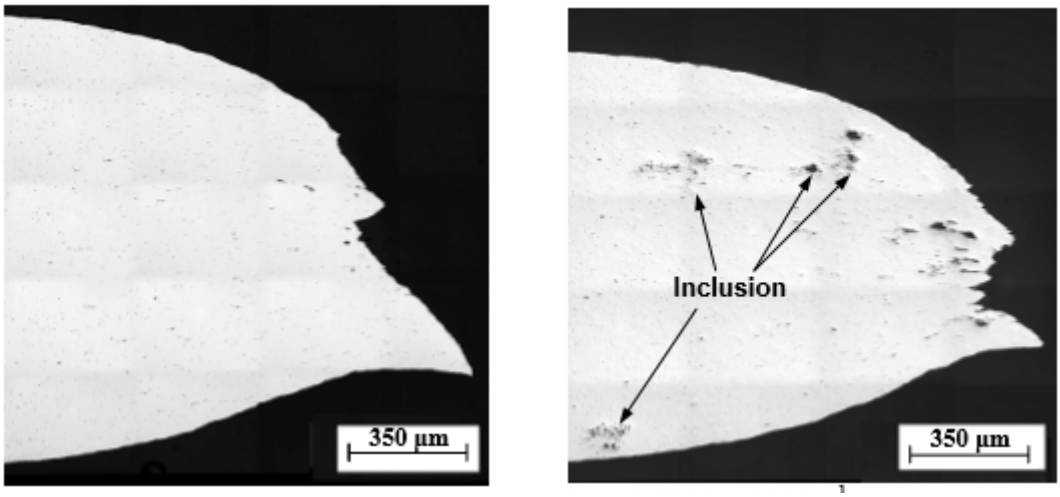

(a) $6.09 \times 10^{-4} s^{-1}$ 0.13% C-steel (b) $0.01829 s^{-1}$ 0.13% C-steel

Figure 4.49: SEM image of high strain rate vs. low strain rate for 0.13% C-steel

Based on the observations, the greatest thickness strain occurs adjacent to the failure region, increases with strain rate. In order to better understand the thickness strain to fracture surface, figure 4.50 was created. As it can be seen the thickness strains are more evident with higher strain rate samples at a much further location from the necked tip. Implication of such finding is at higher displacement (strain) rates, the deformation leading to the failure occurs over a larger region, which would promote formability, making press forming at higher rates inviting. However, the thinning of the material will not be limited to the fractured region, and will prop-

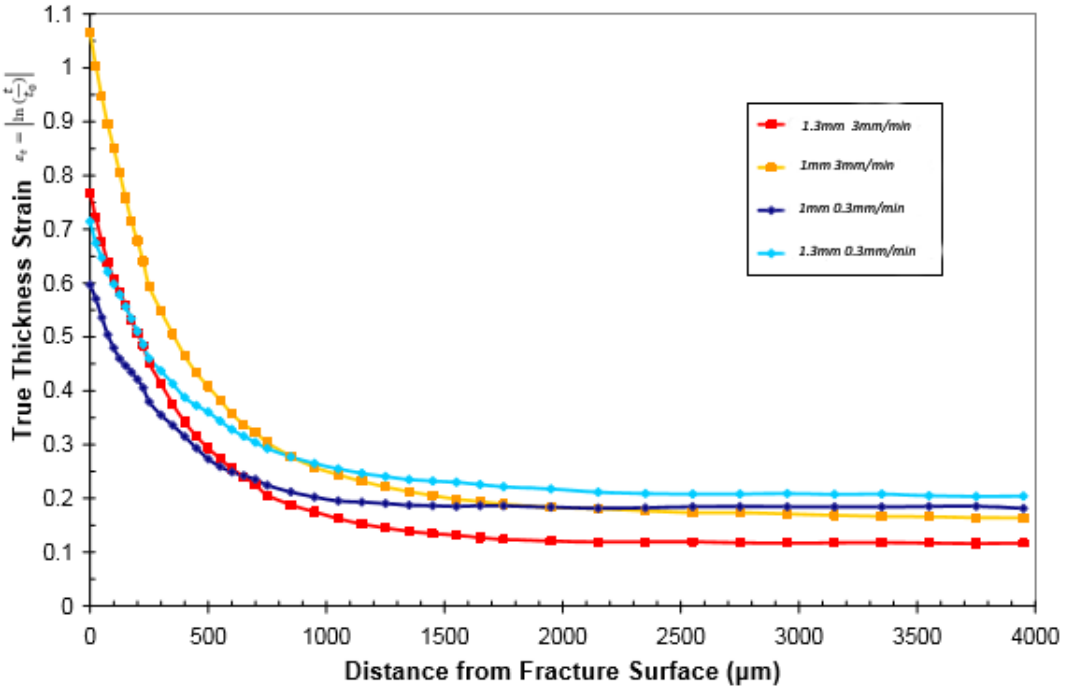

Figure 4.50: Thickness strain variation to fracture surface of 0.13% C-steel

agate through the gauge section; based on transverse strain becoming uniform over $2000\mu m$ away from fracture surface. Therefore, for higher transverse strain value, more necking deformation will occur prior to final failure.

Mentioned before, the leading cause of failure is due to void formation around the necked region. Therefore, a porosity measurment study was carried out in which various points along the gauge length were recorded. Figure 4.51, illustrates the relative function of void density based on distance and strain rate. The dashed and pointed line represent the initial porosity and area fraction based on second phase, respectively.

The comparative void formation between $6.09\times10^{-5}s^{-1}$, $6.09\times10^{-4}s^{-1}$ and $0.01829s^{-1}$, signifies the porosity escalation with increase of strain rate. The maximum porosity percentage between least and highest strain rate is 0.6% and 3.08%. Based on figure 4.51, it can be stated a delay in formation of necking and failure will occur due to high strain rate, which would result in higher damage levels. However, it should be noted over $300\mu m$ void formation will not be substantial, resulting in damage being confined in the fractured tip. Additionally, a few rogue cases have been excluded from this figure where due to unwanted oxides being present within the microstructure, they would assist in further ingrain slippage and fracture.

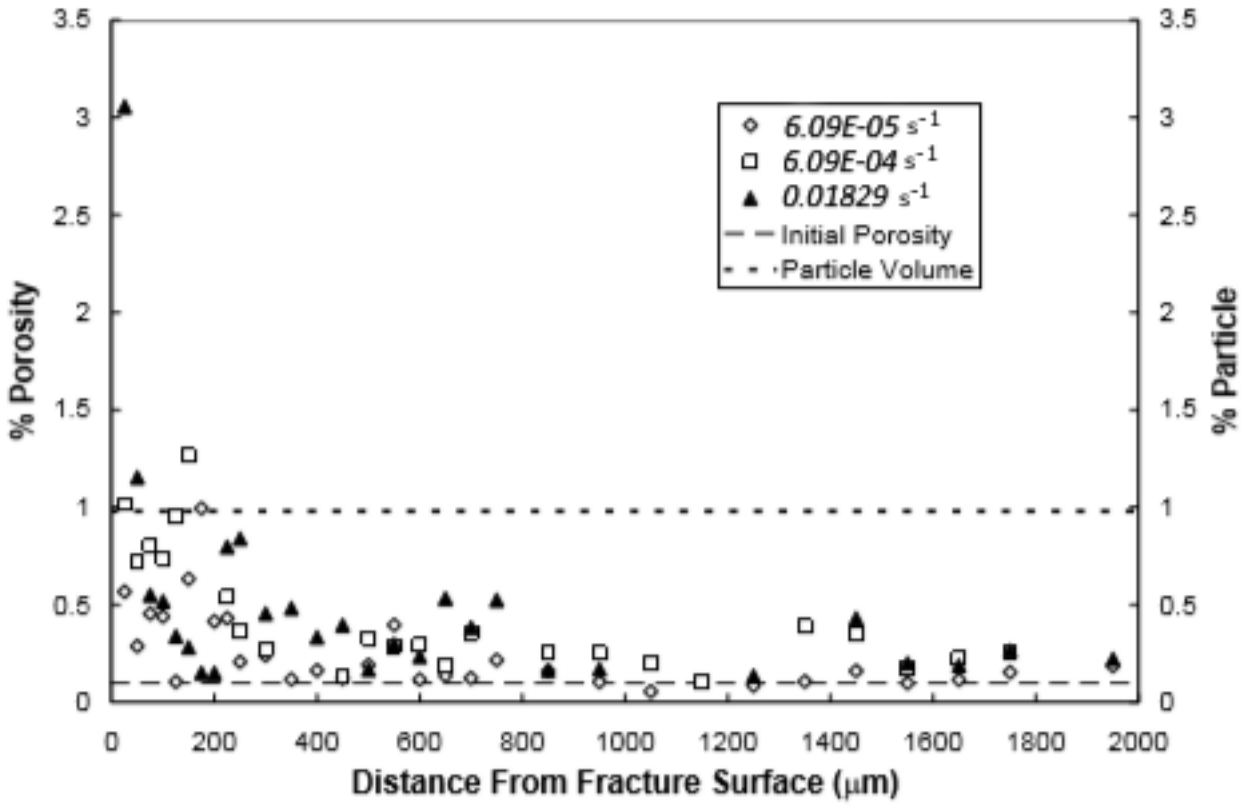

Figure 4.51: Void formation rate based on strain rate on 0.13% C-steel for 1.0 mm

For the cases where higher initial porosity is observed, the failure tend to happen with additional damage. Figure 4.52, exhibits the increase of porosity in the microstructure based on the influence of strain rate, A similar effect was observed in Mukai et al. [106].

A characteristic seen in the images is formation of a "dimple" at the fracture surface. Such morphology indicates ductile failure of the samples. The finding is regardless of environmental conditions, the only implication of such ductile failure is change of cross sectional area; figure 4.53 represents the ductile fracture. The presence of such dimples intertwined with Fe and Mn rich intermetalics (figure 4.54), causes damage to originate from the second phase particles which in turn leads to void nucleation. Slippage in grain boundaries within this region initiates damage and will lead to cracking through the matrix interface.

The cross sectional reduction of area was measured against the strain rate changes for 0.13% C-steel using the SEM. The findings revealed that greater damage and elongation to failure was observed with higher strain rate and thickness sheets,

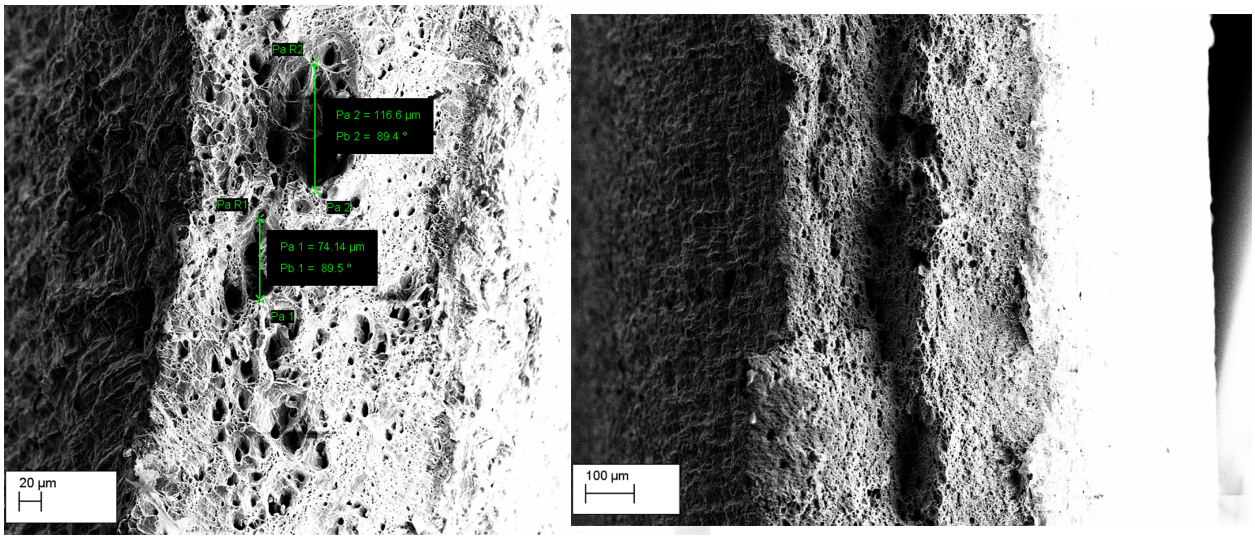

(a) $6.09 \times 10^{-4} s^{-1}$ 0.13% C-steel

(b) $6.09 \times 10^{-5} s^{-1}$ 0.13% C-steel

Figure 4.52: Porosity change based on strain rate variation

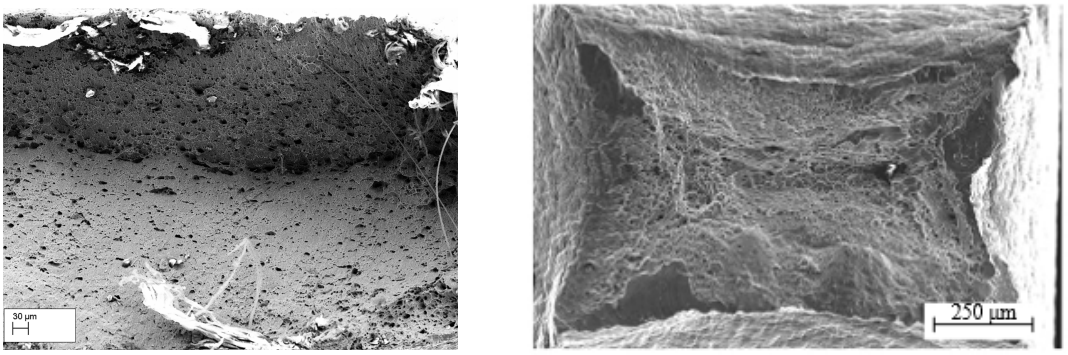

(a) $6.09 \times 10^{-4} s^{-1}$ 0.13% C-steel

(b) $6.09 \times 10^{-3} s^{-1}$ 0.13% C-steel

Figure 4.53: Ductile fracture of 0.13% C-steel

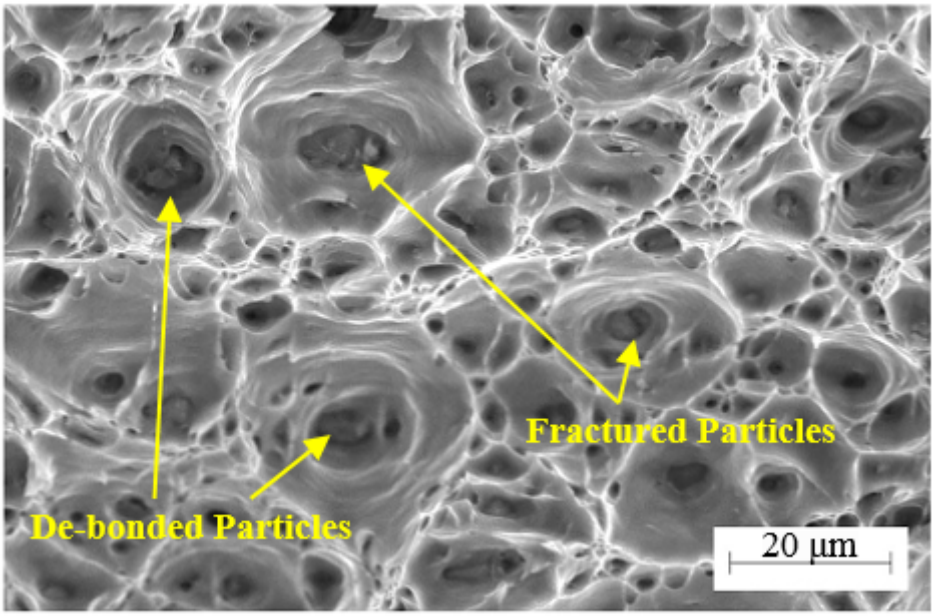

Figure 4.54: Presence of Fe and Mn on 0.13% C-steel for 1.0 mm

which cause sharper necking around the plastic strain region as well as increasing the ductility of the material.

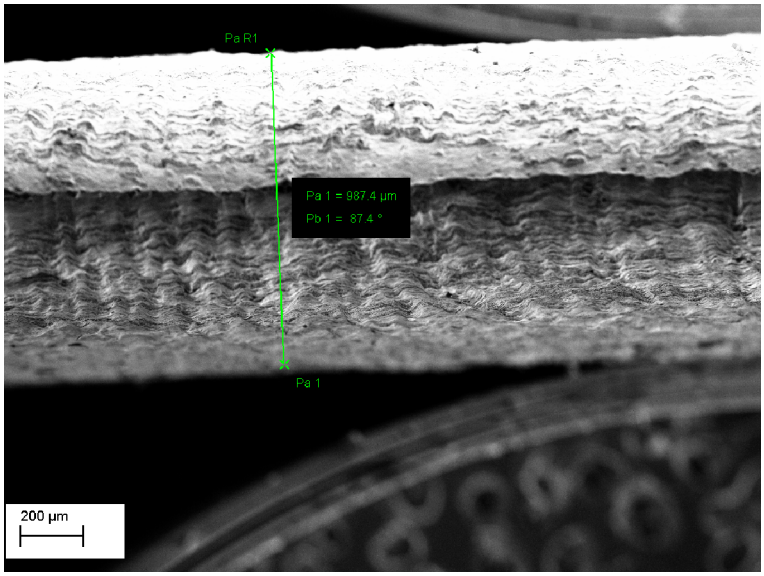

(a) SEM measurment of cross sectional change of sheet steel

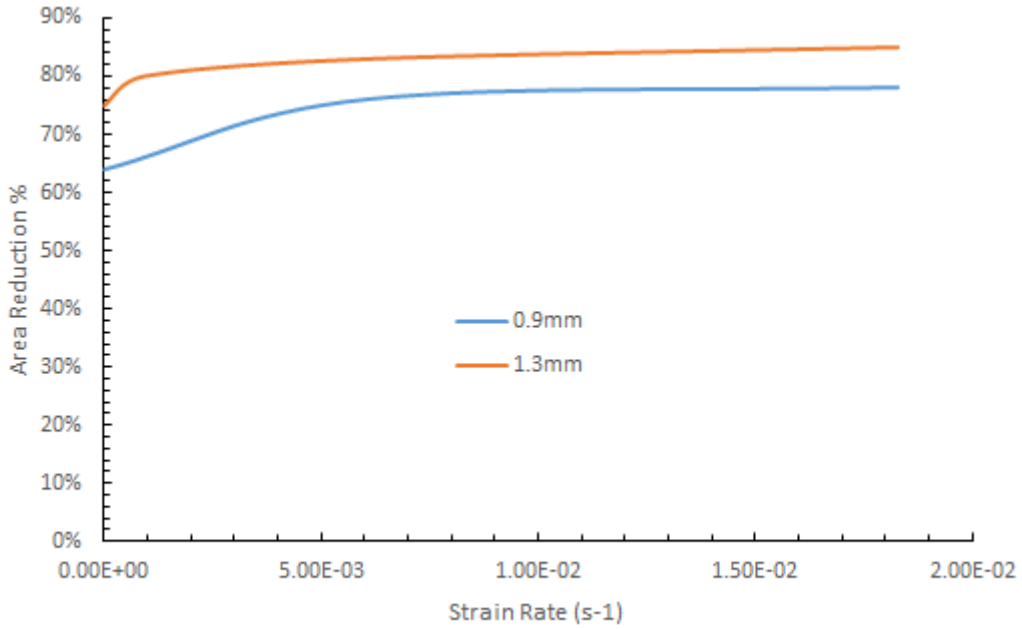

(b) Area reduction vs. varying strain rate

Figure 4.55: Area reduction measurement

Chapter 5

Simulation Process

5.1 Introduction

5.1.1 Description of intent

In this chapter attempt has been made to verify the experimental results explained in chapter 4 by means of Finite Element Analysis (FEA). The approach will be to understand FEA structure in general as related to this work. Later a comprehensive explanation of defining the models will provided.

In order to understand the method in which our chosen platform works when defining the materials a step by step parametric study was carried. The parametric study carried out enabled the adaptation of other frequently used packages within ABAQUS, the FEA program. Subsequently, the investigations on instability of the material and recognising the coefficients of material characteristics, discussed in the previous chapter, lead to construction of a new user subroutine. The sub routine model was compared against the more frequently used models and results related to this finding are put forth.

Lastly, a further study was carried out to determine the onset of necking based on variations in strain and thickness. Through the means of this study a method is proposed for acquiring true stress-strain curves over larger strain levels. The results of this study was verified against J-C results which were outsourced [36][107].

5.1.2 Theory of finite element analysis

5.1.2.1 History of FEA

It was in 60's and with the work of [108] proposed two decades before, Finite Element Analysis opened new frontier for engineers. It was Hrenikoff [109], that developed the idea of estimating the elastic behaviour in one dimensional rods and beams.

A decade later, in 50's Schonberg [110] made use of storage programs to revise the governing equations of nodal displacement to matrix format for faster processing of data as well as increasing the computational power.

After the modification carried out by Schonberg, FE was adopted in different branches of engineering such as, structural analysis, magnetic fields, heat transfer etc. However, at the time FE analysis was considered as an expensive engineering practice due to high cost of the computer capable of tackling the processing required to establish adequate number of elements.

Finite element analysis is based upon discretisation of the model to minute elements, where each element is connected to its neighbouring element by means of nodes. It is the physical alterations of these nodes that will define the governing differential equation of any model related to its internal and external forces.

In order to convert the physical changes of nodes to mathematical language, trial solutions of nodes are formed. Trial solutions will assist in optimising the estimation of the model. Additionally, for every trial solution in order to be able to correctly determine the mathematical model of the solid, in our case, appropriate physical properties as well as precise boundary conditions will be required. Otherwise, verification of the post processing will become void.

The defined conditions around the model will provide a trial solution of strain energy $\tilde{U}_{xyz}$ for a three dimensional model. Additionally, the governing equation of the solid will produce a solution U_{xyz}, in which the objective is to reduce the

absolute difference error E_{xyz}.

$$E_{xyz} = U_{xyz} - \tilde{U}_{xyz}$$

5.1.2.2 FEA sequence

Typically, there are fours steps prior to producing and analysing a model in FE. Figure 5.1 shows the sequence of defining a solution to a problem.

The model is initially defined and prerequisites are established (A); after which the aim is to simplify the model, but not to distort the end result. As such, in the majority of cases points of symmetry are withdrawn from the actual model (see B&C). The last sequence (D) would relate to defining correct boundary conditions as well as proper discretionary of the model.

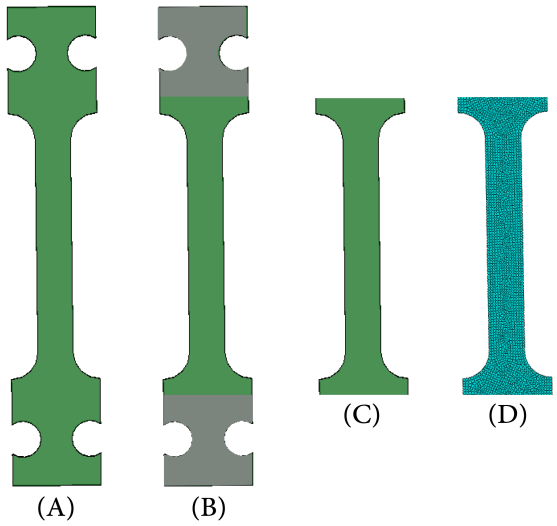

Figure 5.1: Sequence of a typical FEA solution

Albeit, the sequence mentioned above will have sub-steps which would involve defining an adequate governing differential equation to be later converted into an algebraic set of equation within ABAQUS.

5.2 Finite Element Mathematical Modelling

Modelling of any model in FEA packages are carried by developing a trial solution of the problem. The trial solution attempts to resolve the nodal displacements based on the conditions set by the user. However, it is essential to understand the mathematics involved to be able to capitalize upon such solutions when developing any

code based commands for implementation in a FE problem.

Trial solutions can be expressed in three segments:

1. Developing trial solution
2. Optimization of the trial solution
3. Error analysis for reducing and minimising deviation to the exact solution

Figure 5.2 demonstrates the cycle for optimising a trial solution.

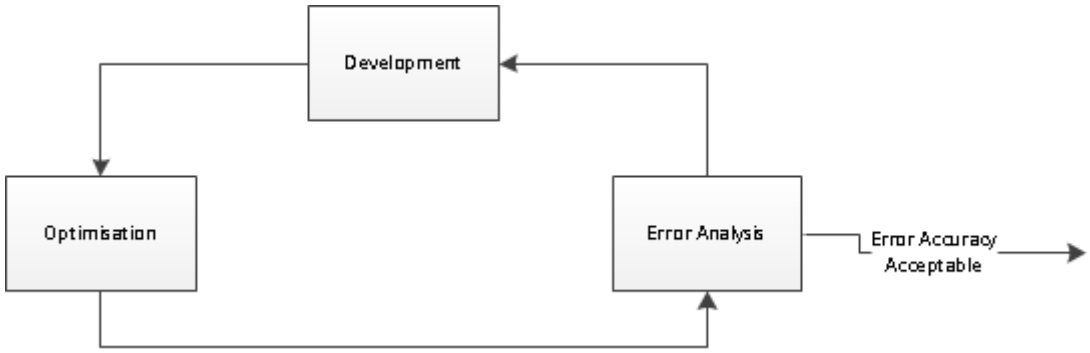

Figure 5.2: Trial solution method adopted from [111]

5.2.1 Trial solution

On the basis of a one dimensional physical model U_x and $\tilde{U}_x$ would denote the product of known function in the model.

$$\tilde{U}_x = \Phi_0(x) + a_1\Phi_1(x) + \cdots + a_N\Phi_N(x) \tag{5.1}$$

Where $\Phi_0(x)$ is a known function, commonly termed the coordinate function. Additionally a_N is considered as undetermined coordinate function. Therefore the trial solution for $\tilde{U}_x$ would be established based on the governing differential equations and loading and boundary conditions of the model. A trial solution in its simplest format considers constant components α_N and to develop the polynomial expressed below:

$$\tilde{U}_x = a_1 + a_2x + a_3x^2 + \cdots + a_Nx^{N-1} \tag{5.2}$$

In order to correctly calculate the trial solution for an isotropic uni-axial solid, the next two sections will describe the means of achieving the governing differential equation in more detail.

5.2.2 Nodal displacement

Finite Element Analysis (FEA) in essence partitions a defined model into finite number of elements for degree of possible evaluations. One the most crucial mathematical relations as the driving force of FEA, is stiffness matrix equation. In order to understand the stiffness matrix, an understanding of governing differential equations is necessary to be able to establish and define the correct nodes, which will be explained later, based on the requirements of the model and its verifications required.

In general a three dimensional elasticity model will involve twelve components. Stress is represented by σ_x,σ_y,σ_z,τ_{xy},τ_{xz} and τ_{yz}, in this form the first three components will describe normal stress and the last three are shear stress upon an element. Additionally, there are six other components relating to the strain components of the element; of which there are three displacement components u, v and w along the global axes of the element, namely x, y and z respectively.

Therefore the stress and strain vector could be written as:

$$\text{Stress Vector:} \quad \sigma = \begin{bmatrix} \sigma_x & \sigma_y & \sigma_z & \tau_{xy} & \tau_{xz} & \tau_{yz} \end{bmatrix}^T \tag{5.3a}$$

$$\text{Strain Vector:} \quad \varepsilon = \begin{bmatrix} \varepsilon_x & \varepsilon_y & \varepsilon_z & \gamma_{xy} & \gamma_{xz} & \gamma_{yz} \end{bmatrix}^T \tag{5.3b}$$

Assuming minimal displacement and strains of nodes, partial strain displacement may be written as followed:

$$\varepsilon_x = \frac{\partial u}{\partial x} \quad , \varepsilon_y = \frac{\partial v}{\partial y} \quad , \varepsilon_z = \frac{\partial w}{\partial z} \tag{5.4}$$

$$\gamma_{xy} = \frac{\partial u}{\partial y} + \frac{\partial v}{\partial x} \quad , \gamma_{xz} = \frac{\partial w}{\partial x} + \frac{\partial u}{\partial z} \quad , \gamma_{yz} = \frac{\partial v}{\partial z} + \frac{\partial w}{\partial y}$$

Therefore for a linear elastic material behaviour, the relation between stress and strain could be stated as:

$$\sigma = \mathbf{S}\varepsilon$$

As a result for an isotropic material, the matrix could be written as [112]:

$$\mathbf{S} = \frac{E}{(1+\nu)(1-2\nu)} \begin{bmatrix} 1-\nu & \nu & \nu & 0 & 0 & 0 \\ \nu & 1-\nu & \nu & 0 & 0 & 0 \\ \nu & \nu & 1-\nu & 0 & 0 & 0 \\ 0 & 0 & 0 & 0.5-\nu & 0 & 0 \\ 0 & 0 & 0 & 0 & 0.5-\nu & 0 \\ 0 & 0 & 0 & 0 & 0 & 0.5-\nu \end{bmatrix} \tag{5.5}$$

Where E and ν, are the Young's modulus and Poisson's ratio, respectively.

In order to construct the correct finite element equation for a three dimensional elasticity, a potential energy functional should be derived.

$$\text{Potential Energy Functional:} \quad W_p(u,v,w) = U - W_s \tag{5.6}$$

Where the strain energy is represented by U and work done through application of load is represented as W_s.

Further the volume integral of strain and surface integral of applied load could be written by means of traction components, along each axes. Therefore the governing volume integral of strain could be written as:

$$U = \frac{1}{2}\iiint_{volume} \varepsilon^T \sigma \, dV = \frac{1}{2}\iiint_{volume} \varepsilon^T \mathbf{S}\varepsilon \, dV \tag{5.7}$$

Assuming traction components have the same direction as the applied force, then:

$$W_s = \iint (T_x u + T_y v + T_z w)\, dS \tag{5.8}$$

Based on figure 5.3, a trial solution may be written as the finite element equation for the parent element shown in (b).

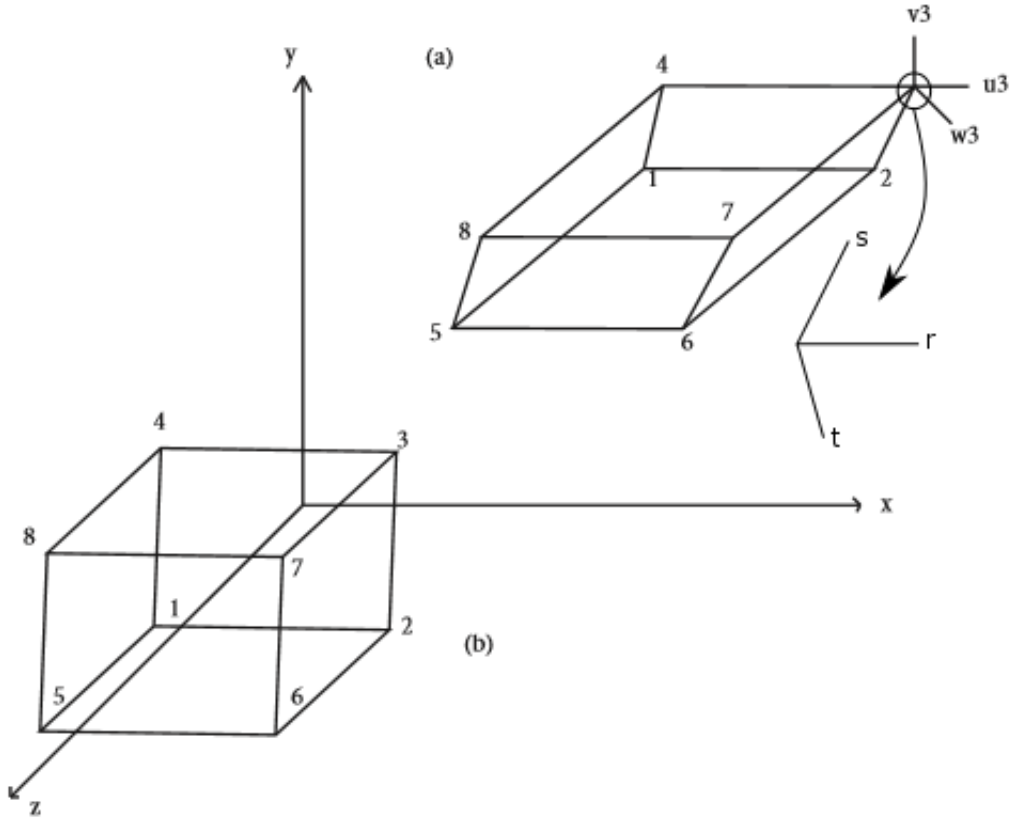

Figure 5.3: Eight node hexahedral element, (a) actual element, (b) parent element

$$\begin{Bmatrix} u \\ v \\ w \end{Bmatrix} = \begin{bmatrix} N_1 & 0 & 0 & N_2 & 0 & 0 & \cdots & N_8 & 0 & 0 \\ 0 & N_1 & 0 & 0 & N_2 & 0 & 0 & \cdots & N_8 & 0 \\ 0 & 0 & N_1 & 0 & 0 & N_2 & 0 & 0 & \cdots & N_8 \end{bmatrix} \begin{Bmatrix} u_1 \\ v_1 \\ w_1 \\ \cdots \\ u_8 \\ v_8 \\ w_8 \end{Bmatrix} = \mathbf{N}^T\mathbf{d} \quad (5.9)$$

By applying Lagrange interpolation to the shape function denoted as $\mathbf{N}$, the new shape function may be expressed as different nodes in co-ordinates r, s and t for every element in any model.

$$N_i = \frac{1}{8}(1 + rr_i)(1 + ss_i)(1 + tt_i) \qquad i = 1, \cdots, 8 \quad (5.10)$$

Based on the concept above we can develop the partial derivatives with reference to u,v and w, which will form the following Jacobian matrix for our hexahedral element in figure 5.3 (a).

$$\begin{Bmatrix} \frac{\partial u}{\partial r} \\ \frac{\partial u}{\partial s} \\ \frac{\partial u}{\partial t} \end{Bmatrix} = \begin{bmatrix} \frac{\partial x}{\partial r} & \frac{\partial y}{\partial r} & \frac{\partial z}{\partial r} \\ \frac{\partial x}{\partial s} & \frac{\partial y}{\partial s} & \frac{\partial z}{\partial s} \\ \frac{\partial x}{\partial t} & \frac{\partial y}{\partial t} & \frac{\partial z}{\partial t} \end{bmatrix} \begin{Bmatrix} \frac{\partial u}{\partial x} \\ \frac{\partial u}{\partial y} \\ \frac{\partial u}{\partial z} \end{Bmatrix} = \mathbf{J} \begin{Bmatrix} \frac{\partial u}{\partial x} \\ \frac{\partial u}{\partial y} \\ \frac{\partial u}{\partial z} \end{Bmatrix} \tag{5.11}$$

Irrelevant to nodes used to describe any element, same approach can be carried for variable number of nodes for description of the element distortion due to applied force to the nodes.
Based on equation 5.11, strain may be computed according to partial derivatives of displacement components; that is displacement of x,y and z with respect to r,s and t(see figure 5.3).

Further equation 5.11, could be used as an inverse matrix function, which would in turn be used against the shape function 5.9. It follows:

$$\begin{Bmatrix} \frac{\partial u}{\partial x} \\ \frac{\partial u}{\partial y} \\ \frac{\partial u}{\partial z} \end{Bmatrix} = \mathbf{J}^{-1} \begin{bmatrix} \frac{\partial N_1}{\partial r} & 0 & 0 & \frac{\partial N_2}{\partial r} & 0 & 0 & \cdots & \frac{\partial N_8}{\partial r} & 0 & 0 \\ \frac{\partial N_1}{\partial s} & 0 & 0 & \frac{\partial N_2}{\partial s} & 0 & 0 & \cdots & \frac{\partial N_8}{\partial s} & 0 & 0 \\ \frac{\partial N_1}{\partial t} & 0 & 0 & \frac{\partial N_2}{\partial t} & 0 & 0 & \cdots & \frac{\partial N_8}{\partial t} & 0 & 0 \end{bmatrix} \begin{Bmatrix} u_1 \\ v_2 \\ \cdots \\ w_8 \end{Bmatrix} = \begin{bmatrix} \mathbf{B}_{ux}^T \\ \mathbf{B}_{uy}^T \\ \mathbf{B}_{uz}^T \end{bmatrix} \mathbf{d} \tag{5.12}$$

The equation 5.12 could now describe the nodal displacement based on the global axes with the help of partial derivatives, as a result same matrix formats could be derived for an isotopic elastic material for the other two directions.

Additionally, global strain of the element could be expressed with respect to its nodal displacements.

$$\begin{Bmatrix} \varepsilon_x \\ \varepsilon_y \\ \varepsilon_z \\ \gamma_{xy} \\ \gamma_{yz} \\ \gamma_{zx} \end{Bmatrix} = \begin{Bmatrix} \dfrac{\partial u}{\partial x} \\ \dfrac{\partial v}{\partial y} \\ \dfrac{\partial w}{\partial z} \\ \dfrac{\partial u}{\partial y} + \dfrac{\partial v}{\partial x} \\ \dfrac{\partial v}{\partial z} + \dfrac{\partial w}{\partial y} \\ \dfrac{\partial w}{\partial x} + \dfrac{\partial u}{\partial z} \end{Bmatrix} = \begin{bmatrix} 1 & 0 & 0 & 0 & 0 & 0 & 0 & 0 & 0 \\ 0 & 0 & 0 & 0 & 1 & 0 & 0 & 0 & 0 \\ 0 & 0 & 0 & 0 & 0 & 0 & 0 & 0 & 1 \\ 0 & 1 & 0 & 1 & 0 & 0 & 0 & 0 & 0 \\ 0 & 0 & 0 & 0 & 0 & 1 & 0 & 1 & 0 \\ 0 & 0 & 1 & 0 & 0 & 0 & 1 & 0 & 0 \end{bmatrix} \begin{Bmatrix} \partial u/\partial x \\ \partial u/\partial y \\ \partial u/\partial z \\ \partial v/\partial x \\ \partial v/\partial y \\ \partial v/\partial z \\ \partial w/\partial x \\ \partial w/\partial y \\ \partial w/\partial z \end{Bmatrix} \tag{5.13}$$

After evaluating the strain of nodal displacements for the element. The stiffness matrix could be derived by means of substituting the strain into strain energy expression discussed earlier (equation 5.7). In the expression below **k** is the stiffness matrix.

$$U = \frac{1}{2}\iiint_{volume} \varepsilon^T \mathbf{C} \varepsilon \, dV = \frac{1}{2}\mathbf{d}^T \iiint_{volume} \mathbf{B}\mathbf{C}\mathbf{B}^T dV \, \mathbf{d} = \frac{1}{2}\mathbf{d}^T \mathbf{k} \mathbf{d} \tag{5.14}$$

$$\mathbf{k} = \iiint_{volume} \mathbf{B}\mathbf{C}\mathbf{B}^T dV = \int_{-1}^{1}\int_{-1}^{1}\int_{-1}^{1} \mathbf{B}\mathbf{C}\mathbf{B}^T det\mathbf{J} \, drdsdt \tag{5.15}$$

As it was shown the matrix **B** in equation 5.12 is not a constant. Therefore individual elements would be assessed for usage in the stiffness matrix. The most common mathematical model for assessing individual terms with a stiffness matrix is implementation of Gaussian integration [112].

5.2.3 Pre-stressing and thermal effect

The model created in ABAQUS was defined with thermal effect simulation as well as nodal displacement. In section 5.2.2 attention was given to the role nodal displacement plays in defining the governing differential equation and the description of stiff matrix was provided.

In this section the aim is to provide the general assembly of thermal effect and pre-stressing of the element.

As expected change in temperature will lead to a linear relation for expansion of the solid, on the assumption of an elastic response. As a result of linear expansion of the solid, associated strain components will in turn be changed. However, shear will be the only components unaffected by change in temperature as they lie normal to the expansion. Therefore, the change in strain based on fluctuation of temperature ΔT is given in the equation below where α is coefficient of thermal expansion

$$\varepsilon_0 = \begin{bmatrix} \alpha\Delta T & \alpha\Delta T & \alpha\Delta T & 0 & 0 & 0 \end{bmatrix}^T \tag{5.16}$$

Additionally, plane stress and strain may be expressed for sheet and circular test pieces as:

$$\text{Plane Stress:} \qquad \varepsilon_0 = \begin{bmatrix} \alpha\Delta T & \alpha\Delta T & -\nu\alpha\Delta T \end{bmatrix}^T \tag{5.17}$$

$$\text{Plane Strain:} \qquad \varepsilon_0 = (1+\nu)\begin{bmatrix} \alpha\Delta T & \alpha\Delta T & 0 \end{bmatrix}^T \tag{5.18}$$

Pre-stressing is denoted as σ_0, which signifies an initial unknown stress in the body. The expression below, describes the relation between stress, strain and pre-stress. However, it should be noted the actual stress developed in the solid is a result of strain development due to defined model constraints.

$$\sigma = \mathbf{C}(\varepsilon - \varepsilon_0) + \sigma_0 \tag{5.19}$$

Where $\mathbf{C}$ is the stiffness matrix the concept explained above, would result in determining the strain energy of the solid due to pre-stressing as a result of change in temperature. Therefore:

$$U = \frac{1}{2}\iiint_{volume} (\varepsilon - \varepsilon_0)^T \mathbf{C}(\varepsilon - \varepsilon_0)\, dV + \iiint_{volume} (\varepsilon - \varepsilon_0)\sigma_0\, dV \tag{5.20}$$

In order to differentiate the term above, we can neglect constants when making appropriate substitutions for plane stress, strain and displacement. The strain energy then can be summed as [112]:

$$U = \frac{1}{2}\mathbf{d}^T\mathbf{k}\mathbf{d} - \mathbf{d}_{\varepsilon_0}^{\mathbf{TQ}} + \mathbf{d}^T\mathbf{Q}_{\sigma_0} \tag{5.21}$$

It worth noting, introducing pre-stress and pre-straining into our system will affect our plane stiffness matrix **k**.

5.2.4 Trial solution optimization

As illustrated in figure 5.2 developing a trial solution would require adjusting the accuracy by means of reducing the error between the approximated solution to the exact solution. There are few methods of optimising the trial solution, two of these methods are namely:

1. (**MWR**): Method of Weighted Residual
2. (**RVM**): Ritz Variational Method

The MWR methods could be applied in partnership with other methods such as least squares or in particular Galerkin function. The means of approximating through MWR is to more pertinent when the solution is developed as a differential polynomial. In order to optimize the solution MWR minimises a single expression in the trial polynomial; whereas RVM tends to minimize a physical quantity in relation to the trial solution [113].

Additionally in order to be able to make use of the optimization methods, error analysis of the FE needs to be understood before conducting the parametric tests of the experimented samples.

Inherently there are two categories of possible error analysis, either physical where the problem is developed appropriately or the model is flawed. Physical problems within broader prospect could arise from a number of sources, such as:

- Boundary conditions are not simplified
- Unsuitable materials definition
- Temperature rate not adequately defined
- Solution is time dependant

- Unknown parameter cannot be isolated
- loading conditions contradict one another

Whereas flaws in model definition could be due to:

- Inconsistent units throughout the model
- Mesh cannot comply with the model created accurately
- Element becoming distorted due coarse meshing
- Boundary conditions negate one another
- Geometry not defined properly
- Mesh option not being suitable to the trial solution
- Plasticity not defined correctly
- Lack of accuracy in increment definition

5.3 Modelling Variables

5.3.1 Elements

As previously discussed, FEA works by means of integrating a model. However, if integration is too much or too little inaccuracies will arise, where areas of high stress will not be adequately estimated. In general every element is surrounded by nodes which would outline its borders. Additionally, nodes will be used for defining the degree of freedom of model. Moreover, as demand for accuracy within a simulation increases, nodes can be altered to reflect that freedom. They can be placed on the surface and inside of an element rather than being placed at the corners. Such technique can be used in higher order governing differential equations. [114]

Due to nature of this study where low strain rate and temperature variation is studied, considering the correct element is essential. A general practice is to

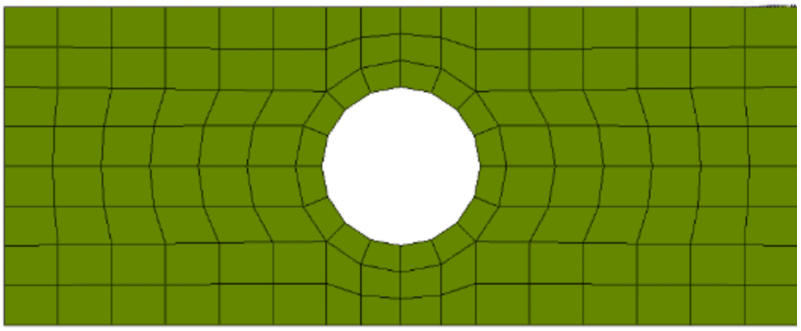

(a) 1^{st} order, 4 noded model

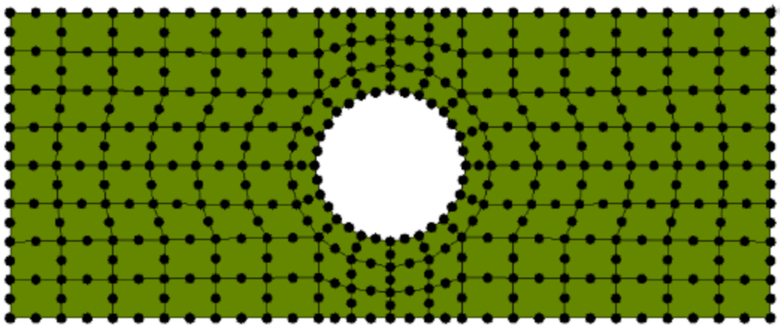

(b) 2^{nd} order, 8 noded model

Figure 5.4: Quadrilateral element arrangement

increase the order of the element's displacement function from linear to quadratic and to cubic by the increase of strain within the deformation needed to be examined.

As can be seen in Figure 5.4, by changing the element from linear 5.4a to 2^{nd} order 5.4b, the geometry of the elements can be refined further. Quadratic elements are better for following a curve compared to a linear element. Linear model could be adjusted to follow a curve to improve its accuracy, however the compromise would be in it involves much more computing time.

A comprehensive element study is required prior to defining the appropriate element option and carrying out a mesh convergence for experimental samples. The model created in this element study was changed for better understanding of element behaviour around a circle as stress concentration is more evident around curves and sharp corners. The study conducted here will also assist in better understanding the stress concentration factor in our experimental uni-axial, dog bone samples.

In this study a plate of length 200 mm to width of 40 mm with uniform thickness

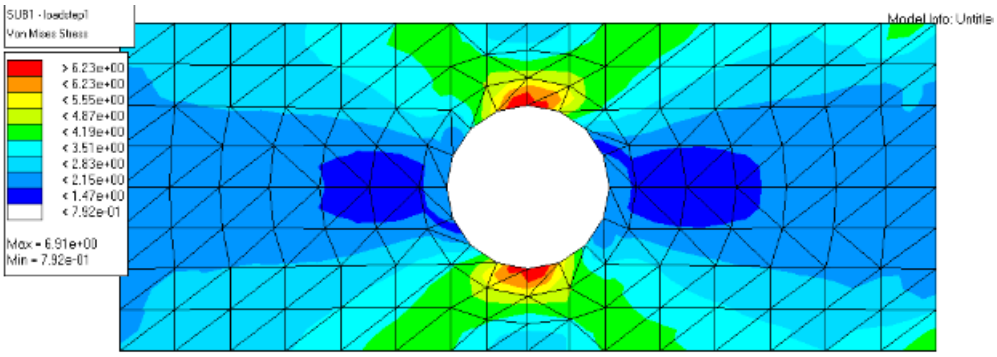

Figure 5.5: Triangular element 2^{nd} order 6 noded model

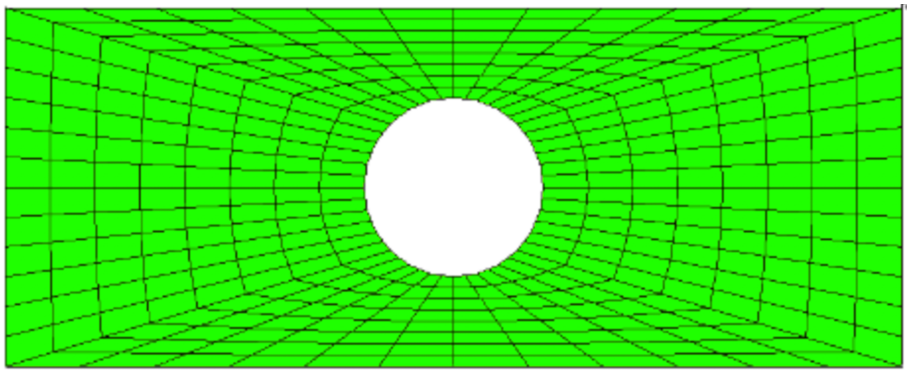

Figure 5.6: Quadrilateral element 4 noded model

was considered and circular hole was created in the middle of the plate with a dimension of 20mm. For this study the exact solution for when the plate is subjected to 900N was considered and determined to be 8.46 MPa.

In each stage after first round of elements are designed a hyper-meshing sequence is carried out, in which the spline technique mapped meshing etc are examined. Additionally the only variable considered is Von-Mises stress.

In general triangular elements figure 5.5 tend to provide better results, however the computation cost increases. Another down side of a triangular element could be due to its stiffness in which it cannot make accurate predictions of model displacement. In models in which displacement conditions have based upon a 2^{nd} order triangular element could result in a high accuracy.

Quad mesh elements figure 5.6, otherwise known as mapped meshes, are extremely useful in CFD analysis since they are not required to continuously deform as they do in structural models since they follow the Eulerian mathematical technique. Hence they are not the most suitable element option when dealing with

Element	Mesh Type	Displacement (mm)	Stress (MPa)
QUAD4	COARSE	0.146e-2	5.47
QUAD4	FINE	0.159e-2	7.14
QUAD4	COARSE RULED	0.092e-2	5.76
QUAD4	FINE RULED	0.108e-2	7.46
QUAD4	COARSE ATM	0.096e-2	5.07
QUAD4	FINE ATM	0.12e-2	6.27
QUAD8	COARSE	0.172e-2	5.49
QUAD8	FINE	0.169e-2	7.18
TRI3	COARSE	0.153e-2	7.13
TRI3	FINE	0.14e-2	7.67
TRI6	COARSE	0.163e-3	6.89
TRI6	FINE	0.168e-2	8.01
HEX8	COARSE	0.152e-2	6.76
HEX8	FINE	0.150e-2	7.32
TETRA4	COARSE	0.14e-2	7.89
TETRA4	FINE	0.139e-2	8.40
TETRA10	COARSE	0.165e-2	7.53
PENTA6	COARSE	0.175e-2	7.37

Table 5.1: Element configuration results

structural analysis.

In sudden impact tests the mesh sizes tend to be bigger as it would prohibit the time step issues which would arise from the size of elements. However, for the majority of element configurations, mesh sizes profit when taken as small as possible, especially around the regions with higher stress factors. The table 5.1 summarises the mesh choice study carried out.

As a result of table 5.1, quadrilateral elements tend to under predict the exact value, however they have a more agreeable nodal displacement predictions compared to a tetrahedral element, although a tetrahedral element would predict the stress of a structure better. Additionally, the ruled mesh both under predicts and over

predicts the stress and displacement respectively. This issue as stated before could make this element a better option for CFD models. If one is to make use of quadrilateral element for solving a structural model, it can be done by calibrating the stress level to extrapolate the final result to the exact solution.

Another point to take from this table is that by increasing the number of nodes in a quadrilateral element, stress will not alter much difference, whereas the displacement prediction will improve.

Improved stress and displacement predictions were observed with a triangular element. However the computational time required was increased as more variables were introduced to refine the model further. Therefore, the decision is made to refrain from using this element.

As a result the element Quad4 of ABAQUS which is plane stress element was opted. The model was developed in a non linear finite element code for the purpose of evaluation. Prior to developing the code for predicting the material stress strain curve, a parametric study was carried out to verify the results. The model was set-up as a 2D planar shell model with different thicknesses to match the requirements of the samples. The 3D model was employed in its 2D planar shell option, giving results suitable for our purpose of predicting a curve of material flow behaviour [114]. Additionally, this element will assist by shortening the simulation time, which for the volume of simulations carried out will be advantageous.

5.3.2 Meshing

Meshing the model and choosing adequate number of elements in a model is of paramount importance if one is to obtain accurate results in the shortest amount of time. First, the model needs to be created, since the clampes are holding the specimen and would act to defy any loadings and deformation, the model was created based on figure 5.7. This technique will also enable the model to require less elements.

Time	Deflection
0	0
0.001	0.048
0.002	0.1065
0.003	0.1515
0.004	0.21
⋮	⋮
0.545 (a)	23.80

Table 5.2: Time parameter definition, (a) maximum deflection

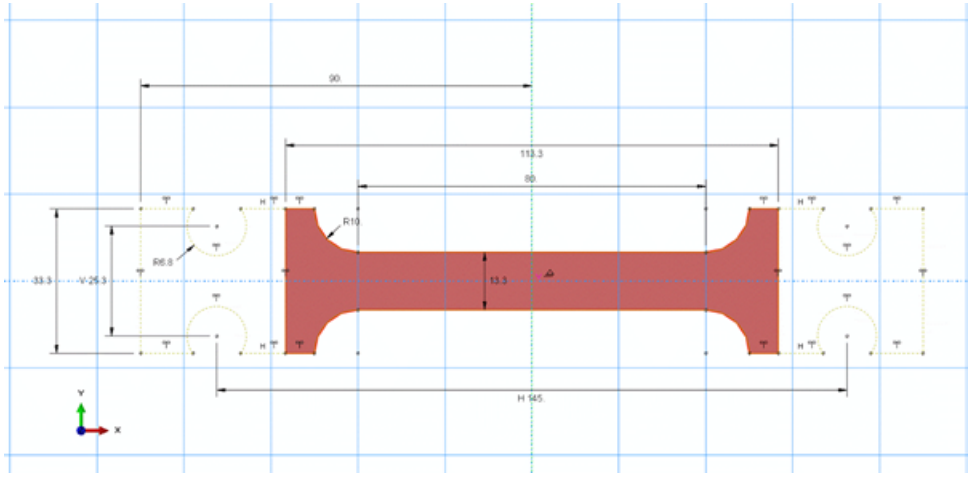

Figure 5.7: Model created for simulation analysis

Since the model has to enable plasticity to occur, a deformable model was chosen as the basis. Further, the ratio of the length to width is calculated to be 1/15, a shell model was chosen, which enables the model to produce faster result without interfering with accuracy.

The experimentally tested samples are loaded axially, therefore the model should prohibit any bending, as a result a solid section was opted for the model. Further since the instantaneous deflections was produced by the acquisition system whilst conducting the experiment. Although as cross head movement, by means of post processing the deflection values, could be used for the time parameter. The time parameter was chosen as the last increment of the maximum deflection, similar to table 5.2.

Mesh refinement should be considered, as this technique could alter the accuracy,

below in figure 5.8 are two examples of models with and without refined mesh.

As a result the optimum number of element for the geometry at hand was investigated. The elements number studied, was aimed to find the least number of element for the best accuracy. Therefore elements numbers 568,4402,8236 and 13968 were considered which resulted in the figure below.

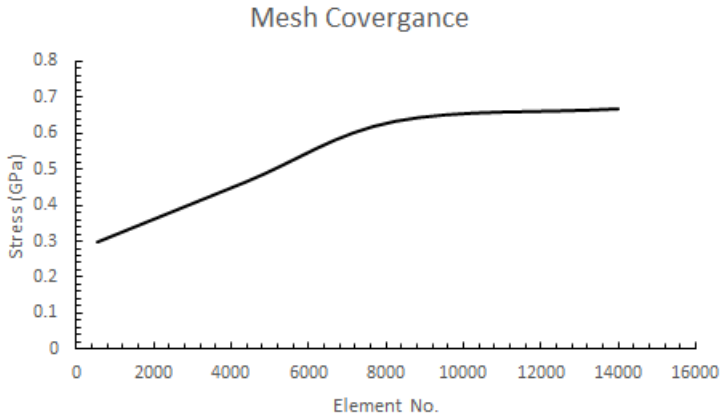

Figure 5.9: Mesh sensitivity

Based on figure 5.9, the model was developed with 8,235 elements as its is the most accurate with least element numbers. Subsequently, the element was refined by increasing the seeding numbers around the regions of interest in terms of high stress concentration. Figure 5.11 suggests the seed numbers allocated for the model.

Reduced integration was opted for this model over full integration for the effect it has on reducing computing time and storage required. However, with RI method zero energy deformation might arise, as such there are no straining components in the stiffness matrix. It can follow an effect commonly refereed to as hour glassing of the elements, in which elements will extort beyond their set limits. Therefore an additional stiffness matrix was adopted into the governing differential equation to account for this phenomenon.

The model was setup to simulate the behaviour in two stages. The first was to recognise the temperature condition of the sample, once the former was achieved the displacement was initiated. The initial displacement was developed to consider and initiate the residual slack in the clamps. Subsequently the the maximum displacement was defined through time parameters described before. However, prior to commencing the code would need time to define and account for the slack, which

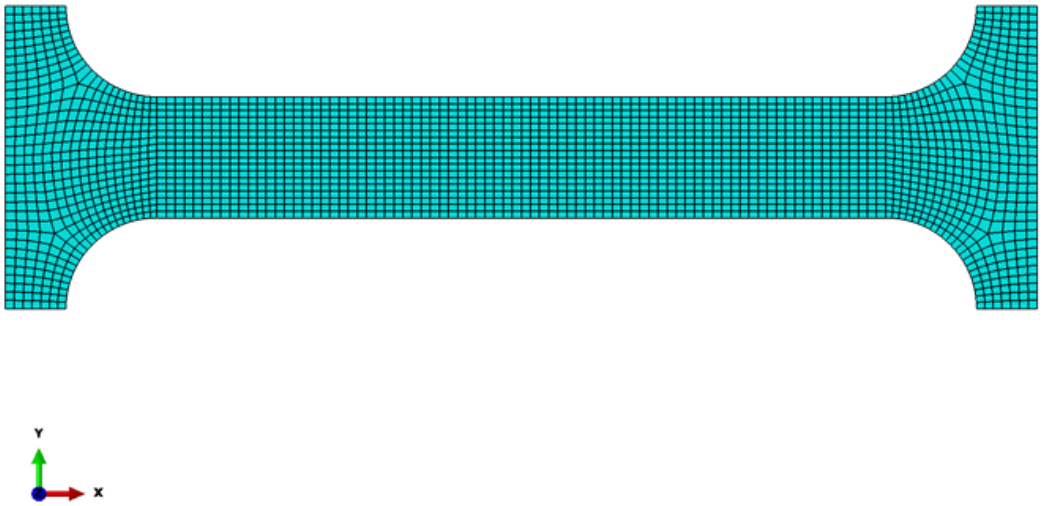

(a) Element meshed without refinement

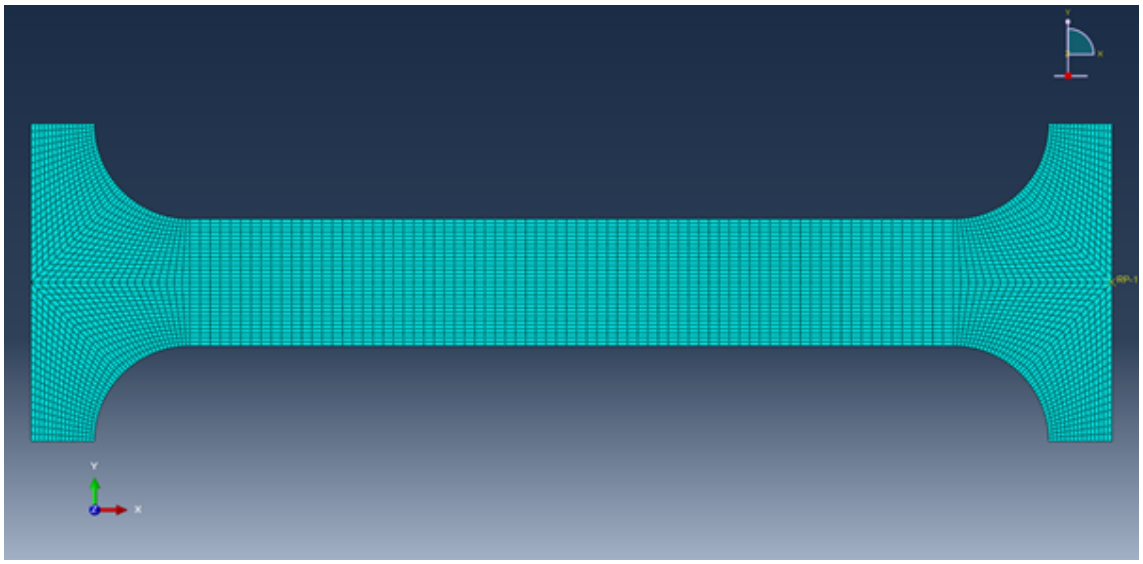

(b) Element meshed with refinement

Figure 5.8: Element mesh comparison

(a) Quarter model stress

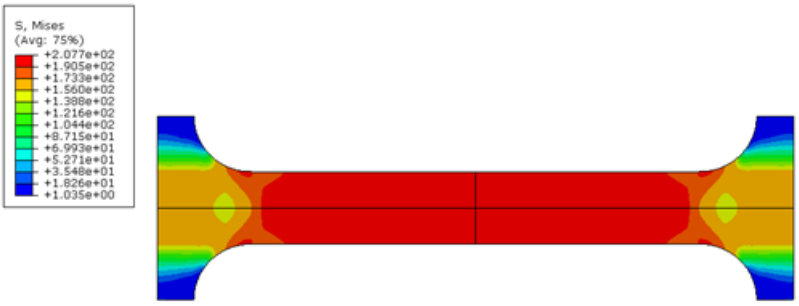

(b) Full model stress

Figure 5.10: Verifying no difference between quarter model and full model

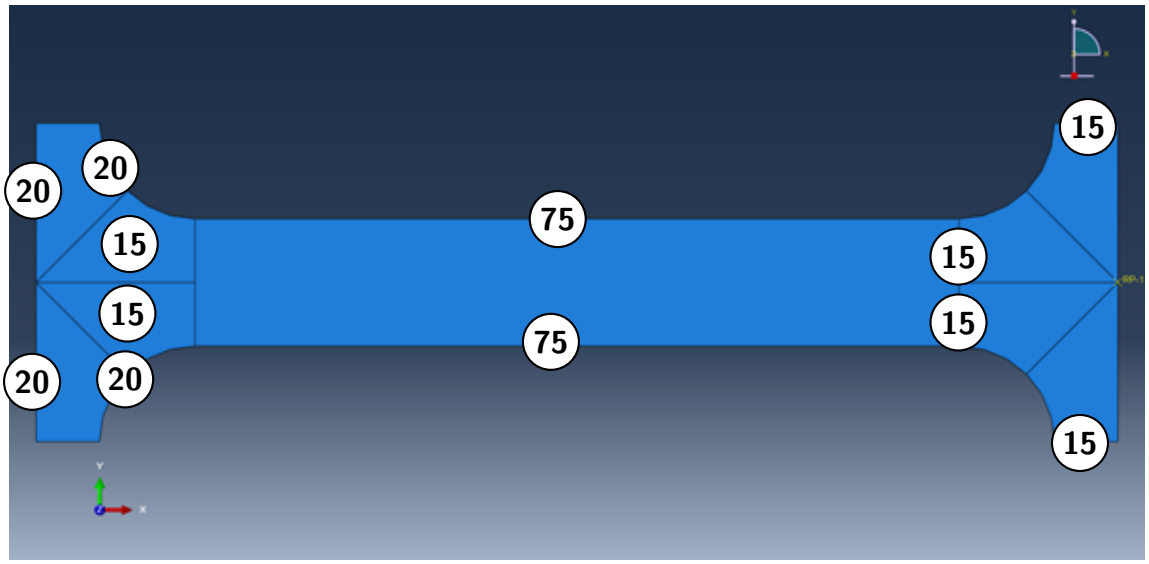

Figure 5.11: Seeding of the model based on the sectioning

would take $0.1ms$ and it would be kept constant all through out the simulation as demonstrated in figure 5.12. As one end of the specimen is stretched the other side will stay stress free, the procedure will take place for the other end. The two end of each sample from now will be refereed to as A, B. The total time required for the a full simulation cycle will be depended upon the prerequisite samples and the frequency of the material data. Therefore no fixed simulation time was calculated.

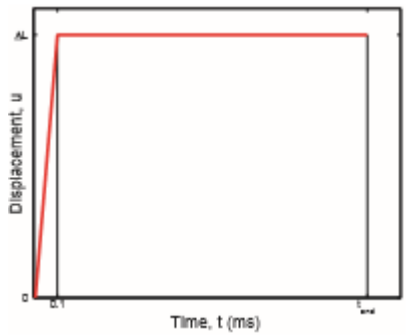

Figure 5.12: Total required for initial slacking to be remove for each end

In order to correctly measure the strain rate, a slight calibration was required due to the equipments available to this research, displacement was defined by the expression below:

$$\Delta L = \varepsilon_{AB} L_{AB} = \frac{N}{EA} L_{AB} = \frac{N L_{AB}}{EA} \tag{5.22}$$

Where E is the Young's modulus, A is the Cross sectional area, N is the force applied and ε_{AB} is the strain.

Where the apllied force N, is expressed as:

$$N = 2AE\varepsilon_{in} \tag{5.23}$$

Where the term ε_{in} is the strain at the instability point of the material.By means of substituting the two expressions 5.23 and 5.22, a third equation could be derived in which nodal diplacmenet could be determined based on strain at the point of instability and length of the specimen.

$$\Delta L = 2L_{AB}\varepsilon_{in} \tag{5.24}$$

As a result the above equation assists in determining the strain with less than 2% in accuracy when being compared against experimental data. This method of verification, enabled to accurately predict the experimental results to the point of instability. As for elongating and predicting the exact point of strain over the instability point, a subroutine module was created.

5.3.3 Material model

An important requirement for an accurate result is correct material behaviour. Depending on the sort of analysis, a material behaviour could be chosen in ABAQUS. Based on the parametric study carried three separate modules were chosen for the elastic, plastic and damaged behaviour. Therefore, referring to the experimental data, standard data was chosen for each section of the material behaviour. It is worthwhile mentioning the units used in ABAQUS were based on GPa and mm. The parametric study was conducted in order to investigate the accuracy of prediction based on material, empirical and computational models.

Additionally, the plastic region was developed by defining its first strain value as zero, the reason for such adaptation is due recognising the plastic behaviour is developed once the yield stress has surpassed, and an initial point of data is required.

Damage behaviour was created based on FLSD (Forming Limit Stress Diagram) technique, since it was deemed the most appropriate method of damage simulation on sheet metals [100]. This method has the advantage of enabling the user to make use of temperature variation in damage behaviour. In order to make use of FLSD technique, Minor and Major stress and strain values of the experimental results are required. Below are examples of such values for 1mm 0.13% C-steel carried at 6.09×10^{-4}.

- Major Principal Stress: 347.92 MPa
- Minor Principal Stress: 305.98 MPa

Additionally the Johnson-Cook model available in ABAQUS was used, in order to make a comparison between the readily available FLSD and the J-C model. As discussed previously the parameters to run a J-C model were established by means of least squares method. Table below provides the J-C Parameters for the Aluminium AA6063 at ambient temperature and $6.09 \times 10^{-4} s^{-1}$.

Alloy	A	Q_1	C_1	Q_2	C_2	C	m
AA6063	46.52	45.12	3.47	27.30	51.98	2.20e-14	5

Table 5.3: Johnson-Cook values for AA6063 at ambient temperature and $6.09 \times 10^{-4} s^{-1}$

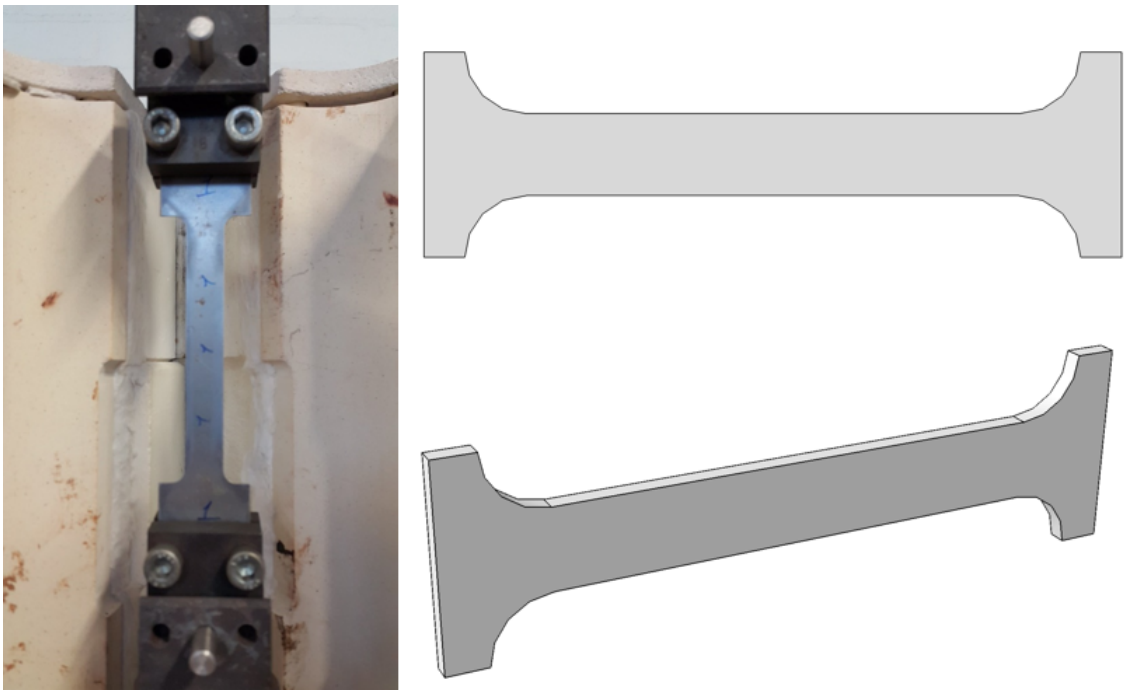

Figure 5.13: 3D and 2D model based on experimental setup

Defining the accurate yield point in the simulation when carrying out the JC model is crucial. As a result based on the work carried by Chen et, al. [115] a yield function based on the behaviour of isotropic materials was created.

$$\sigma_{eq} = \left\{ \frac{1}{2}(|\sigma_1 - \sigma_2|)^m + |\sigma_2 - \sigma_3|^m + |\sigma_3 - \sigma_1|)^m \right\}^{1/m} \tag{5.25}$$

Where σ_1, σ_2 and σ_3 represent the principle stress and m represents the material constant. The value was set at 2, in order to comply with Von Mises function. However, if the said parameter was set as ∞, Tresca Yield function could have been drived [115].

The initial step in describing a material model, was to establish the FEA model in purely elastic behaviour. The reason of such decision was eliminating other behaviours which could prohibit accurate investigation of the behaviours.

As initial step was carried out a plastic and damage material model was defined for the model created. Figure below represent the study carried out.

As can be seen, defining material models with a FEA program although to some extend can predict the behaviour, is not the optimal solution. In all the cases from figure 5.14 to 5.19 the elastic flow of the material could be predicted with accuracy.

However the problem arises with introducing plasticity and damage into the model. Damage was defined in order to comply with necking behaviour of the samples. Figure 5.17 is a great example of adopting a common damage definition with FEA models. As deformation reaches instability point the strain cannot be simulated by the model any further. The erratic behaviour of this figure in damage recognition manages to suggest higher strain rate are more accurate, as lower strain rate values cannot be predicted accurately.

5.3.4 Boundary condition

In order for the model to simulate the experimental setup, an accurate description of the surrounding physical conditions, commonly known as boundary conditions has to be prescribed. Demonstrated below is the 3D and 2D model based on the experimental setup.

As with the experimentation, the upper end of the sample was fixed and the lower end was displaced by means of a screw driven machine. Therefore for the FEA model same conditions were drawn. Figure 5.20 represents the model's boundary conditions.

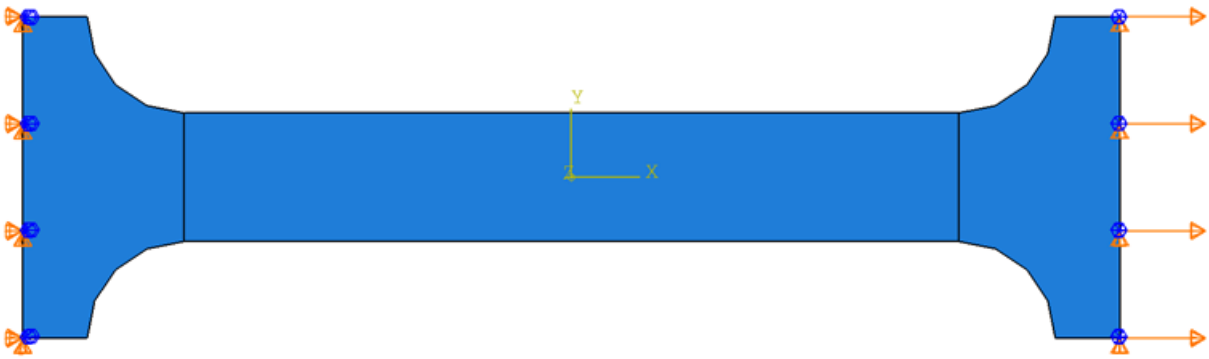

Figure 5.20: Boundary conditions of the simulated model

In this instant the upper end was fixed by three principal axes, whereas the lower end was only constraint in y axis and displacement was permitted in x direction; to ensure uni-axiallity of the model.

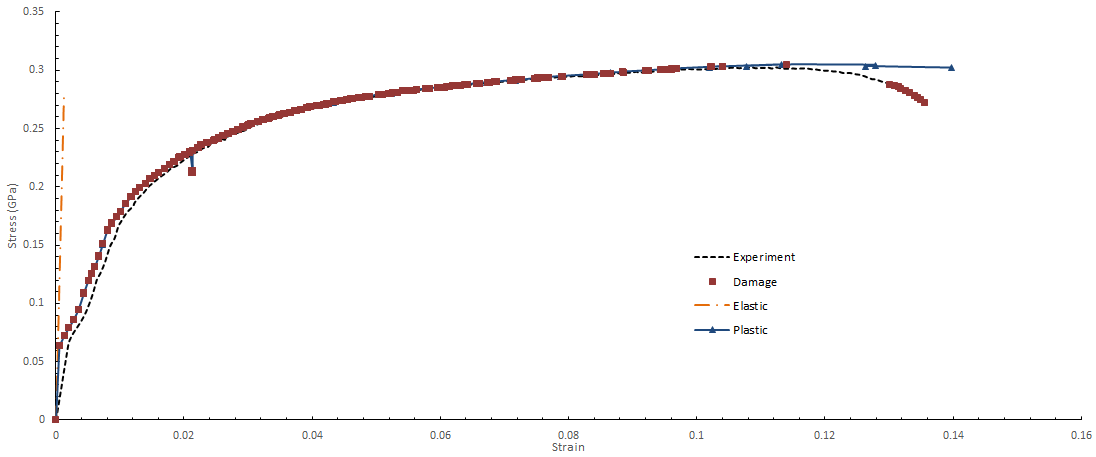

Figure 5.14: Parametric material modelling for 0.13% C-steel at $1mm-3mm/min-350°C$

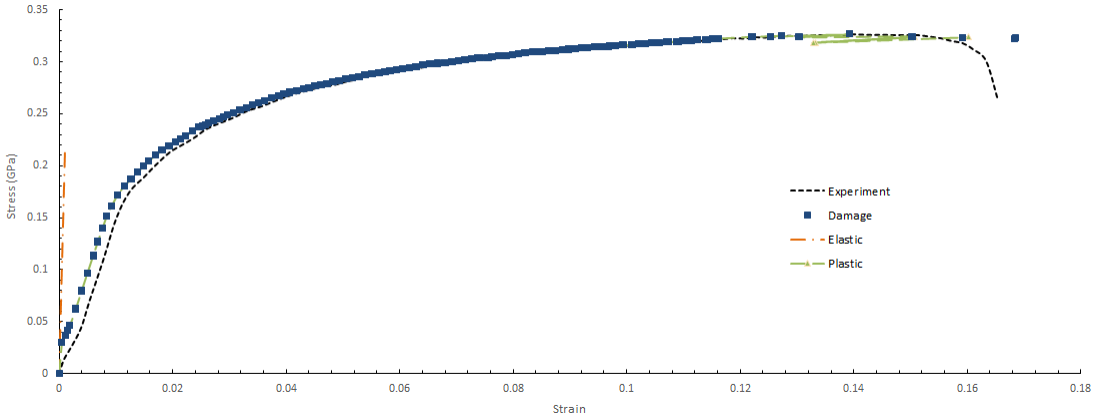

Figure 5.15: Parametric material modelling for 0.13% C-steel at $1mm - 90mm/min - 350°C$

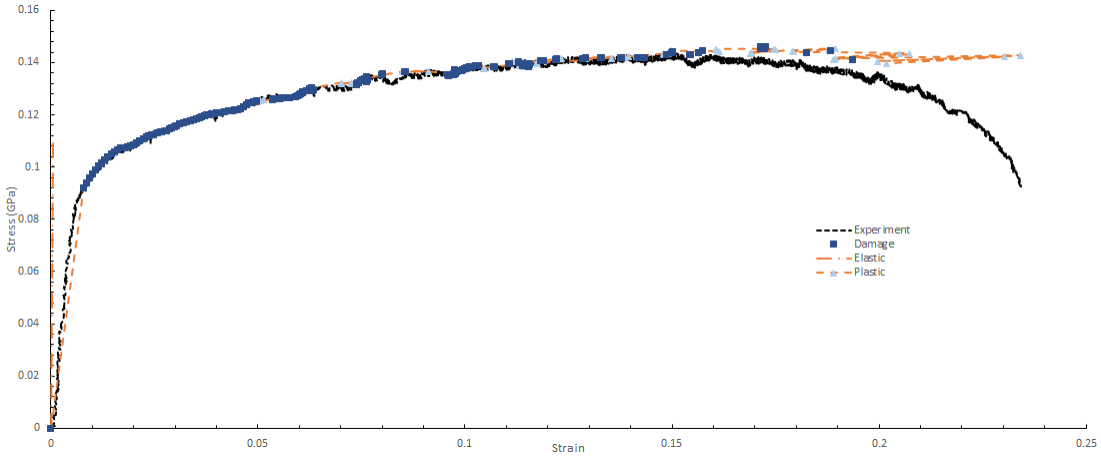

Figure 5.16: Parametric material modelling for 0.13% C-steel at $06mm - 0.3mm/min - 500°C$

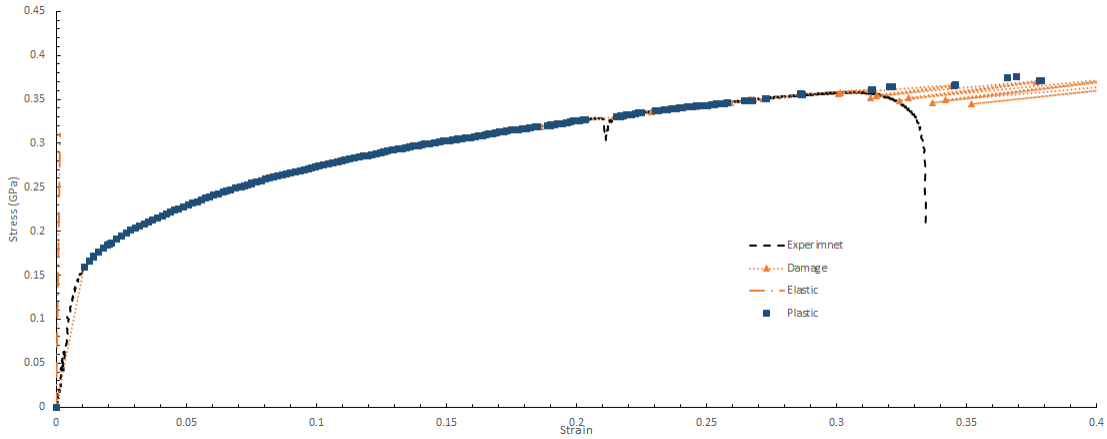

Figure 5.17: Parametric material modelling for 0.13% C-steel at $0.9mm - 0.3mm/min - 23°C$

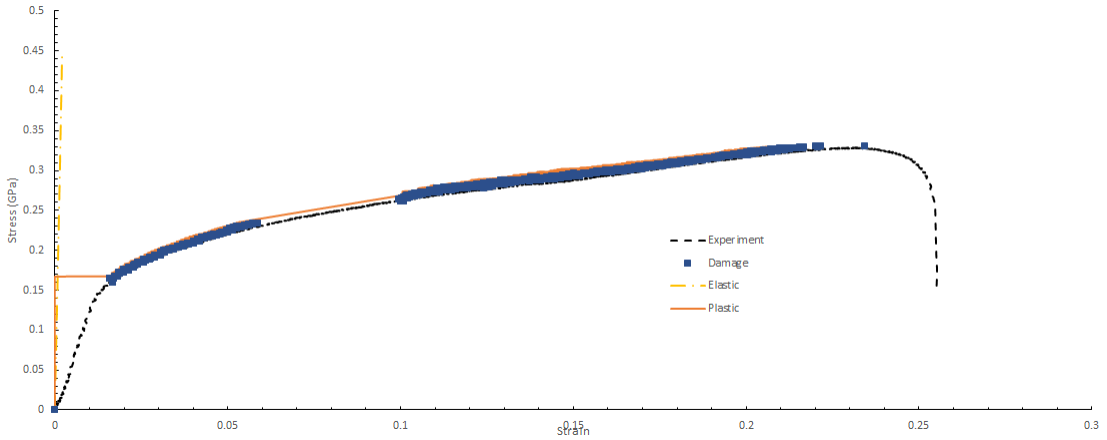

Figure 5.18: Parametric material modelling for 0.13% C-steel at $1.3mm - 0.3mm/min - 300°C$

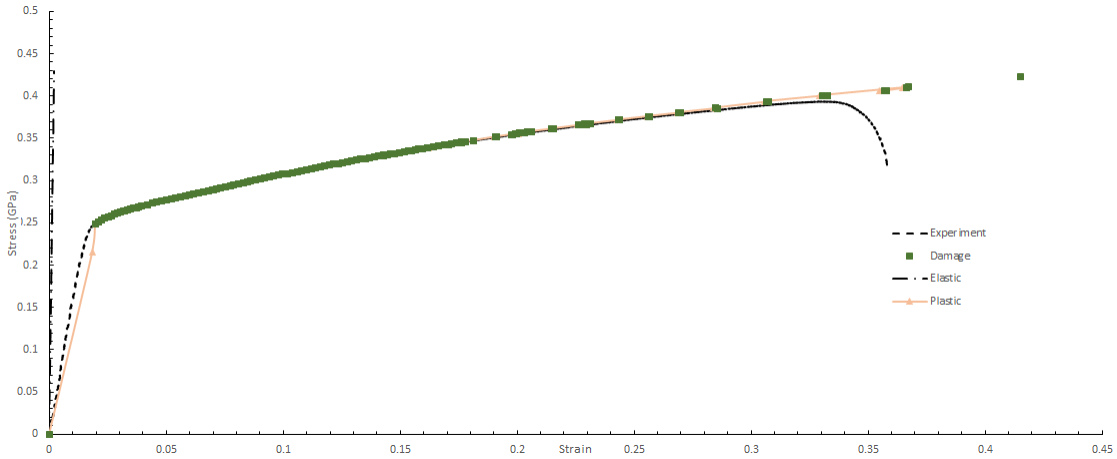

Figure 5.19: Parametric material modelling for 0.13% C-steel at $2.8mm - 0.3mm/min - 23°C$

5.4 Necking Elongation

The tensile experiments carried out and explained in the last two chapters, signified elongation to failure will increase with increase of strain rate. As such, a study on quasi-static regime was conducted to further investigate the findings.

Elmagd etal [116], concluded the additional elongation with increase of strain rate, increases the strain rate hardening in the necked region. Subsequently the necked region will diffuse along the gauge length. For this investigation, localised strain rate was compared to the nominal strain rate along the gauge length. As can be seen in figure 5.21, the necking occurs over a distance of $0.89mm$ which would gradually expands. The onset of necking can be seen over a distance of $1.50mm$. Movement of the region reduces to zero at the stationary side of the of sample, whilst the other side accelerates. A set of nodes were chosen over the region, where the relative velocity assisted in defining the strain rate over the necked region. The neck appears numerically when the slope of the behaviour law is lower than the stress value. In explicit code the wave propagation will help by localising the neck area by creating the instability, for implicit code the localization comes from other instabilities mesh, accuracy, type of elements .

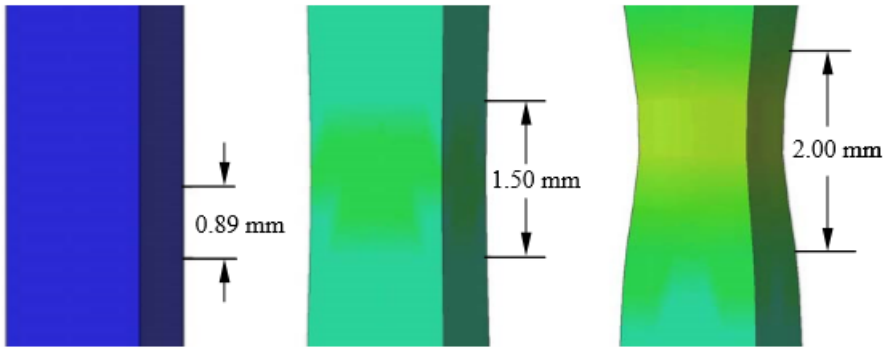

Figure 5.21: Effective plastic strain exhibiting necked region deformation

In order to better understand the effect of strain rate, dynamic strain regime of $1500s^{-1}$, was also adopted for the numerical simulation. Such strain rate could represent strain rate available in a split Hopkinson bar experiment of which samples are unifrom and needed for thin specs. The findings showed the strain rate present in the necked region increases linearly with a slight step function at higher spectrum

of nominal strain rate. Such change of behavioural function occurs at short period of time. The numerical simulation was carried out on aluminium alloy data tested, which signifies flow stress is dependent on strain rate linearly.

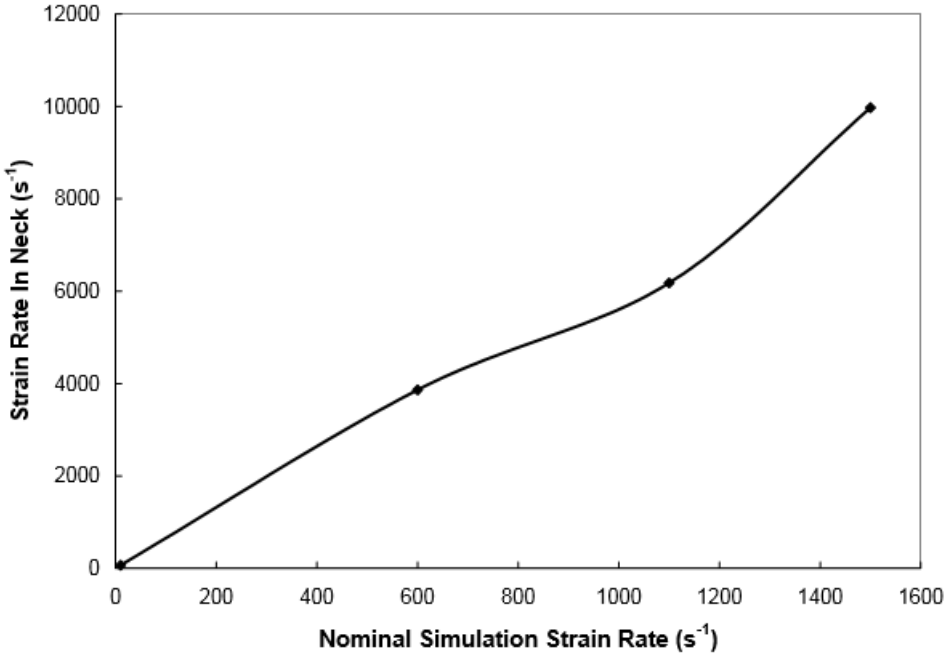

Figure 5.22: Nominal strain rate against necked strain rate based on numerical simulation

5.5 Subroutine Modelling

To this date whenever a simulation is conducted, the need for acquiring the material characteristics is paramount. In a more traditional sense the material needs to be tested in an experimental set-up and later make use of the raw data. The same issues linger as empirical formulations such as Johnson-Cook and Zerrili-Armstrong are used. Similar to table 5.3 the parameters would need to be calculated. However based on the study carried out on polynomial fitting of the stress strain curves of the materials, a new method is proposed to gradually eliminate the need for conducting experiments for the purpose of material property acquisition.

Following the findings of the coefficients depending on behavioural status of the polynomial coefficients $x_1, \cdots, x_4$ which depends upon the restrictions by the Considére effect. Tables 5.4 to 5.9 below are the coefficients based on fixed strain rate at varying temperature for carbon steel AISI1010; other tables are available in

APPENDIX.

Temperature	x_4	x_3	x_2	x_1	C
$23°C$	-44.483	40.297	-13.862	2.7645	0.1788
$300°C$	-182.96	107.1	-22.133	3.0826	0.2016
$400°C$	-336.12	145.92	-22.351	2.0823	0.1634
$500°C$	-180.49	78.734	-13.596	1.2006	0.0933
$600°C$	-437.36	153.88	-19.185	0.9996	0.0784

Table 5.4: Coefficient values for 0.6mm 0.13% C-steel at $6.09 \times 10^{-5} s^{-1}$

Temperature	x_4	x_3	x_2	x_1	C
$23°C$	-63.596	47.346	-13.408	2.1347	0.1606
$300°C$	-478.92	199	-31.121	2.9765	0.1756
$400°C$	-128.85	58.901	-11.453	1.3878	0.1415
$500°C$	-392.25	155.12	-21.302	1.1072	0.0603
$600°C$	-153	48.569	-6.0557	0.448	0.0603

Table 5.5: Coefficient values for 0.9mm 0.13% C-steel at $6.09 \times 10^{-5} s^{-1}$

Temperature	x_4	x_3	x_2	x_1	C
$23°C$	-31.259	26.457	-8.8132	1.8027	0.159
$300°C$	-454.55	226.7	-40.734	3.0806	0.1494
$400°C$	-571.79	190.17	-24.174	1.9266	0.1481
$500°C$	-69.513	27.939	-5.2781	0.3805	0.0633
$600°C$	-118.76	52.279	-9.3959	0.8208	0.0748

Table 5.6: Coefficient values for 1.1mm 0.13% C-steel at $6.09 \times 10^{-5} s^{-1}$

Temperature	x_4	x_3	x_2	x_1	C
$23°C$	-24.055	21.608	-7.7023	1.7702	0.1508
$300°C$	-242.62	125.19	-23.427	2.435	0.1606
$400°C$	-255.29	103.09	-16.292	1.5998	0.1124
$500°C$	-49.868	103.09	-16.292	1.5998	0.1124
$600°C$	-117.69	51.369	-9.214	0.7854	0.0749

Table 5.7: Coefficient values for 1.3mm 0.13% C-steel at $6.09 \times 10^{-5} s^{-1}$

Temperature	x_4	x_3	x_2	x_1	C
$23°C$	-267.78	149.42	29.643	3.0392	0.2137
$300°C$	-99.627	67.394	-15.095	2.2645	0.1915
$400°C$	-252.2	108.54	-18.047	1.629	0.1628
$500°C$	-407.96	149.08	-21.437	1.6764	0.0838
$600°C$	-214.23	86.98	-14.847	1.11968	0.0698

Table 5.8: Coefficient values for 1.9mm 0.13% C-steel at $6.09 \times 10^{-5} s^{-1}$

Temperature	x_4	x_3	x_2	x_1	C
$23°C$	-16.886	11.888	-3.63	0.9476	0.2492
$300°C$	-663.22	270.17	-40.583	3.3021	0.218
$400°C$	-480.22	172.35	-22.407	1.7182	0.1867
$500°C$	-86.829	30.917	-3.9991	0.3626	0.1373
$600°C$	-250.33	82.976	-10.583	0.5717	0.0604

Table 5.9: Coefficient values for 2.8mm 0.13% C-steel at $6.09 \times 10^{-5} s^{-1}$

In cases were a non-standard user material is required, where such models are not available through defined module in a FEA program a user defined material property module could be created. In this situation user written code could account for instability and localization phenomena. In addition to these, the model could be used to produce case by case meshing, contouring and $x - y$ plots.

The user defined material module in ABAQUS is known as UMAT for implicit analysis. For making use of such coding capability a few major parameters are required; explicit definition of stress based on Cauchy stress, rate of stress, dependence of the model to time, temperature and strain. A user defined material in ABAQUS should follow one the three integration methods if dealing with a constitutive rate equation such as this work.

1. Forward Euler

2. Backward Euler

3. Mid-point method

Forward integration method unfortunately have a stability limit, in which the maximum stability has to be defined to a value less than the elastic strain magnitude. Also the time increment must be controlled. This limitation is not present with the other two coding methods, although they required local iteration of the matrix function. In this case local iteration of the values could assist with interpolation of the coefficients.

UMAT could enable the option of user defined state variables, as well as accurate definition of stress tensor components for post processing. Internal energy of the system and deformation could be prescribed by the end user according to the test environment with ease. The UMAT code, could assign difference between the old and new arrays of information due to its structure, which makes handling of large data and subsequent runs of the code easier.

An additional method known as operator-split is adopted for this code in which the code splits into an elastic and plastic part. The benefit of such method is that it is calculating the stress tensor initially on the assumption of fully elastic behaviour. Later the algorithm is updated by the calculated stress tensor only when the yield condition is satisfied. Further, Newton-Raphson method is applied in two different scenarios. Firstly NR is used to account for over stressing of the model by influx of deformation. Secondly NR is implemented as a means of interpolation between the material coefficients. If an environmental condition had not been tested by means of interpolation new coefficients are calculated and the matrix is formed. In general the model follows the flow sequence below.

5.5.1 Elastic-plastic behaviour

This elastic part of the model is derived from Hooke's law on the basis of a quadratic strain energy function $\tau = \frac{1}{2}C_{klmn}\varepsilon_{kl}\varepsilon_{mn}$, in which the expression is described by:

$$\frac{\partial \varepsilon_{ij}}{\partial \varepsilon_{kl}} = \delta_{ij}\delta_{jl} \tag{5.26}$$

Equation 5.26 exhibits asymmetry conditions in which the stress and strain axes are not following the same path, whereas for an elastic behaviour model symmetry

has to be applied. The matrix below describes the symmetry of an isotropic elastic behaviour.

$$\begin{bmatrix} C_{1111} & C_{1122} & C_{1133} & 0 & 0 & 0 \\ & C_{2222} & C_{2233} & 0 & 0 & 0 \\ & & C_{3333} & 0 & 0 & 0 \\ & \text{Symmetry} & & C_{2323} & 0 & 0 \\ & & & & C_{1313} & 0 \\ & & & & & C_{1212} \end{bmatrix}$$

Therefore in order to restore the symmetry:

$$\frac{\partial \varepsilon_{kl}}{\partial \varepsilon_{ij}} = \frac{1}{2}(\delta_{ij}\delta_{jl} + \delta_{ij}\delta_{jk}) \tag{5.27}$$

Also for the stress tensor we can compute from the energy function as follows:

$$\sigma_{ij}(\varepsilon) = \frac{\partial \psi}{\partial \varepsilon_{ij}} \tag{5.28a}$$

$$= \frac{\partial}{\partial \varepsilon_{ij}}(\frac{1}{2}C_{klmn}\varepsilon_{kl}\varepsilon_{mn}) \tag{5.28b}$$

$$= \frac{1}{2}C_{klmn}(\frac{\partial \varepsilon_{kl}}{\partial \varepsilon_{ij}}\varepsilon_{mm} + \varepsilon_{kl}\frac{\partial \varepsilon_{mn}}{\partial \varepsilon_{ij}}) \tag{5.28c}$$

By means of substituting equation 5.27 into equation 5.28c:

$$\sigma_{ij}(\varepsilon) = \frac{1}{2}C_{klmn}(\delta_{ki}\delta_{lj}\varepsilon_{kl} + \varepsilon_{kl}\delta_{mi}\delta_{nj}) \tag{5.29}$$

$$= \frac{1}{2}(C_{ijmn}\varepsilon_{mm} + C_{klij}\varepsilon_{kl}) \tag{5.30}$$

On the basis of $C_{klij} = C_{ijkl}$, the following may be derived.

$$\sigma_{ij} = C_{ijkl}\varepsilon_{kl} \tag{5.31}$$

The elastic section of the code is associated with the assumption of strain to be fully elastic. It should be noted the σ and ε had been assigned based on stress and strain tensor. Therefore the expression below is provided:

$$\underline{C} = \lambda_L \underline{M} + 2\mu_L \underline{I} \tag{5.32}$$

In which $\underline{C}$ is the elastic tensor, $\underline{M}$ is the second order identity tensor (δ_{ij}), $\underline{I}$ is the fourth order identity tensor (eq. 5.27), and the terms μ_L and λ_L are Lamé constants. The latter could be expressed by means of Young's modulus E and Poisson's ratio ν.

$$\mu_L = \frac{E}{2(1+\nu)} \tag{5.33a}$$

$$\lambda_L = \nu \frac{E}{(1-2\nu)(1+\nu)} \tag{5.33b}$$

If the condition of fully elastic behaviour in this time step remains true i.e. $f < 0$, the result is stored for the current increment, which would result in the following.

$$\sigma_{new} = \sigma_{trial} \tag{5.34}$$

However, in cases where elastic condition is not met the equivalant plastic strain would be calculated by means of plastic multiplier $\dot{\gamma}$. After which the stress tensors would need to be adjusted since the elastic condition was incorrect.

$$\dot{\gamma} = \frac{f_{trial}}{2\mu_L \left[1 + \frac{H}{3\mu_L}\right]} \tag{5.35}$$

Where $f_{trail} = (\bar{\sigma} - \tau_y)/\bar{\sigma}$ and $\bar{\sigma}$ is the equivalent stress defined from two stress invariants J_2 and J_3.

The updated mapping would follow the stress tensor description .

$$\sigma_{new} = \sigma_{trail} - \sigma_{return} \tag{5.36}$$

The plastic stress thus could be corrected with plastic multiplier.

$$\sigma_{return} = 2\mu_L \dot{\gamma} \frac{\partial f}{\partial \sigma_{ij}} \tag{5.37}$$

Since for a uni-axial tensile test during the plastic deformation $\dot{\varepsilon}_{ii} = 0$ due to incompressibility, the remark $\bar{\varepsilon}^p = \varepsilon^p$ could be made; the equivalent plastic strain rate could be calculated.

$$\dot{\bar{\varepsilon}} = \sqrt{\frac{2}{3}\dot{\gamma}\frac{\partial f}{\partial \underline{\sigma}} : \dot{\gamma}\frac{\partial f}{\partial \underline{\sigma}}} \equiv \sqrt{\frac{2}{3}\dot{\varepsilon}_{ij}\dot{\varepsilon}_{ij}} \tag{5.38}$$

With reference to the second part of code, since the conditions of the test had to be identified irrespective to the parameters; the objective stress rate was based on the Jaumann rate of Cauchy stress analysis, where derivatives of stress are not based on the frame of reference.

In terms of isotropic elasticity the above sentence could be demonstrated from equation 5.32 as:

$$\sigma_{ij} = \lambda\delta_{ij}\varepsilon^{el}_{kk} + 2\mu\varepsilon^{el}_{ij} \tag{5.39}$$

Therefore in Jaumann rate form:

$$\dot{\sigma}^{J}_{ij} = \lambda\delta_{ij}\dot{\varepsilon}^{el}_{kk} + 2\mu\dot{\varepsilon}^{el}_{ij} \tag{5.40}$$

On the basis of integrating the above equation:

$$\Delta\sigma^{J}_{ij} = \lambda\delta_{ij}\Delta\varepsilon^{el}_{kk} + 2\mu\Delta\varepsilon^{el}_{ij} \tag{5.41}$$

Additionally, the equivalent plastic strain and yield function validation in the second stage of this code has to be corrected to account for non linearity of path. Therefore the yield function adopts stress deviators for plasticity:

$$S_{ij} = \sigma_{ij} - \frac{1}{3}\delta_{ij}\sigma_{kk} \tag{5.42}$$

Further the equivalent plastic strain was modified based on integration the rate dependent path:

$$\bar{\varepsilon}^{plastic} = \int_0^t \dot{\bar{\varepsilon}}^{plastic} dt \tag{5.43}$$

5.5.2 Interpolation

The code was aimed to make it as simple for the user as possible. As a consequence the user was provided with only three parameters to describe the environment of

the test. Table 5.10 describes the content of user interface.

Input variable	Parameter
1	Thickness
2	Strain Rate
3	Temperature

Table 5.10: User input variables

However, the environmental conditions could easily be changed according to the requirements of the test; in order to provide the code with more flexibility and expandability, an interpolation relation was defined between the coefficients. Since the coefficients apply to a path tensor between neighbouring data points, a weighted linear interpolation was chosen. The weighted technique was adopted so the closer environmental condition would have the higher effect on the generated coefficient.

$$y = y_0 \left(1 - \frac{x - x_0}{x_1 - x_0}\right) + y_1 \left(\frac{x - x_0}{x_1 - x_0}\right) \tag{5.44}$$

On the basis of this weight interpolation, an algorithm for the FORTRAN code was generated. The algorithm is presented in the figure below.

The algorithm was created in four conditional loops; for the primary loop if the chosen conditions already exist in the coefficients archive the code will bypass any interpolation and will revert to conducting the calculations. The second loop is defined for cases, were two of the three environmental parameters exist in the archive and the temperature parameter will be interpolated, the three parameters then proceed to calculations.

In cases where either thickness or strain rate do not match the archive and temperature parameter is correct/incorrect; the third loop is executed. This loop will then revert back to loop number two for measurements of temperature parameter and the final acquired coefficients are submitted for processing.

In cases where neither strain rate nor thickness exists in the archive, loop number four is executed. After adjustment to the two parameters, this loop being similar to loop number three will revert back to loop number two for possible adjustments of the temperature parameter.

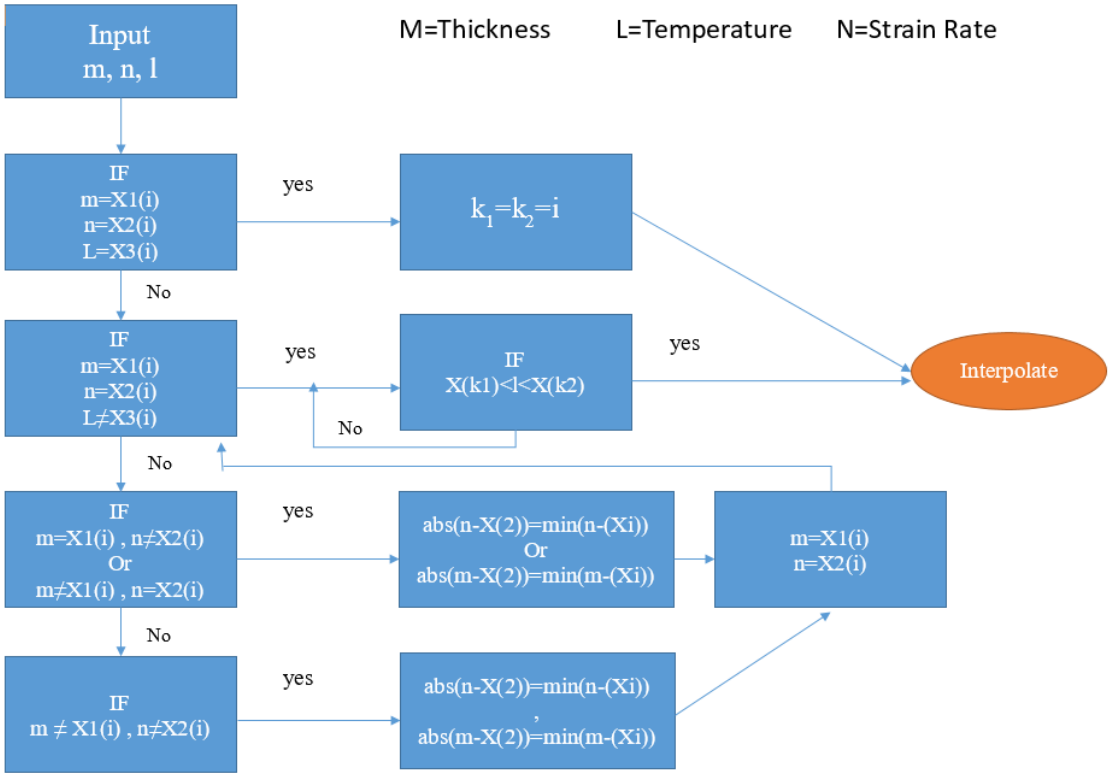

Figure 5.23: Interpolation algorithm of the user defined code

5.6 Validation

5.6.1 Empirical verification

As described in chapter 4 the experimental values of sheet metals were compared to the J-C and Z-A models. Additionally, here in order to identify the strain rate sensitivity of the materials with J-C and Z-A a static and quasi static (QS) simulation study is conducted. Alongside this a description of elastic, plastic and damage parameters is made.

This study will also aim to validate the ductility and rate of hardening of each material based on its temperature and strain rate dependence. The strain rate adopted in this study modelled the cross head movements available experimentally despite prolonging the computation time of each individual simulation.

The thermal softening of the material was studied, by means of adjusting the temperature between $23°C \leq T \leq 600°C$ and at a fixed strain rate. However, ther-

mal effects are more evident at higher strain rates, therefore for this analysis a higher rate of strain of $1500s^{-1}$ was adopted. The strain rates chosen are of typical rate available in a Split Hopkinson Tensile Bar (SHTB). Nominal strain was evaluated based on the experimental data of elongated gauge length and simulated elongation of gauge length. The expressions involved with J-C and Z-A were discussed previously (eq. 4.13 and eq. 4.33), but in order to account for dependency of shear modulus μ upon temperature, the expression below was used:

$$\left(\frac{\mu(T)}{\mu(293)}\right) = B_1 + B_2T + B_3T \tag{5.45}$$

Where the constants B_2, B_3 are set to zero and B_1 is set to the required modulus ration at T, k. Additional the Hall-petch effect value in Z-A formulation was defined as zero.

The behaviour modifications explained above resulted in establishing the verification of experimental to simulated results. Provided below in figures 5.24 to 5.26 are Z-A and J-C model predictions to the experimental results of aluminium AA6063, carbon steel 0.13% C-steel and stainless steel 18/8.

As expected aluminium specimen represented the highest strain sensitivity compared to other alloys. It should be noted the C parameter in JC model follows thickness effect, as it shows fluctuations based on similar strain rates and temperature but varying thicknesses. With regards to steel the strain rate parameter was calculated to be 0.016 to 0.011, which is in agreement to the work carried out by Kang et al.[117], but The parameter C_4 in Z-A model was discovered to be lower than theirs.

The two models appear to follow the flow curve of the material with acceptable accuracy. The Z-A model tend to follow more closely as it accounts for the damage in the material internally rather than externally (loss of section area and necking). Both models appear to be able to capture the trend up until $300°C$, however the micro-structure changes are not envisaged in either model, where temperature surpasses $300°C$. Neither model can predict the hardening at greater temperatures.

Furthermore, both models overestimate the flow stress observed at strain above 17%.

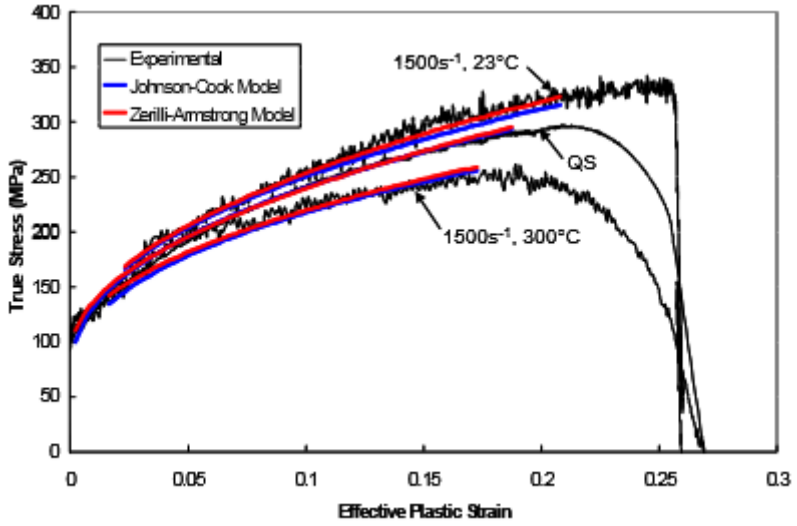

Figure 5.24: Comparison between numerical J-C results to experimental results with varying temperature On AA6063 and quasi static strain rate

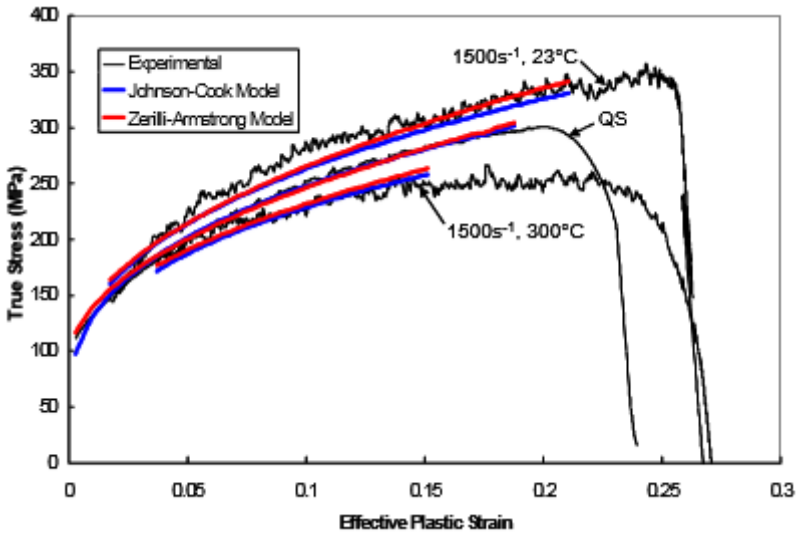

Figure 5.25: Comparison between numerical J-C results to experimental results with varying temperature on 0.13% C-steel and quasi static strain rate

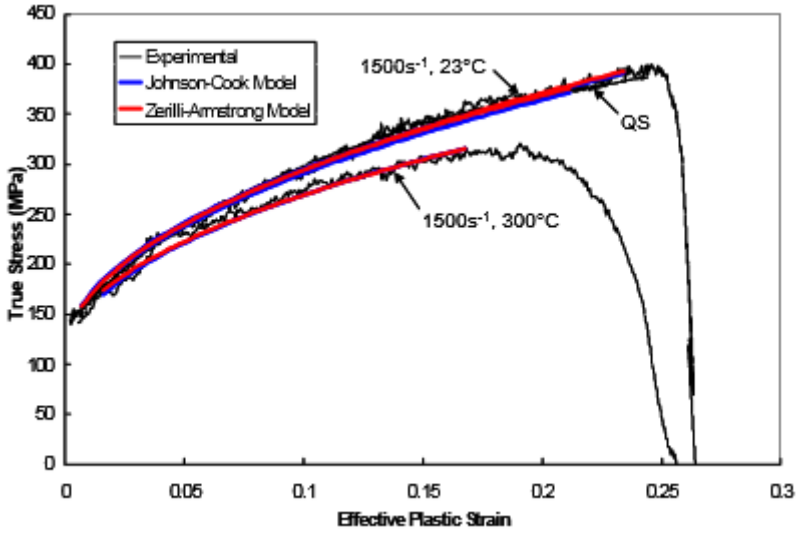

Figure 5.26: Comparison between numerical J-C results to experimental results with varying temperature on 18/8 stainless steel

5.6.2 Mathematical verification

The following graphs (fig. 5.27 and fig. 5.28) are extracted by means of user defined code. These examples show the condition of ambient temperature with cross head movement of 0.3mm/min for sample thickness of 1.1mm . The simulated results endorse the experimental results with exceptional accuracy as shown. For the mentioned test:

Parameter	Simulation		Experiment	Difference (%)	
	2D	3D		2D	3D
Equivalent Plastic Strain	0.314	0.314	0.314	0	0
Plastic strain at necking	0.372	0.374	0.371	0.2	0.8
Von-Mises stress at necking	0.376	0.374	0.378	0.5	1.06

Table 5.11: Experimental result verification based on simulated results

Table 5.11 aims to make a comparison between the code driven simulation to experimentally handled results. In terms of conducting the simulation in a 2D or 3D format for an isotropic model, there is negligible difference to persuade the user to invest significantly more time for computing purposes. The experimental results for the mentioned condition were extracted; a 2D simulation proves 0% difference when conducting the code. The biggest difference was observed for a 3D Von-Mises

stress comparison with 1.06% difference.

Considering other available codes where a 3% difference is deemed appropriate, the 0.5% difference for a 2D model is exceptionally accurate. Although the conducted code must be mainly adopted to plastic behaviour of a material. Figures below present equivalent plastic strain, plastic strain and Von-mises stress at the point of necking in a 2D and 3D format.

As can be seen, the maximum plastic strain figure 5.27b would take place near the void formation of the material. The formation of voids have already been discussed in chapter 4. A note to make based on figure 5.27b is that the least measure of strain occurrs around the curvature, but this might not be the case for an anisotropic material [62].

The maximum nodal displacement as expected is at the onset of necking, this statement can be observed by referring to figures 5.27a and 5.28a. The onset of necking has been determined on the basis of the Considére criterion, in which the rate of hardening of the material equals the maximum stress.

Based on the simulation above, a stress-strain graph could be generated. The plot produced could be highly reliable for plastic behaviour, since the polynomial interpolation coded, focused on mapping the plastic behaviour.

Figure 5.29, shows plastic reliability of the model. As can be seen the code predicts the exact point of necking at $0.30s^{-1}$. Additionally, as code was modelled after determining the shift from 1D to 3D point, the simulation does not determine the maximum elongation strain accurately. However any simulation after Considére's point of instability is unreliable despite the model being capable of predicting higher strain levels due to the its structure.

In order to verify the interpolation capability of the FEA code, separate environmental conditions were assigned which had not been studied in the lab previously. For this task four new conditions conditions were introduced. The final FEA results would then need to be verified against the newly conducted lab results. The thickness parameter could not be changed due to manufacturing limitation present

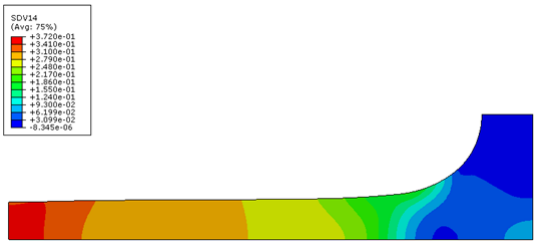

(a) Plastic strain at onset of necking

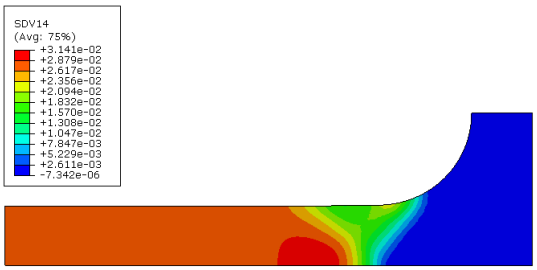

(b) Equivalant plastic strain

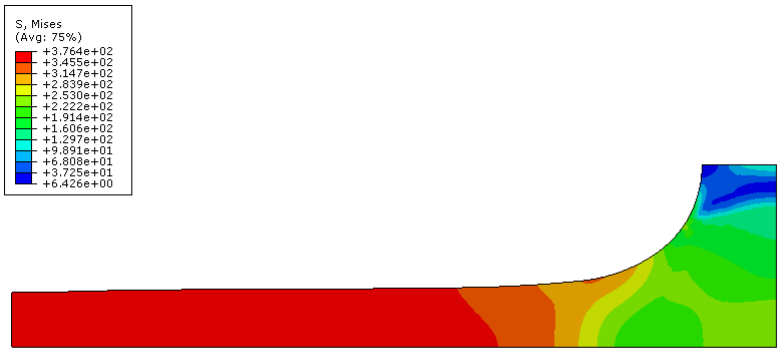

(c) Von-Mises stress at onset of necking

Figure 5.27: 2D FEA Results

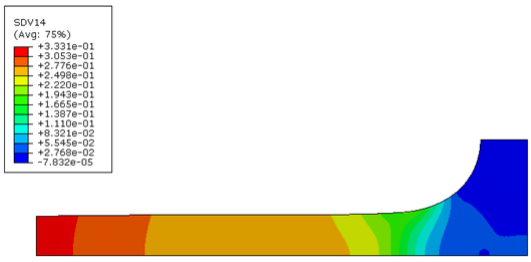

(a) Plastic strain at onset of necking

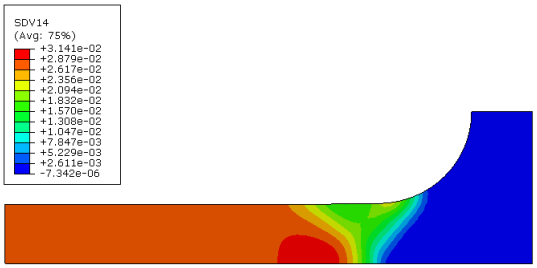

(b) Equivalant plastic strain

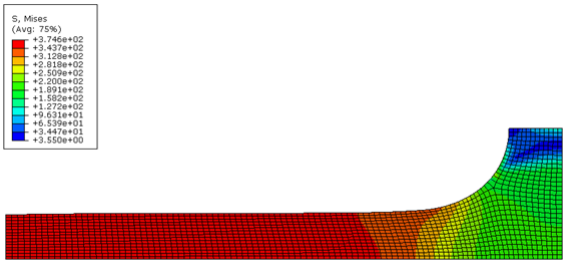

(c) Von-Mises stress at onset of necking

Figure 5.28: 3D FEA simulated results

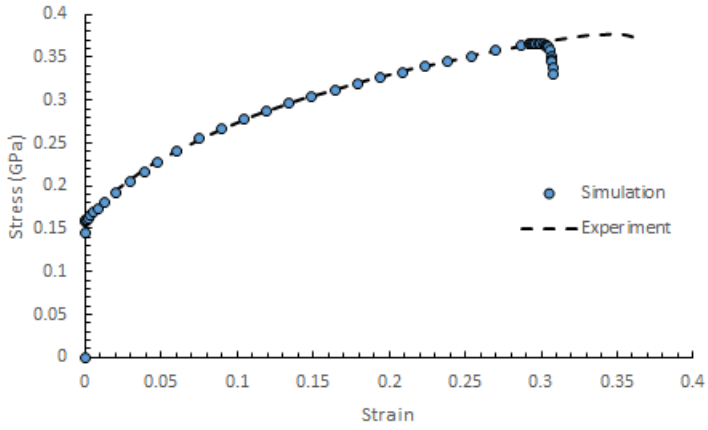

Figure 5.29: Stress vs. strain comparison of FEA and lab results

at the time of testing. As a result where strain rate and temperature were modified, table 5.12 expresses the new parameters investigated.

Test	Strain Rate (s^{-1})	Temperature (°C)	Thickness (mm)
(a)	5×10^{-2}	350	1.1
(b)	4×10^{-3}	280	0.6
(c)	6×10^{-2}	480	1.3
(d)	6×10^{-3}	550	1.3

Table 5.12: Modified parameters for verifying FEA interpolation

The simulation, as before, was conducted on a isotropic material, the aim being to predict the stress strain behaviour of the material 0.13% C-steel. Figures 5.30-5.33 below illustrate the predictions, along with the subsequent experimental test results.

The reverse engineered verification, similar to the first approach managed to predict the flow curve of the of material characteristics successfully. The only slight under predicted result could be seen in figure 5.30, which is believed to be due more to the calibration needs of the tensile testing machine, than with the FEA code itself.

In this FEA code the final results were in better agreement compared to the investigated empirical models, namely J-C and Z-A model. Essentially, the model proposed could in time overcome all physical restrictions by being applied to a wide range of temperatures and strain rates. However the older empirical models will always struggle to expand as they were designed with certain environmental condition

in mind. Moreover, the expandability of the coefficient archive could result in this computational approach replacing the empirical approach in near future.

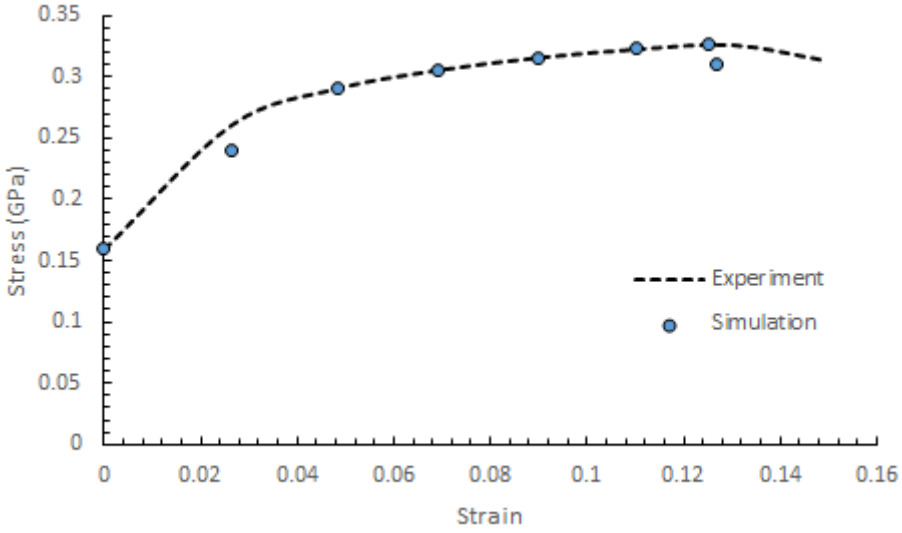

Figure 5.30: FEA verification for environmental condition (a)

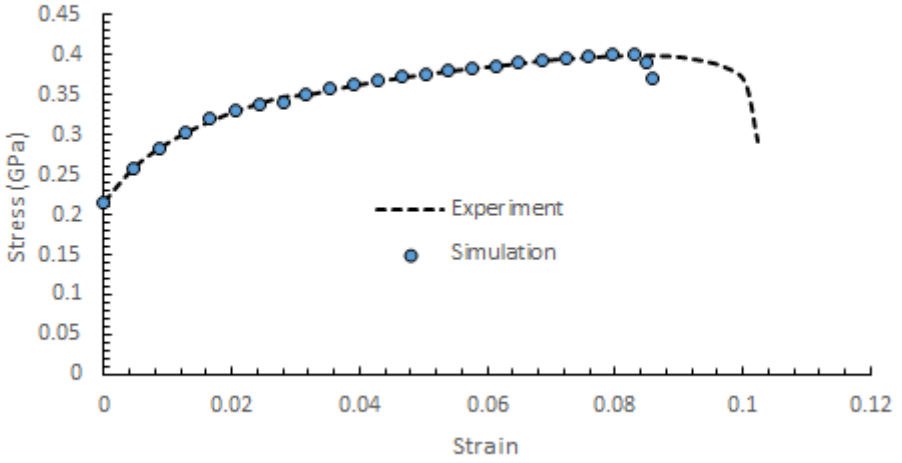

Figure 5.31: FEA verification for environmental condition (b)

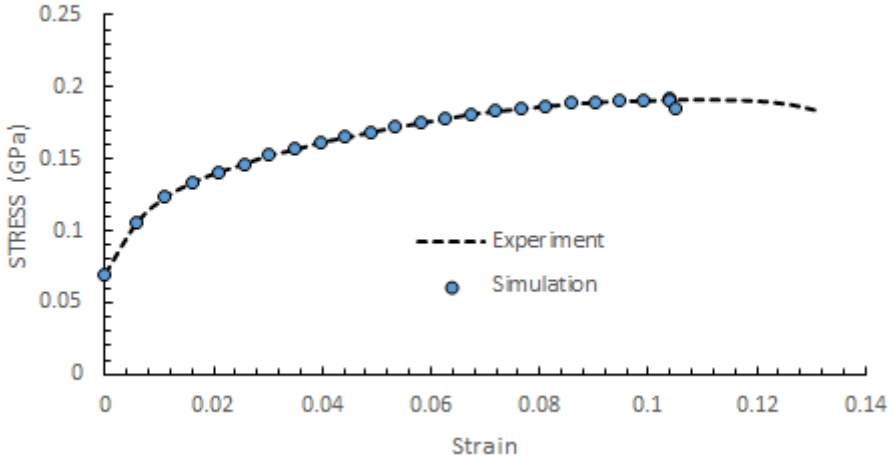

Figure 5.32: FEA verification for environmental condition (c)

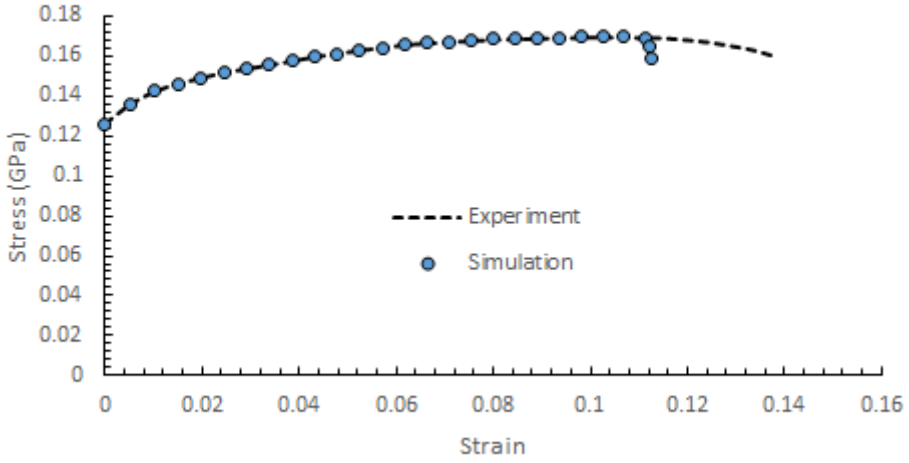

Figure 5.33: FEA verification for environmental condition (d)

5.7 Conclusion

The flow curve behavioural analysis was studied in the chapter, based upon single element isotropic models. The study managed to show uniaxiality effect based on creep and quasi static strain rate regime will be present through the flow of the sample to the point of instability; this effect was evident with mathematical model approach.

The material model approach although, accurate for higher strain rates, proves

to be unrealiable for creep regimes and temperature above $300°C$. The simulation justified that yield stress value will not be altered as much as strain hardening rate and by increasing the strain rate, similar results have been found by other researchers [118] [119]. Additionally, strengths of the alloys tested were influenced by change in strain rate. However the elongation to failure of the materials were, at lower temperature, observed to be sensitive to change in strain rate. In order to fully evaluate the strain rate sensitivity, much higher rates need to be considered similar to split hopkinson tensile tests. The energy absorption prior to failure, visualized as elongation of material, will have great impact on cold formed metal engineering.

Considére criterion strain at the onset of necking increases by increase of strain rate. The finding implied the ductility of a material could be increased, which will be manifested by retarding the formation of necking as a result of increasing the strain hardening rate. The increase in ductility could be further magnified by increasing the thickness of sheet metal.

The empirical approach suggested Z-A model could better predict elongation to failure for most materials, whereas J-C model could well be useful for more strain rate sensitive materials. The models provided in quasi static regimes, show that once localization has occurred, the magnitude of local strain rate increases. The Z-A model, managed to suggest that ductility of the material is influenced by rate sensitivity, as the strain rate parameter was observed to be positive. The flow stress predictions of the two models, was in favour of Z-A for the strain rates tested. This finding could be endorsed by the experimental results, in which strain rate hardening was increased with increase in strain rate. Similar findings can be found in comparison of uni axial testing to bulge forming and plate compression test. The empirical model failed to predict the level of strain at failure, which can be improved by including the model parameters to the point of failure. Additionally, each model could add a damage parameter for accounting of micro-structure changes, which would result in alloy softening of material due to an increase of void formation.

The mathematical approach, in which the FEA model was adopted based on

polynomial fitting (eq. 4.46) of the flow curves was investigated. The new proposed model was illustrated to have exceptional accuracy for predicting the instability point of the material. Although, the basic concept of the model fails to incorporate the accurate elasticity, the model could adopt itself to many environmental conditions by means of interpolating the coefficients of its polynomial variable. The model is capable of considering various strain rate, where Z-A and J-C can be accurate to limited strain levels. A note to make is the high temperature instrumented tests are required to obtain the function $E = E(T)$ reliably; where the elastic strain is added within the total strain decomposition:

$$\begin{aligned} \varepsilon^T &= \varepsilon^e + \varepsilon^p \\ &= \frac{\sigma}{E(T)} + \text{polynomial requirement} \end{aligned} \tag{5.46}$$

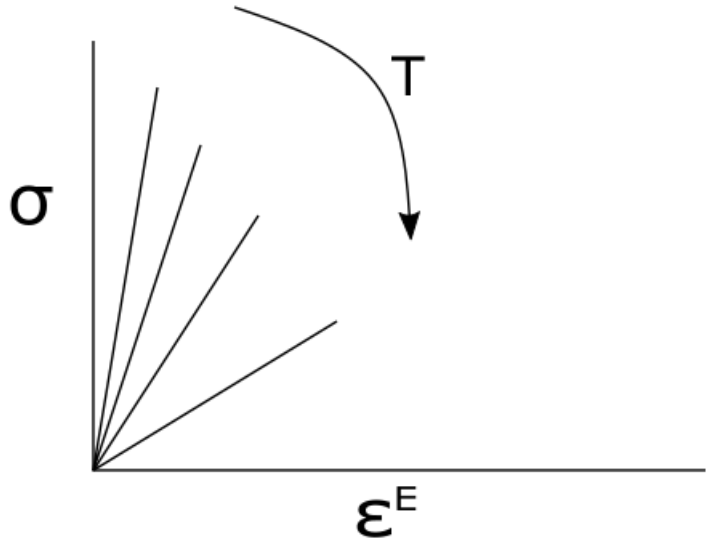

Figure 5.34: Temperature trend based on elastic strain and stress

Chapter 6

Fitting Ramberg-Osgood's Stress-Strain Equation

6.1 Introduction

There is no doubt that the correlation developed in field of stress – strain process for materials are very useful for research teams in terms of deep understanding of physical process and mechanical properties of materials.

Ramberg-Osgood equation is a good example of correlations which were studied by research teams extensively [120, 121, 122, 123]. The Ramberg - Osgood equation in the general form is expressed by equation 6.1.

$$\varepsilon = \frac{\sigma}{E} + \beta(\frac{\sigma}{E})(\frac{\sigma}{\sigma_0})^{\eta_t} \tag{6.1}$$

Where strain ε is associated stress σ in Pa, E is Young's modulus in Pa , σ_0 is yield stress and β and η_t are dimensionless constants. The accuracy of ε is related to β and η_t significantly. In some studies the value of $\beta = 0.86$ for non dimensionless computation was proposed [7, 124]. Since the value of ε is more affected by η_t in comparison to β, therefore a function was developed to calculate an accurate value for η_t in equation 6.2 and equation 6.3.

For high strength steels (G550), $20 \leq T \leq 800°C$:

$$\eta_t = -3.05x10^{-7}T^3 + 0.0005T^2 - 0.2615T + 62.653 \tag{6.2}$$

For low strength steels (G250), $350 \leq T \leq 800°C$:

$$\eta_t = 0.000138T^2 - 0.085468T + 19.212 \tag{6.3}$$

The linear term $\frac{\sigma}{E}$ in the equation 6.1 the called elastic strain and the parabolic term $\beta(\frac{\sigma}{E})(\frac{\sigma}{\sigma_0})^{\eta_t}$ is the plastic strain.
This correlation helps researchers to understand the relation between the parameters and enable them to categorize the main factors in several groups to minimise the number of experiments. This results in saving in cost and time.

6.2 Ramberg-Osgood Equation in Alternative Form

The Ramberg–Osgood correlation was studied by some researchers in alternative form which contains no element of yield stress. This alternative form of the correlation can be achieved by manipulating equation 6.1. The value of β in equation 6.1 can be replaced by equation 6.4.

$$\beta = K(\frac{\sigma_0}{E})^{\eta} \tag{6.4}$$

Where K is a dimensionless constant parameter. Replacing equation 6.4 in equation 6.1 results in equation equation 6.5.

$$\varepsilon = \sigma/E[1 + K(\frac{\sigma}{E})^{\eta}] \tag{6.5}$$

6.3 Dimensionless Analysis

Dimensionless analysis is useful to study the stress – strain process. Dimensionless parameters are the ratio of several main physical factors. They can be used in this technique to minimize the time and cost and increase accuracy.

Due to complication of stress- strain process in materials and also high number of parameters involved in this process in some cases it is almost impossible to analyse

the process without using dimensionless analysis. Consequently the dimensionless parameters not only facilitate stress–strain analyses but also enable researchers to extrapolate more from experimentally achieved data. Dimensionless parameters are well known and widely used in different fields. Reynolds number (Re) and Nusselt number (Nu) are good examples in fluid mechanics and heat transfer respectively.

The process of stress – strain in materials were studied by researchers extensively [125, 126, 127, 128]. There are many experimental published studies available in this field. Unfortunately not many analytical studies are available which could be related to the complication of differing stress–strain behaviour between materials leading researchers to consider experimental studies rather than the analytical approach.

In this work an analytical study highlights the benefits of using Ramberg – Osgood correlation. This correlation has been used extensively as a strong tool since 1943 to evaluate strain in materials without considering any experimental measurements which could be very costly in some cases. Correlations are characterized by number of parameters for which the constant coefficients need to be determined prior to calculation. The main problem arises when constants are not calculated accurately.

In this work the effect of constants in Ramberg – Osgood's correlation is studied and compared. A new method is proposed to calculate accurate values of the constant parameters. Therein a new modified form of Ramberg – Osgood correlation is proposed and the benefits of using this form compared to original form of Ramberg – Osgood correlation are discussed. New dimensionless parameters are introduced and their benefits discussed. It is also concluded that the accuracy of calculation has been improved by using the modified version of Ramberg – Osgood correlation.

6.3.1 Error analysis

The error induced in the calculated values of β and η_t and their effects on the theoretical calculation of strain (ε) is to be analysed and discussed in this section. Differentiating the strain from equation 6.1, with respect to β and η_t , which results

Temperature $°C$	r
23	2.6789
300	2.5414
400	1.7417
500	1.3466
600	1.0844

Table 6.1: Error fraction of 0.6 mm 0.13% C-steel sample

in equation 6.6a and 6.6b respectively.

$$\frac{\partial \varepsilon}{\partial \beta} = (\frac{\sigma}{E})(\frac{\sigma}{\sigma_0})^{\eta_t} \tag{6.6a}$$

$$\frac{\partial \varepsilon}{\partial \eta_t} = \beta(\frac{\sigma}{E})(\frac{\sigma}{\sigma_0})^{\eta_t} ln\frac{\sigma}{\sigma_0} \tag{6.6b}$$

$$\frac{\frac{\partial \varepsilon}{\partial \eta_t}}{\frac{\partial \varepsilon}{\partial \beta}} = \beta ln\frac{\sigma}{\sigma_0} \tag{6.6c}$$

Equation 6.6c is obtained by dividing equation 6.6b by equation 6.6a, which shows that the error on ε with respect to η_t divided by error on ε with respect to β is not a function of η_t and this value in equation 6.6c is called *error fraction* (r). Presented in table 6.1 is the error fraction values of 0.6 mm sheet samples.

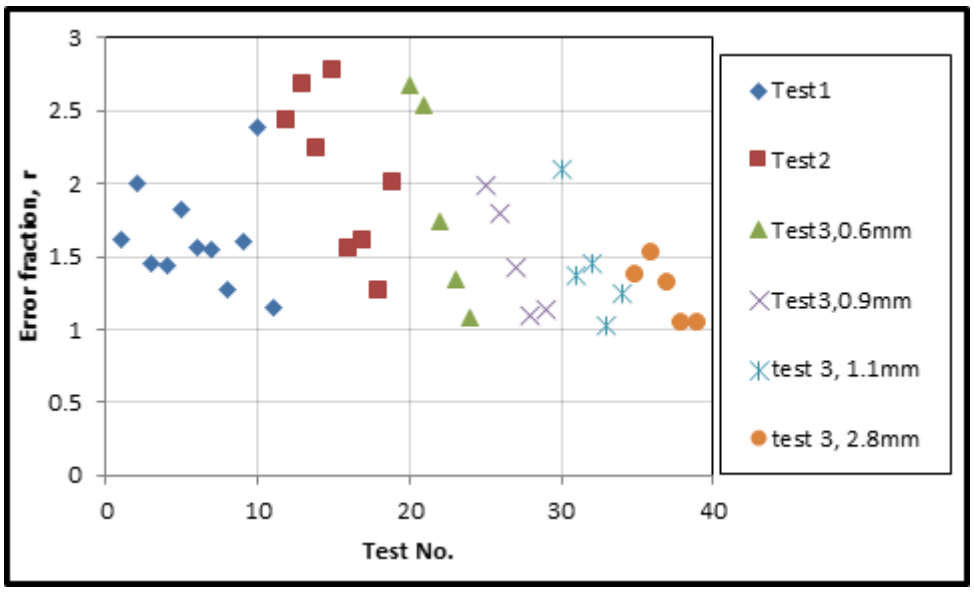

Figure 6.1: Variation of error fraction for different test conditions

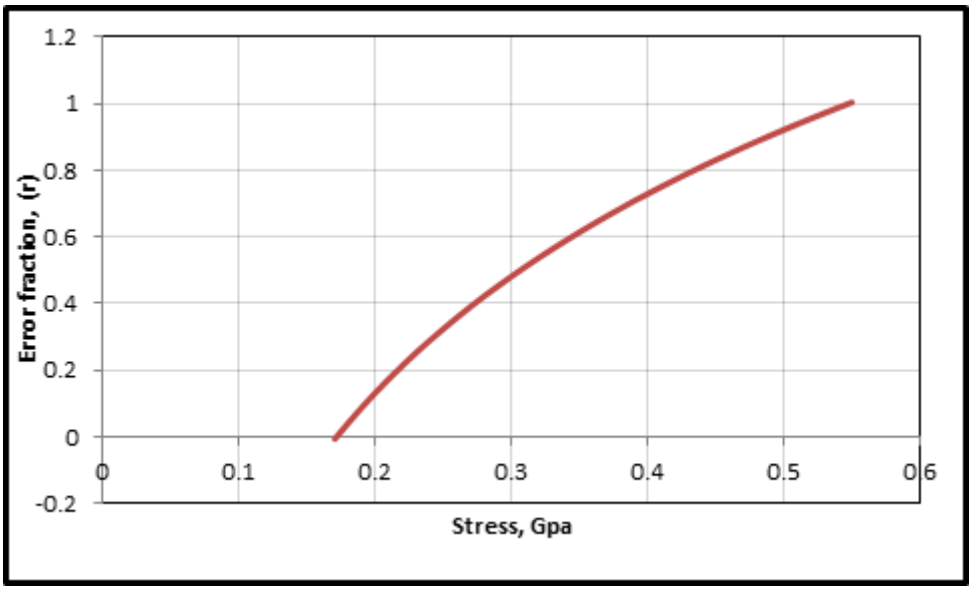

Figure 6.2: Variation of error fraction against associated stress at 3mm/min and 300°C

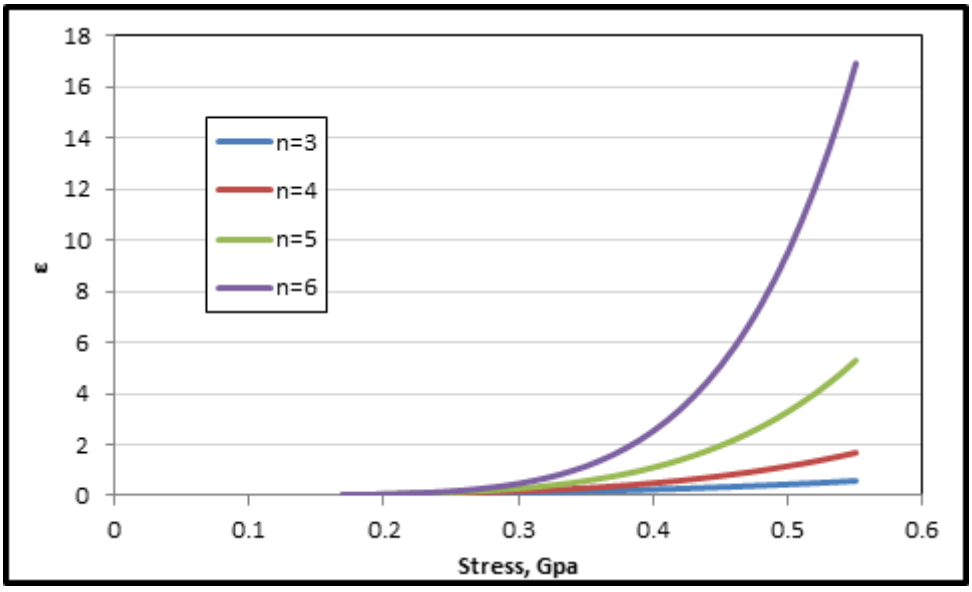

Figure 6.3: Variation of ε against σ for the values of $\eta_t = 3, 4, 5, 6$

According to figure 6.1 the accuracy of η_t affects the calculated values of ε. Figure 6.2 indicates that the value of error fraction increases by increasing the value of stress and consequently the value of error fraction is more significant at plastic region. Figure 6.3 indicates the variation of ε against σ for the values of $\eta_t = 3, 4, 5, 6$. This figure shows that ε can be affected by the values of η_t significantly.

6.4 Best Fit Procedure for Ramberg-Osgood Equation

Equation 6.1 can be rearranged and expressed as equation 6.7.

$$\frac{\varepsilon - \frac{\sigma}{E}}{\beta(\frac{\sigma_0}{E})} = (\frac{\sigma}{\sigma_0})^{\eta_t} \tag{6.7}$$

By considering two dimensionless parameters in equations 6.8a and 6.8b equation 6.7 can be expressed as equation 6.8c.

$$\pi_1 = \frac{\varepsilon - \frac{\sigma}{E}}{\beta(\frac{\sigma}{E})} \tag{6.8a}$$

$$\pi_2 = \frac{\sigma}{\sigma_0} \tag{6.8b}$$

$$\pi_1 = \pi_2^{\eta_t} \tag{6.8c}$$

Taking natural logarithm from both sides results in equation 6.9.

$$ln\pi_1 = \eta_t ln\pi_2 \tag{6.9}$$

Equation 6.10 expresses equation of straight line where:

$$\begin{aligned} y &= ln\pi_1 \\ x &= ln\pi_2 \end{aligned} \tag{6.10}$$

Equation 6.10 also indicates a line with zero y intercept therefore equation 6.11d can equated to zero.

$$b = \frac{n\sum lnxy - \sum x \sum y}{n\sum x^2 - (\sum x)^2} \tag{6.11a}$$

$$b = \frac{n\sum ln\pi_1 ln\pi_2 - \sum ln\pi_2 \sum ln\pi_1}{n\sum (ln\pi_2)^2 - (\sum ln\pi_2)^2} \tag{6.11b}$$

$$b = 0 \qquad \therefore \tag{6.11c}$$

$$\sum ln\pi_1 ln\pi_2 - \sum ln\pi_2 \sum ln\pi_1 = 0 \tag{6.11d}$$

Equation 6.11d can be written in terms of term $n-1$ and results in equation 6.12.

$$[ln\pi_{1n}ln\pi_{2n} + \sum_{n-1}^{n-1} ln\pi_1 ln\pi_2] - [\sum_{n-1}^{n} ln\pi_2][ln\pi_{1n} + \sum_{n-1}^{n-1} ln\pi_1] = 0 \tag{6.12}$$

The value of π_{1n} in equation 6.12 is unknown and can be calculated by equation 6.13.

$$\pi_{1n} = exp\frac{(\sum_{n-1}^{n} ln\pi_2)(\sum_{n-1}^{n-1} ln\pi_1) - \sum_{n-1}^{n-1} ln\pi_1 ln\pi_2}{ln\pi_{2n} - \sum_{n-1}^{n} ln\pi_2} \tag{6.13}$$

Replacing value from equation 6.8a in equation 6.13 and further simplification the value can be calculated by equation 6.15.

$$\frac{\varepsilon - \frac{\sigma}{E}}{\beta(\frac{\sigma_0}{E})} = exp[\frac{(\sum_{n-1}^{n} ln\pi_2)(\sum_{n-1}^{n-1} ln\pi_1) - \sum_{n-1}^{n-1} ln\pi_1 ln\pi_2}{ln\pi_{2n} - \sum_{n-1}^{n} ln\pi_2}] \tag{6.14}$$

$$\varepsilon_n = \frac{\sigma_n}{E} + \beta(\frac{\sigma_0}{E})exp[\frac{(\sum_{n-1}^{n} ln\pi_2)(\sum_{n-1}^{n-1} ln\pi_1) - \sum_{n-1}^{n-1} ln\pi_1 ln\pi_2}{ln\pi_{2n} - \sum_{n-1}^{n} ln\pi_2}] \tag{6.15}$$

In equation 6.15 all right hand side parameters are known through sets of experiments and measurements. A note to make is the least square modification is intended to provide best fit R-O parameters. These values can be used to calculate the value of ε. The parameter η_t was eliminated in equation 6.15 and the parameters$\pi, \sigma_0, \sigma_n, E$ and β can be used to calculate the value of ε. It is clear that the variation of η_t can not affect the accuracy of calculation in equation 6.15. Therefore it is concluded that equation 6.15 can provide an accurate results in comparison to equation 6.1. These results will be demonstrated by using the experiments and measurements which have been collected at Brunel University.

6.5 Variation of Mechanical Properties with Temperature

The properties of steels were studied extensively by researchers. Poh [129] developed a correlation which expresses the relation between σ and ε explicitly . Equation 6.16 shows the correlation.

$$\sigma = \frac{\varepsilon}{2\,|\varepsilon|}[a - |a| - \beta_6(1 + \frac{|\beta_1|\,\varepsilon\,|\beta_4 - \beta_1\beta_7| - |a|}{\beta_6 - \beta_1\beta_7}) + (\frac{(\beta_2 - \beta_3)b}{(1 + \left|\frac{(\beta_2 - \beta_3)b}{\beta_5}\right|^{\beta_9})^{1/\beta_9}} + \beta_3 b) \times (1 + \frac{|b| - |(b - \beta_{10})|}{\beta_{10}}) \tag{6.16}$$

Where:

$$a = \beta_1\,|\varepsilon| + \beta_4 + \beta_6 \tag{6.17}$$

and

$$b = |\varepsilon| - \beta_8 - \frac{\beta_4}{\beta_1} \tag{6.18}$$

Parameters β_1 to β_{10} are the values which control the shape of curve in figure 6.4.

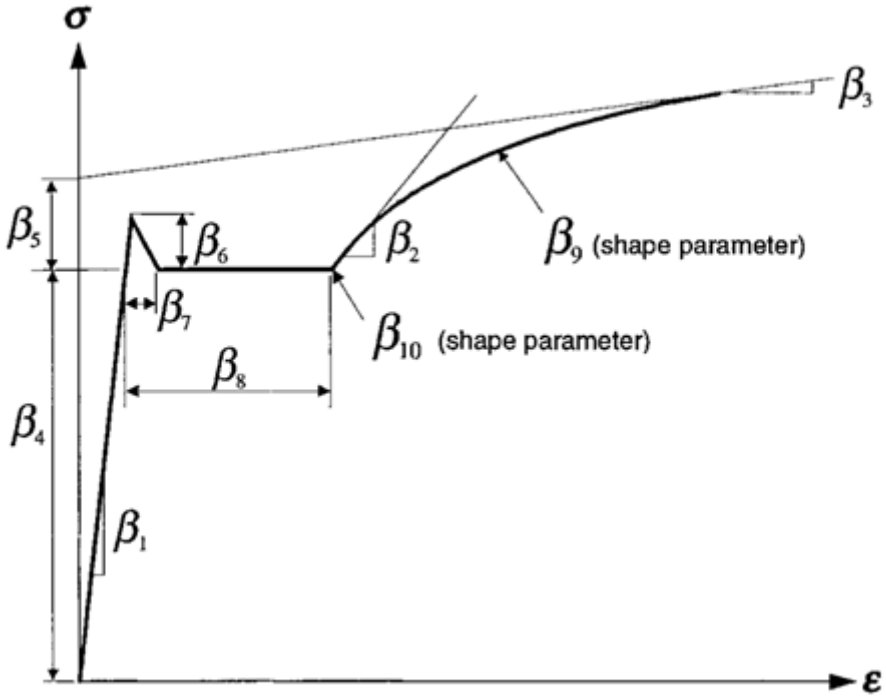

Figure 6.4: Poh's general stress-strain equation [129]

The variation of mechanical properties in terms of temperature was studied experimentally are reported in this section.

According to figures 6.6-6.5-6.7, it was found that the values of yield stress, ultimate tensile strength and elastic stiffness are reduced by increasing the temperature.

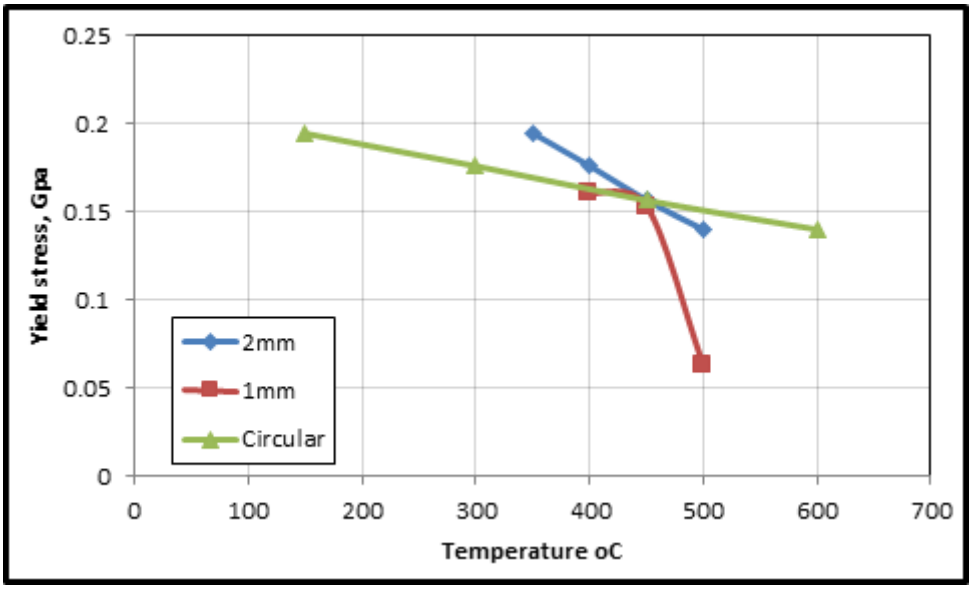

Figure 6.5: Variation of yield stress vgainst variation of temperature

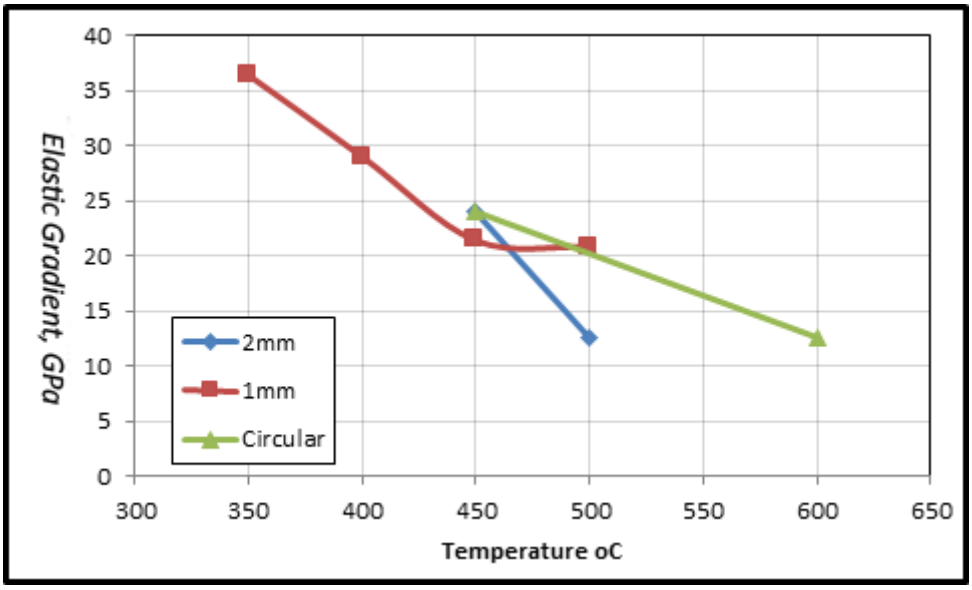

Figure 6.6: Variation of elastic gradient against variation of temperature

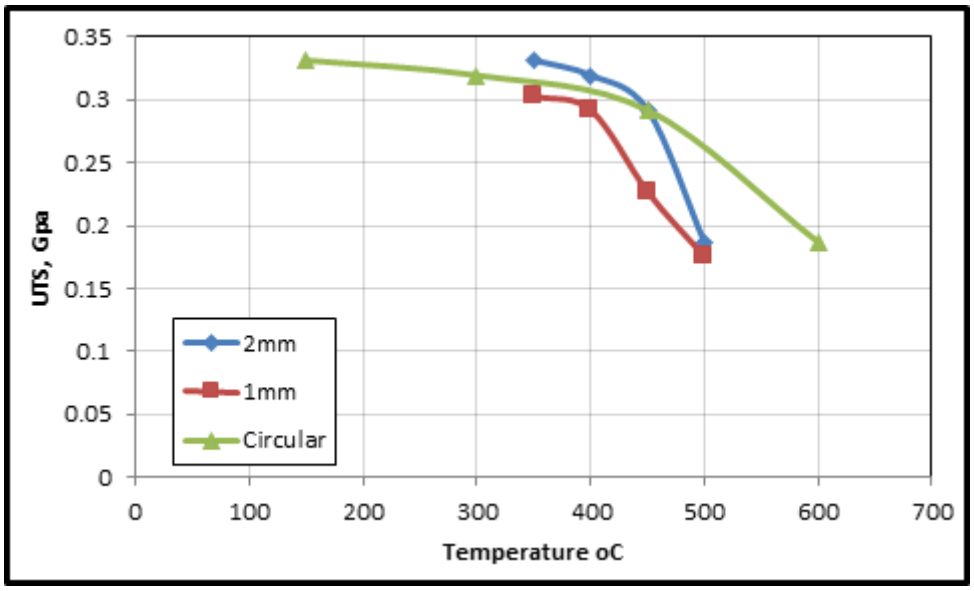

Figure 6.7: Variation of ultimate tensile strength against variation of temperature

Also it was found that the shape of specimen is not affecting the findings.

6.6 Evaluation of Exponential Factor in Ramberg-Osgood Correlation

As it was discussed the variation of constant values can affect the accuracy of calculation in a Ramberg – Osgood correlation. The technique presented in this work expresses how dimensionless parameters π_1 and π_2 calculate the value of exponential factor η_t in Ramberg–Osgood correlation. Since the variation of β does not alter the value of strain considerably, a value of $\beta = 0.86$ as proposed in [7] and [124].

Where:

$$\pi_1 = \frac{\varepsilon - \dfrac{\sigma}{E}}{\beta(\dfrac{\sigma}{E})} \qquad \pi_2 = \frac{\sigma}{\sigma_0} \tag{6.19}$$

The values of (π_1) was plotted against (π_2) in figure 6.8. The gradient of the straight line in figure 6.8 is equal to the value of η in Ramberg–Osgood equation.

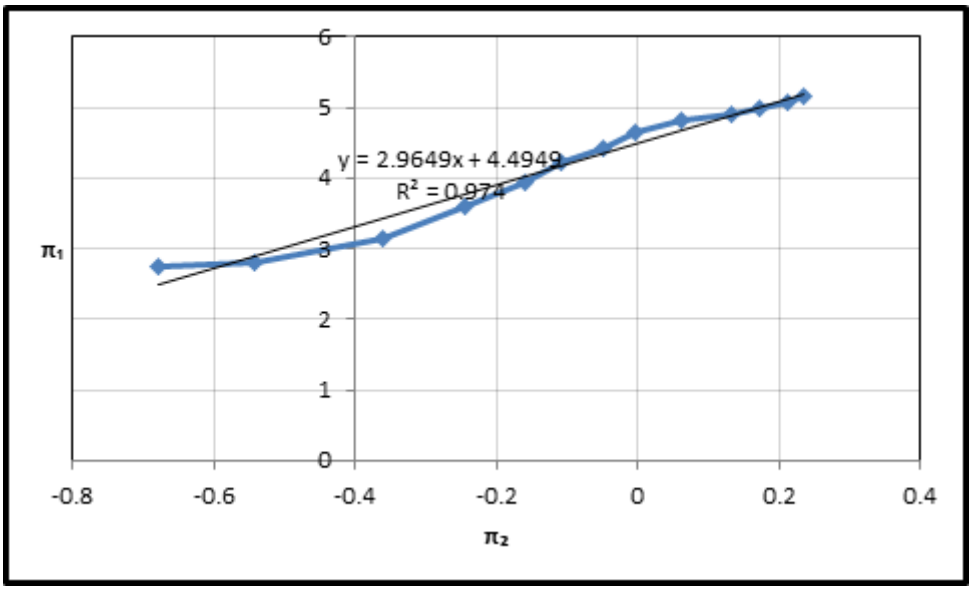

Figure 6.8: Variation of $ln(\pi_1)$ against $ln(\pi_2)$

The equation of fitted line in form of can be calculated by using equations below.

$$a = \frac{n\sum xy - \sum x\sigma y}{n\sum x^2 - (\sum x)^2} \tag{6.20a}$$

$$b = \frac{\sum x^2 \sum y - \sum x \sum xy}{n\sum x^2 - (\sum x)^2} \tag{6.20b}$$

The value of $\eta = 2.9649$ has been calculated by using figure 6.8. The Ramberg – Osgood equation can be expressed by using the gradient value of η_t.

$$\varepsilon = \frac{\sigma}{E} + 0.86(\frac{\sigma}{E})(\frac{\sigma}{\sigma_0})^{2.9649} \tag{6.21}$$

Figure 6.9 shows the variation of stress in GPa against the total strain using experimental data and Ramberg–Osgood correlation. In this figure value of η_t has been calculated by the technique proposed in this study. Figure 6.9 indicates that the variation of experimental values and calculated values are matched even though the absolute values are not perfectly matched for the values of ε less than 0.0025 .

The value of η_t can be calculated as a linear average using the definitions of π_1 and π_2.

Using equation 6.9 results in calculated values of η_t corresponding to each strain rate measurement. The final value of η_t can be calculated as an average. Equation below expresses the final value of η_t in terms of calculated π_1 and π_2.

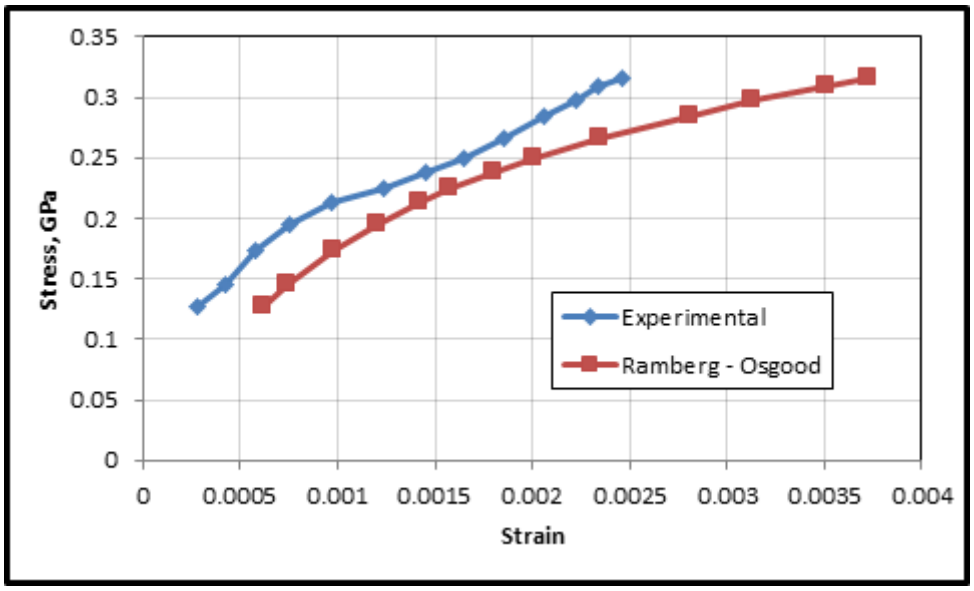

Figure 6.9: Variation of stress against strain for experimental data and calculated values using R-O correlation based on fixed exponential factor

$$\eta_t = \frac{1}{n}\sum_{i=1}^{n}(\frac{ln\pi_1}{ln\pi_2})_i \tag{6.22}$$

Where n is the number of measurements. Figure 6.10 shows the results of equation 6.22.

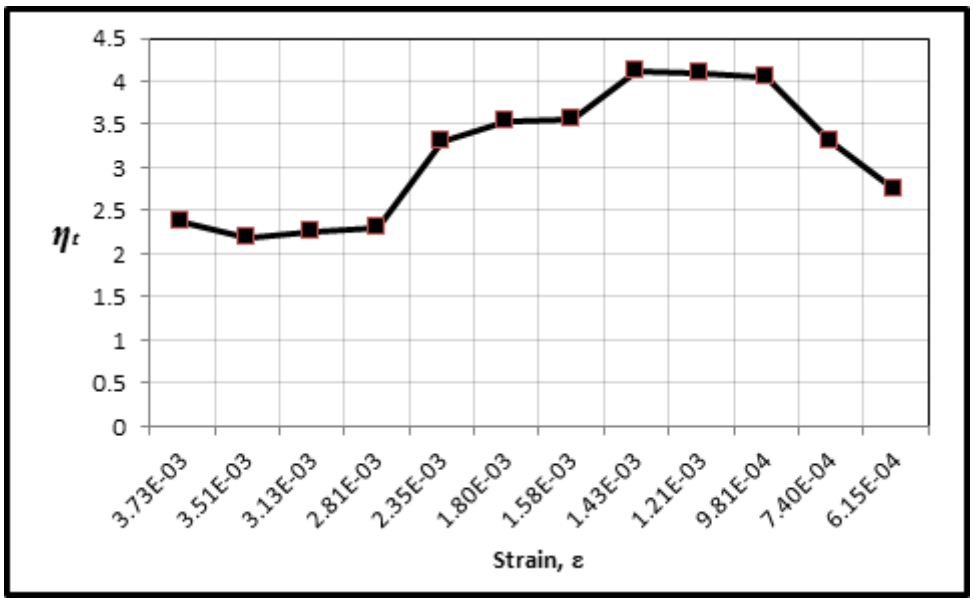

Figure 6.10: Calculated values of η_t against strain ε by using the average value

Using the results in figure 6.10 along with equation 6.22 results in equation below.

$$\eta_t = \frac{1}{12}\sum_{i=1}^{12}(\frac{ln\pi_1}{ln\pi_2})_i = 3.1524 \tag{6.23}$$

It was found that values of η_t using average value technique 6% more in comparison to the calculated values using fitting straight line. It can be concluded that using average value and fitting a straight line produce very close values for η_t.

Figure 6.11 shows the calculated value for ε against applied stress by using the result in equation 6.23.

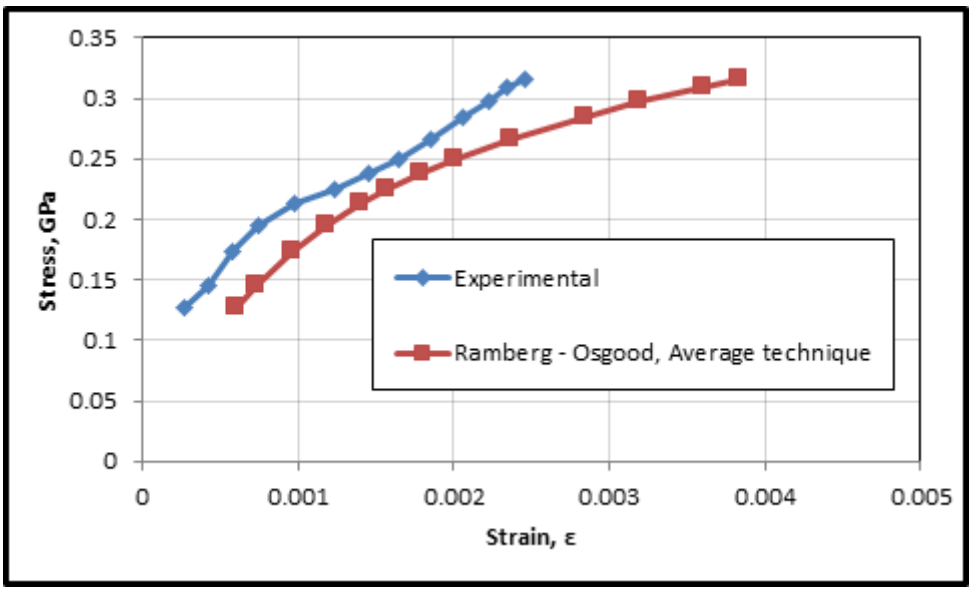

Figure 6.11: Applied stress against calculated values of ε from R-O (at $23°C$, 2.8 mm 0.2% C-sheet metal and $6.09 \times 10^{-5} s^{-1}$)

It is clear that the accuracy of constants in Ramberg–Osgood correlation can affect the accuracy of calculated strain values. The fitting procedure has not been expressed in terms of exponential factor and consequently the accuracy of η cannot affect the accuracy of R-O calculated strain. In a modified fit the value of ε can be calculated in terms of σ, E, β and σ_0.

Figure 6.12 shows the variation of stress (GPa) against the calculated strain values by using the modified fit of Ramberg–Osgood's equation.

According to figure 6.12 there is a good agreement between experimental measurements and the R-O equation. The fit may underestimate strain marginally but error is small enough to be neglected.

6.7 Error Calculation-Propagation Function

The error propagation function (ω) can be used to compare the experimental measurements and calculated values for the strain by using original forms of Ram-

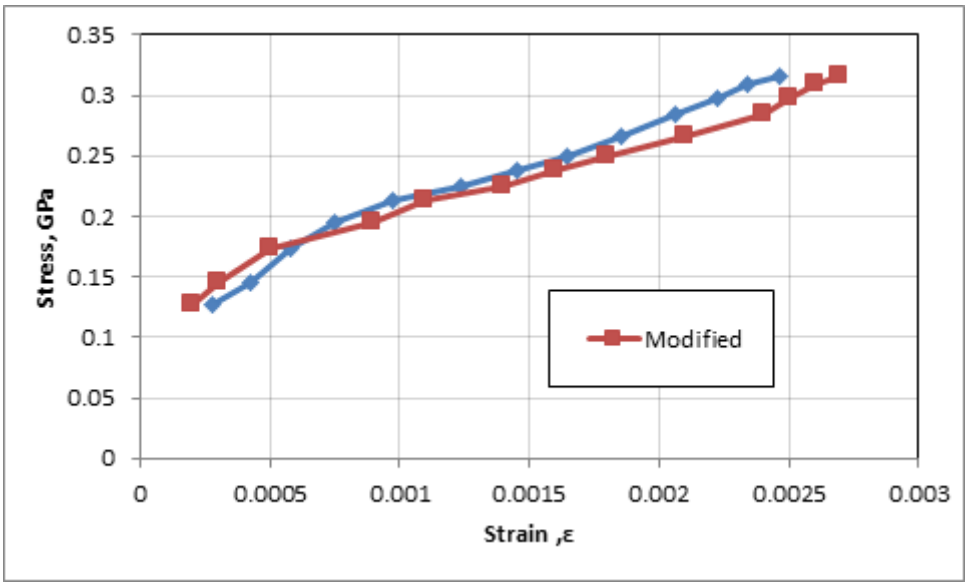

Figure 6.12: Variation of stress against total strain from R-O correlation (at $23°C$, 2.8 mm 0.2% C sheet metal and $6.09 \times 10^{-5} s^{-1}$)

berg–Osgood's equation and the best fit version proposed in this study.

$$\omega = \sqrt{\sum_{i=1}^{n} (\varepsilon_i - \varepsilon_{exp})^2} \tag{6.24}$$

The absolute values of strain were calculated by using Ramberg–Osgood equation. The value of η was found using the techniques proposed in this study enabling the values of strain from the present best fit procedure. The error propagation values were calculated by original forms ($\eta_t = 2.96$ and $\eta_t = 3.15$) and its best fit Ramberg–Osgood correlation. The results are plotted along with experimental measurements in figure 6.13.

Figure 6.13 shows the values for propagation function vary between the modified and original correlations for different values of applied tensile stress. No significant differences were calculated for Ramberg–Osgood original forms (using average values and fitting a straight line techniques). For the values of $\sigma < 0.25$ GPa the difference between the two approaches are small but for values of $\sigma > 0.25$ GPa the modified version provides better results in having negligible error. This is because the modified fit is not expressed in terms of η_t, consequently the accuracy of η_t cannot affect the calculated strain. Thus the calculated strain from the modified fit lie closer to experimental measurements.

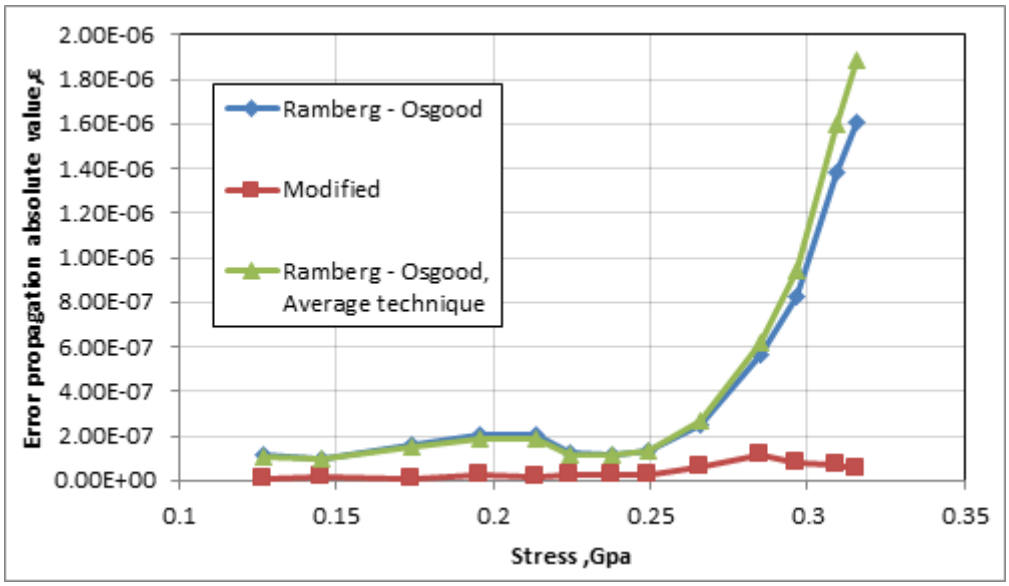

Figure 6.13: Error propagation values versus stress determined for original RO correlation and best fit modification

6.8 Conclusion

It was found that calculating exponential factor by using the techniques discussed in this work can improve the accuracy of Ramberg–Osgood correlation as well as using modified version of Ramberg–Osgood correlation.

As it was discussed the modified version can be used to calculate the value of strain without calculating the value of η_t which could results in improving the accuracy and also simplifying the calculations. The modified correlation can be used on different materials to calculate the strain values.

It was found that using calculated values of η_t the Ramberg–Osgood correlation can improve the accuracy of correlation fit to experimental data. In contrast the calculated strain values are overestimated from both averaging and line fitting techniques.

It was found that the calculated values for strain by using the modified Ramberg–Osgood correlation can improve the accuracy of calculation significantly. According the figure 6.14 the calculated values overestimate strain for $\varepsilon < 0.0005$, but thereafter the calculated strains match experiment better than found from averaging

and line fitting technique.

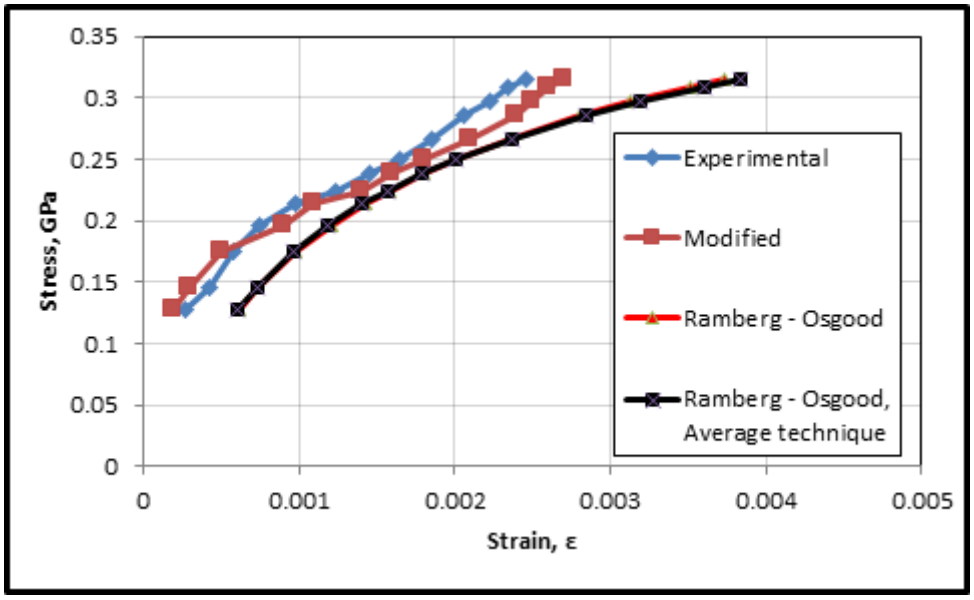

Figure 6.14: Variation of stress against total strain using experimental data, modified version of R-O correlation and original forms of R-O correlation by using fitting a line and average value technique (at $23°C$, 2.8 mm 0.2% C-sheet metal and $6.09 \times 10^{-5} s^{-1}$)

Chapter 7

Conclusion

The main objective of this thesis was to investigate the characteristics of cold formed metals, based on three parameters, namely thickness, strain rate and temperature. By means of gaining better understanding of thickness effect upon variations of stress strain curves, similarities were tried to be established. A series of tests with varying strain level limit were conducted, uni-axial tensile testing along with biaxial bulge forming and compression testing. The three tests enabled creating a correlation by increase of strain levels. Additionally, the objective was set to develop a mathematical model to predict metals behaviour in elastic condition, plastic deformation and initiation of damage.

The principal work of this thesis:

In the first stage which comprised the main body of the experimentation, three defining uni-axial tests were conducted. The first stage was conducted with strain rate variation in mind, later material adjustments were chosen with significantly more temperature variation. Subsequently, same geometries as the first stage were chosen for the third investigation, which focused its attention on thickness variation. The temperatures chosen varied from $23°C$ to $600°C$, also the thickness variation spanned from 0.6 mm to 2.8 mm.

In order to explain the experimental result; Ramberg-Osgood, Johnson-Cook and Armstrong-Zerrili models were studied and their predictions compared. For

verification purposes, the characteristics of materials were investigated in reduction factor method, which enabled determining the thickness effect upon the material behaviour.

Furthermore, a series of micro-structure studies were carried out, which enabled better understanding of necking phenomenon. The necking formation was based on Considére criterion, out of which a set of polynomial instability equations were derived. The instability equation enabled the increase of limiting strain from 1D to 3D testing, which was then used in creating the archive of coefficients that would relate to material behaviour under different environmental conditions.

Recognising a down fall in Ramberg-Osgood when defining parameter η, work was carried out to produce a linear variation of that parameter. The work progressed by introducing a modified R-O model to incorporate wider range of strain levels, with an improved fit compared to the original proposal.

A procedure for deriving the parameters required in the Z-A and J-C equation was developed and expressed on the basis of a uni-axial tensile testing. In order to verify the two models, the derived procedures were both compared against other researchers and carried out in an finite element analysis method.

As opposed to an standard tensile specimen geometry, a non-standard dog-bone dimensions were chosen. The decision was made based on the requirement to achieve both quasi-static and creep regime strain rates, by using a standard screwdriven tensile machine.

For an isotropic material simulation, where orthotropy behaviour effect on a material is less, defining the damage parameters out of isotropic material behaviour is sufficient. As a consequence, the polynomial coefficients parameters were deemed appropriate for defining the plasticity and damage behaviour of the model for the materials tested. The simulation carried out, was a combination of inbuilt commands and user defined codes through Fortran and ABAQUS. Therefore a UMAT

code was constructed to verify the experimental works. Prior to verifying the user defined code, a series of studies on the concept of meshing was created to best be implemented on the model, as well as employing the Z-A and J-C empirical models; for which an under-conservative trend was observed. However the User defined model was proven to work accurately with 0.2% error in some instances.

An interpolation algorithm was derived in order for the user defined code to predict and analyse material parameter coefficients within range of environmental tests. The data generated was later applied in laboratory tensile tests conducted in the same conditions for verification. The result of such approach proved reliability of both the interpolation algorithm and written code.

7.1 Future Work

The experimental work carried in this experiment offered a better understanding when characterising the material behaviour over larger strain level and temperatures. However as such, an inelastic reserve capacity experimental work may be suggested in order to define the strain limits based on the work provided. Additionally other suggestions may be mentioned:

- The characteristics behaviour of the experimental work could be verified against compression testing, in order to verify the the result and simulate such findings based on the the code available.
- Establishing a TSHB apparatus for expanding the strain rate tested and its dynamic range. In general the limits of environmental conditions will need to be developed further; new archive of coefficients has to be expressed.
- Re-fitting the empirical models at higher strain rates. High strain rates may be achieved by means of drop tower, or electro-magnetic forming experiments to exceed the strain rate level even more.
- Performing notched sample tensile tests, in order to analyse the tri-axility related to them for comparative purposes against uni-axial and biaxial.

- Adaptation of Hill's yield criteria, for anisotropic analysis and kinematic strain hardening.
- Expanding the current library of coefficients is of utmost importance. similar study could be carried out to wider range of materials as well as temperatures and strain rates. The current library of the data is provided in Appendix B.
- The study was carried out with materials being tested at uniform temperatures. However, in real life scenarios such structures will be non-uniformly heated. Therefore further work is recommended in this area.

As a whole, it is the authors intention to create a hand book of common engineering alloys and to archive the coefficients of the flow curves. Additional testing is required at extended environmental conditions. As such, the coefficient interpolation will will be come smaller and more accurate by means of eliminating non-linear proportional differences and applying a linear relation between the flow curve coefficients.

Bibliography

[1] R Arrieux, C Bedrin, and M Boivin. "Determination of an intrinsic forming limit stress diagram for isotropic sheets". In: *Proceedings of the 12th IDDRG Congress*. Vol. 2. 1982, pp. 61–71.

[2] Thanuja Ranawaka. "Distortional buckling behaviour of cold-formed steel compression members at elevated temperatures". In: (2006).

[3] Leslie Philip Pook. *Linear elastic fracture mechanics for engineers: theory and applications*. Computational Mechanics, 2000.

[4] Mansoo Joun et al. "Finite element analysis of tensile testing with emphasis on necking". In: *Computational Materials Science* 41.1 (2007), pp. 63–69.

[5] Ju Chen and Ben Young. "Experimental investigation of cold-formed steel material at elevated temperatures". In: *Thin-Walled Structures* 45.1 (2007), pp. 96–110.

[6] Jung Hoon Lee, Mahen Mahendran, and Pentti Makelainen. "Prediction of mechanical properties of light gauge steels at elevated temperatures". In: *Journal of Constructional Steel Research* 59.12 (2003), pp. 1517–1532.

[7] Thanuja Ranawaka and Mahen Mahendran. "Experimental study of the mechanical properties of light gauge cold-formed steels at elevated temperatures". In: *Fire Safety Journal* 44.2 (2009), pp. 219–229.

[8] Jyri Outinen and Pentti Mäkeläinen. "Mechanical properties of structural steel at elevated temperatures and after cooling down". In: *Fire and materials* 28.2-4 (2004), pp. 237–251.

[9] EC Eurocode. "3: Design of steel structures–Part 1.2: General rules–Structural fire design". In: *Brussels: European Committee for Standardization. DD ENV* (1993), pp. 1–2.

[10] BS BSI. "5950, Structural use of steelwork in building, part 8, code of practice for fire resistant design". In: *British Standards Institution, London* (1990).

[11] J Outinen, O Kaitila, and P Mäkeläinen. "A STUDY FOR THE DEVELOPMENT OF THE DESIGN OF STEEL STRUCTURES SN FSRE CONDITIONS". In: (2000).

[12] P Makelainen and K Miller. "Mechanical Properties of Cold-Formed Galvanized Sheet Steel Z32 at Elevated Temperatures". In: *Helsinki University of Technology, Finland* (1983).

[13] JT Gerlich, Peter Clive Robert Collier, and Andrew Hamilton Buchanan. "Design of Light Steel-framed Walls for Fire Resistance". In: *Fire and Materials* 20.2 (1996), pp. 79–96.

[14] KH Klippstein. "Strength of cold-formed studs exposed to fire". In: *American Iron and Steel Institute, Washington DC, USA* (1980).

[15] Walter Ramberg and William R Osgood. "Description of stress-strain curves by three parameters". In: (1943).

[16] Dolamune Kankanamge. "Flexural Behaviour of Cold-fomred Steel Beams at Elevated Temperature". In: (2009).

[17] Ulric S Lindholm. "High strain rate tests". In: *Techniques of metals research* 5.Part 1 (1971).

[18] Jonas A Zukas et al. "Impact dynamics". In: *Journal of Applied Mechanics* 50 (1983), p. 702.

[19] K Janghorban and S Esmaeili. "Deformation-mechanism map for Ti-6wt% Al alloy". In: *Journal of Materials science* 26.12 (1991), pp. 3362–3365.

[20] I McEnteggart and RD Lohr. "Mechanical testing machine criteria". In: *Materials metrology and standards for structural performance*. Springer, 1995, pp. 19–33.

[21] George T Gray. "Classic Split-Hopkinson Pressure Bar Testing." In: *Materials Park, OH: ASM International, 2000.* (2000), pp. 462–476.

[22] GE Dieter. *Mechanical Metallurgy*. McGraw-Hill Book Company, 1998, pp. 659–660.

[23] JR Davis. “Tensile testing second edition”. In: *ASM International, The material information society* (2004).

[24] R Mahmudi, R Mohammadi, and P Sepehrband. “Determination of tearing energy from uniaxial tension tests of aluminum alloy sheet”. In: *Journal of materials processing technology* 147.2 (2004), pp. 185–190.

[25] NA Fleck et al. “Strain gradient plasticity: theory and experiment”. In: *Acta Metallurgica et Materialia* 42.2 (1994), pp. 475–487.

[26] Yun Ling. “Uniaxial true stress-strain after necking”. In: *AMP Journal of Technology* 5 (1996), pp. 37–48.

[27] S Ifergane et al. “Study of fracture evolution in copper sheets by in situ tensile test and EBSD analysis”. In: *Journal of materials science* 45.23 (2010), pp. 6345–6352.

[28] E Lothian, K Hermann, and M Stewart. “An atlas of metal damage”. In: *Wolf Publishing Limited, ISBN 0* 7234 (1981), p. 07509.

[29] Hongcheng Huang and Liang Xue. “Prediction of slant ductile fracture using damage plasticity theory”. In: *International Journal of Pressure Vessels and Piping* 86.5 (2009), pp. 319–328.

[30] Andrzej Neimitz and Jaroslaw Galkiewicz. “Fracture toughness of structural components: influence of constraint”. In: *International Journal of Pressure Vessels and Piping* 83.1 (2006), pp. 42–54.

[31] Ted L Anderson and TL Anderson. *Fracture mechanics: fundamentals and applications*. CRC press, 2005.

[32] Donald R Askeland and Pradeep P Phulé. “Mechanical properties and behavior”. In: *The Science and Engineering of Materials* 5 (2006), pp. 214–215.

[33] ZL Zhang and E Niemi. “A new failure criterion for the Gurson-Tvergaard dilational constitutive model”. In: *International Journal of Fracture* 70.4 (1994), pp. 321–334.

[34] AR Ragab. “A model for ductile fracture based on internal necking of spheroidal voids”. In: *Acta Materialia* 52.13 (2004), pp. 3997–4009.

[35] Jagabanduhu Chakrabarty. *Theory of plasticity*. Butterworth-Heinemann, 2012.

[36] David Rees. *Basic engineering plasticity: an introduction with engineering and manufacturing applications*. Butterworth-heinemann, 2012.

[37] Roger T Fenner and JN Reddy. *Mechanics of solids*. CRC Press, 1991.

[38] KS Raghavan. "A simple technique to generate in-plane forming limit curves and selected applications". In: *Metallurgical and materials transactions A* 26.8 (1995), pp. 2075–2084.

[39] Jun-hua Liu, M Ahmetoglu, and T Altan. "Evaluation of sheet metal formability, viscous pressure forming (VPF) dome test". In: *Journal of Materials Processing Technology* 98.1 (2000), pp. 1–6.

[40] AB Watts and Hugh Ford. "An experimental investigation of the yielding of strip between smooth dies". In: *Proceedings of the Institution of Mechanical Engineers, Part B: Journal of Engineering Manufacture* 1.1-12 (1953), pp. 448–464.

[41] William Johnson and Peter Bassindale Mellor. *Plasticity for mechanical engineers*. van Nostrand, 1962.

[42] AMS Hamouda and MSJ Hashmi. "Modelling the impact and penetration events of modern engineering materials: characteristics of computer codes and material models". In: *Journal of materials processing technology* 56.1 (1996), pp. 847–862.

[43] William L Oberkampf, Timothy G Trucano, and Charles Hirsch. "Verification, validation, and predictive capability in computational engineering and physics". In: *Applied Mechanics Reviews* 57.5 (2004), pp. 345–384.

[44] Guillaume Altmeyer. "Modélisation théorique et numérique des critères d'instabilité plastique. Application à la prédiction des phénomènes de striction et de localisation lors d'opérations d'emboutissage." PhD thesis. Arts et Métiers ParisTech, 2011.

[45] P Hora, L Tong, and J Reissner. "A prediction method for ductile sheet metal failure in FE-simulation". In: *Proceedings of Numisheet*. Vol. 96. 1996, pp. 252–256.

[46] Zdzisław Marciniak, Kazimierz Kuczyński, and Tadeusz Pokora. "Influence of the plastic properties of a material on the forming limit diagram for sheet metal in tension". In: *International Journal of Mechanical Sciences* 15.10 (1973), pp. 789–800.

[47] JD Bressan and JA Williams. "The use of a shear instability criterion to predict local necking in sheet metal deformation". In: *International Journal of Mechanical Sciences* 25.3 (1983), pp. 155–168.

[48] Stuart Philip Keeler and Walter A Backofen. "Plastic instability and fracture in sheets stretched over rigid punches". In: *Asm Trans Q* 56.1 (1963), pp. 25–48.

[49] A Ofenheimer et al. "Cost effective strategy to predict formability in two-step sheet forming operations". In: *Hora. P.(ed.): Numisheet* (2008).

[50] Frieder Neukamm, Markus Feucht, and André Haufe. "Considering damage history in crashworthiness simulations". In: *Ls-Dyna Anwenderforum* (2009).

[51] W Volk and J Suh. "Reliable and robust evaluation of local necking with a generalized thinning limit diagram". In: *Proceedings of 5th Forming Technology Forum, Zürich, Switzerland*. 2012, pp. 115–120.

[52] Wolfram Volk et al. "Failure prediction for nonlinear strain paths in sheet metal forming". In: *CIRP Annals-Manufacturing Technology* 61.1 (2012), pp. 259–262.

[53] W Müschenborn and HM Sonne. "Einfluß des Formänderungsweges auf die Grenzformänderungen des Feinblechs". In: *Arch. Eisenhüttenwes* 46 (1975), pp. 597–602.

[54] Kengo Yoshida and Toshihiko Kuwabara. "Effect of strain hardening behavior on forming limit stresses of steel tube subjected to nonproportional loading paths". In: *International journal of plasticity* 23.7 (2007), pp. 1260–1284.

[55] Danielle Zeng et al. “A path independent forming limit criterion for sheet metal forming simulations”. In: *SAE International Journal of Materials and Manufacturing* 1.2008-01-1445 (2008), pp. 809–817.

[56] T Stoughton, JW Yoon, and M Liewald. “Advances in metal forming limits under nonlinear and out-of-plane forming conditions”. In: *New developments in sheet metal forming* (2012), pp. 221–240.

[57] Gorton M Goodwin. *Application of strain analysis to sheet metal forming problems in the press shop*. Tech. rep. SAE technical paper, 1968.

[58] Alejandro F Graf and William F Hosford. “Calculations of forming limit”. In: *Metallurgical Transactions A* 24.11 (1993), pp. 2497–2501.

[59] HJ Kleemola and JO Kumpulainen. “Factors influencing the forming limit diagram: part II—influence of sheet thickness”. In: *Journal of Mechanical Working Technology* 3.3 (1980), pp. 303–311.

[60] Alexandra Werber et al. “Assessment of forming limit stress curves as failure criterion for non-proportional forming processes”. In: *Production Engineering* 7.2-3 (2013), pp. 213–221.

[61] Thomas B Stoughton and Xinhai Zhu. “Review of theoretical models of the strain-based FLD and their relevance to the stress-based FLD”. In: *International Journal of Plasticity* 20.8 (2004), pp. 1463–1486.

[62] S Stören and JR Rice. “Localized necking in thin sheets”. In: *Journal of the Mechanics and Physics of Solids* 23.6 (1975), pp. 421–441.

[63] H_W Swift. “Plastic instability under plane stress”. In: *Journal of the Mechanics and Physics of Solids* 1.1 (1952), pp. 1–18.

[64] Michael Brünig. “Numerical analysis and modeling of large deformation and necking behavior of tensile specimens”. In: *Finite Elements in Analysis and Design* 28.4 (1998), pp. 303–319.

[65] Stéphane Dumoulin et al. “Determination of the equivalent stress–equivalent strain relationship of a copper sample under tensile loading”. In: *Journal of Materials Processing Technology* 133.1 (2003), pp. 79–83.

[66] Christian F Niordson and Pia Redanz. "Size-effects in plane strain sheet-necking". In: *Journal of the Mechanics and Physics of Solids* 52.11 (2004), pp. 2431–2454.

[67] Kazutake Komori. "Simulation of tensile test by node separation method". In: *Journal of materials processing technology* 125 (2002), pp. 608–612.

[68] Kristina Nilsson. "Effects of inertia on dynamic neck formation in tensile bars". In: *European Journal of Mechanics-A/Solids* 20.5 (2001), pp. 713–729.

[69] KS Zhang. "Fracture prediction and necking analysis". In: *Engineering fracture mechanics* 52.3 (1995), pp. 575–582.

[70] Eduardo E Cabezas and Diego J Celentano. "Experimental and numerical analysis of the tensile test using sheet specimens". In: *Finite Elements in Analysis and Design* 40.5 (2004), pp. 555–575.

[71] SW Lee and MS Joun. "Rigid–viscoplastic finite element analysis of the piercing process in the automatic simulation of multi-stage forging processes". In: *Journal of Materials Processing Technology* 104.3 (2000), pp. 207–214.

[72] MP Sidey and DP Teague. "Elevated temperature data for structural grades of galvanized steel". In: *British Steel (Welsh Laboratories) Report, UK* (1988).

[73] Keith J Laidler. "The development of the Arrhenius equation". In: *J. Chem. Educ* 61.6 (1984), p. 494.

[74] D Ravi Kumar and K Swaminathan. "Tensile deformation behaviour of two aluminium alloys at elevated temperatures". In: *Materials at high temperatures* 16.4 (1999), pp. 161–172.

[75] Military Handbook. "MIL-HDBK-5H: metallic materials and elements for aerospace vehicle structures". In: *US Department of Defense* (1998), p. 32.

[76] MS Binning and PG Partridge. "Subzero tensile properties of 7010 aluminium alloy and Ti-6A1-4V and IMI550 titanium alloys in sheet form". In: *Cryogenics* 24.2 (1984), pp. 97–105.

[77] Raymond D Lohr. *Ultra high temperature mechanical testing*. CRC Press, 1995.

[78] Vernon John. *Testing of materials*. Macmillan Publishers Limited, 1992.

[79] Harmer Elmer Davis, George Earl Troxell, and George FW Hauck. "The testing of engineering materials". In: (1982).

[80] ENISO DIN. "6892-2: 2011: Metallic materials-Tensile testing-Part 2: Method of test at elevated temperature". In: *German version EN ISO* (2011), pp. 6892–2.

[81] AS. "Methods for the tensile testing of metals at elevated temperatures". In: *Australian Standard* (1979).

[82] DJ Steinberg, SG Cochran, and MW Guinan. "A constitutive model for metals applicable at high-strain rate". In: *Journal of Applied Physics* 51.3 (1980), pp. 1498–1504.

[83] DJ Steinberg and CM Lund. "A constitutive model for strain rates from 10-4 to 106 s- 1". In: *Journal of Applied Physics* 65.4 (1989), pp. 1528–1533.

[84] Sol Rubin Bodner and Paul Southworth Symonds. "Experimental and theoretical investigation of the plastic deformation of cantilever beams subjected to impulsive loading". In: *Journal of Applied Mechanics* 29.4 (1962), pp. 719–728.

[85] Shun Rong Chen and George T Gray III. "Constitutive behavior of tungsten and tantalum: experiments and modeling". In: *Proceedings of the 2nd international conference on tungsten and refractory metals, metal powders industries federation, Princeton, New Jersey*. 1995, pp. 489–498.

[86] GR Johnson et al. "Response of various metals to large torsional strains over a large range of strain rates—Part 1: Ductile metals". In: *Journal of Engineering Materials and Technology* 105.1 (1983), pp. 42–47.

[87] GR Johnson et al. "Response of various metals to large torsional strains over a large range of strain rates—Part 2: less ductile metals". In: *Journal of Engineering Materials and Technology* 105.1 (1983), pp. 48–53.

[88] Gordon R Johnson and William H Cook. "A constitutive model and data for metals subjected to large strains, high strain rates and high temperatures". In: *Proceedings of the 7th International Symposium on Ballistics*. Vol. 21. The Hague, The Netherlands. 1983, pp. 541–547.

[89] TJ Holmquist and GR Johnson. "Determination of constants and comparison of results for various constitutive models". In: *Le Journal de Physique IV* 1.C3 (1991), pp. C3–853.

[90] Xicheng Huang, Jianshi Zhu, and Wenjun Hu. "INDENTIFICATION OF JOHNSON-COOK CONSTITUTIVE MODEL PARAMETERS FOR HIGHT STRAIN RATE DEFORMATION". In: ().

[91] B Langrand et al. "Identification technique of constitutive model parameters for crashworthiness modelling". In: *Aerospace Science and Technology* 3.4 (1999), pp. 215–227.

[92] Frank J Zerilli and Ronald W Armstrong. "Dislocation-mechanics-based constitutive relations for material dynamics calculations". In: *Journal of Applied Physics* 61.5 (1987), pp. 1816–1825.

[93] EO Hall. "The deformation and ageing of mild steel: III discussion of results". In: *Proceedings of the Physical Society. Section B* 64.9 (1951), p. 747.

[94] Niels Hansen. "Hall–Petch relation and boundary strengthening". In: *Scripta Materialia* 51.8 (2004), pp. 801–806.

[95] BD Goldthorpe. "Constitutive equations for annealed and explosively shocked iron for application to high strain rates and large strains". In: *Le Journal de Physique IV* 1.C3 (1991), pp. C3–829.

[96] YC Lin and Xiao-Min Chen. "A combined Johnson–Cook and Zerilli–Armstrong model for hot compressed typical high-strength alloy steel". In: *Computational Materials Science* 49.3 (2010), pp. 628–633.

[97] Yu Cao, Johan Ahlström, and Birger Karlsson. "The influence of temperatures and strain rates on the mechanical behavior of dual phase steel in different conditions". In: *Journal of Materials Research and Technology* 4.1 (2015), pp. 68–74.

[98] L Djapic Oosterkamp, A Ivankovic, and G Venizelos. "High strain rate properties of selected aluminium alloys". In: *Materials Science and Engineering: A* 278.1 (2000), pp. 225–235.

[99] AT ROOM. "School of Mechanical and Manufacture Engineering, Dublin City University, Ireland". In: *Advances in Engineering Plasticity and its Applications* (2012), p. 251.

[100] Ricardo Hernández Rossi et al. "FLSD as a good choice in sheet forming of AHSS". In: *2011 SIMULIA Customer Conference*. Dassault Systèmes. 2011, pp. 238–246.

[101] Anil K Sachdev. "Effect of retained austenite on the yielding and deformation behavior of a dual phase steel". In: *Acta Metallurgica* 31.12 (1983), pp. 2037–2042.

[102] Peter Hedström et al. "Load partitioning and strain-induced martensite formation during tensile loading of a metastable austenitic stainless steel". In: *Metallurgical and Materials Transactions A* 40.5 (2009), pp. 1039–1048.

[103] Andrew Magee and Leila Ladani. "Strength and failure of ultrafine grain and bimodal Al-Mg alloy at high temperature". In: *Light Metals* 1 (2013), pp. 279–282.

[104] L Weber et al. "On the use of Considere's criterion in tensile testing of materials which accumulate internal damage". In: *Scripta materialia* 41.5 (1999), pp. 549–551.

[105] E Mecozzi and B Zhao. "Development of stress-strain relationships of cold-formed lightweight steel at elevated temperatures". In: *Proceedings of 4th European Conference on Steel and Composite Structures-Eurosteel 2005*. 2005, pp. 41–49.

[106] Toshiji Mukai, Kenji Higashi, and Shinji Tanimura. "Influence of the magnesium concentration on the relationship between fracture mechanism and strain rate in high purity Al Mg alloys". In: *Materials Science and Engineering: A* 176.1-2 (1994), pp. 181–189.

[107] DWA Rees. "Forming properties of four high-strength sheet steels". In: *Proceedings of the Institution of Mechanical Engineers, Part B: Journal of Engineering Manufacture* 220.11 (2006), pp. 1815–1825.

[108] Richard Courant et al. "Variational methods for the solution of problems of equilibrium and vibrations". In: *Bull. Amer. Math. Soc* 49.1 (1943), pp. 1–23.

[109] Alexander Hrennikoff. "Solution of problems of elasticity by the framework method". In: *Journal of applied mechanics* 8.4 (1941), pp. 169–175.

[110] Isaac Jacob Schönberg. "Contributions to the problem of approximation of equidistant data by analytic functions". In: *IJ Schoenberg Selected Papers*. Springer, 1988, pp. 3–57.

[111] DS Burrent. "Finite Element Analysis: from Concepts to Application". In: *Reading: Addison-Wesley* 5 (1987), pp. 128–206.

[112] David Hutton. *Fundamentals of finite element analysis*. McGraw-Hill, 2004.

[113] P Seshu. *Textbook of finite element analysis*. PHI Learning Pvt. Ltd., 2003.

[114] *ABAQUS/CAE user's manual:version 6.13*. abaqus, 2003.

[115] Y Chen et al. "Stress–strain behaviour of aluminium alloys at a wide range of strain rates". In: *International Journal of Solids and Structures* 46.21 (2009), pp. 3825–3835.

[116] E El-Magd and M Abouridouane. "Influence of strain rate and temperature on the compressive ductility of AI, Mg and Ti alloys". In: *Journal de Physique IV (Proceedings)*. Vol. 110. EDP sciences. 2003, pp. 15–20.

[117] WJ Kang et al. "Modified Johnson-Cook model for vehicle body crashworthiness simulation". In: *International journal of vehicle design* 21.4-5 (1999), pp. 424–435.

[118] FJ Zerilli and RW Armstrong. "The effect of dislocation drag on the stress-strain behavior of fcc metals". In: *Acta Metallurgica et Materialia* 40.8 (1992), pp. 1803–1808.

[119] FJ Zerilli and RW Armstrong. "Dislocation mechanics based constitutive relations for dynamic straining to tensile instability". In: *Shock compression of condensed matter* (1989), pp. 357–361.

[120] Timothy K Hight and John F Brandeau. “Mathematical modeling of the stress strain-strain rate behavior of bone using the Ramberg-Osgood equation”. In: *Journal of biomechanics* 16.6 (1983), pp. 445–450.

[121] Naser Mostaghel and Ryan A Byrd. “Inversion of Ramberg–Osgood equation and description of hysteresis loops”. In: *International Journal of Non-Linear Mechanics* 37.8 (2002), pp. 1319–1335.

[122] Masayuki Kamaya. “Ramberg–Osgood type stress–strain curve estimation using yield and ultimate strengths for failure assessments”. In: *International Journal of Pressure Vessels and Piping* 137 (2016), pp. 1–12.

[123] Jun-sheng Zhao, Yuan-tong Gu, and Wen-xin Fan. “Variable-based Ramberg–Osgood constitutive model of power spinning bushing”. In: *Transactions of Nonferrous Metals Society of China* 25.9 (2015), pp. 3080–3087.

[124] Nirosha Dolamune Kankanamge and Mahen Mahendran. “Mechanical properties of cold-formed steels at elevated temperatures”. In: *Thin-Walled Structures* 49.1 (2011), pp. 26–44.

[125] Tudor Sireteanu et al. “A comparative study of the dynamic behavior of Ramberg–Osgood and Bouc–Wen hysteresis models with application to seismic protection devices”. In: *Engineering Structures* 76 (2014), pp. 255–269.

[126] Adam Niesłony et al. “New method for evaluation of the Manson–Coffin–Basquin and Ramberg–Osgood equations with respect to compatibility”. In: *International Journal of Fatigue* 30.10 (2008), pp. 1967–1977.

[127] A Navarro. “An unconditionally convergent iterative algorithm for the intersection of Neuber’s and Molski–Glinka’s rules with the Ramberg–Osgood stress–strain relationship”. In: *Theoretical and Applied Fracture Mechanics* 69 (2014), pp. 53–62.

[128] RP Skelton, HJ Maier, and H-J Christ. “The Bauschinger effect, Masing model and the Ramberg–Osgood relation for cyclic deformation in metals”. In: *Materials Science and Engineering: A* 238.2 (1997), pp. 377–390.

[129] KW Poh. “Stress-strain-temperature relationship for structural steel”. In: *Journal of Materials in Civil Engineering* 13.5 (2001), pp. 371–379.

Appendices

Appendix A

Appendix A

A.1 Uni-axial

A.1.1 Flat samples

Provided below are Stress Strain responses carried with the dogbone geometry in uni-axial tension.

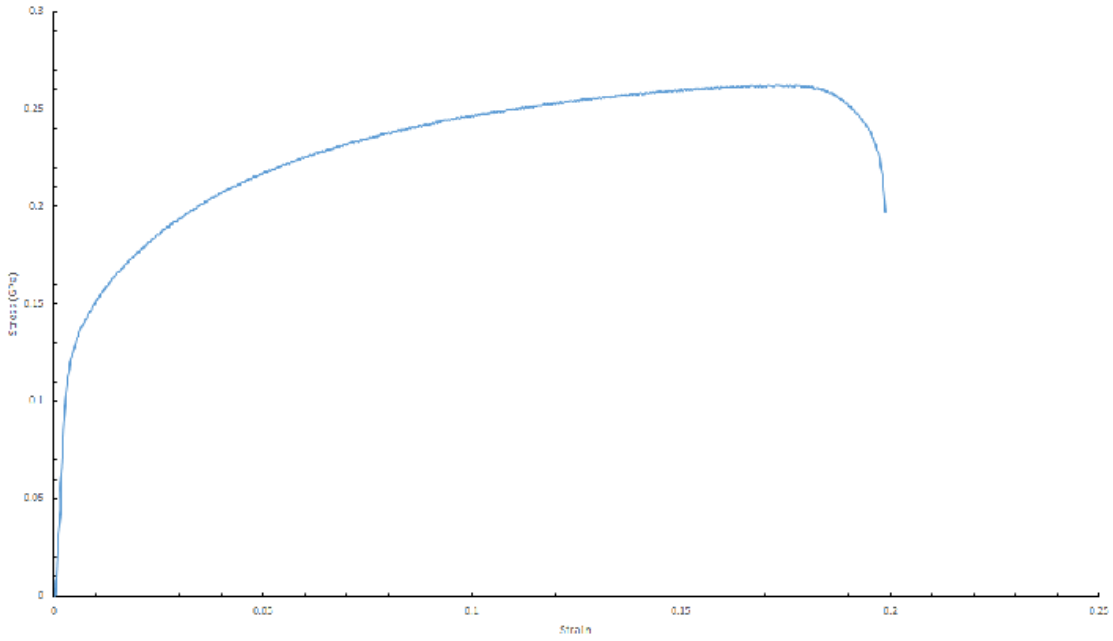

Figure A.1: Stress strain response for 0.13% C-steel, 1mm, 3mm/min and 23C

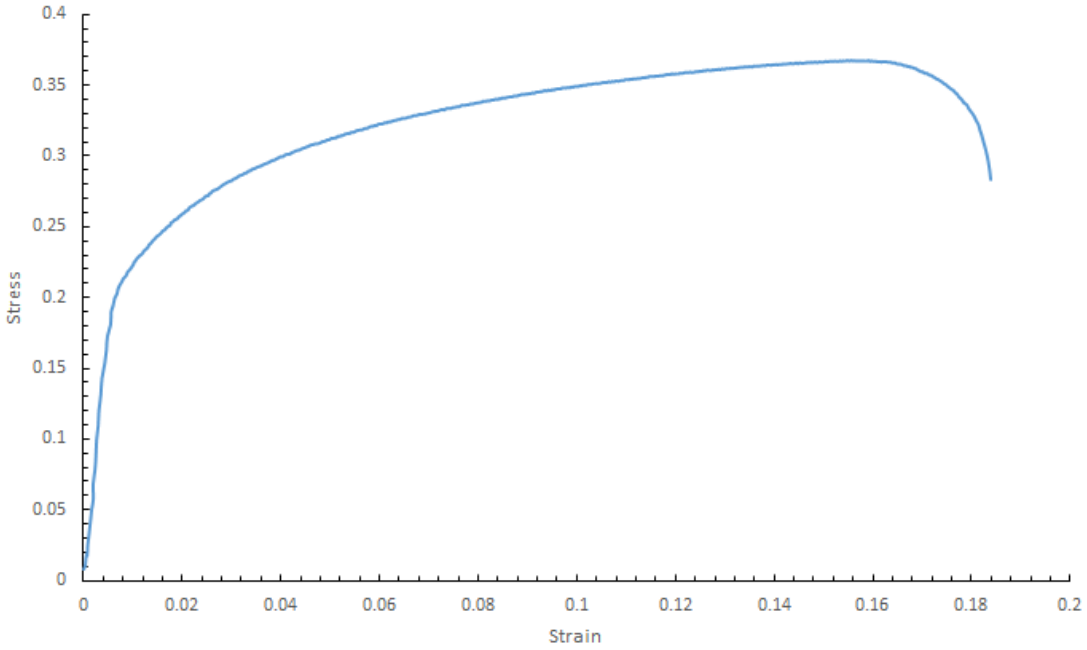

Figure A.2: Stress strain response for 0.13% C-steel, 2mm, 3mm/min and 23C

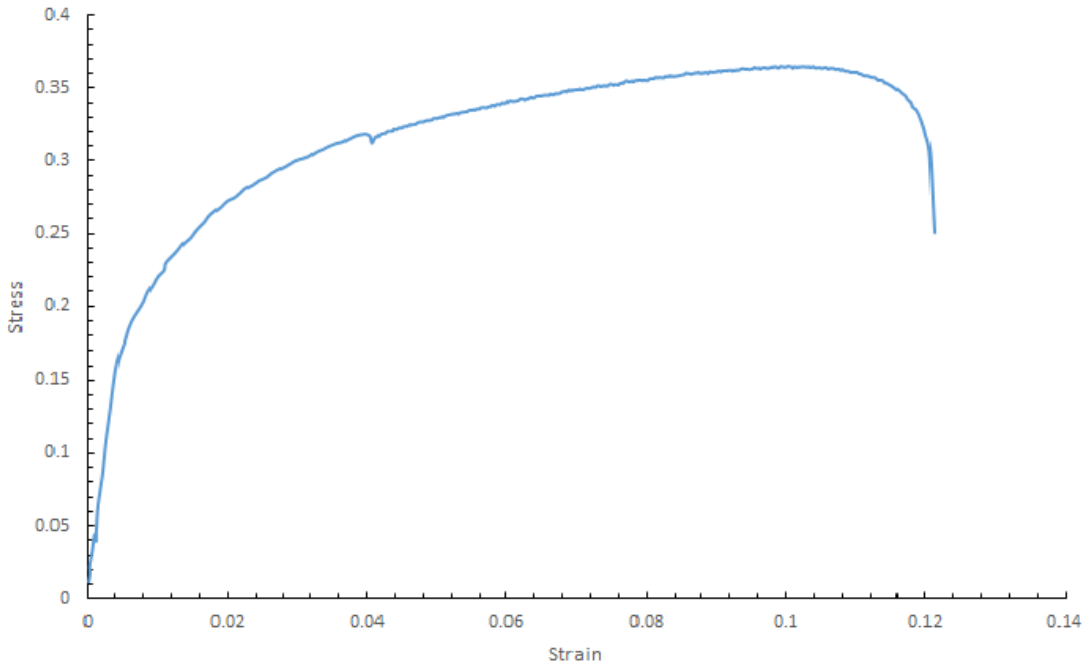

Figure A.3: Stress strain response for 0.13% C-steel, 1mm, 3mm/min and 300C

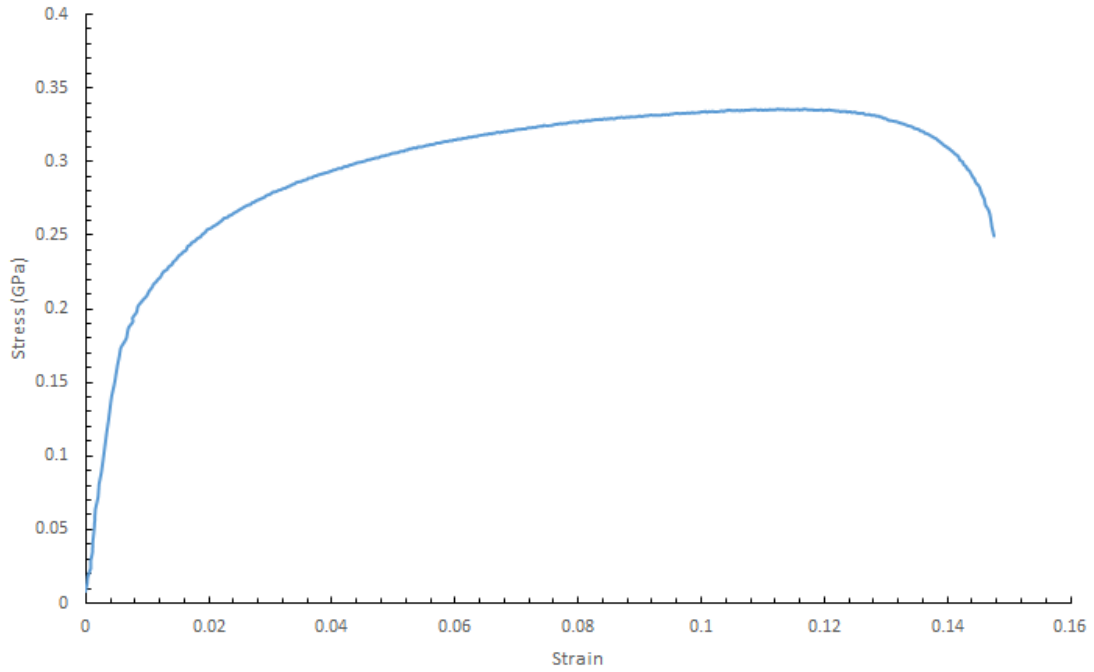

Figure A.4: Stress strain response for 0.13% C-steel, 2mm, 3mm/min and 300C

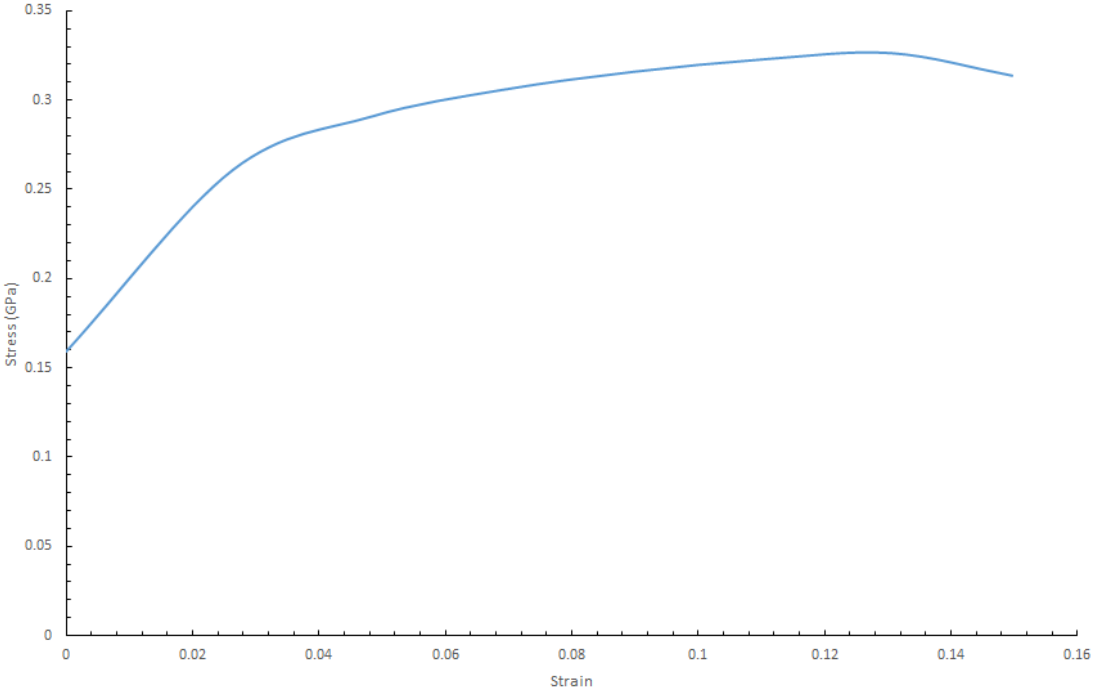

Figure A.5: Stress strain response for 0.13% C-steel, 1mm, 90mm/min and 350C

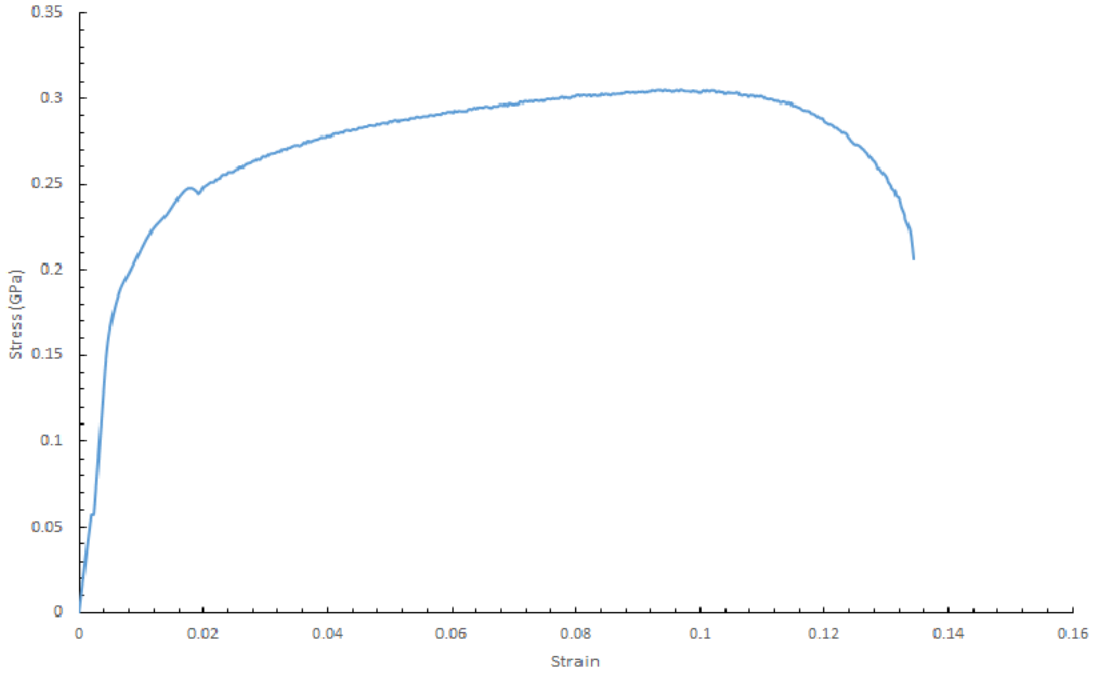

Figure A.6: Stress strain response for 0.13% C-steel, 1mm, 3mm/min and 350C

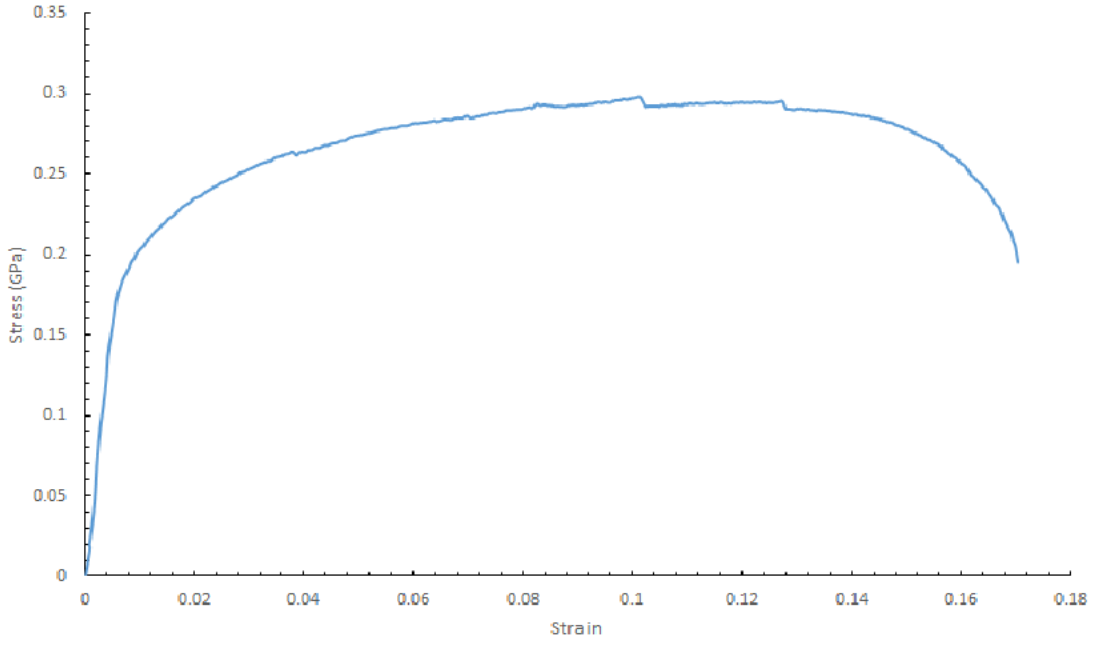

Figure A.7: Stress strain response for 0.13% C-steel, 2mm, 3mm/min and 350C

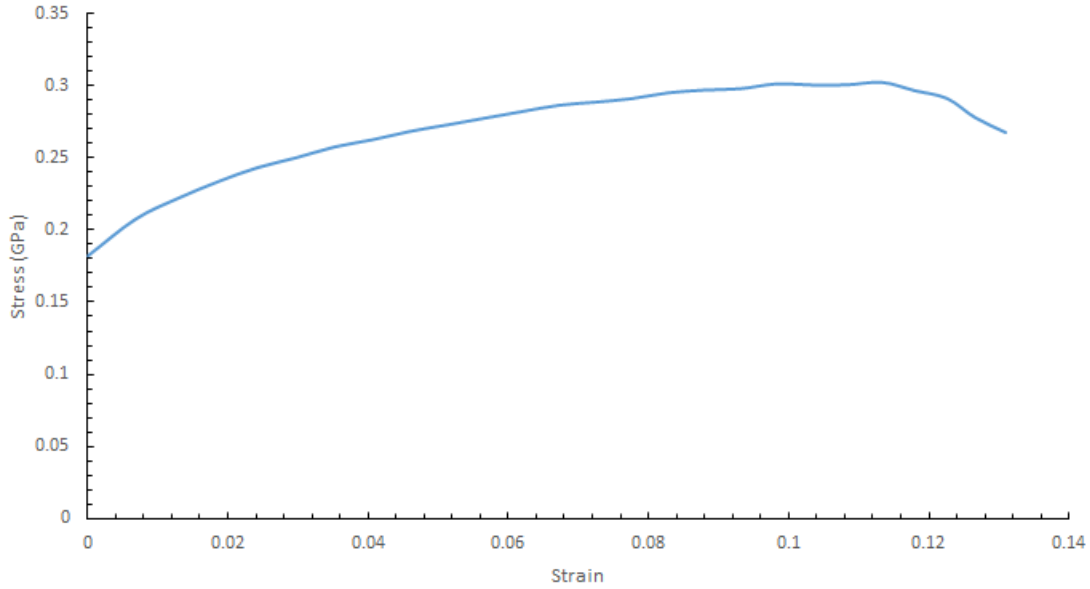

Figure A.8: Stress strain response for 0.13% C-steel, 1mm, 0.3mm/min and 350C

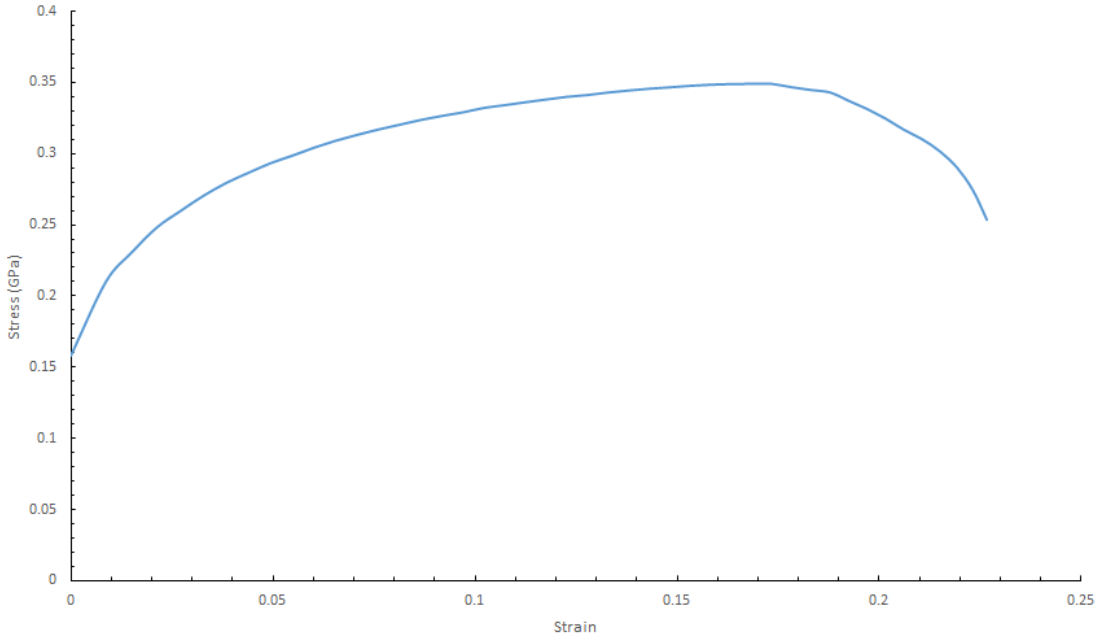

Figure A.9: Stress strain response for 0.13% C-steel, 2mm, 0.3mm/min and 350C

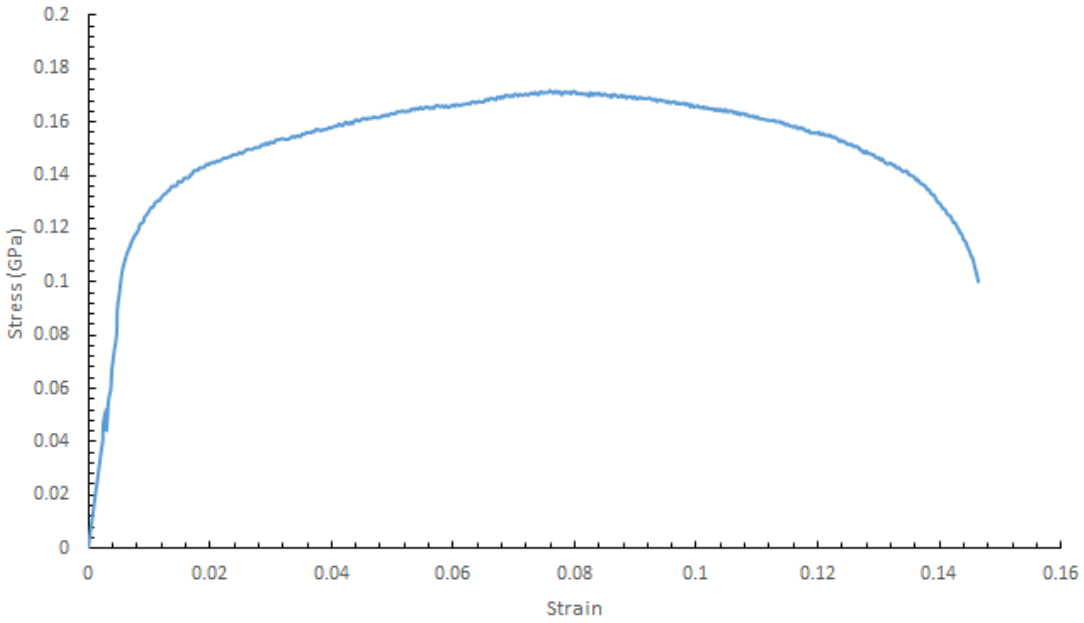

Figure A.10: Stress strain response for 0.13% C-steel, 1mm, 3mm/min and 400C

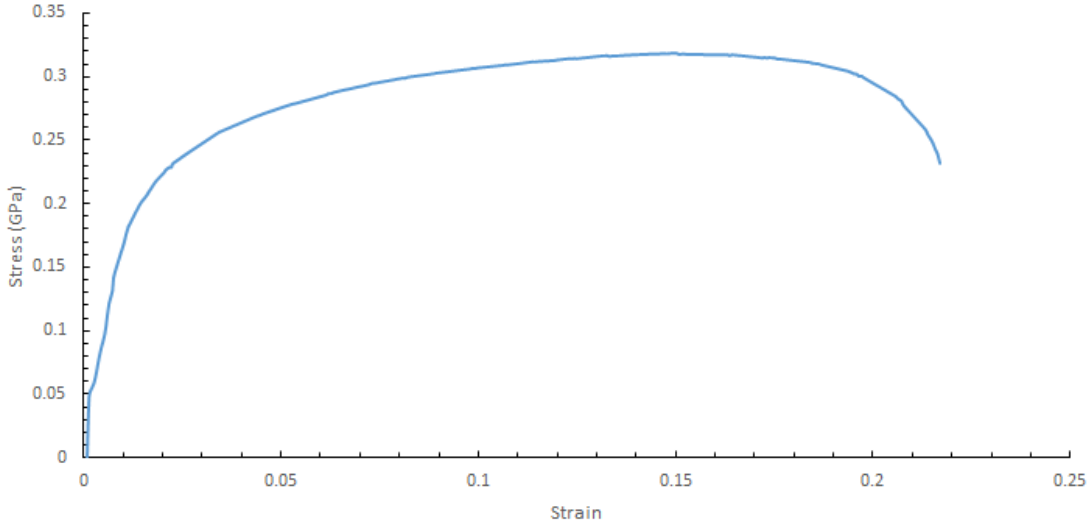

Figure A.11: Stress strain response for 0.13% C-steel, 2mm, 3mm/min and 400C

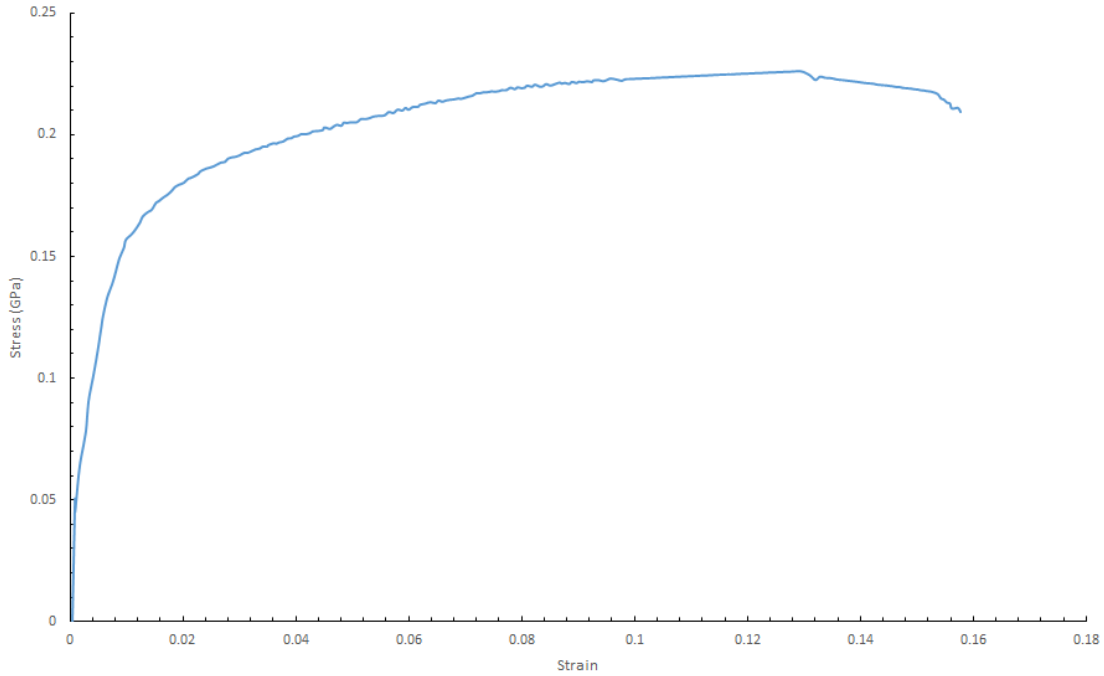

Figure A.12: Stress strain response for 0.13% C-steel, 1mm, 3mm/min and 450C

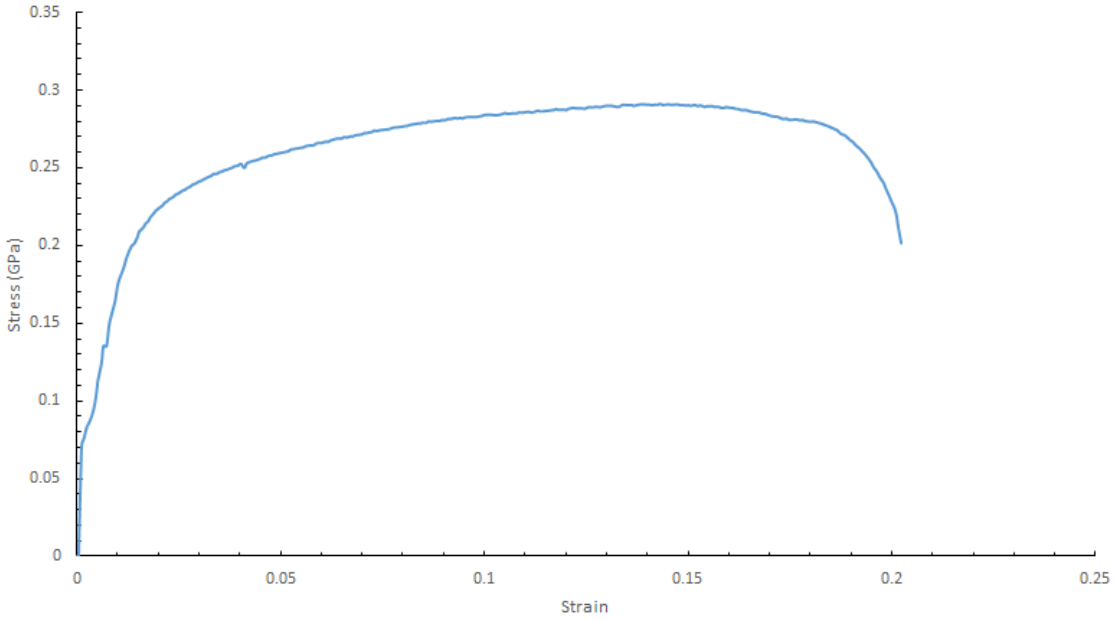

Figure A.13: Stress strain response for 0.13% C-steel, 2mm, 3mm/min and 450C

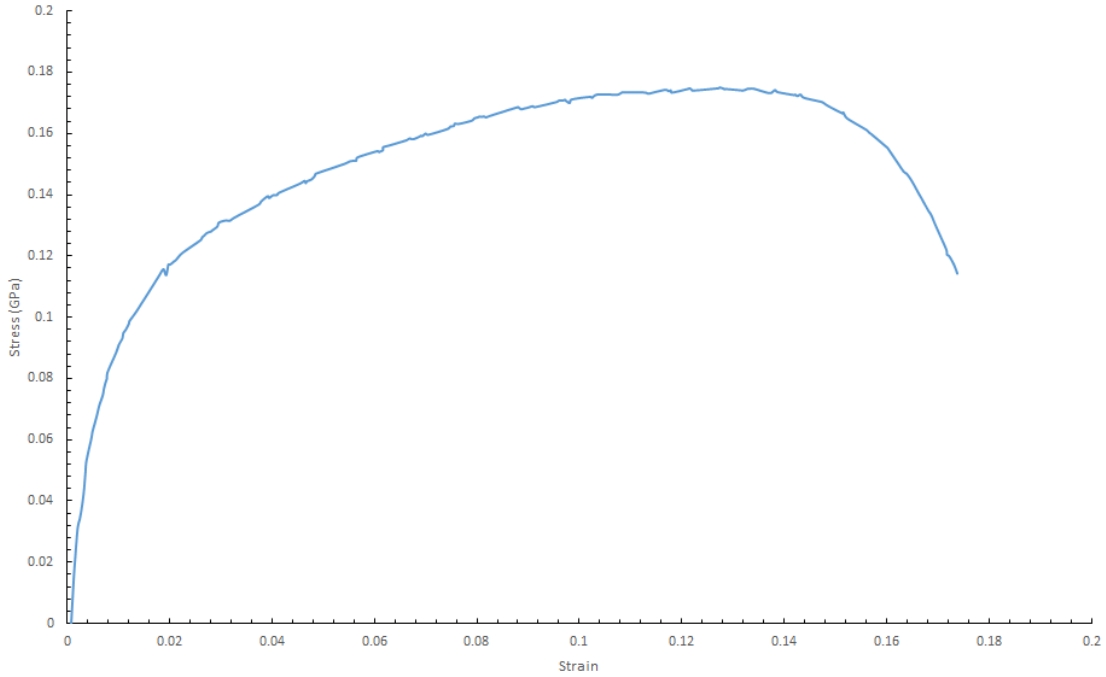

Figure A.14: Stress strain response for 0.13% C-steel, 1mm, 3mm/min and 500C

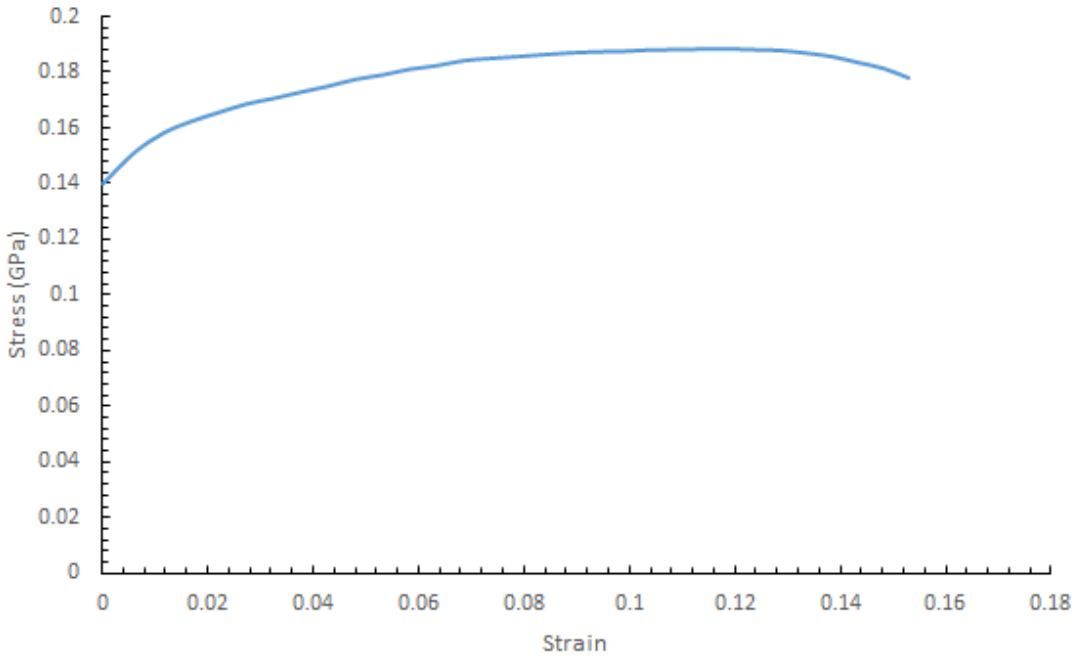

Figure A.15: Stress strain response for 0.13% C-steel, 2mm, 3mm/min and 500C

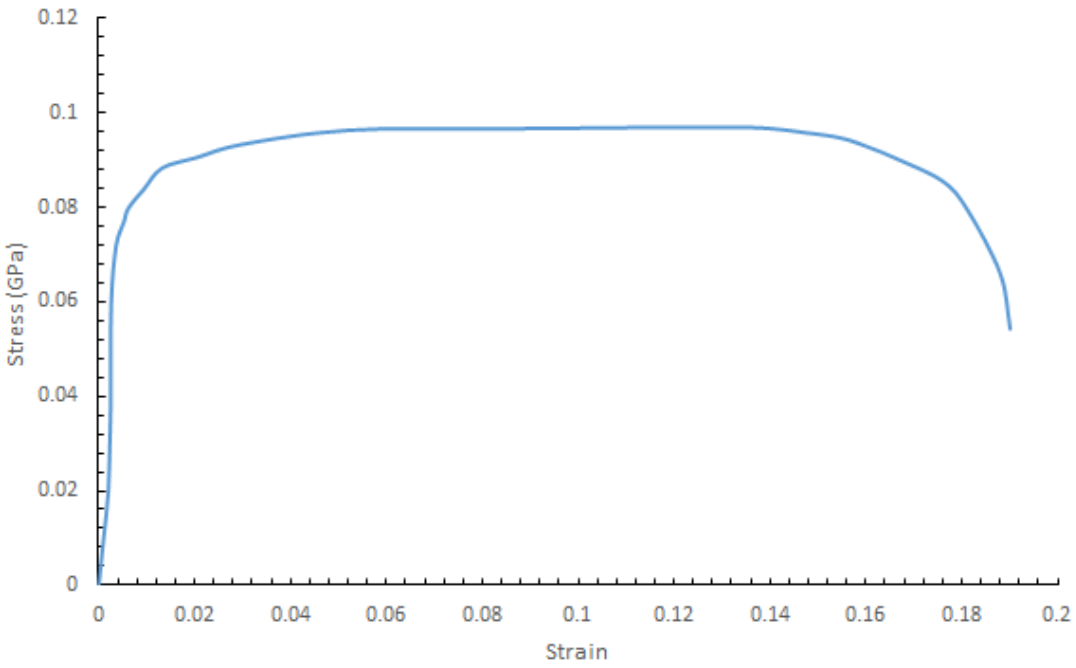

Figure A.16: Stress strain response for 0.13% C-steel, 0.6mm, 0.3mm/min and 600C

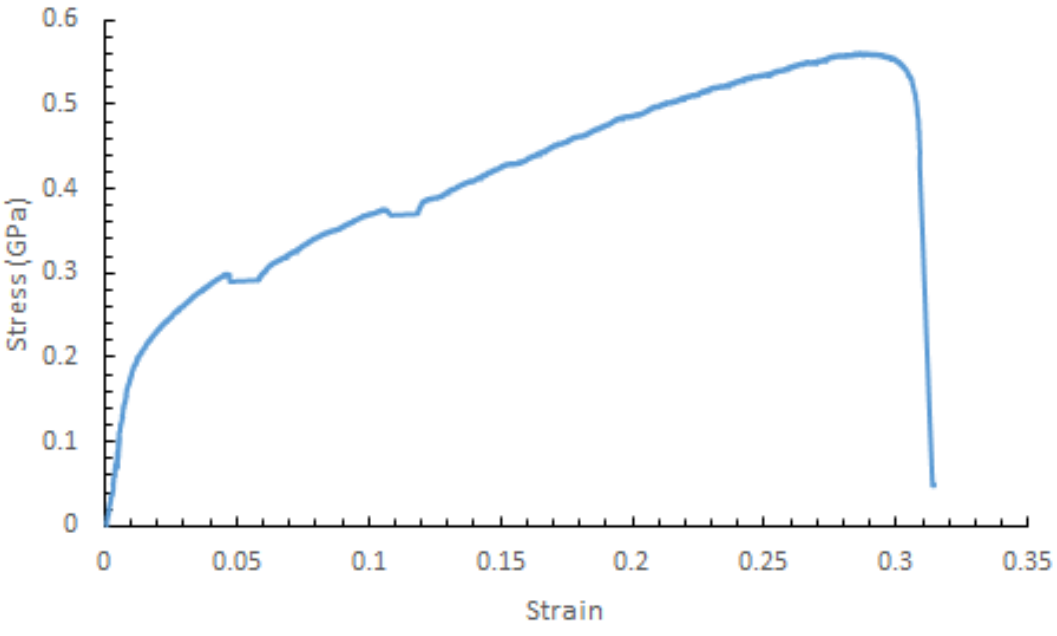

Figure A.17: Stress strain response for 0.13% C-steel, 0.6mm, 0.3mm/min and 300C

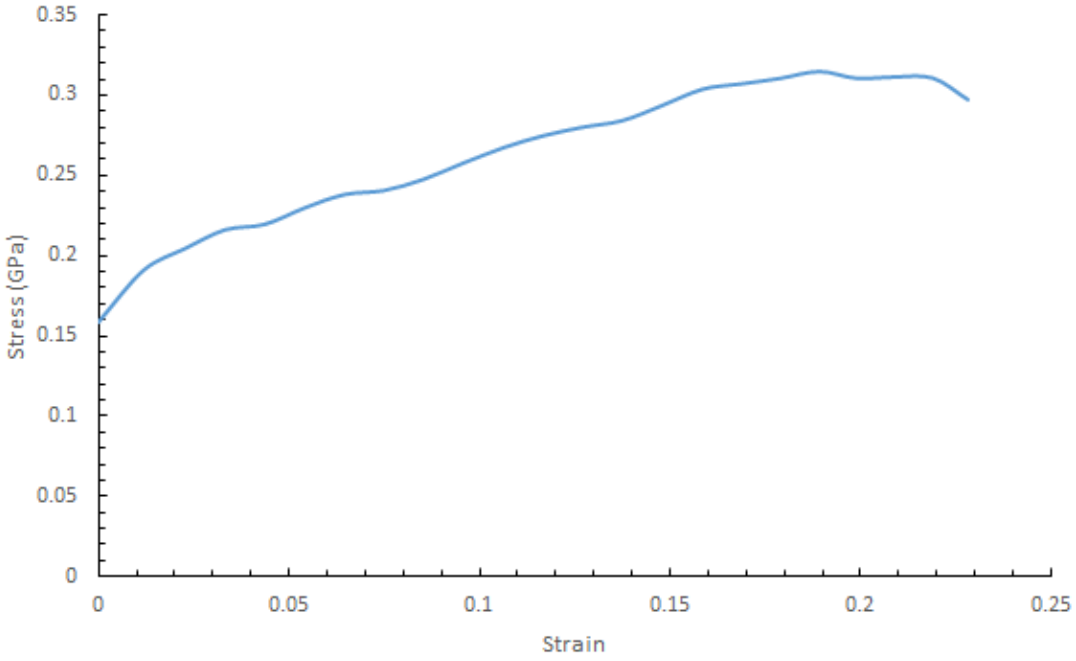

Figure A.18: Stress strain response for 0.13% C-steel, 0.6mm, 0.3mm/min and 400C

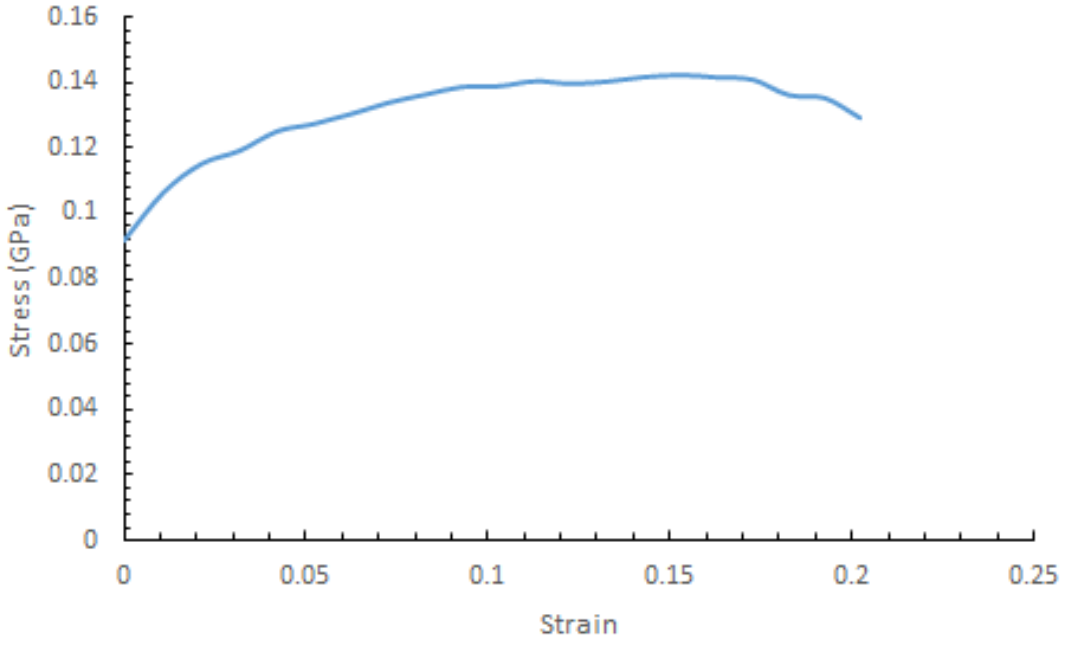

Figure A.19: Stress strain response for 0.13% C-steel, 0.6mm, 0.3mm/min and 500C

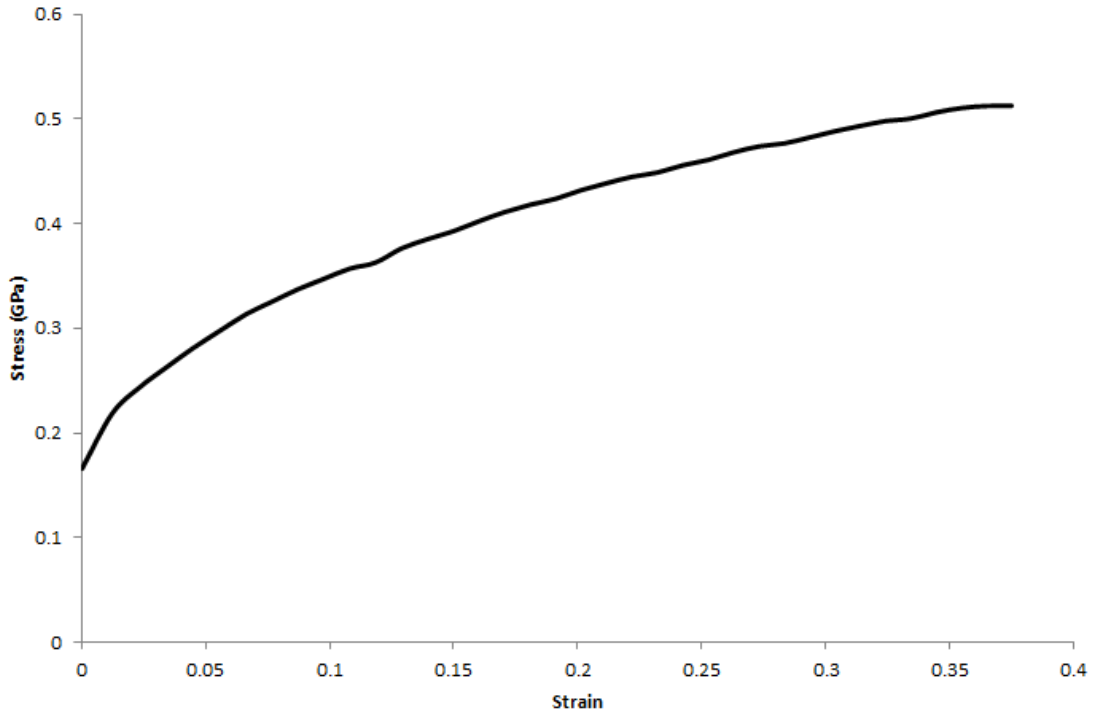

Figure A.20: Stress strain response for 0.13% C-steel, 0.6mm, 0.3mm/min and 23C

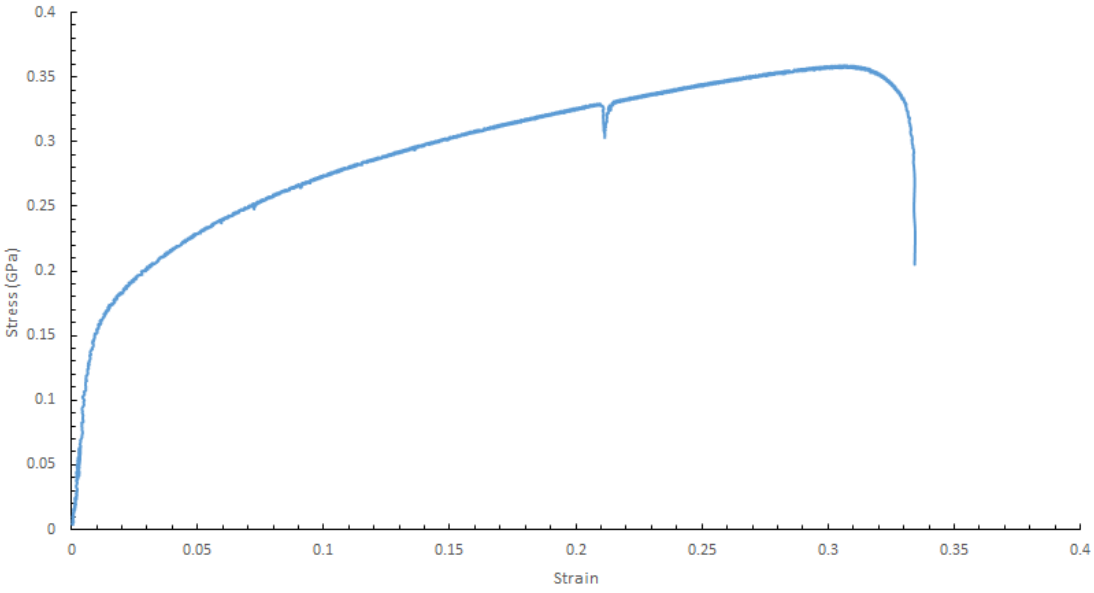

Figure A.21: Stress strain response for 0.13% C-steel, 0.9mm, 0.3mm/min and 23C

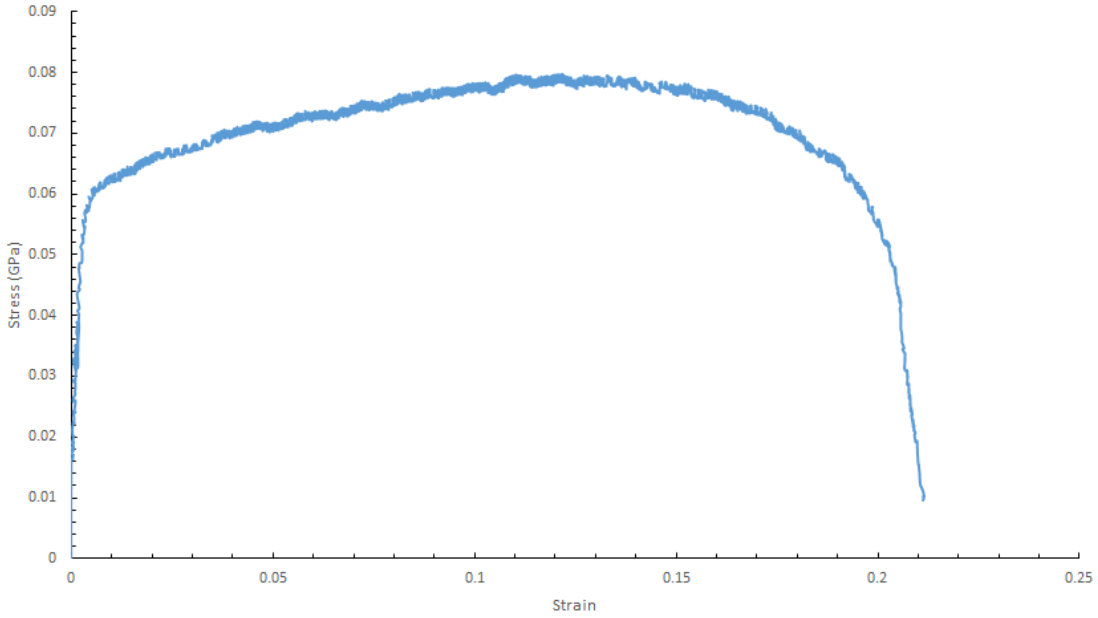

Figure A.22: Stress strain response for 0.13% C-steel, 0.9mm, 0.3mm/min and 600C

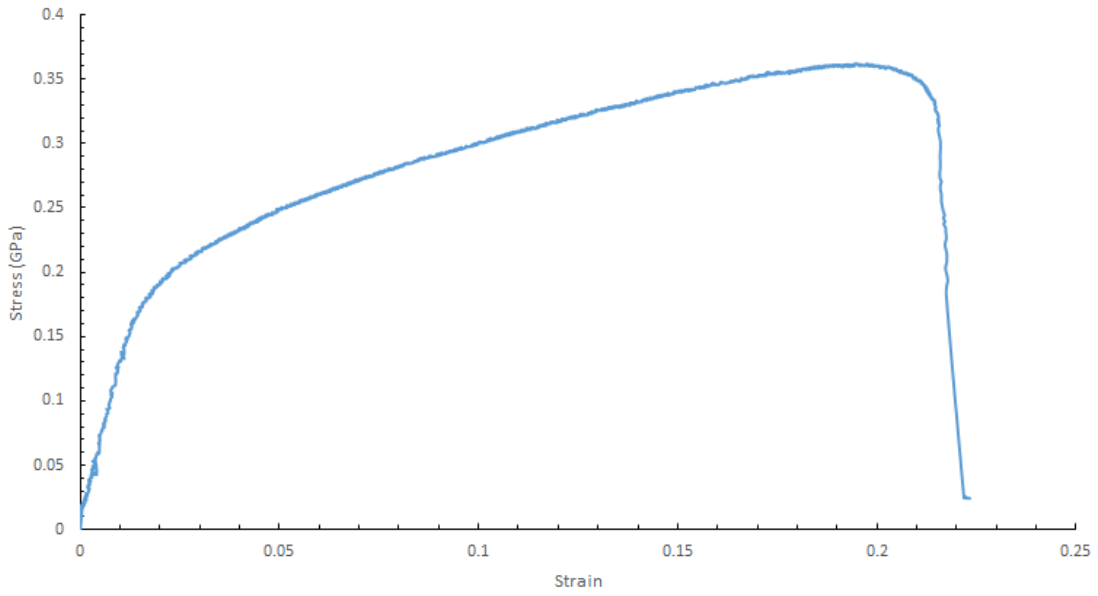

Figure A.23: Stress strain response for 0.13% C-steel, 0.9mm, 0.3mm/min and 300C

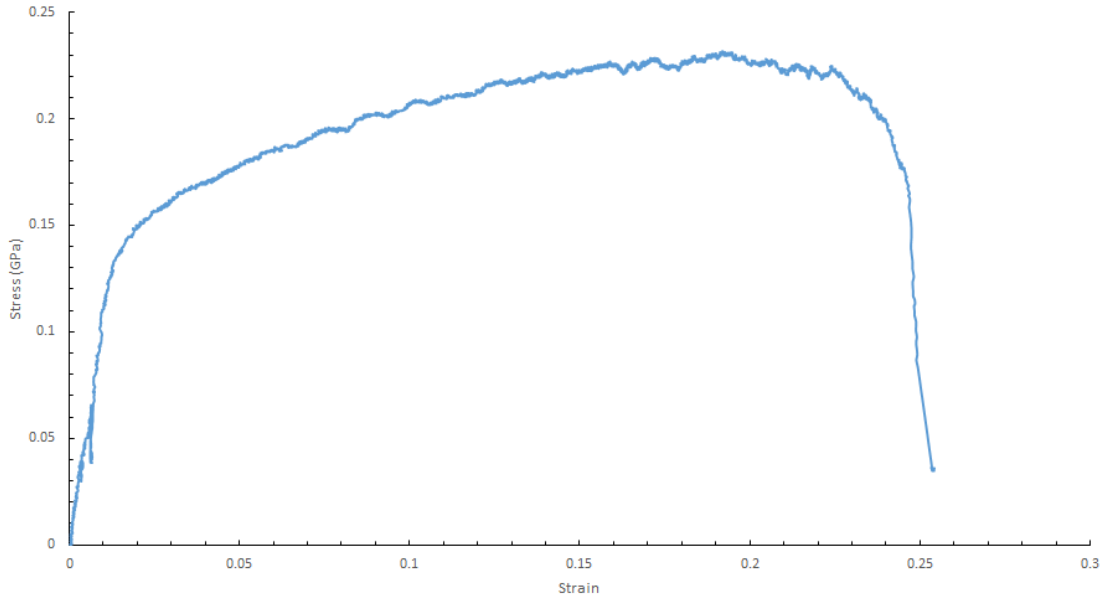

Figure A.24: Stress strain response for 0.13% C-steel, 0.9mm, 0.3mm/min and 400C

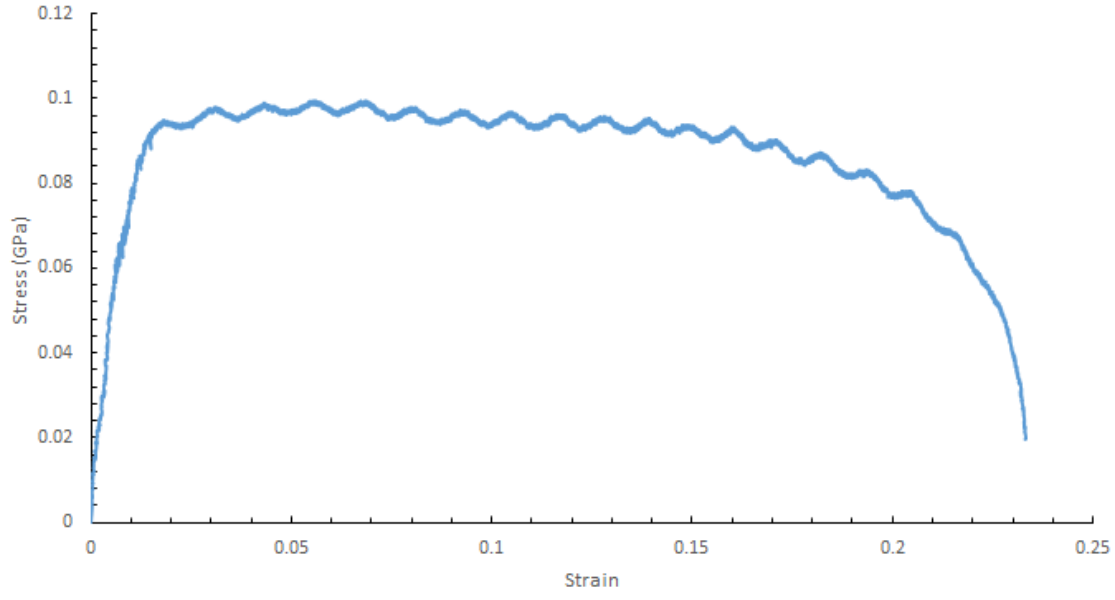

Figure A.25: Stress strain response for 0.13% C-steel, 0.9mm, 0.3mm/min and 500C

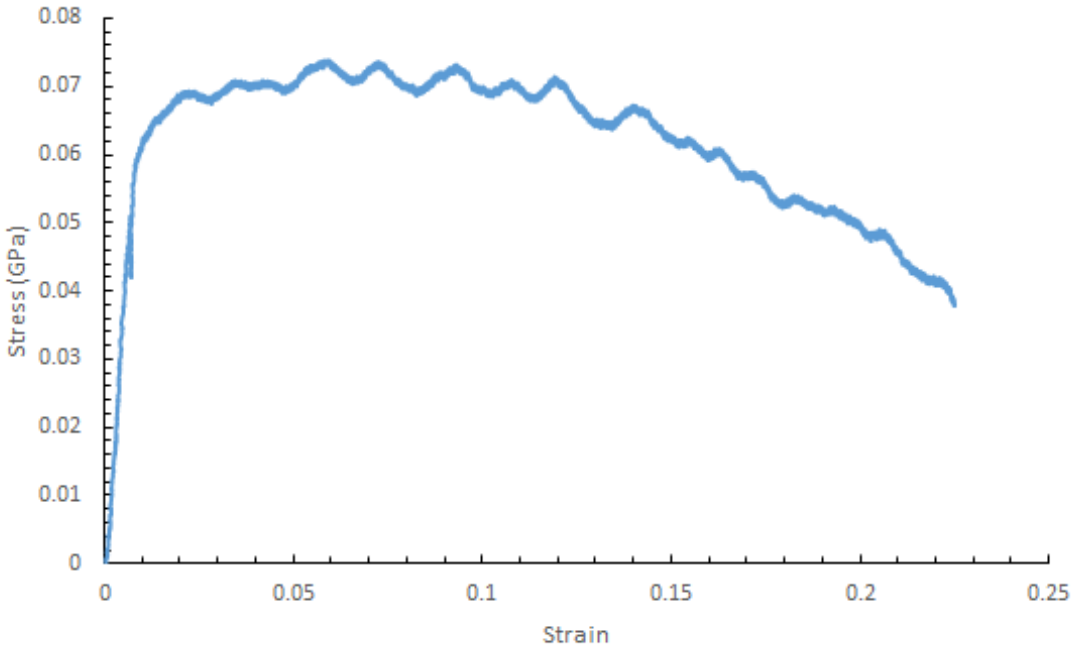

Figure A.26: Stress strain response for 0.13% C-steel, 1.1mm, 0.3mm/min and 500C

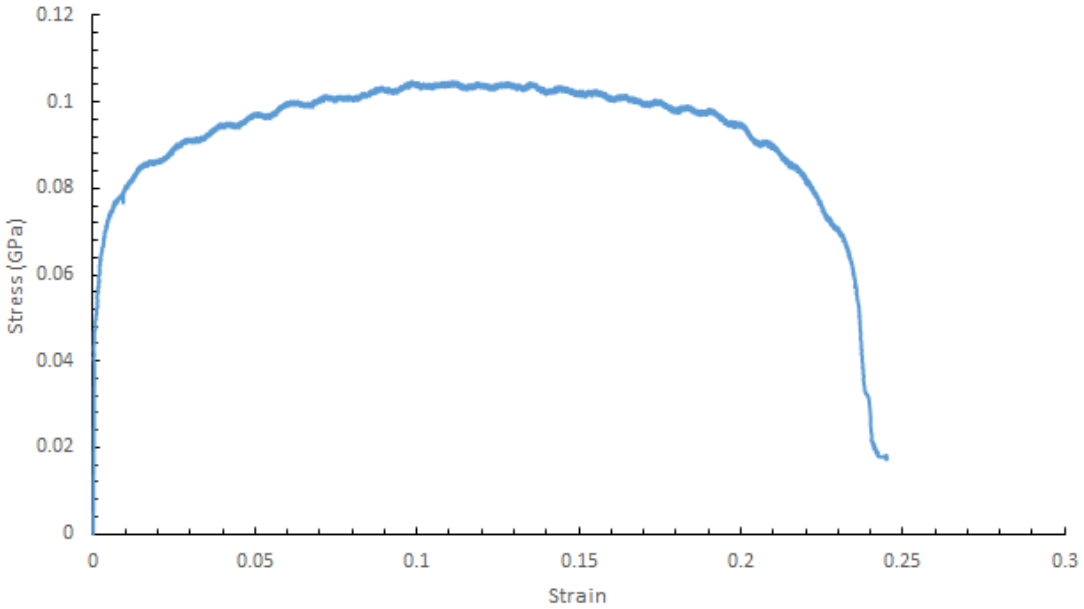

Figure A.27: Stress strain response for 0.13% C-steel, 1.1mm, 0.3mm/min and 600C

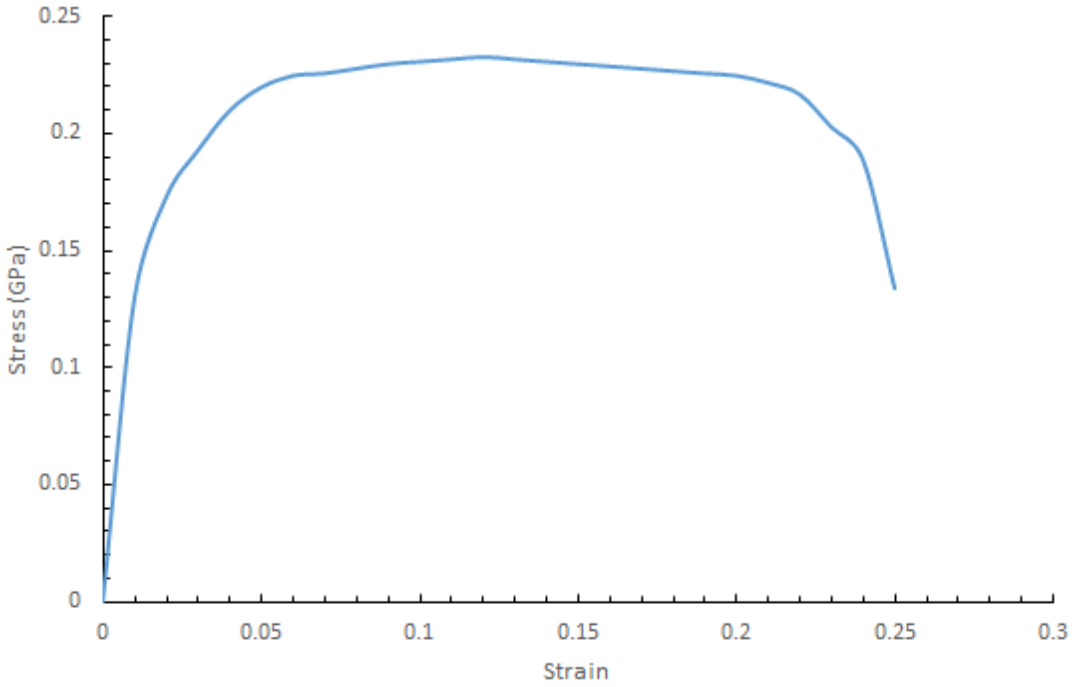

Figure A.28: Stress strain response for 0.13% C-steel, 1.1mm, 0.3mm/min and 300C

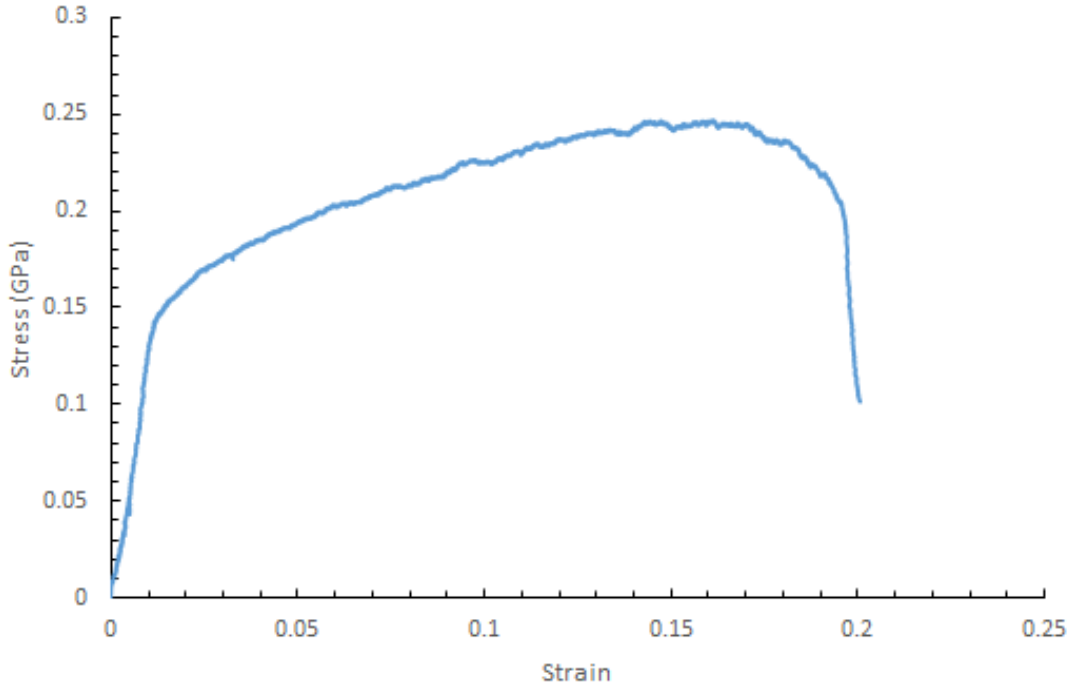

Figure A.29: Stress strain response for 0.13% C-steel, 1.1mm, 0.3mm/min and 400C

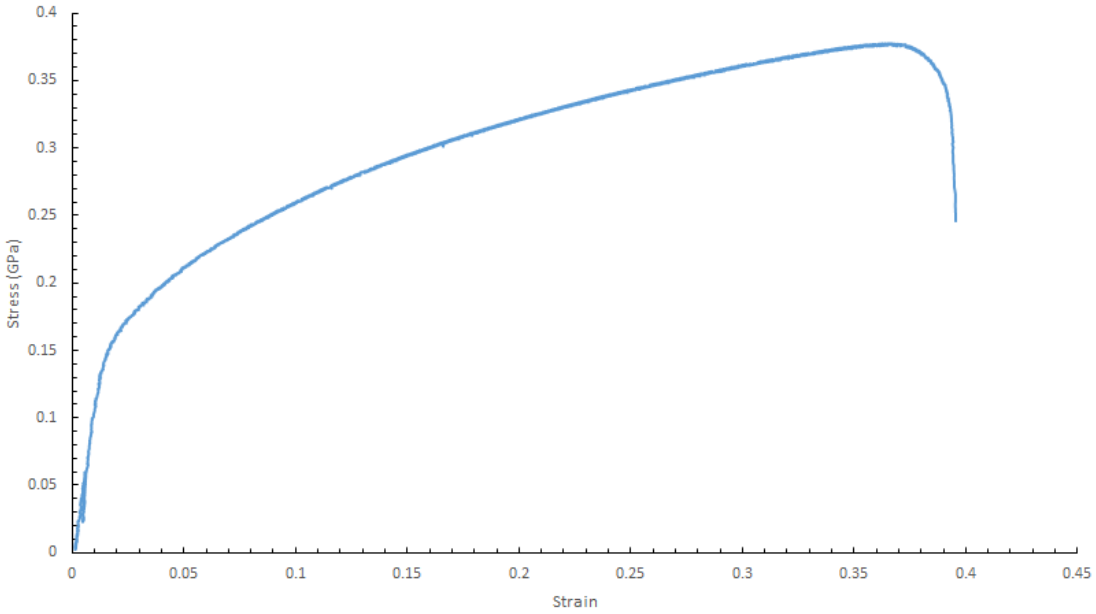

Figure A.30: Stress strain response for 0.13% C-steel, 1.1mm, 0.3mm/min and 23C

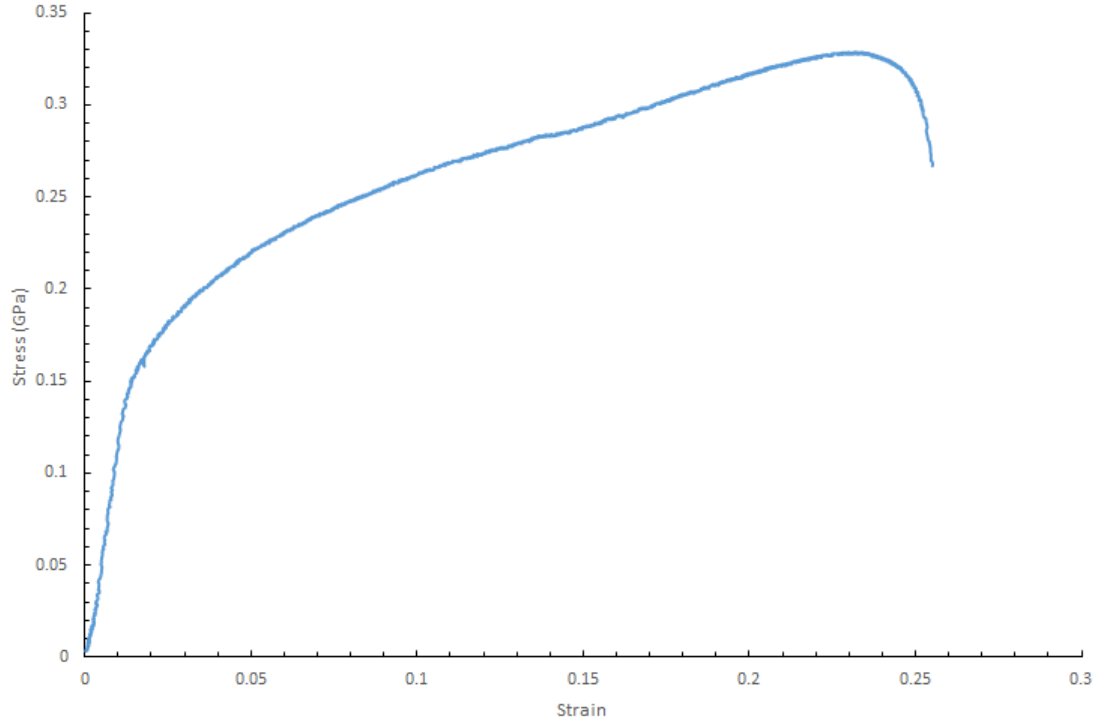

Figure A.31: Stress strain response for 0.13% C-steel, 1.3mm, 0.3mm/min and 300C

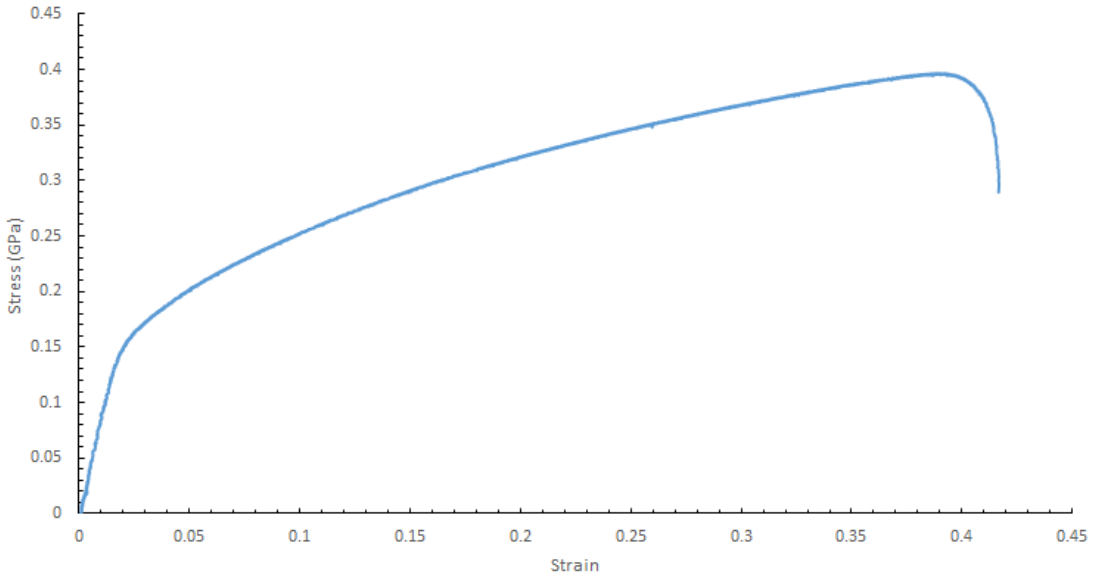

Figure A.32: Stress strain response for 0.13% C-steel, 1.3mm, 0.3mm/min and 400C

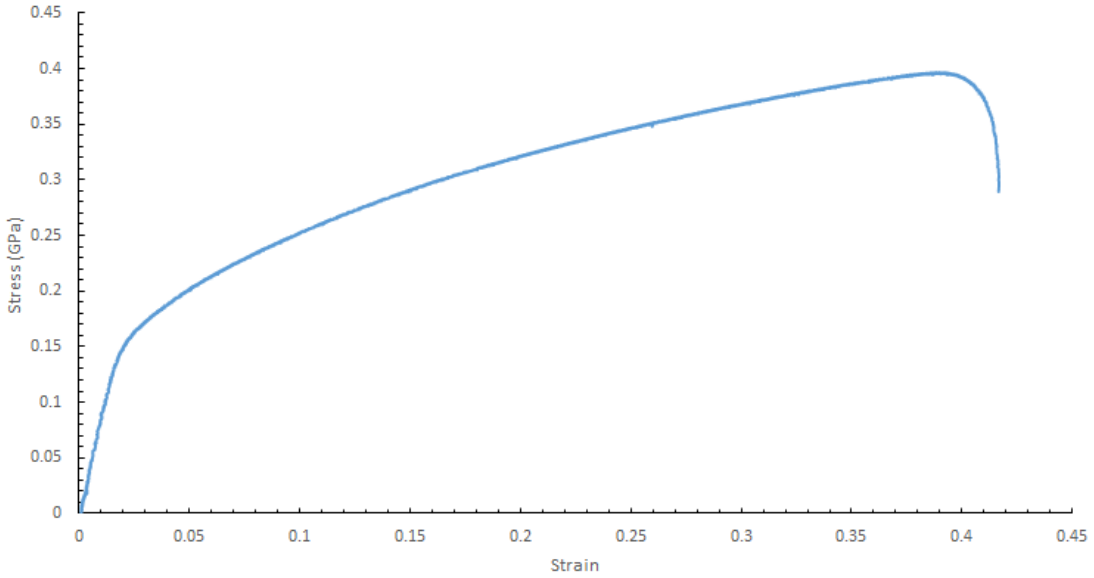

Figure A.33: Stress strain response for 0.13% C-steel, 1.3mm, 0.3mm/min and 23C

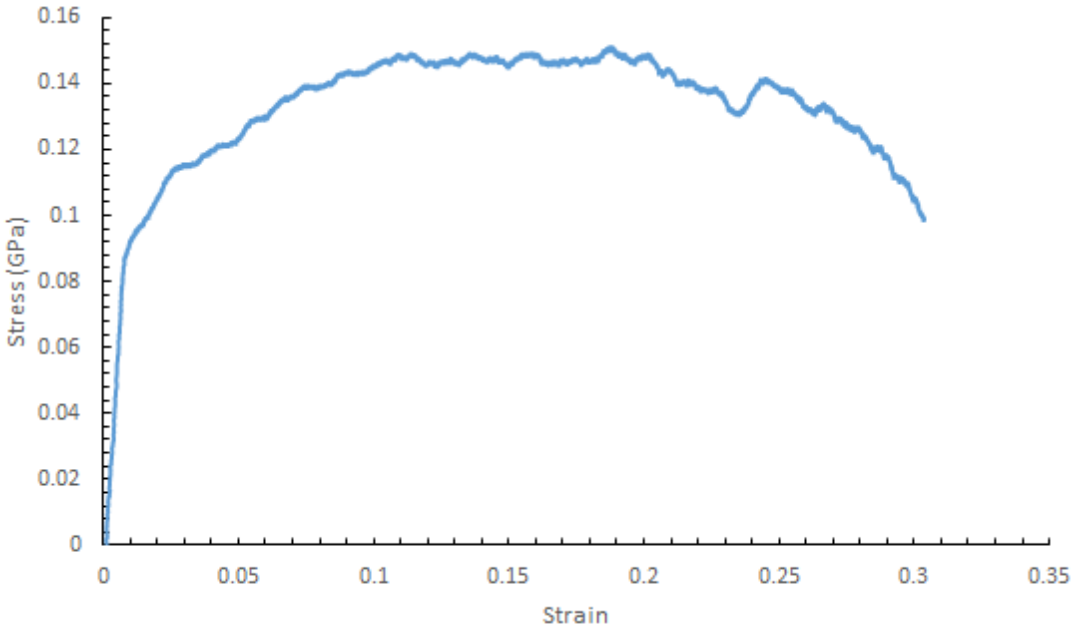

Figure A.34: Stress strain response for 0.13% C-steel, 1.3mm, 0.3mm/min and 500C

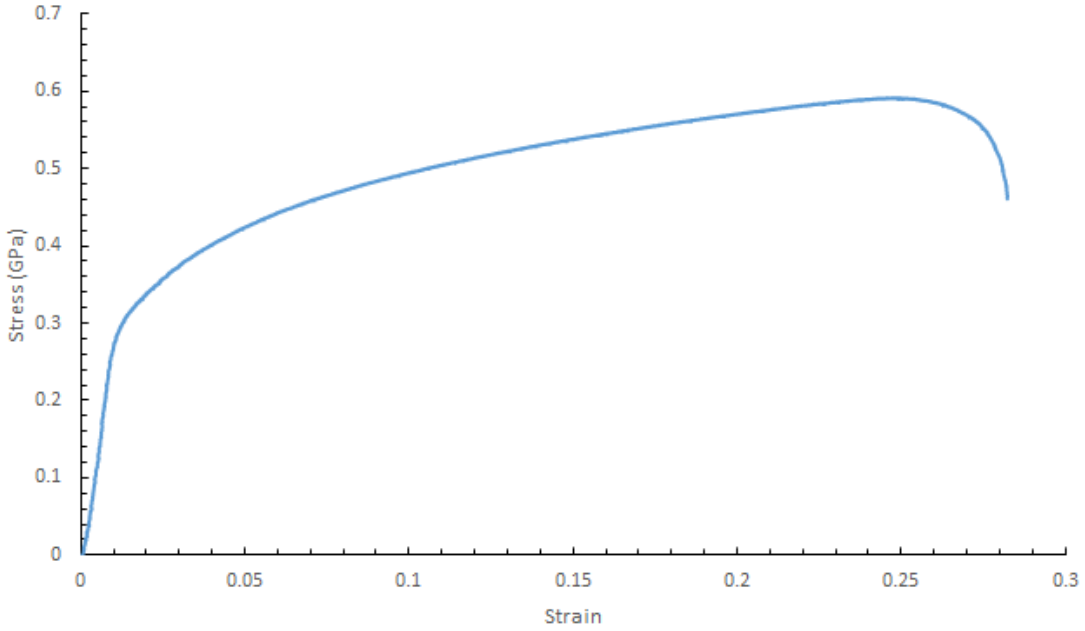

Figure A.35: Stress strain response for 0.13% C-steel, 1.3mm, 0.3mm/min and 600C

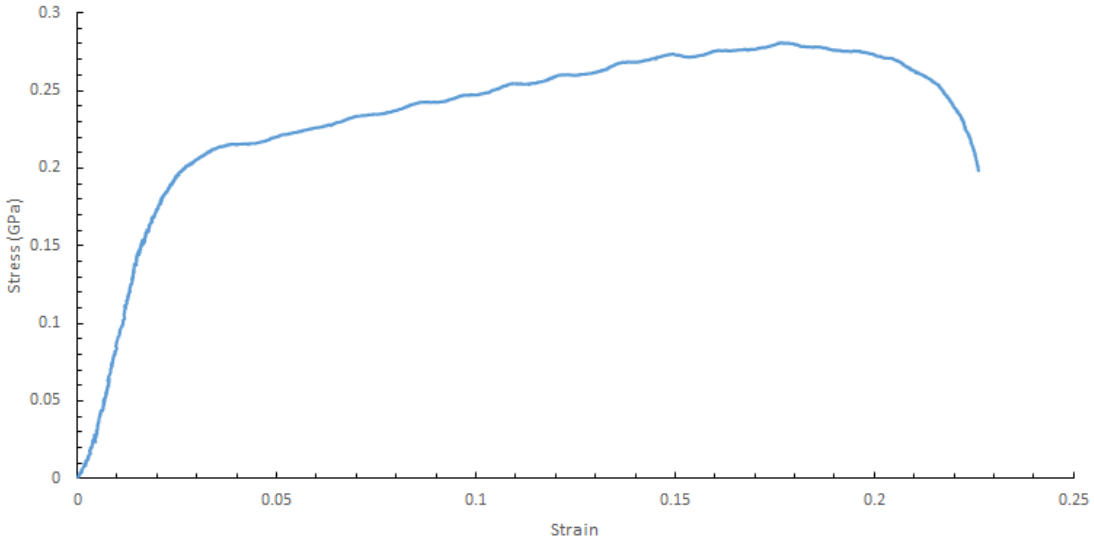

Figure A.36: Stress strain response for 0.13% C-steel, 2.8mm, 0.3mm/min and 400C

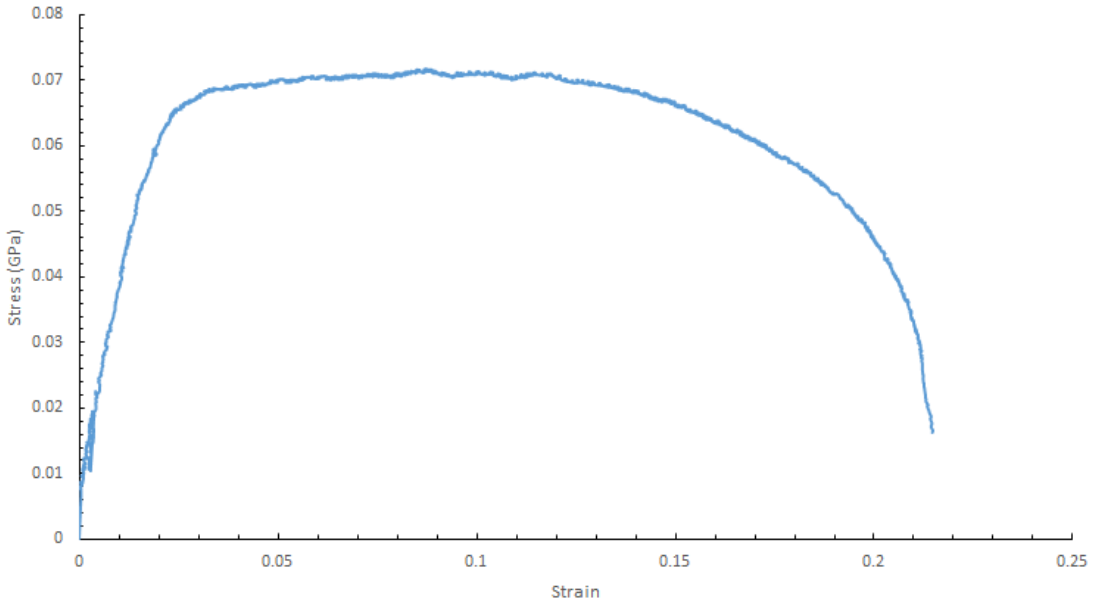

Figure A.37: Stress strain response for 0.13% C-steel, 2.8mm, 0.3mm/min and 600C

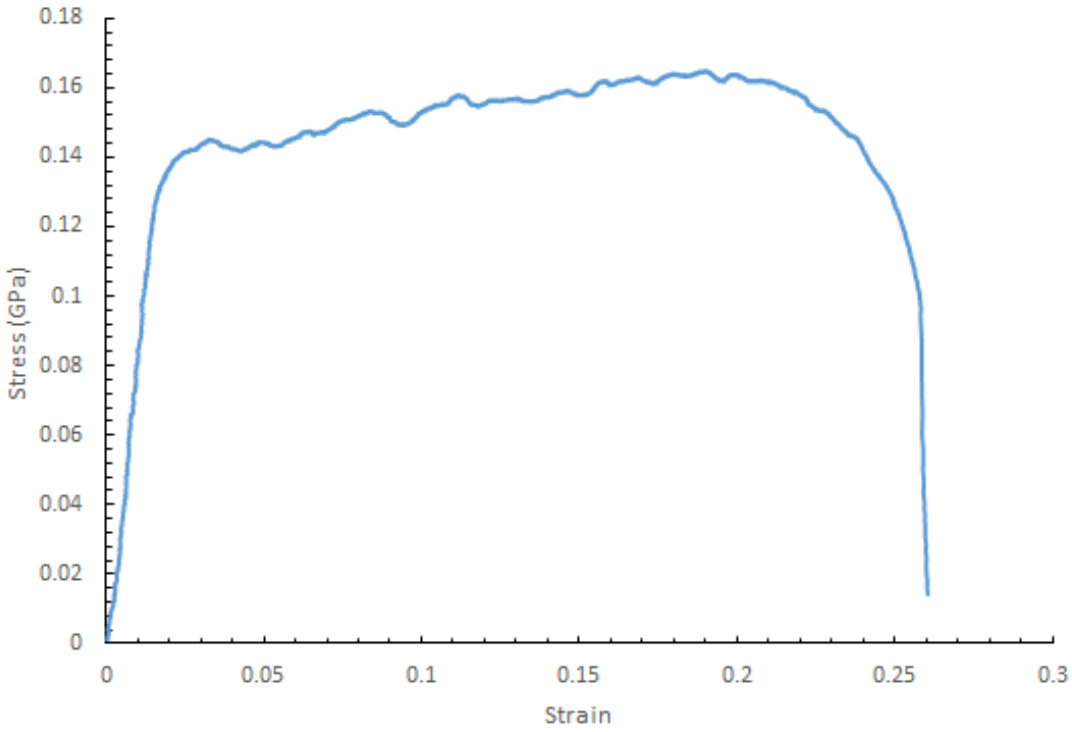

Figure A.38: Stress strain response for 0.13% C-steel, 2.8mm, 0.3mm/min and 500C

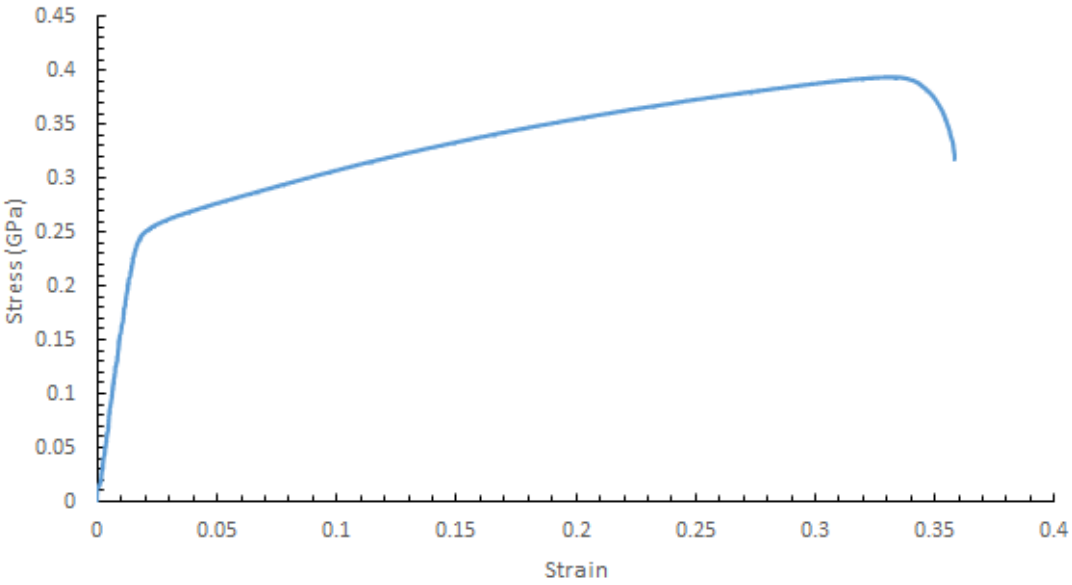

Figure A.39: Stress strain response for 0.13% C-steel, 2.8mm, 0.3mm/min and 23C

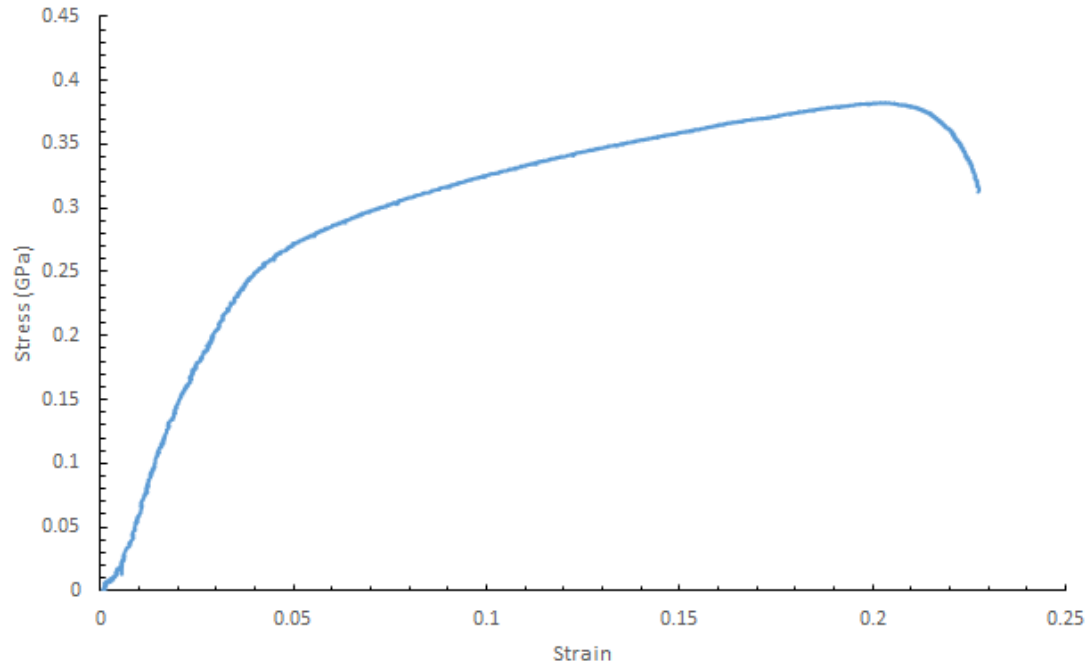

Figure A.40: Stress strain response for 0.13% C-steel, 2.8mm, 0.3mm/min and 300C

A.1.2 Round samples

Provided below are Stress Strain responses carried with the dumbbell geometry in uni-axial tension.

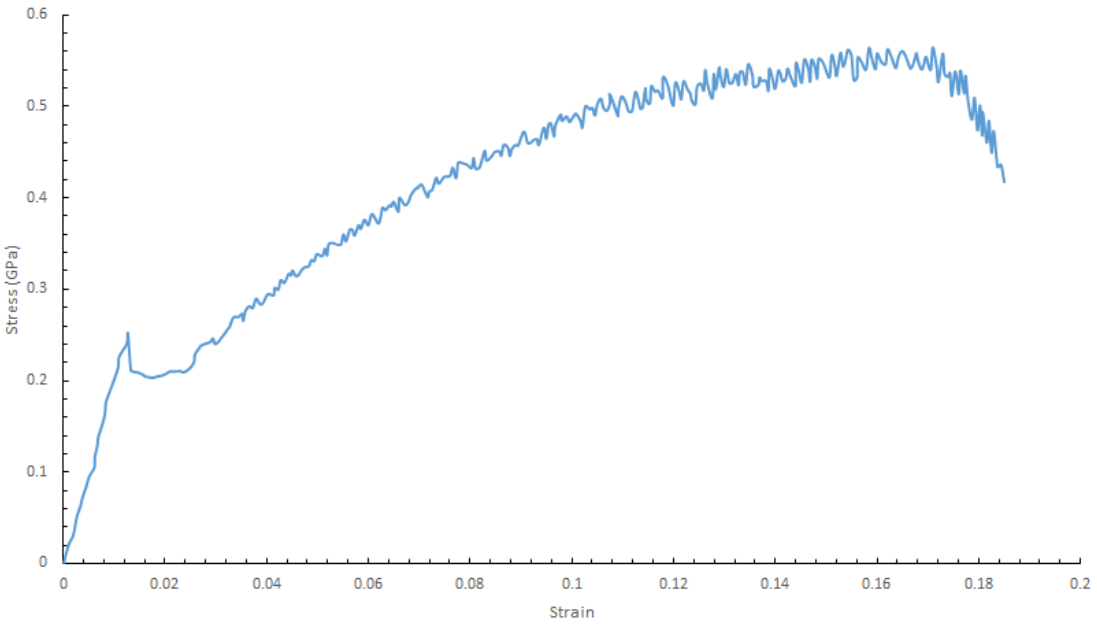

Figure A.41: Stress strain response for 0.13% C-steel, 3mm/min and 150C

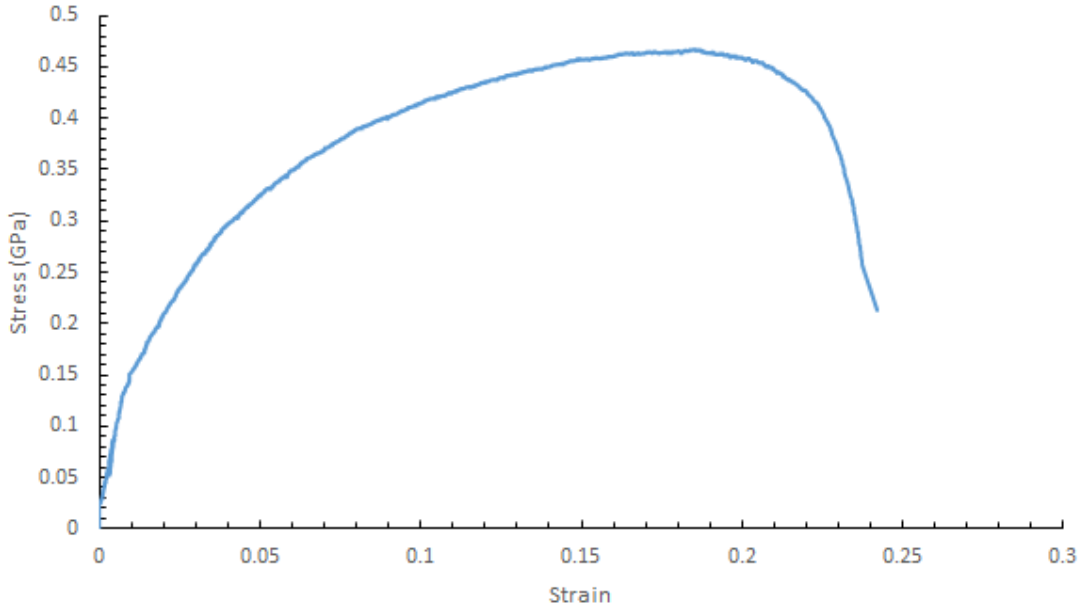

Figure A.42: Stress strain response for 0.13% C-steel, 0.3mm/min and 300C

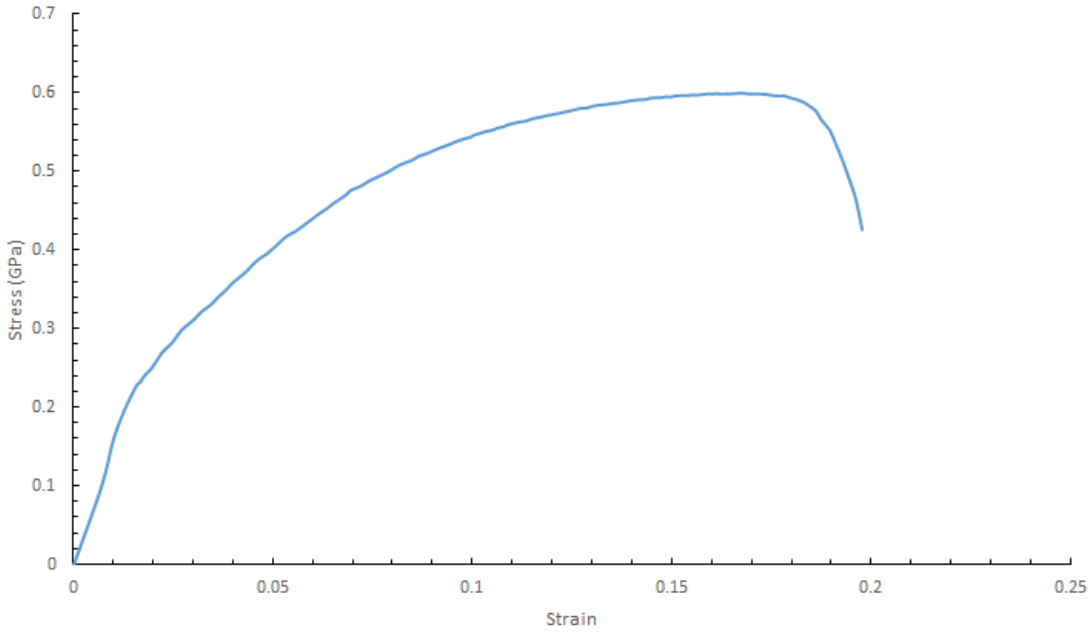

Figure A.43: Stress strain response for 0.13% C-steel, 30mm/min and 300C

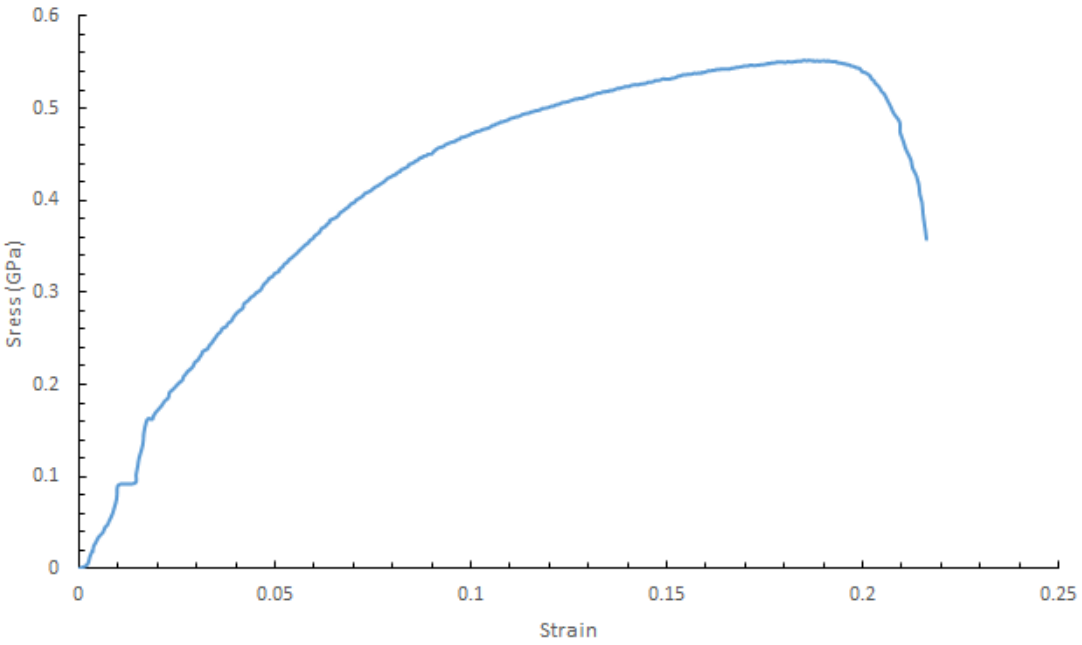

Figure A.44: Stress strain response for 0.13% C-steel, 3mm/min and 300C

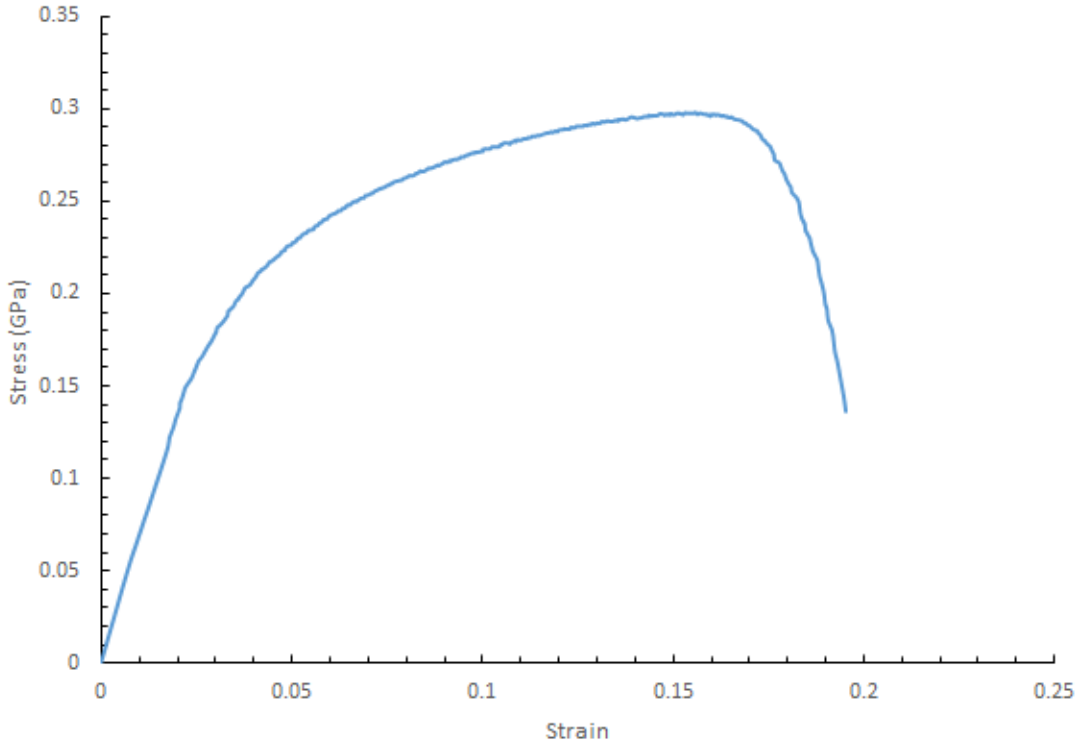

Figure A.45: Stress strain response for 0.13% C-steel, 3mm/min and 450C

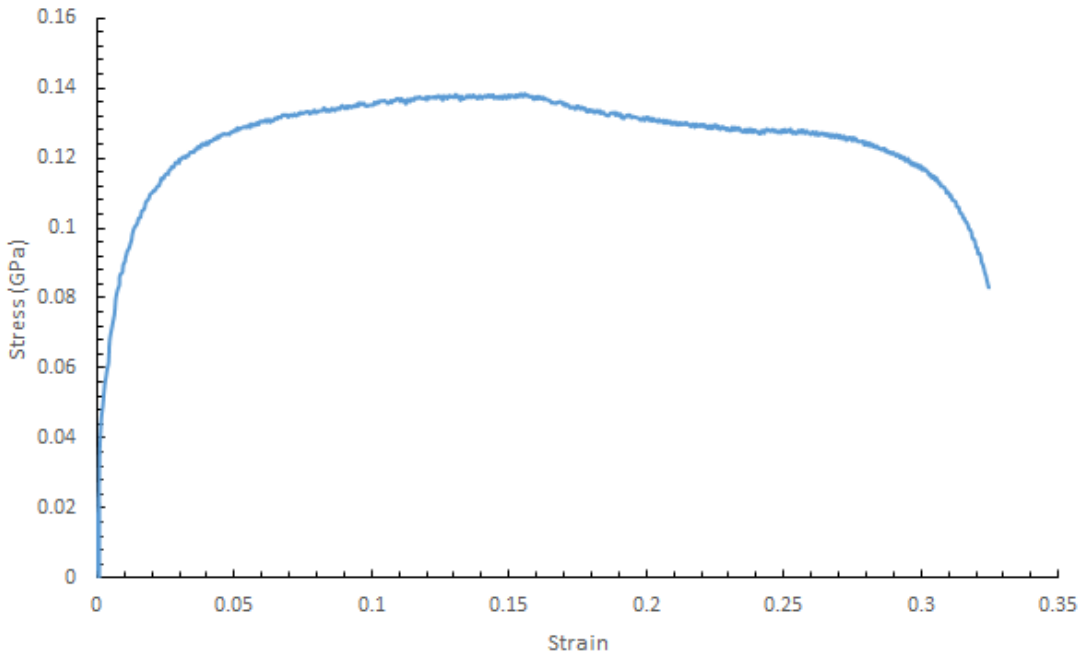

Figure A.46: Stress strain response for 0.13% C-steel, 3mm/min and 600C

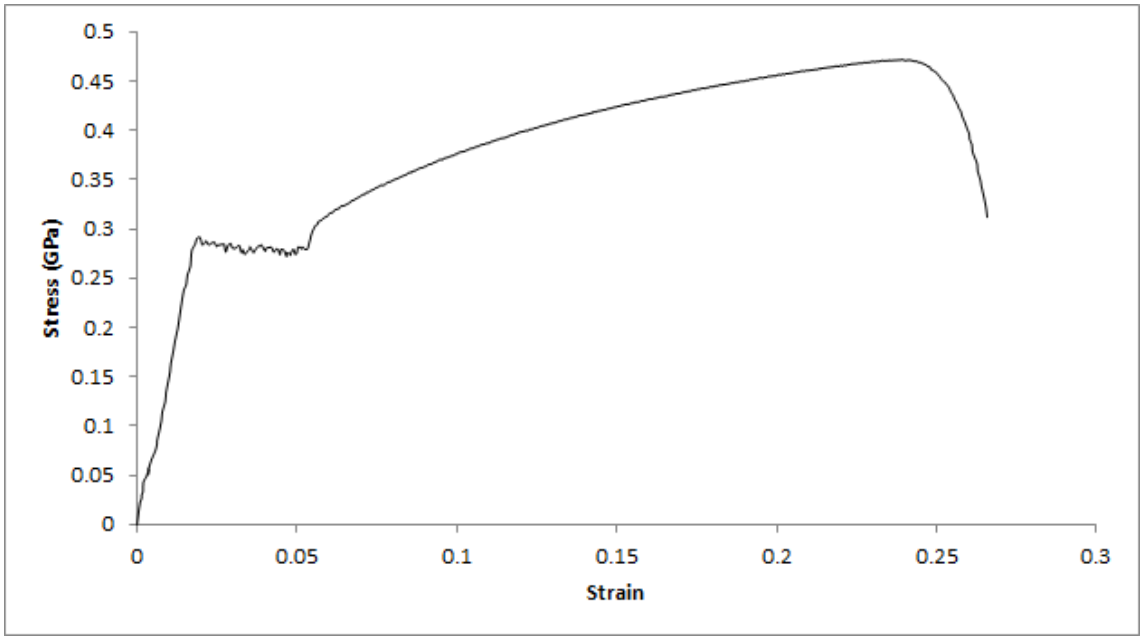

Figure A.47: Stress strain response for 0.13% C-steel, 3mm/min and 23C

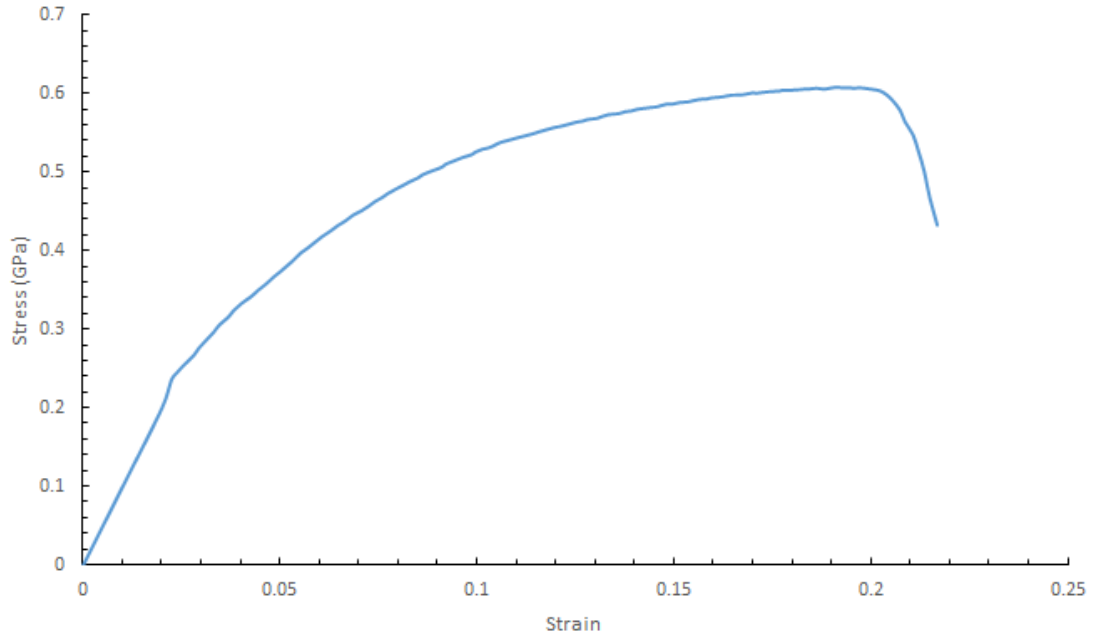

Figure A.48: Stress strain response for 0.13% C-steel, 90mm/min and 300C

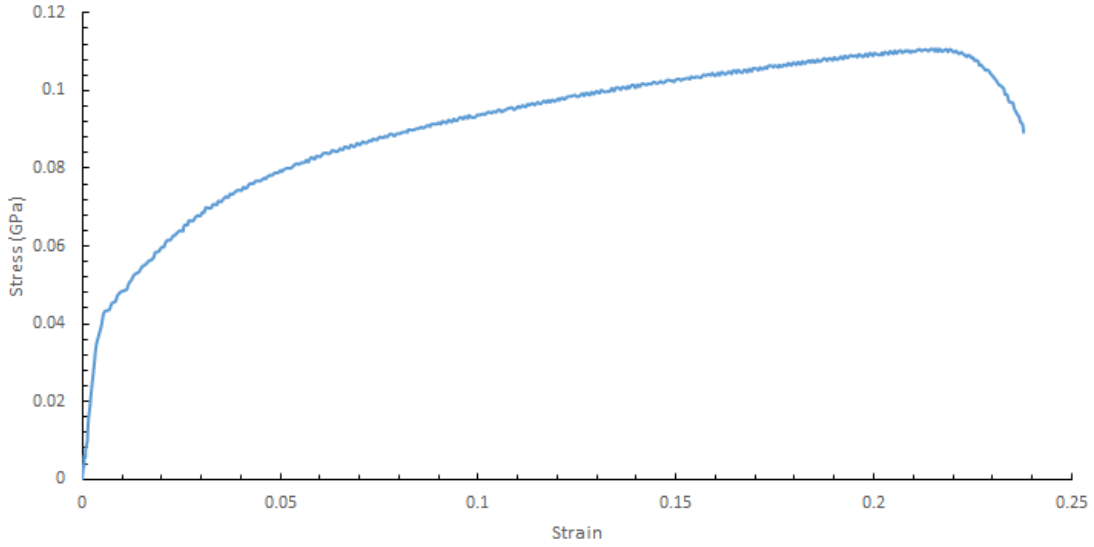

Figure A.49: Stress strain response for AISI 6063, 3mm/min and 50C

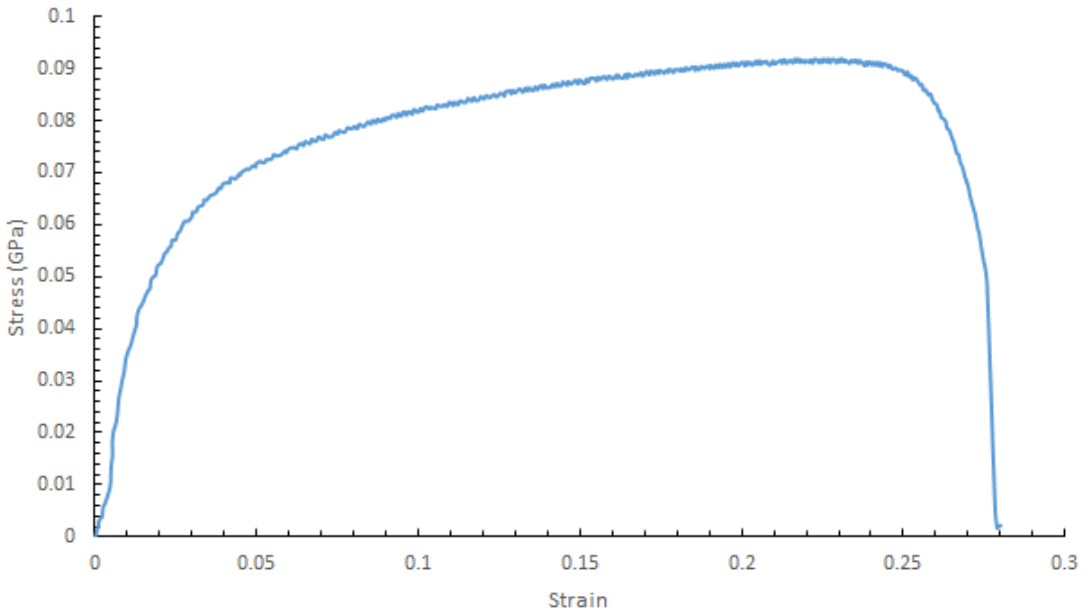

Figure A.50: Stress strain response for AISI 6063, 3mm/min and 150C

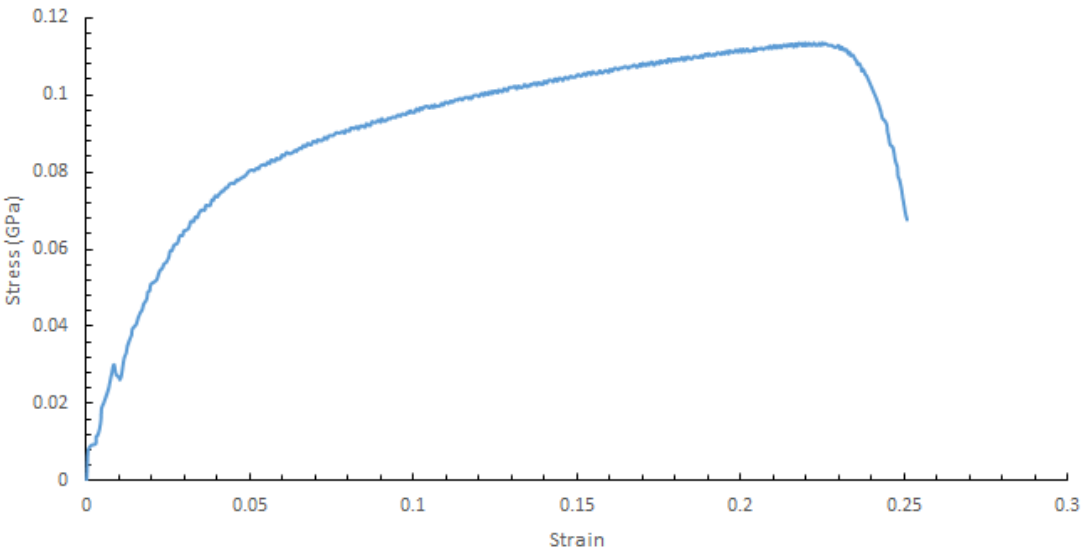

Figure A.51: Stress strain response for AISI 6063, 3mm/min and 100C

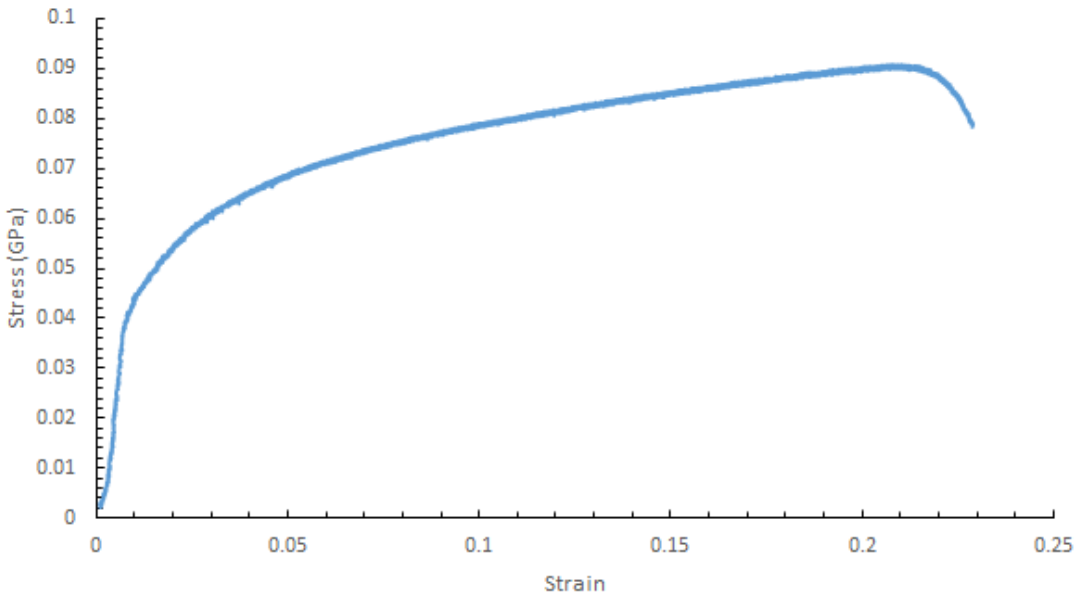

Figure A.52: Stress strain response for AISI 6063, 0.3mm/min and 100C

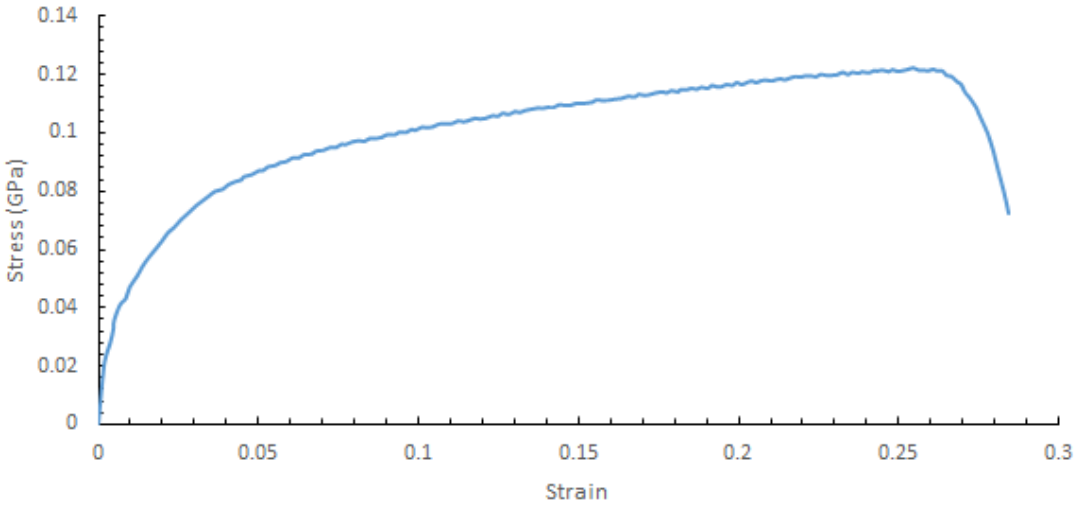

Figure A.53: Stress strain response for AISI 6063, 30mm/min and 100C

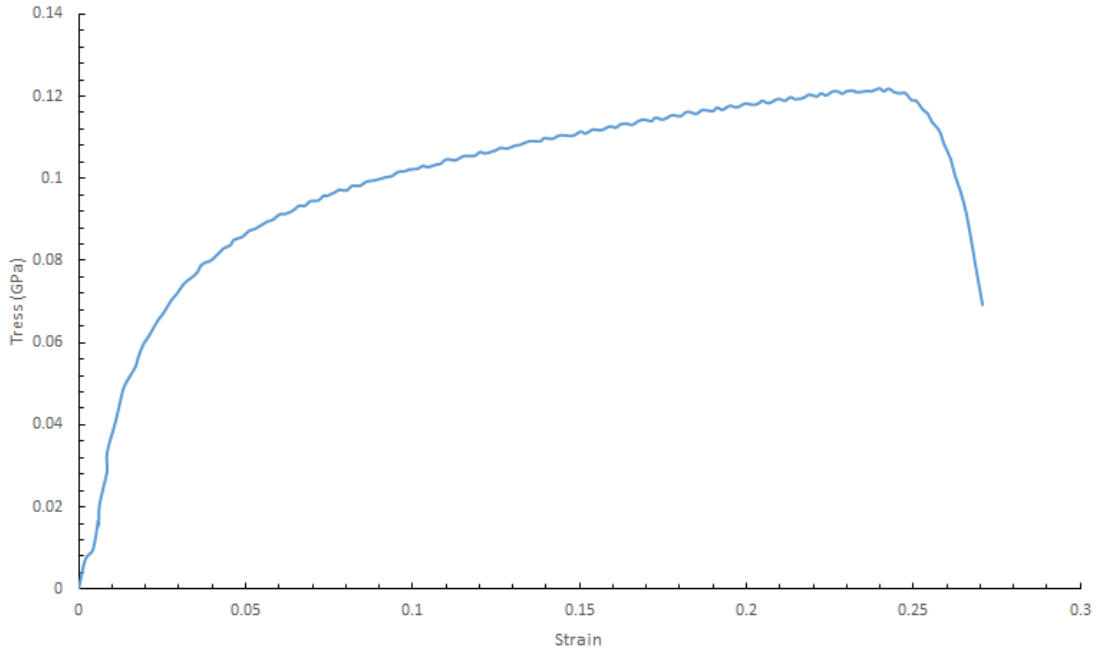

Figure A.54: Stress strain response for AISI 6063, 90mm/min and 100C

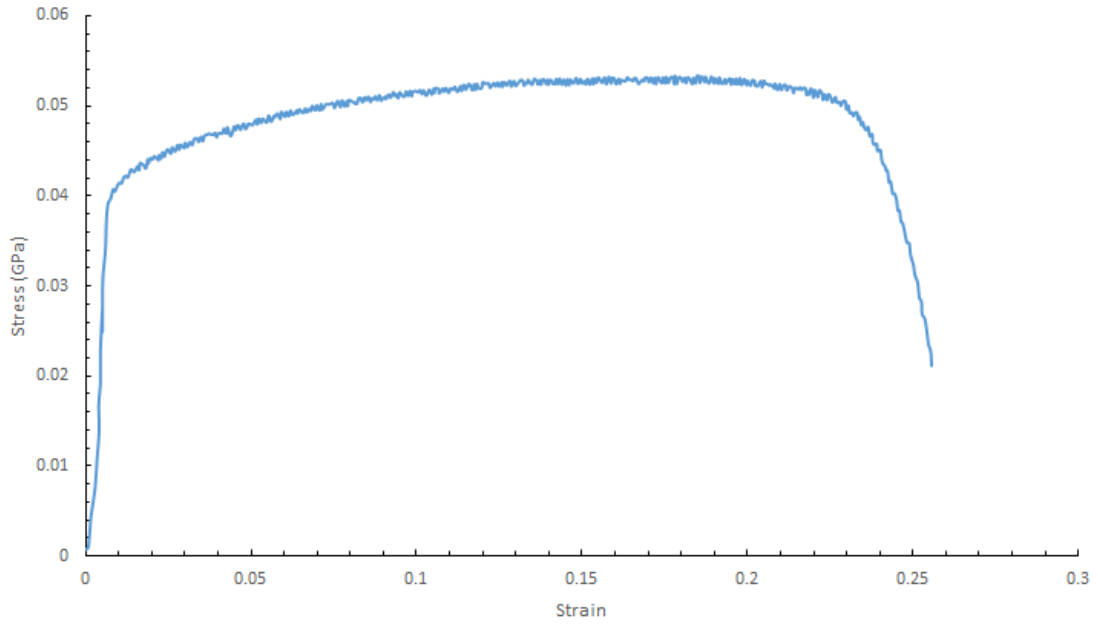

Figure A.55: Stress strain response for AISI 6063, 3mm/min and 200C

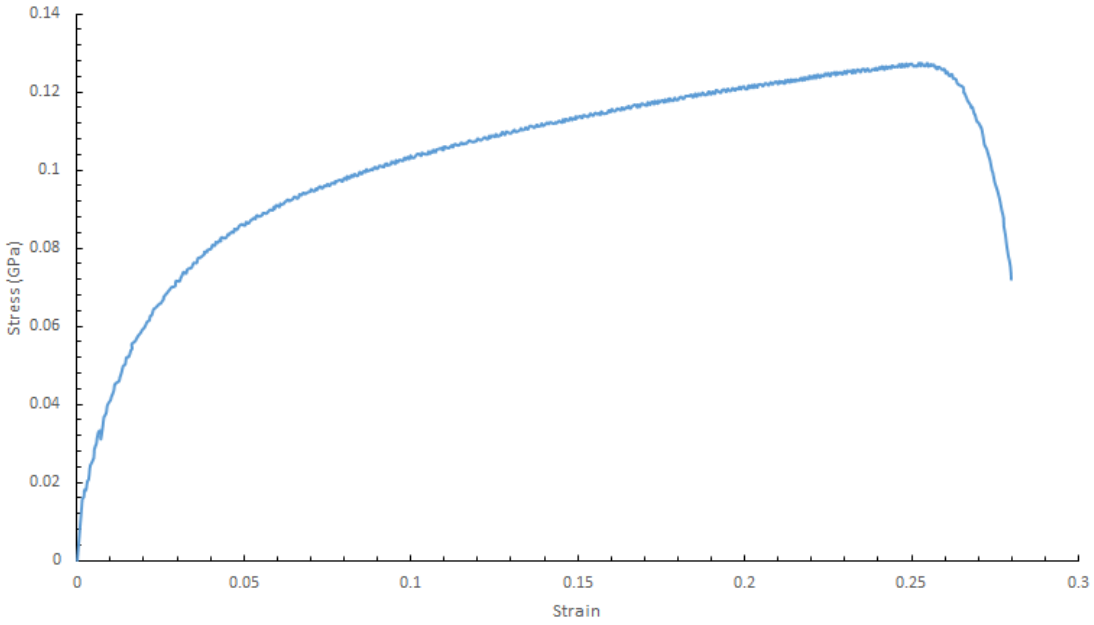

Figure A.56: Stress strain response for AISI 6063, 3mm/min and 23C

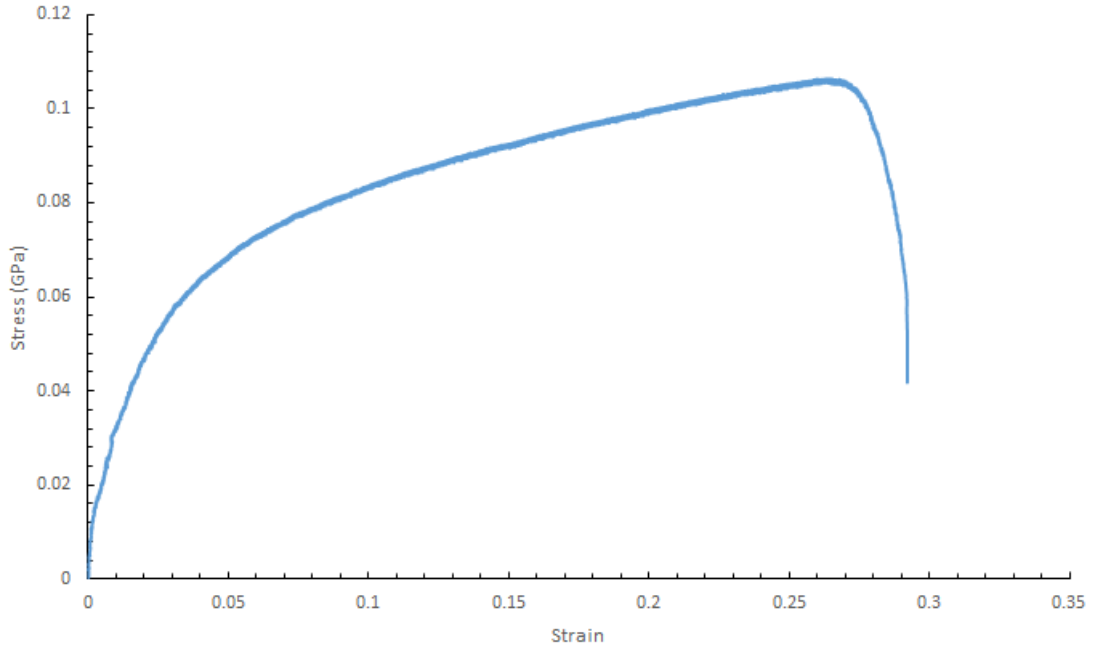

Figure A.57: Stress strain response for AISI 6063, 0.3mm/min and 23C

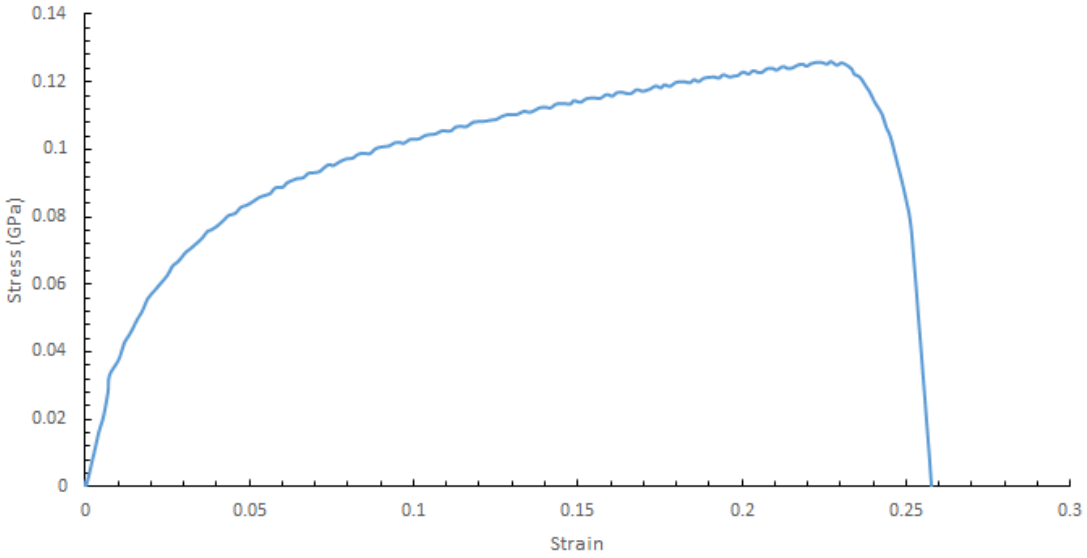

Figure A.58: Stress strain response for AISI 6063, 30mm/min and 23C

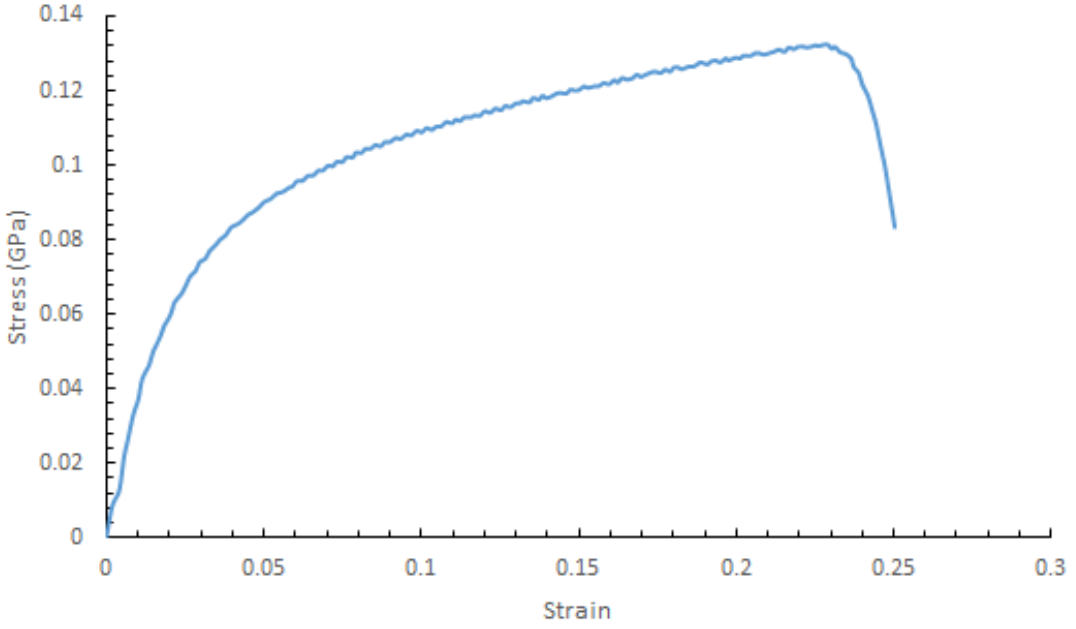

Figure A.59: Stress strain response for AISI 6063, 90mm/min and 23C

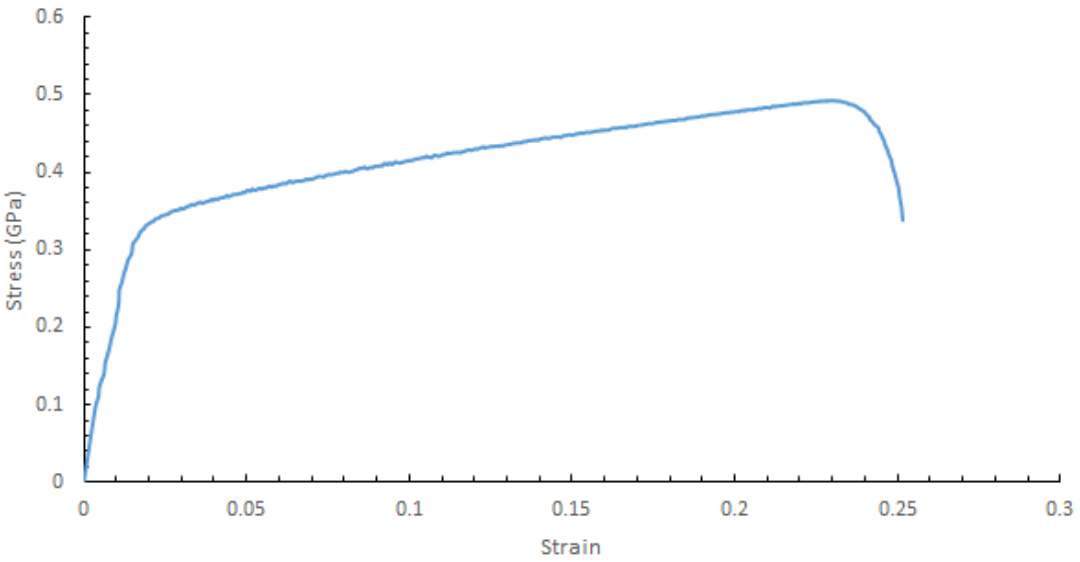

Figure A.60: Stress strain response for 60/40 brass, 3mm/min and 80C

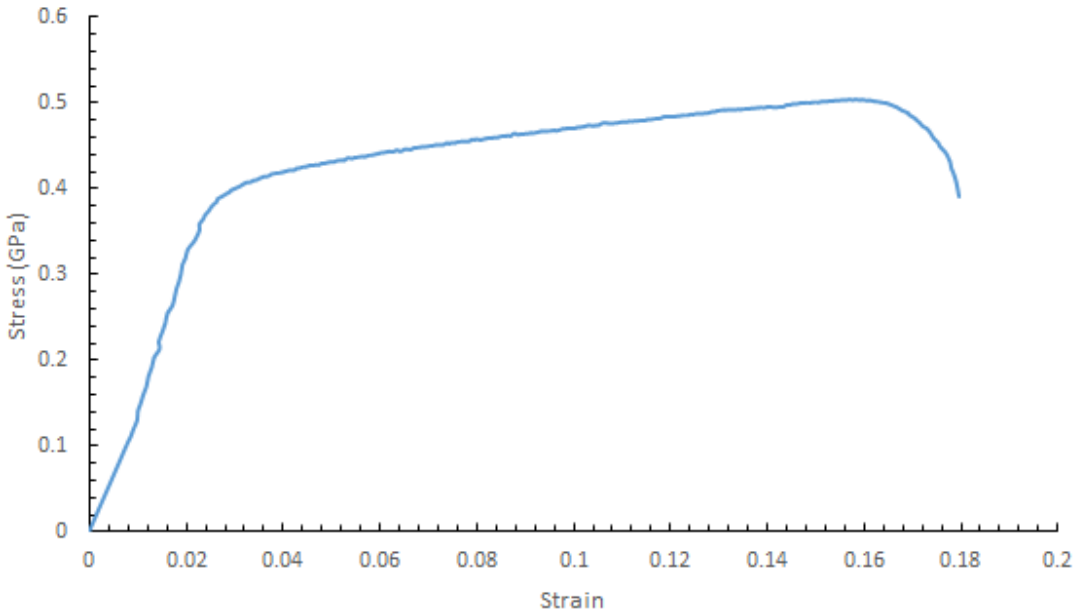

Figure A.61: Stress strain response for 60/40 brass, 3mm/min and 160C

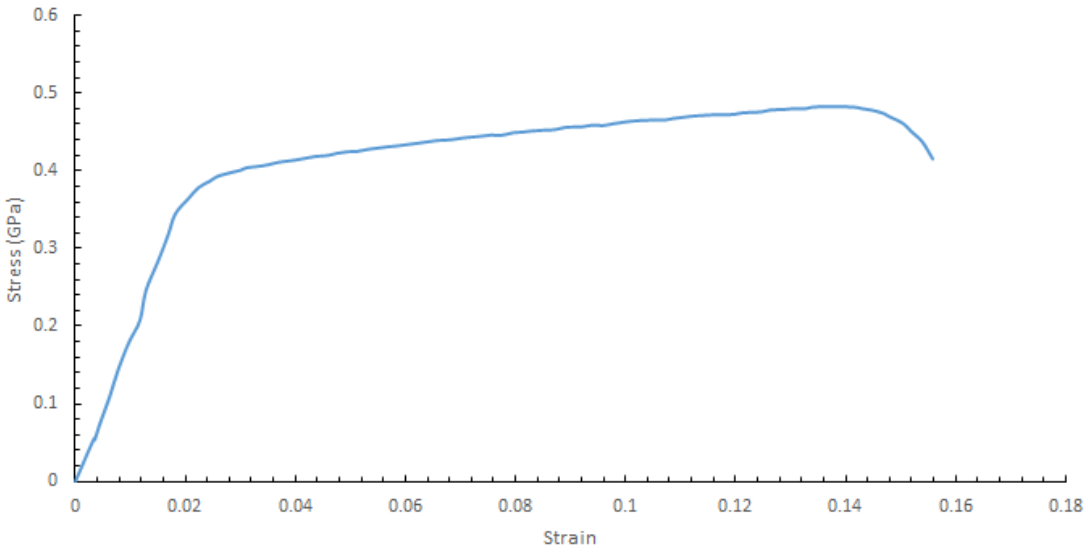

Figure A.62: Stress strain response for 60/40 brass, 30mm/min and 160C

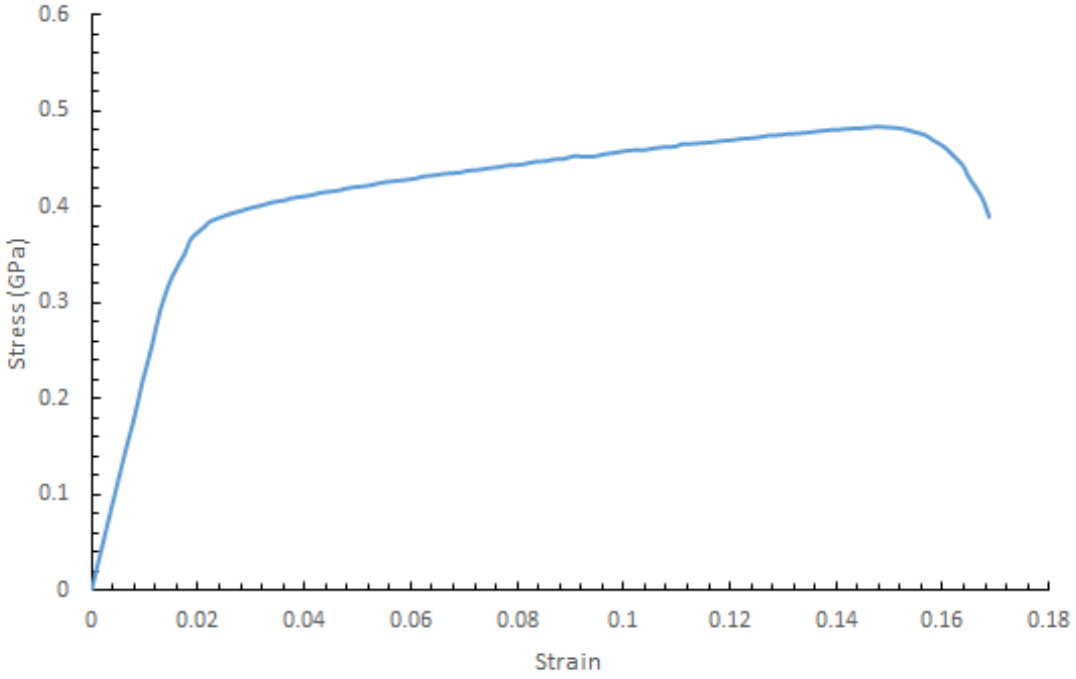

Figure A.63: Stress strain response for 60/40 brass, 90mm/min and 160C

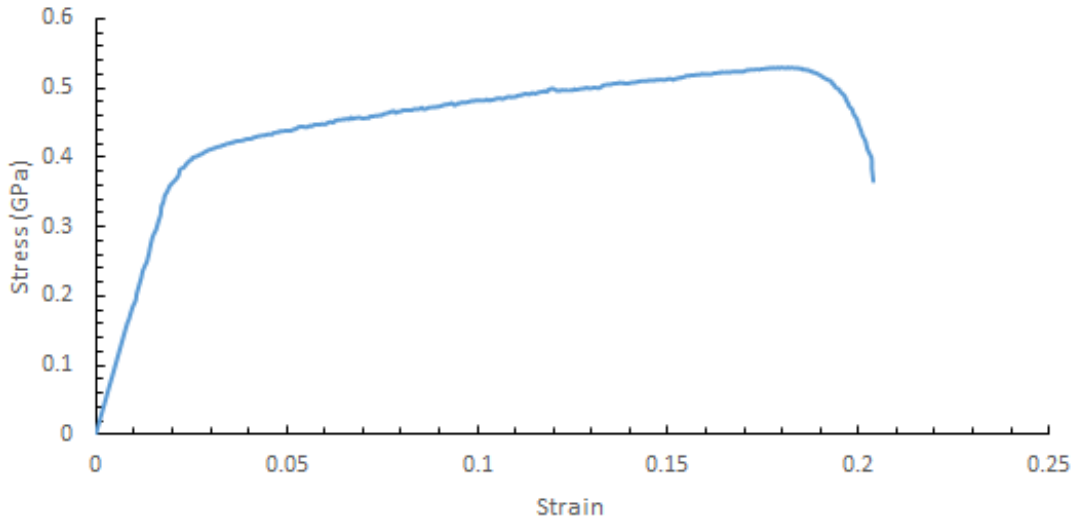

Figure A.64: Stress strain response for 60/40 brass, 3mm/min and 23C

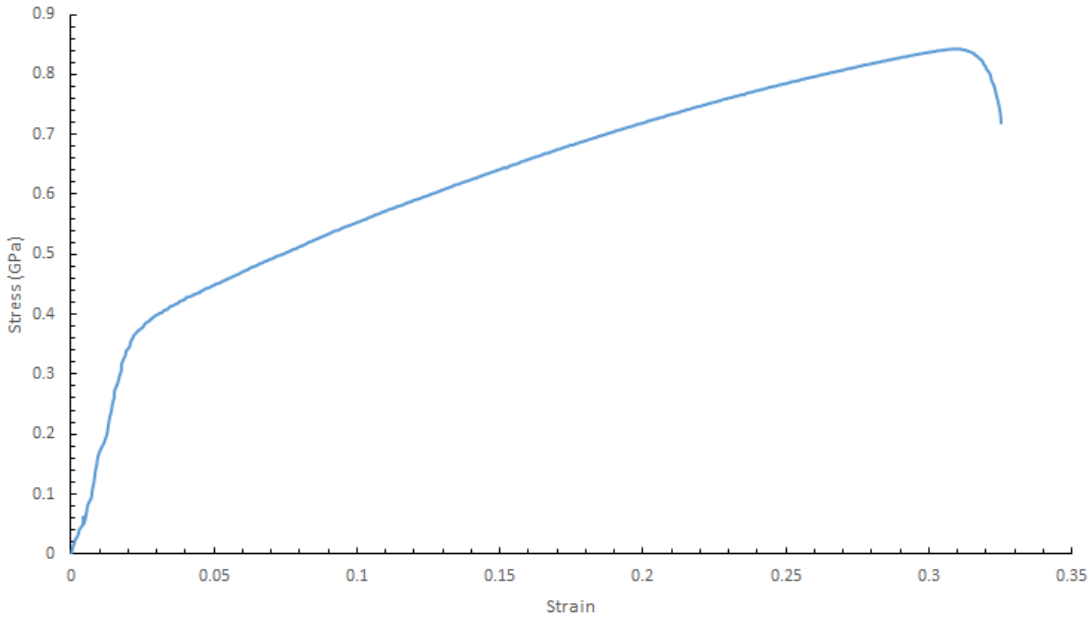

Figure A.65: Stress strain response for 18/8 stainless steel, 0.3mm/min and 23C

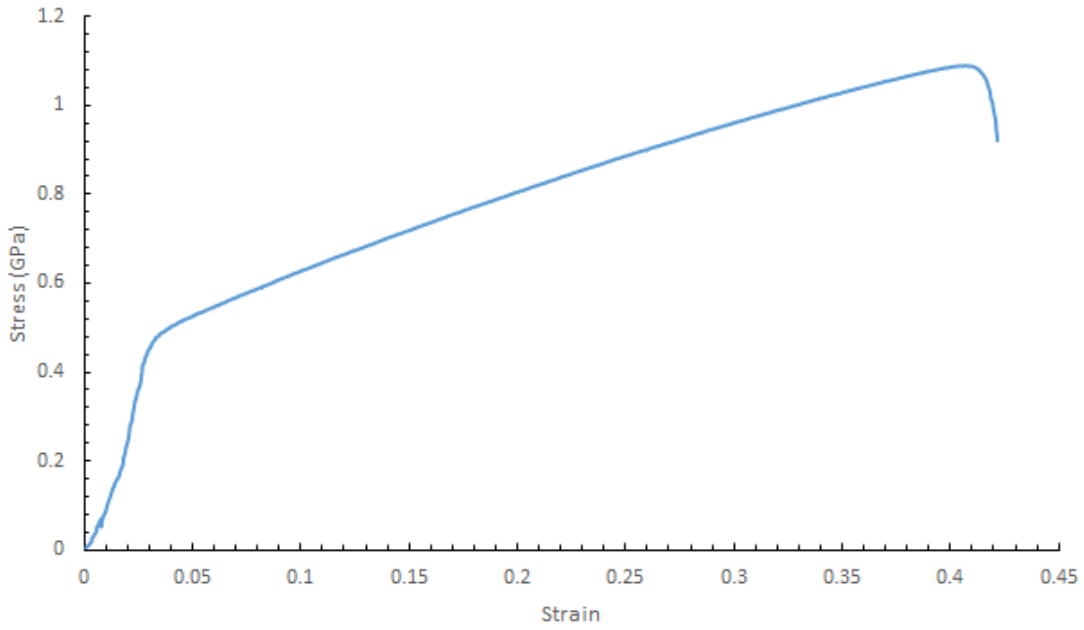

Figure A.66: Stress strain response for 18/8 stainless steel, 3mm/min and 23C

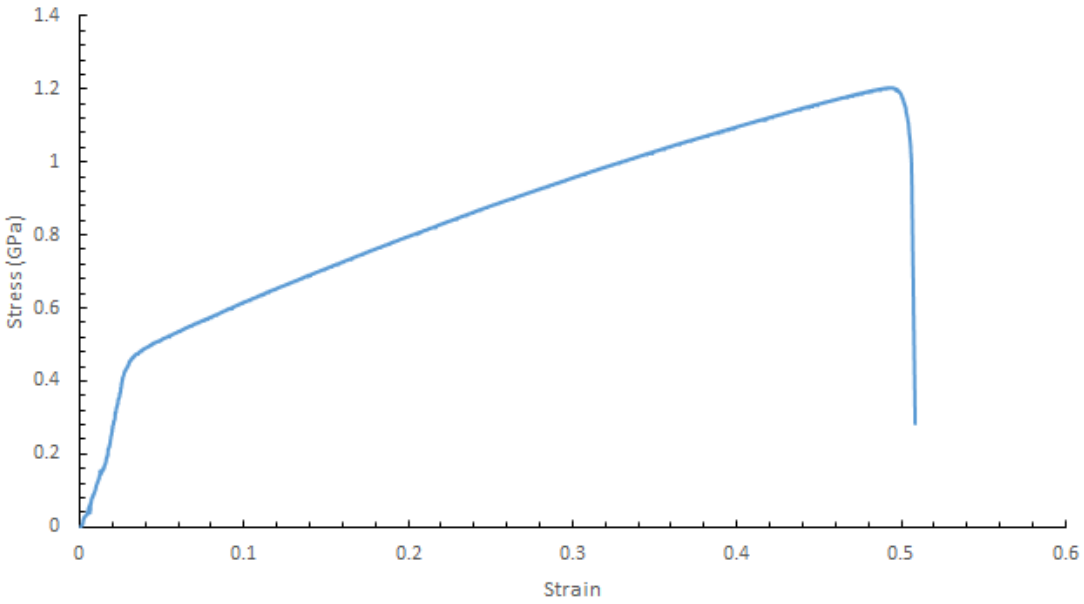

Figure A.67: Stress strain response for 18/8 stainless steel, 30mm/min and 23C

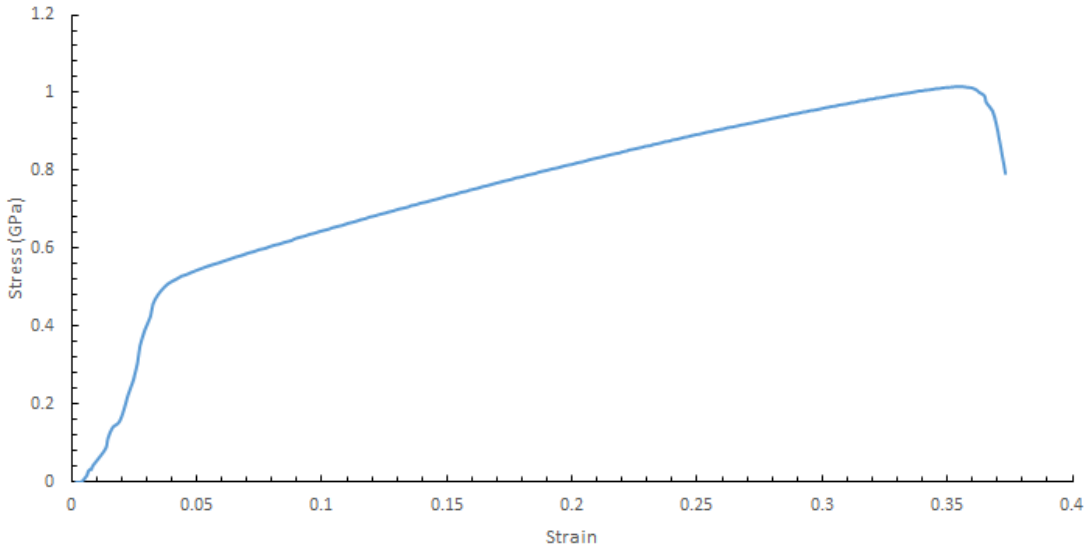

Figure A.68: Stress strain response for 18/8 stainless steel, 90mm/min and 23C

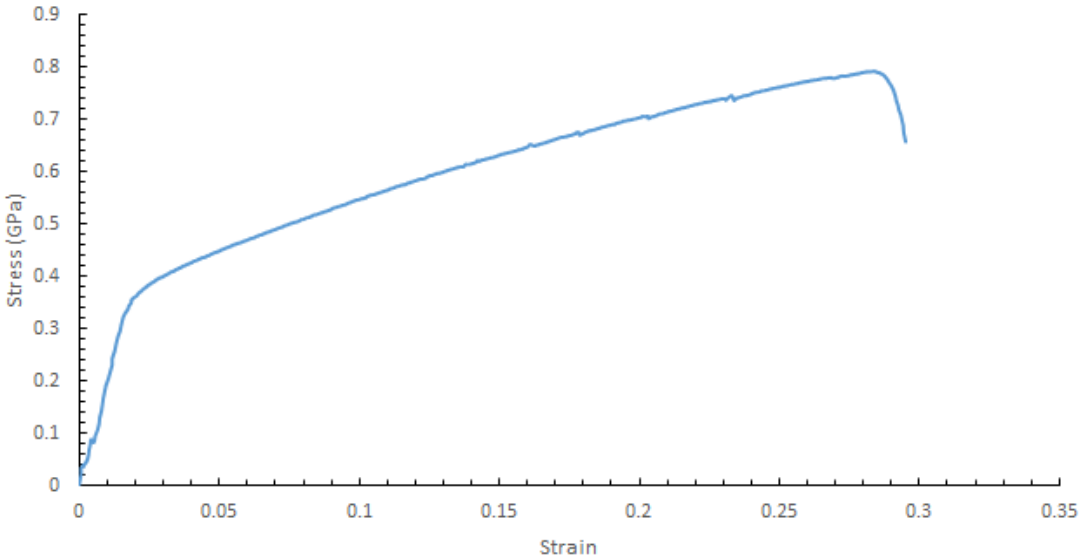

Figure A.69: Stress strain response for 18/8 stainless steel, 3mm/min and 300C

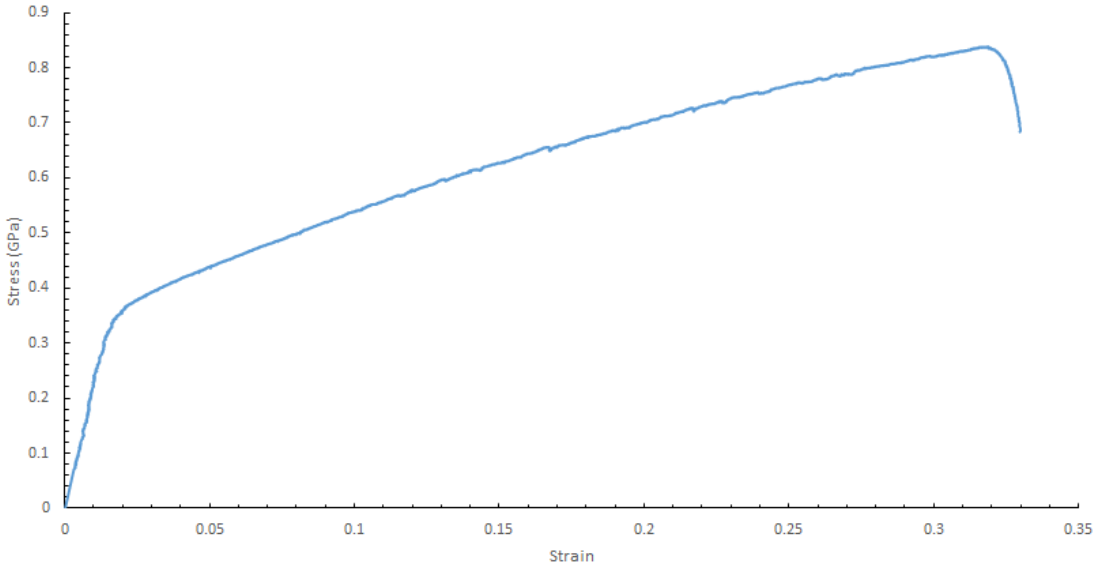

Figure A.70: Stress strain response for 18/8 stainless steel, 0.3mm/min and 300C

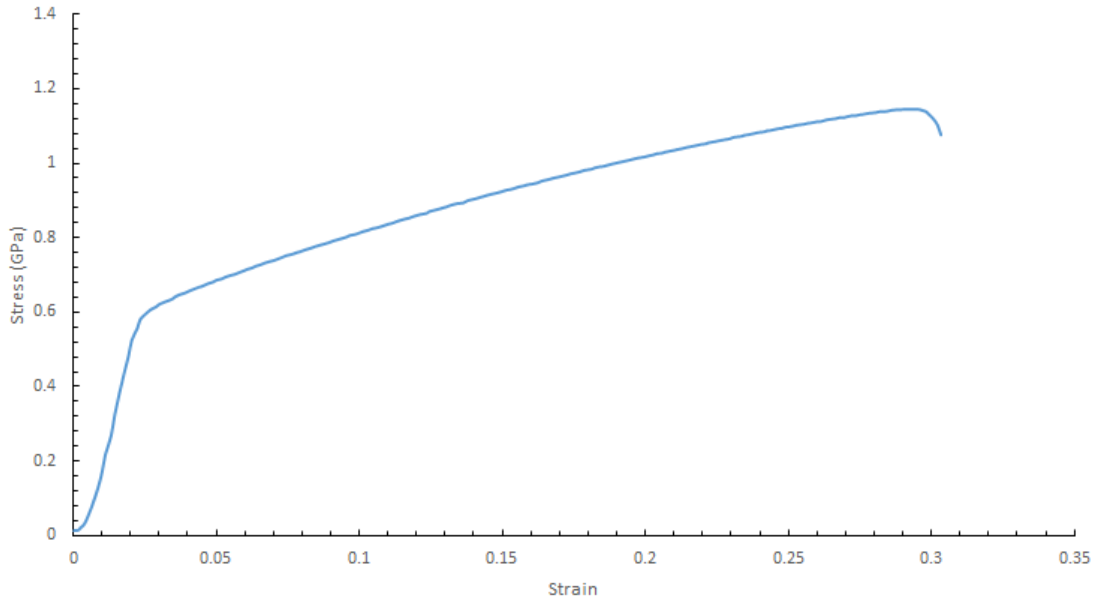

Figure A.71: Stress strain response for 18/8 stainless steel, 3mm/min and 100C

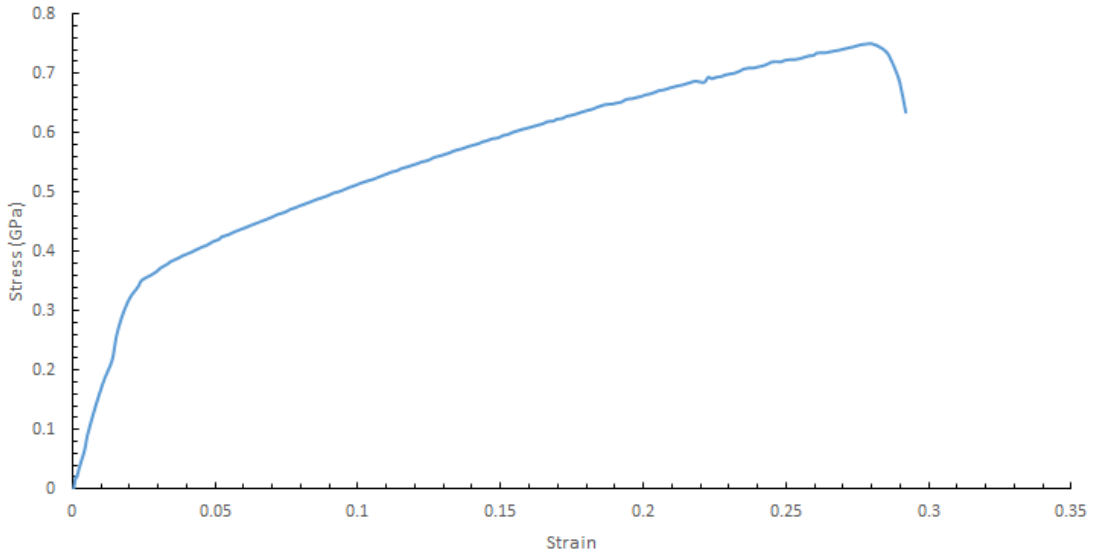

Figure A.72: Stress strain response for 18/8 stainless steel, 30mm/min and 300C

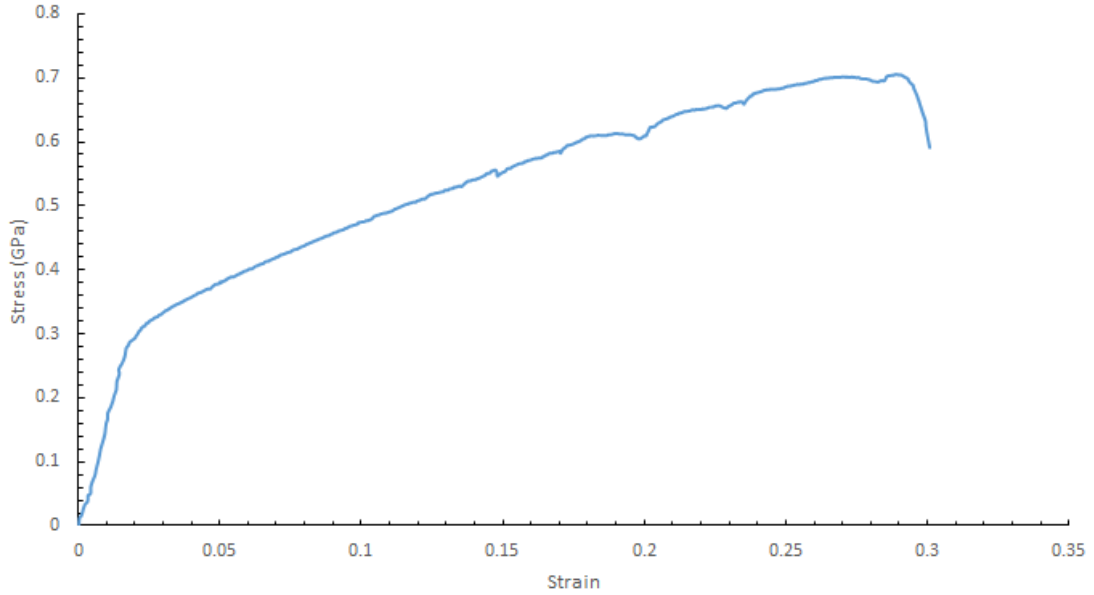

Figure A.73: Stress strain response for 18/8 stainless steel, 3mm/min and 450C

A.2 Bi-axial

A.2.1 Bulge forming

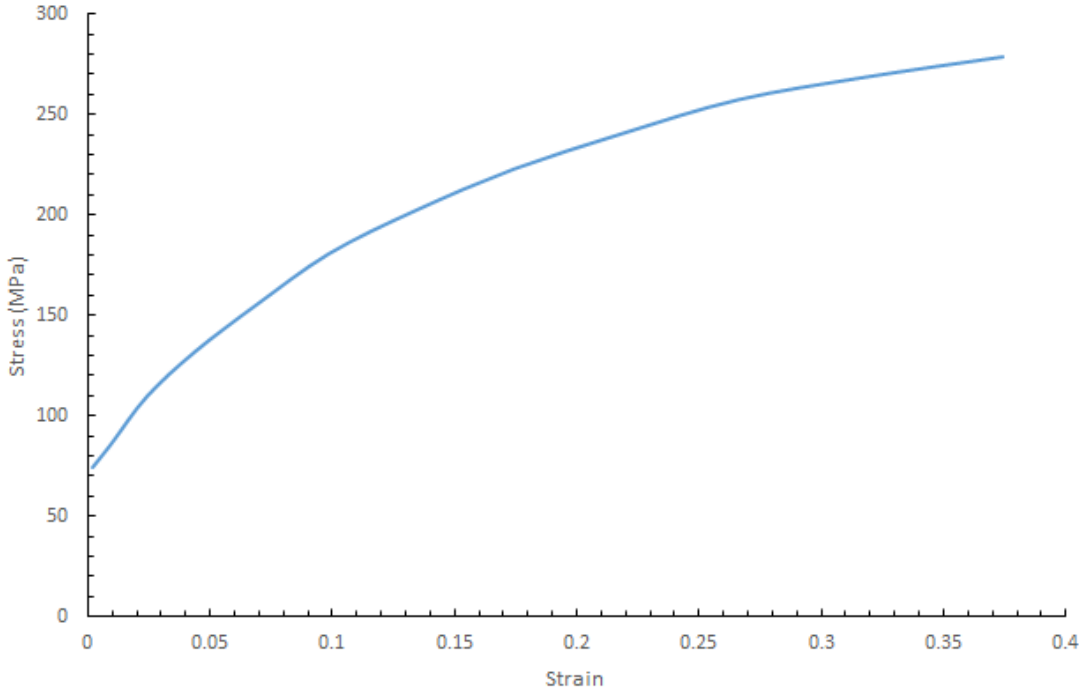

Figure A.74: Stress strain response for AA 5754

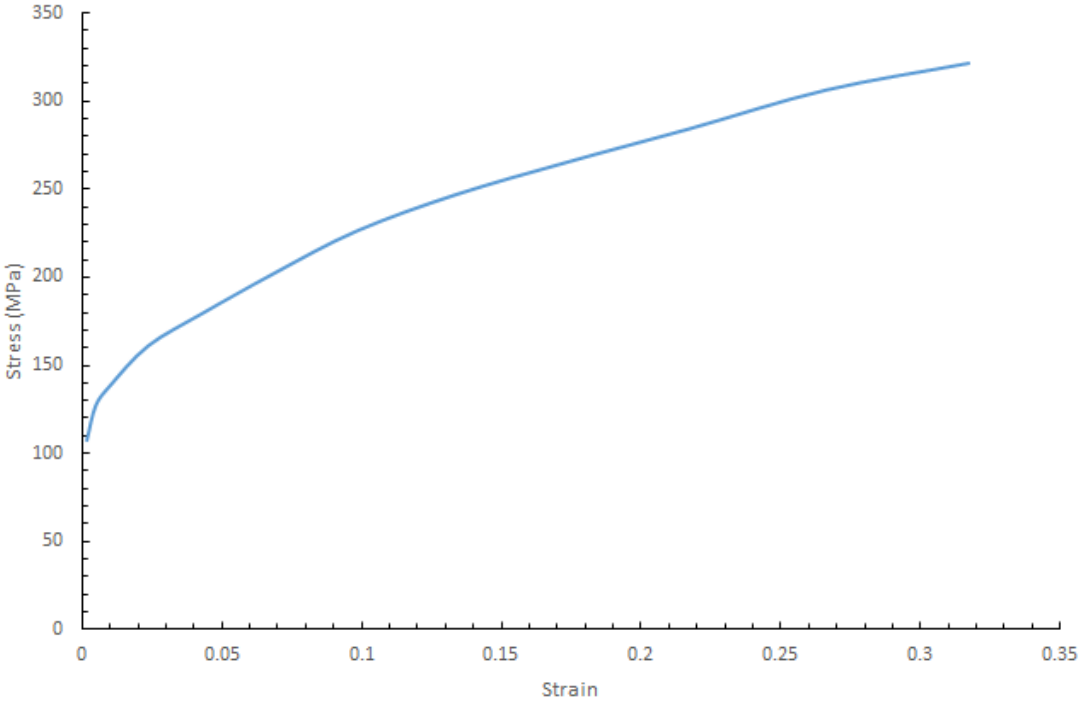

Figure A.75: Stress strain response for AA 6111

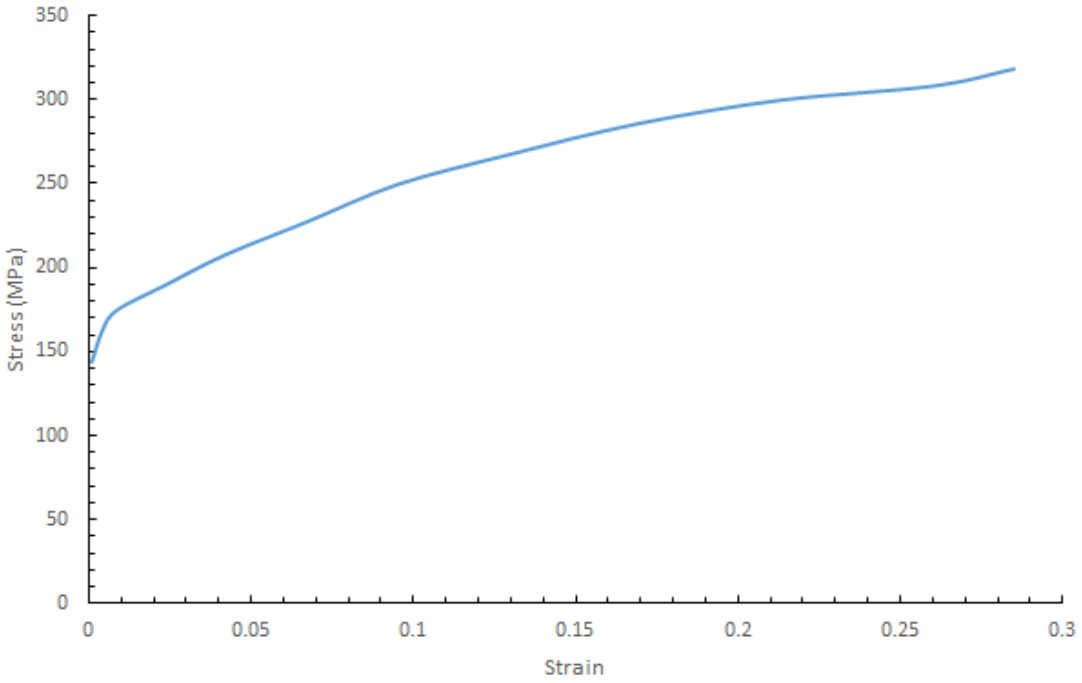

Figure A.76: Stress strain response for AC 300

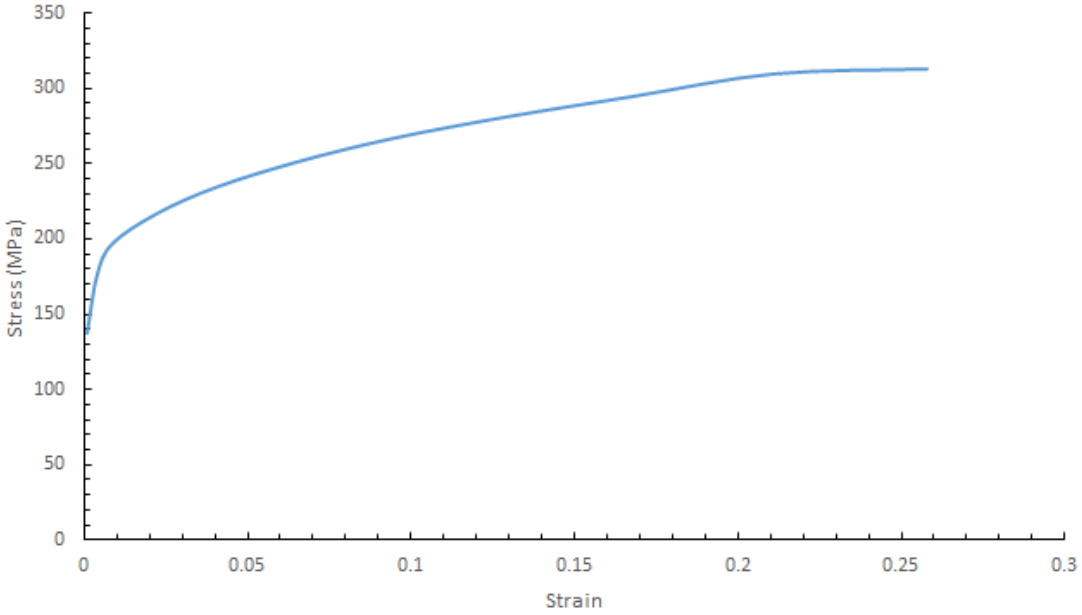

Figure A.77: Stress strain response for AC 220

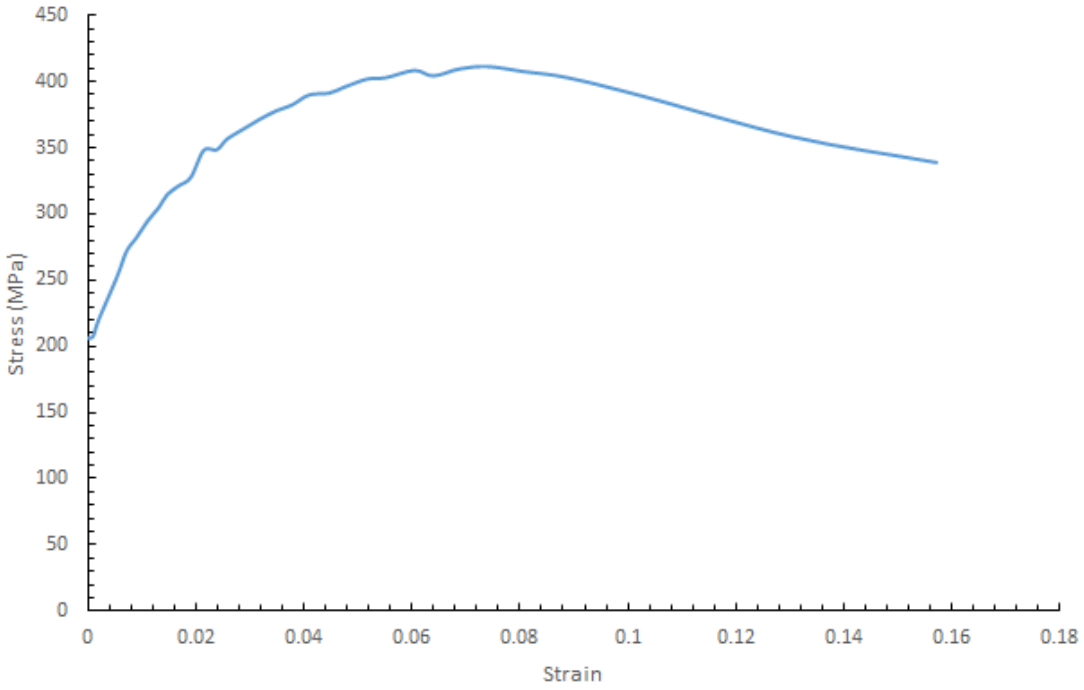

Figure A.78: Stress strain response for 0.13% C-steel

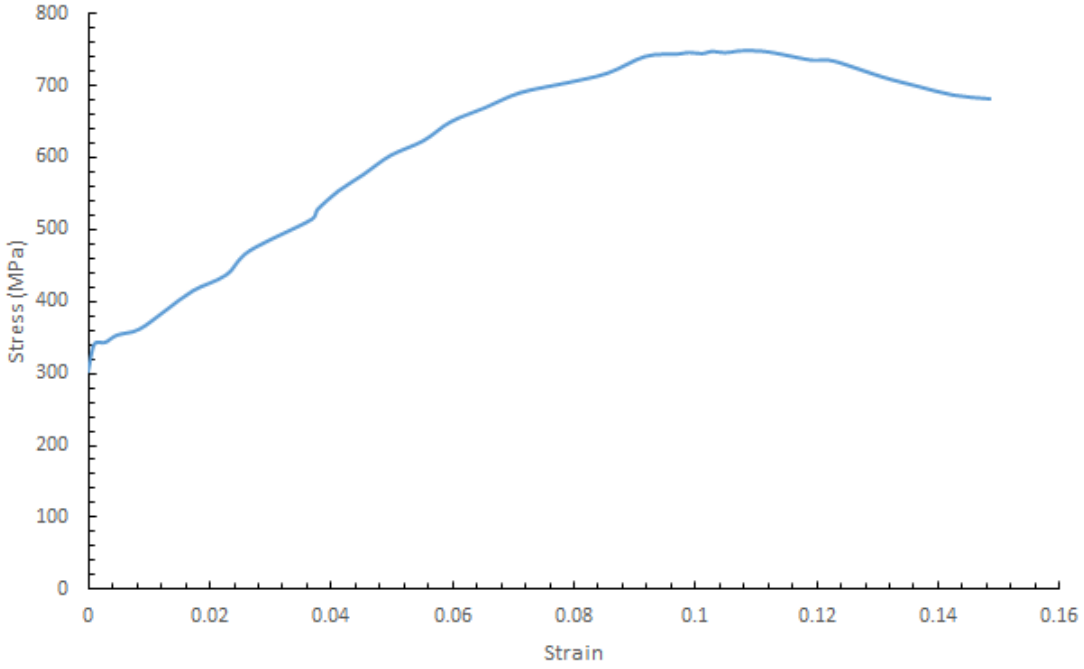

Figure A.79: Stress strain response for 18/8 stainless steel

A.2.2 Compression plate

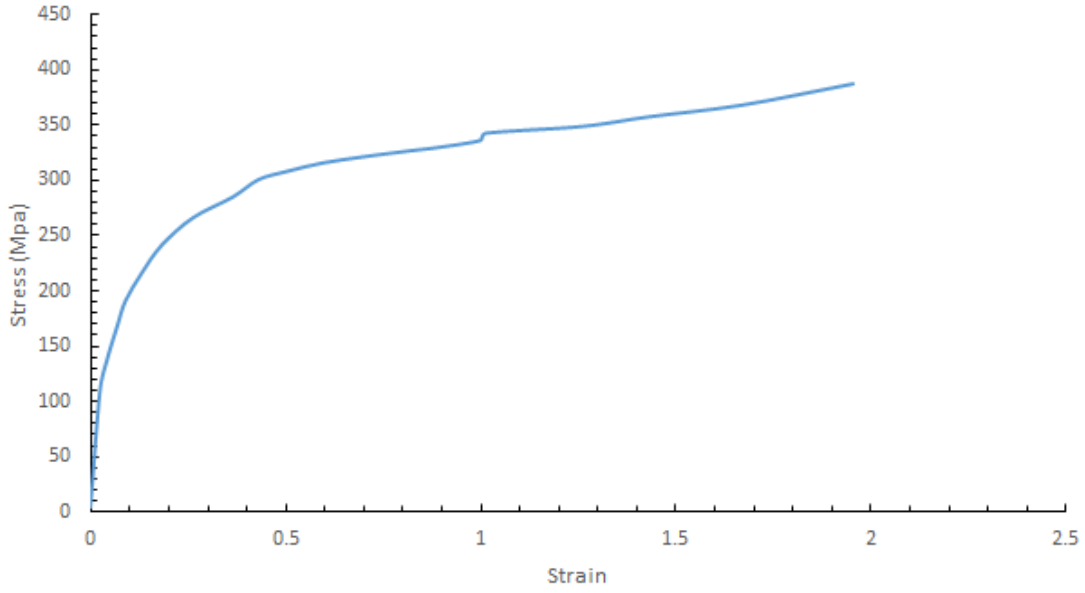

Figure A.80: Stress strain response for AA 5754-18

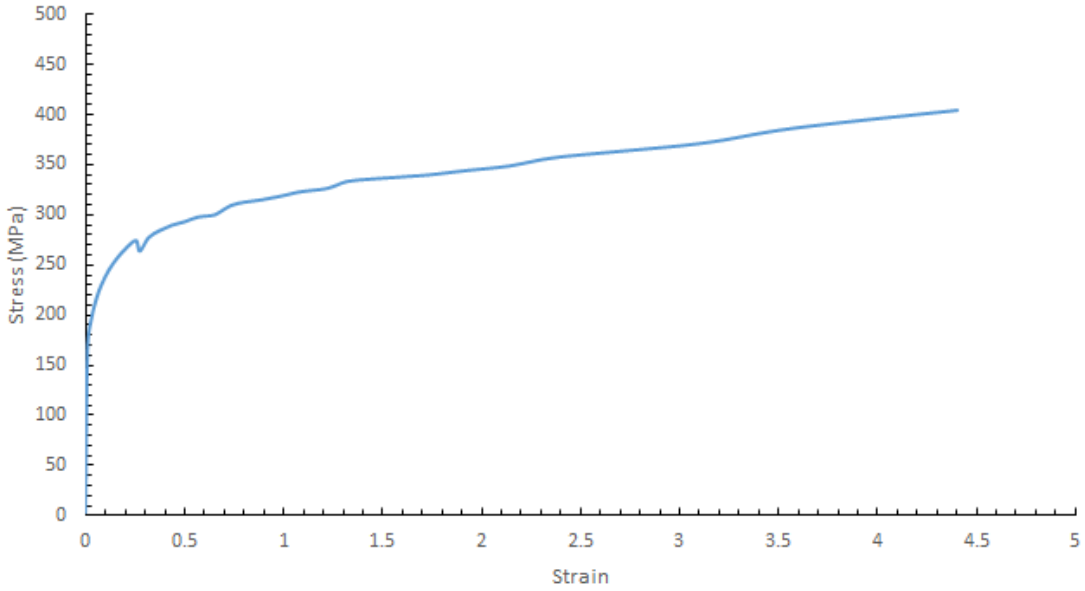

Figure A.81: Stress strain response for AA 5754-30

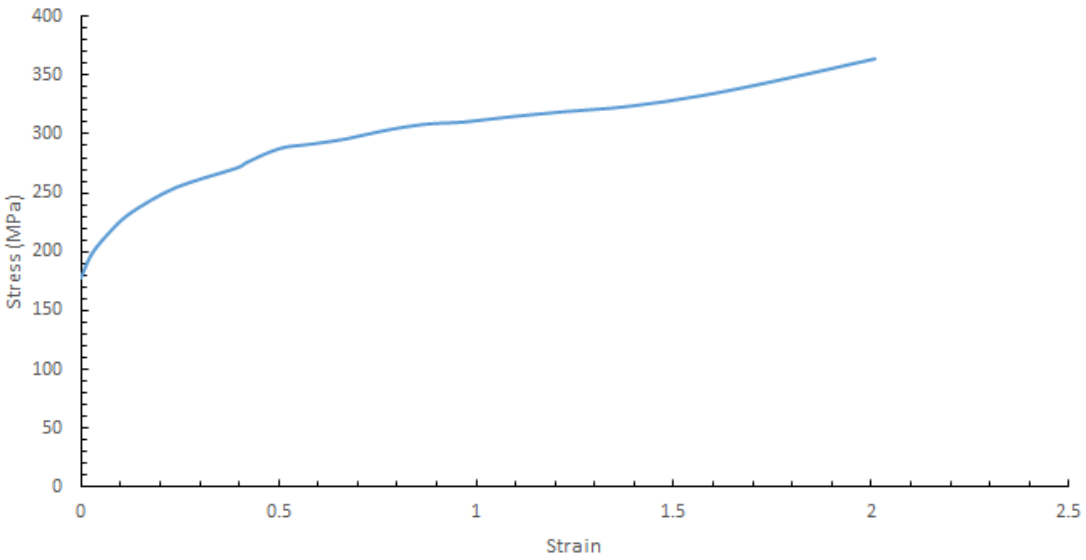

Figure A.82: Stress strain response for AC 300-23

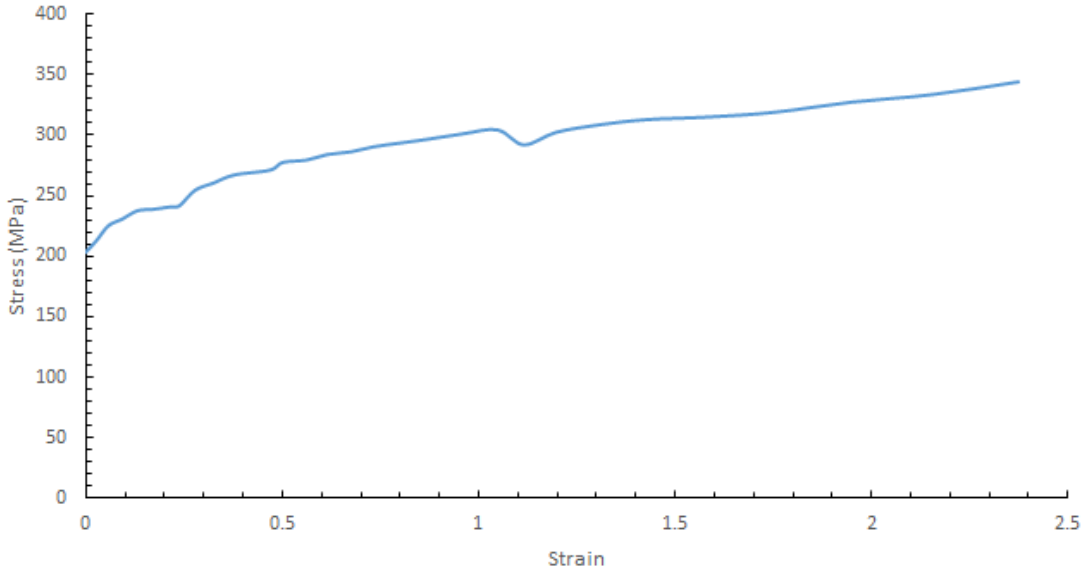

Figure A.83: Stress strain response for AC 300-31

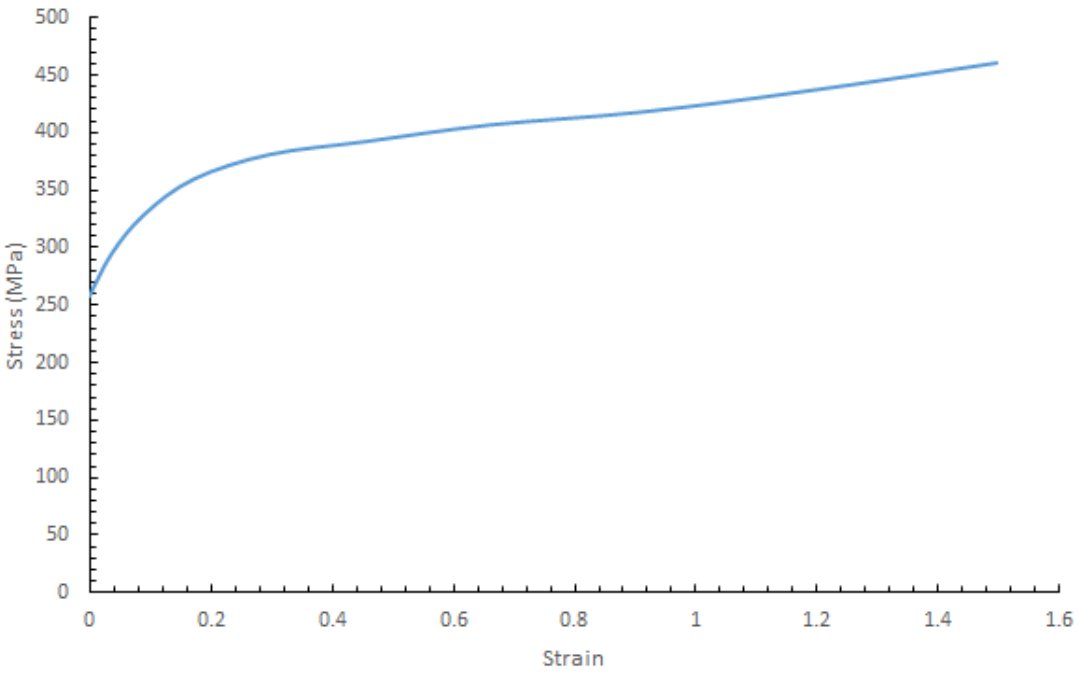

Figure A.84: Stress strain response for AA 6111

A.3 Reduction Factor

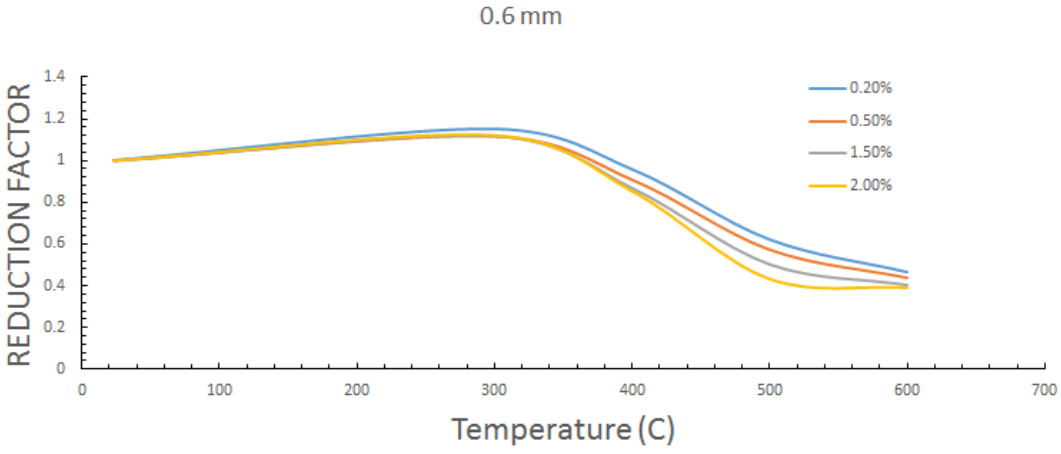

Figure A.85: Reduction factor curves for 0.6 mm sheet steel

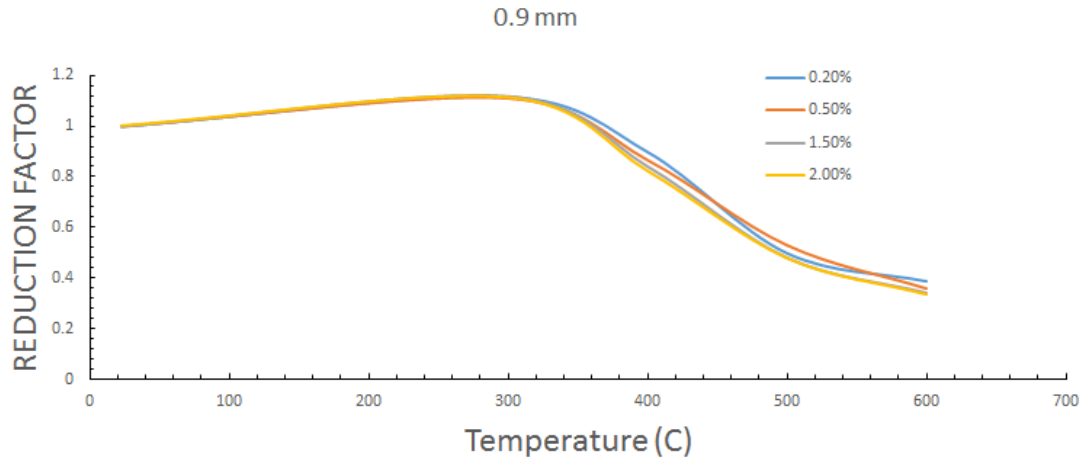

Figure A.86: Reduction factor curves for 0.9 mm sheet steel

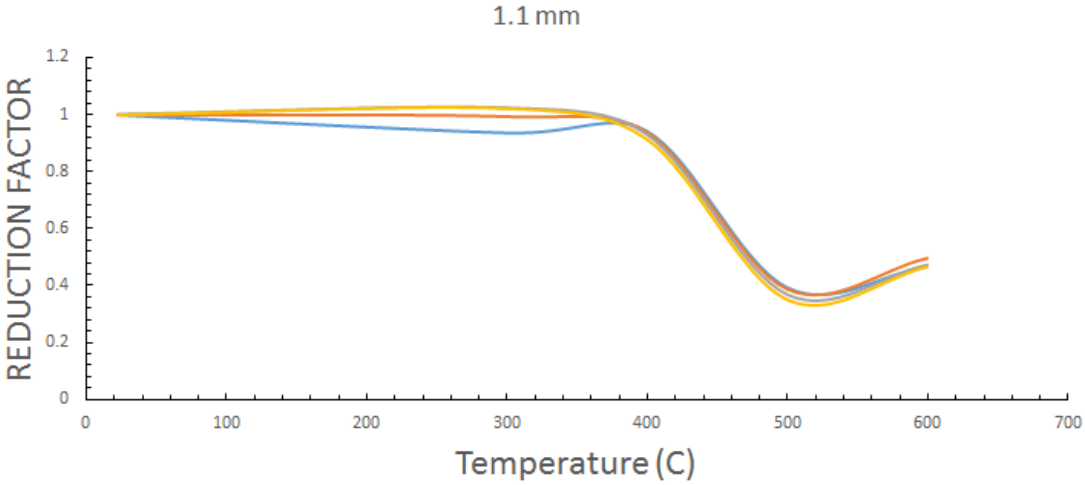

Figure A.87: Reduction factor curves for 1.1 mm sheet steel

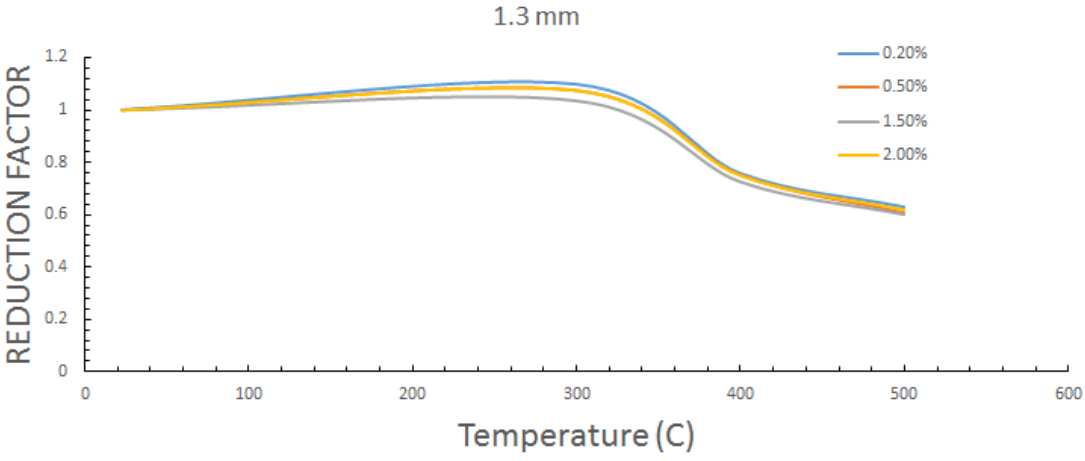

Figure A.88: Reduction factor curves for 1.3 mm sheet steel

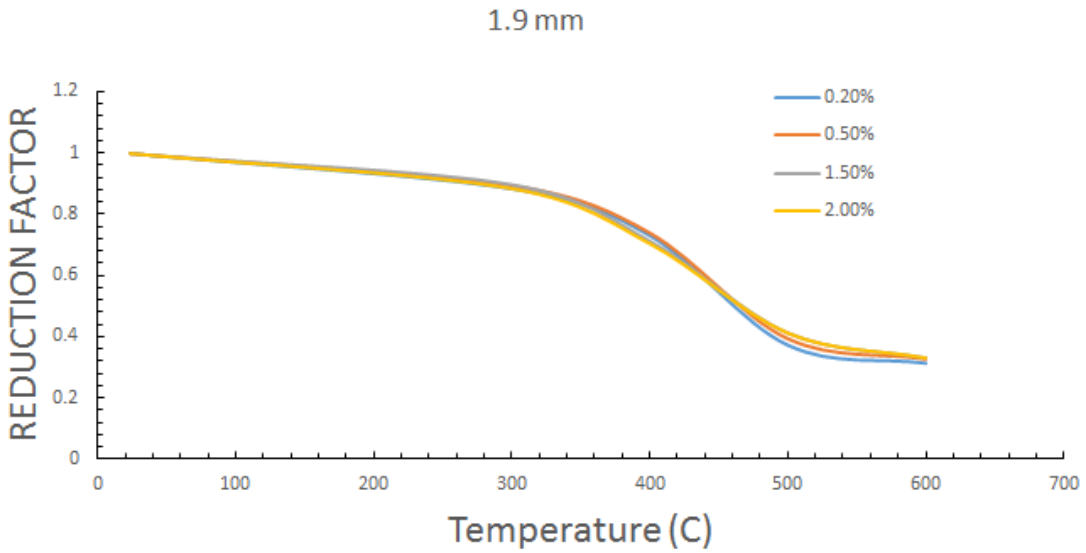

Figure A.89: Reduction factor curves for 1.9 mm sheet steel

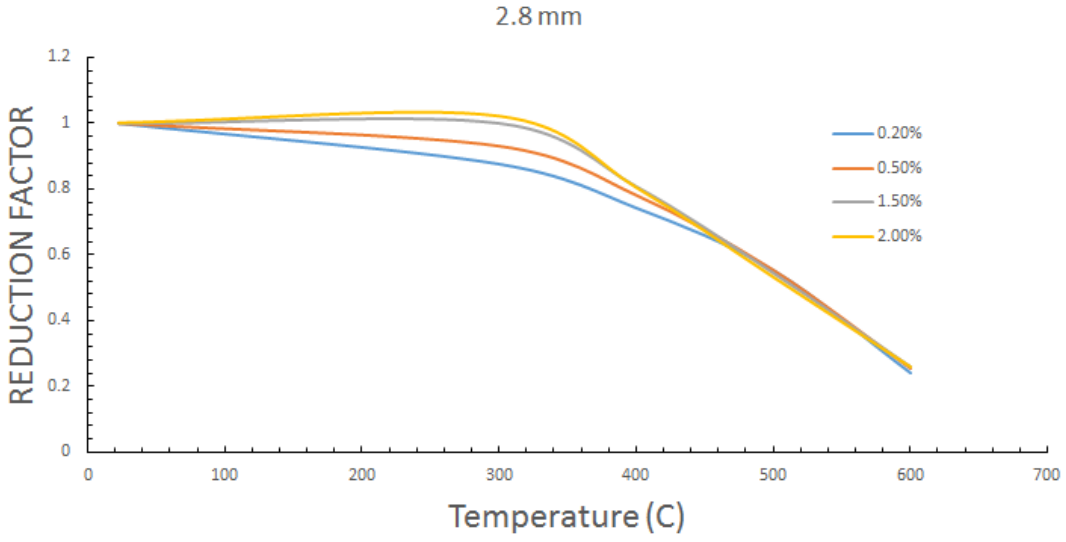

Figure A.90: Reduction factor curves for 2.8 mm sheet steel

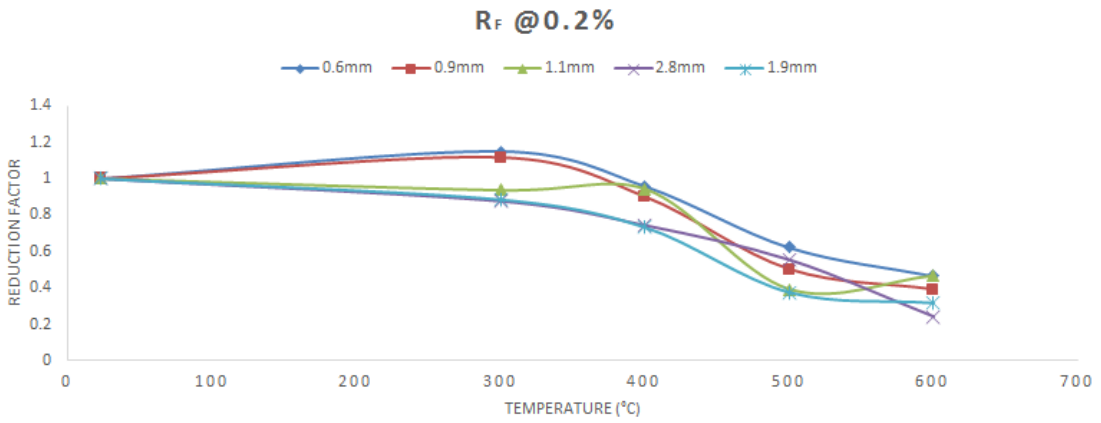

Figure A.91: Reduction factor curves for 0.2% strain value of sheet steel

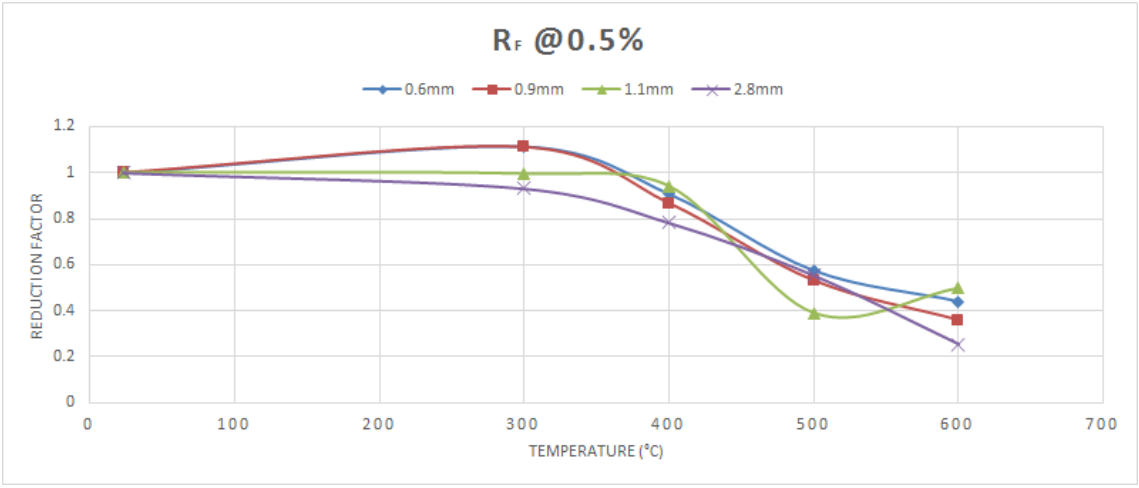

Figure A.92: Reduction factor curves for 0.5% strain value of sheet steel

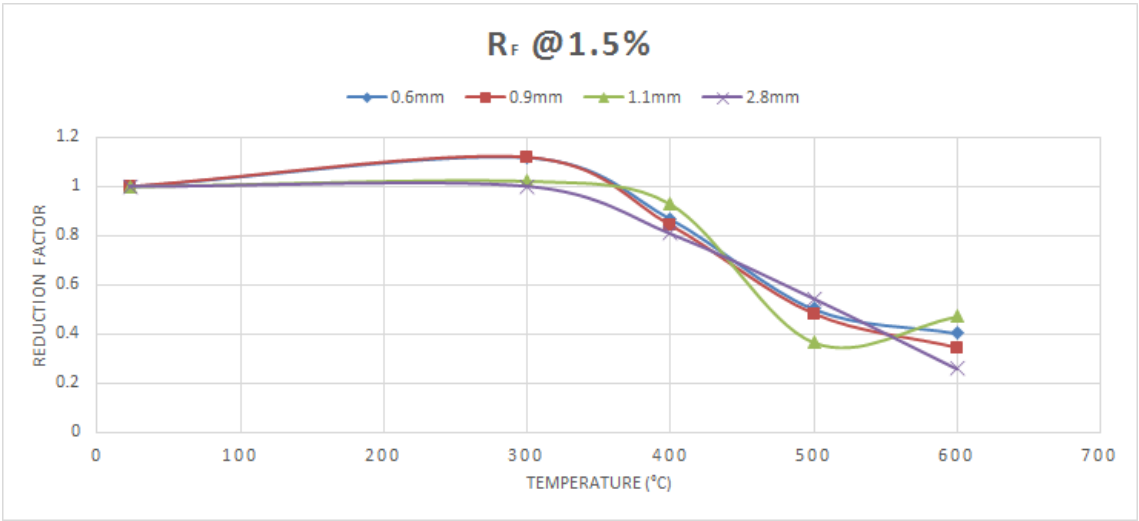

Figure A.93: Reduction factor curves for 1.5% strain value of sheet steel

Appendix B

Appendix B

B.1 Source Code

```
C ------------------------------------------------------------------
C EELAS - ELASTIC STRAINS
C EPLAS - PLASTIC STRAINS
C FLOW  - DIRECTION OF PLASTIC FLOW
C NDI   - Number of direct stress components at this point.
C EMOD  - Elastic Modulus
C ROTSIG- Will rotate a tensor with an orientation matrix
C EQPLAS- EQUIVALENT PLASTIC STRAIN
C ------------------------------------------------------------------
C UMAT FOR ISOTROPIC ELASTICITY AND ISOTROPIC MISES
C PLASTICITY CANNOT BE USED FOR PLANE STRESS
C ------------------------------------------------------------------
C PROPS(1)=E **** PROPS(2)=NU***PROPS(3..)=SYIELD AN HARDENING DATA
C CALLS UHARD FOR CURVE OF YIELD STRESS VS. PLASTIC STRAIN
C ------------------------------------------------------------------
      SUBROUTINE UMAT(STRESS,STATEV,DDSDDE,SSE,SPD,SCD,RPL,
     1 DDSDDT,DRPLDE,DRPLDT,STRAN,DSTRAN,TIME,DTIME,TEMP,DTEMP,
     2 PREDEF,DPRED,CMNAME,NDI,NSHR,NTENS,NSTATV,PROPS, NPROPS,
     3 COORDS,DROT,PNEWDT,CELENT,DFGRD0,DFGRD1,NOEL,NPT,LAYER,
```

```
     4 KSPT,KSTEP,KINC)
      INCLUDE 'ABA_PARAM.INC'
      CHARACTER*8 CMNAME
      DIMENSION STRESS(NTENS),STATEV(NSTATV),DDSDDE(NTENS,NTENS),
      1 DDSDDT(NTENS),DRPLDE(NTENS),STRAN(NTENS),DSTRAN(NTENS),
      2 PREDEF(1),DPRED(1),PROPS(NPROPS),COORDS(3),DROT(3,3),
      3 DFGRD0(3,3),DFGRD1(3,3)

      DIMENSION EELAS(6),EPLAS(6),FLOW(6), HARD(3)
      REAL*8 DSTRESS(6), DDS(6,6)
      PARAMETER(ZERO=0.D0, ONE=1.D0, TWO=2.D0, THREE=3.D0, SIX=6.D0,
      1 ENUMAX=.4999D0, NEWTON=10, TOLER=1.0D-6)
!**********************************************************************
!**********************************************************************
!**********************************************************************
      dimension Xf(44,11)
      real x1,x2,x3,i,j,k,n,m,l,DX3,DX33

      m=PROPS(1)
      n=PROPS(2)
      l=PROPS(3)
        DXU3=1000.
        DXL3=1000.
        DX1_C=1000.
        DX2_C=1000.
        SENS=0.

        IF(KINC.LE.1)THEN

      OPEN (unit=10,FILE='E:\sina.txt')
          READ(10,*) ((Xf(I,J),J=1,11),I=1,44)
      close(10)
```

```
!————————————————————— 1ST LOOP ——————————————
101     CONTINUE
        DO i=1,44
        X1=Xf(i,2)
        X2=Xf(i,3)
          X3=Xf(i,4)
             IF(X1.EQ.m.AND.X2.EQ.n.AND.X3.EQ.l)THEN
             k11=i
             k22=i
             GOTO 100
             ELSE
             CONTINUE
             ENDIF
          ENDDO
!————————————————————— 2ND LOOP ——————————————

          DO i=1,44
        X1=Xf(i,2)
        X2=Xf(i,3)
          X3=Xf(i,4)
             IF(X1.EQ.m.AND.X2.EQ.n)THEN
             DX3=ABS(X3-l)
             SENS=2.

                IF      (DX3.LT.DXL3.AND.X3.LT.l)THEN
                k11=i
                DXL3=DX3
                ELSEIF(DX3.LT.DXU3.AND.X3.GT.l)THEN
                    k22=i
                DXU3=DX3
                ENDIF
```

```
                ELSE
                CONTINUE
                ENDIF

            ENDDO
C
            IF(SENS.EQ.2.)THEN
            GOTO 100
            ELSE
            CONTINUE
            ENDIF
C
!————————————————————— 3RD LOOP ——————————————
            DO i=1,44
          X1=Xf(i,2)
          X2=Xf(i,3)
            DX1=ABS(X1-m)
            DX2=ABS(X2-n)
                IF      (X1.EQ.m.AND.DX2.LT.DX2_C)THEN
              DX2_C=DX2
              SENS=3.
              k=i
                GOTO 111
                ELSEIF(X2.EQ.n.AND.DX1.LT.DX1_C)THEN
              DX1_C=DX1
              SENS=3.
              GOTO 111
                ENDIF
111         CONTINUE
          ENDDO
```

```
      IF (SENS.EQ.3.) THEN
        CONTINUE
        ELSE
        GOTO 4
        ENDIF

        m=Xf(k,2)
      n=Xf(k,3)
      GOTO 101

!------------------------------ 4TH LOOP ------------------

4     CONTINUE
        DO i=1,44
      X1=Xf(i,2)
      X2=Xf(i,3)
        DX1=ABS(X1-m)
        DX2=ABS(X2-n)
            IF (DX1.LT.DX1_C) THEN
       DX1_C=DX1
                IF (DX2.LT.DX2_C) THEN
                DX2_C=DX2
                        k=i
                  ENDIF
        ENDIF


      ENDDO
        m=Xf(k,2)
      n=Xf(k,3)
      GOTO 101
```

```
!-------------------------------------------------------------
!-----------------------Interpolation-------------------------
!-------------------------------------------------------------

100     CONTINUE

        statev(21)=k11
          statev(22)=k22

        IF(k11.EQ.k22)THEN
            DO j=4,11
         statev(20+j)= xf(k11,j)
         ENDDO
        ELSE
         DO j=4,11
         statev(20+j)= xf(k11,j)
     1              +(xf(k22,j)-xf(k11,j))/(xf(k22,4)-xf(k11,4))
     2              *(1-xf(k11,4))
         ENDDO
        ENDIF

        ENDIF

        DO j=4,11
          statev(20+j)= statev(20+j)
        ENDDO

!*************************************************************
!*************************************************************

C
```

```
C ———————————— ISOTROPIC ELASTICITY ————————————

C ELASTIC PROPERTIES
      EMOD=210.e3
      ENU=0.3
      EBULK3=EMOD/(ONE-TWO*ENU)      !  E/(1-2*NU)
      EG2=EMOD/(ONE+ENU)             !  E/(1+NU)
      EG=EG2/TWO                     !  E/2(1+NU)
      EG3=THREE*EG                   !  3E/2(1+NU)
      ELAM=(EBULK3-EG2)/THREE

!———————————— 3D ELASTIC STIFFNESS ————————————
      DO K1=1,NDI
        DO K2=1,NDI
          DDSDDE(K2,K1)=ELAM
        END DO
        DDSDDE(K1,K1)=EG2+ELAM
      END DO
      DO K1=NDI+1,NTENS
        DDSDDE(K1,K1)=EG
      END DO

C
C CALCULATE PREDICTOR STRESS
      DO K1=1,NTENS
        DO K2=1,NTENS
        STRESS(K2)=STRESS(K2)+DDSDDE(K2, K1)*DSTRAN(K1)
        END DO
```

```
      END DO

************************************************************

C RECOVER ELASTIC AND PLASTIC STRAINS AND ROTATE FORWARD
C ALSO RECOVER EQUIVALENT PLASTIC STRAIN
      CALL ROTSIG(STATEV(1),DROT,EELAS,2,NDI,NSHR)
      CALL ROTSIG(STATEV(NTENS+1),DROT,EPLAS,2,NDI,NSHR)
      EQPLAS=STATEV(1+2*NTENS)

C CALCULATE  ELASTIC STRAIN
      DO K1=1,NTENS
            EELAS(K1)=EELAS(K1)+DSTRAN(K1)
      END DO

C
C CALCULATE EQUIVALENT VON MISES STRESS
      SMISES=(STRESS(1)-STRESS(2))**2+(STRESS(2)-STRESS(3))**2
     1      +(STRESS(3)-STRESS(1))**2
      DO K1=NDI+1,NTENS
      SMISES=SMISES+SIX*STRESS(K1)**2
      END DO
      SMISES=SQRT(SMISES/TWO)
C
C GET YIELD STRESS FROM THE SPECIFIED HARDENING CURVE
      NVALUE=NPROPS/2-1
      CALL UHARD(SYIEL0,HARD,EQPLAS,EQPLASRT,TIME,DTIME,TEMP,
     1 DTEMP,NOEL,NPT,LAYER,KSPT,KSTEP,KINC,CMNAME,NSTATV,
     2 STATEV,NUMFIELDV,PREDEF,DPRED,NVALUE,PROPS(3))

C
```

```
C DETERMINE IF ACTIVELY YIELDING
      IF (SMISES.GT.(ONE+TOLER)*SYIEL0) THEN
C ACTIVELY YIELDING
C SEPARATE THE HYDROSTATIC FROM THE DEVIATORIC STRESS
C CALCULATE THE FLOW DIRECTION
      SHYDRO=(STRESS(1)+STRESS(2)+STRESS(3))/THREE
      DO K1=1,NDI
      FLOW(K1)=(STRESS(K1)-SHYDRO)/SMISES
      END DO
      DO K1=NDI+1,NTENS
      FLOW(K1)=STRESS(K1)/SMISES
      END DO
C
C SOLVE FOR EQUIVALENT VON MISES STRESS
C AND EQUIVALENT PLASTIC STRAIN INCREMENT USING NEWTON ITERATION

      DEQPL=ZERO
      DO KEWTON=1,NEWTON
      RHS=SMISES-EG3*DEQPL-SYIELD
      DEQPL=DEQPL+RHS/(EG3+HARD(1))
      CALL UHARD(SYIELD,HARD,EQPLAS+DEQPL,EQPLASRT,TIME,DTIME,TEMP,
     1 DTEMP,NOEL,NPT,LAYER,KSPT,KSTEP,KINC,CMNAME,NSTATV,
     2 STATEV,NUMFIELDV,PREDEF,DPRED,NVALUE)
      WRITE(6,*) EQPLAS
      IF(ABS(RHS).LT.TOLER*SYIELD) GOTO 10
      END DO
C
C WRITE WARNING MESSAGE TO THE .MSG FILE

10    CONTINUE
C
C UPDATE STRESS, ELASTIC AND PLASTIC STRAINS AND
```

```
C EQUIVALENT PLASTIC STRAIN
C
      DO K1=1,NDI
      STRESS(K1)=FLOW(K1)*SYIELD+SHYDRO
      EPLAS(K1)=EPLAS(K1)+THREE/TWO*FLOW(K1)*DEQPL
      EELAS(K1)=EELAS(K1)-THREE/TWO*FLOW(K1)*DEQPL
      END DO
      DO K1=NDI+1,NTENS
      STRESS(K1)=FLOW(K1)*SYIELD
      EPLAS(K1)=EPLAS(K1)+THREE*FLOW(K1)*DEQPL
      EELAS(K1)=EELAS(K1)-THREE*FLOW(K1)*DEQPL
      END DO
      EQPLAS=EQPLAS+DEQPL
C
C CALCULATE PLASTIC DISSIPATION
C
      SPD=DEQPL*(SYIEL0+SYIELD)/TWO
C
C FORMULATE THE JACOBIAN (MATERIAL TANGENT)
C FIRST CALCULATE EFFECTIVE MODULI
C
      EFFG=EG*SYIELD/SMISES
      EFFG2=TWO*EFFG
      EFFG3=THREE/TWO*EFFG2
      EFFLAM=(EBULK3-EFFG2)/THREE
      EFFHRD=EG3*HARD(1)/(EG3+HARD(1))-EFFG3
      DO K1=1,NDI
        DO K2=1,NDI
        DDSDDE(K2,K1)=EFFLAM
        END DO
        DDSDDE(K1,K1)=EFFG2+EFFLAM
      END DO
```

```
            DO K1=NDI+1,NTENS
                DDSDDE(K1,K1)=EFFG
            END DO
            DO K1=1,NTENS
             DO K2=1,NTENS
                DDSDDE(K2, K1)=DDSDDE(K2,K1)+EFFHRD*FLOW(K2)*FLOW(K1)
                END DO
            END DO
            ENDIF
C
C STORE ELASTIC AND (EQUIVALENT) PLASTIC STRAINS
C IN STATE VARIABLE ARRAY
C
            DO K1=1, NTENS
            STATEV(K1)=EELAS(K1)
            STATEV(K1+NTENS)=EPLAS(K1)
            END DO
            STATEV(1+2*NTENS)=EQPLAS
            STATEV(14)=EQPLAS
C
            RETURN
            END
!-----------------------------------------------------------------------
            SUBROUTINE UHARD(SYIELD,HARD,EQPLAS,EQPLASRT,TIME,DTIME,TEMP,
            1 DTEMP,NOEL,NPT,LAYER,KSPT,KSTEP,KINC,CMNAME,NSTATV,STATEV,
           2 NUMFIELDV,PREDEF,DPRED,NVALUE,TABLE,PROPS,NPROPS)
            INCLUDE 'ABA_PARAM.INC'
            CHARACTER*80 CMNAME
            DIMENSION HARD(3),STATEV(NSTATV),TIME(*),
            1 PREDEF(NUMFIELDV),DPRED(*),PROPS(NPROPS)
            DIMENSION TABLE(2,NVALUE)
            PARAMETER(ZERO=0.D0)
```

```
      SYIEL0=STATEV(29)*1000.

         HARD(1)=  1000.*(
         1            4*STATEV(25)*EQPLAS**3+
     2          3*STATEV(26)*EQPLAS**2+
         3            2*STATEV(27)*EQPLAS**1+
         4            1*STATEV(28)*EQPLAS**0)

         SYIELD=1000.*(
     1          STATEV(25)*EQPLAS**4+
     2          STATEV(26)*EQPLAS**3+
         3            STATEV(27)*EQPLAS**2+
         4            STATEV(28)*EQPLAS**1+
     5       STATEV(29)*EQPLAS**0)


      kfg=STATEV(32)
         STATEV(32)=SYIELD


!*****************************************************************
!*****************************************************************


         RETURN
         END
```

B.2 Polynomial Tables

a4	a3	a2	a1
-0.003352529	-0.048122118	-0.246950001	-0.701568
-0.005960451	-0.069241601	-0.294628138	-0.627858
-0.003576988	-0.052284131	-0.272435178	-0.674058
-0.004985161	-0.062013072	-0.286394573	-0.645568
-0.002051719	-0.035803573	-0.233606098	-0.730239498
-0.007058188	0.077564646	-0.313262863	0.604107
-0.006636296	-0.073093066	-0.305316864	-0.615168
-0.009759302	-0.09458383	-0.305761311	-0.590706062
-0.002061909	-0.035579466	-0.230828254	-0.731253321
-0.012829245	-0.098759849	-0.328583808	-0.55776
-0.00416038	-0.055349896	-0.276833865	-0.66425507
-0.011152554	-0.097659613	-0.329558432	-0.562497872
-0.003700875	-0.053632721	-0.280148566	-0.663612412
-0.001122189	-0.024177884	-0.195495758	-0.777830878
-0.020009754	-0.132617311	-0.353097978	-0.495778441

Table B.2: 2nd stage polynomial coefficients 0.13% C-steel

	x4	x3	x2	x1	c	Newton Method
1mm,3mmmin,amb	-4873.07	2014.5	-297.731	24.36	1	-0.0288
2mm,3mmmin,amb	-7165.58	2513.89	-323.043	20.79	1	-0.0302
1mm,3mmmin,300c	-63596.7	14315.54	-1148.74	43.77	1	-0.0154
2mm,3mmmin,300c	-19801	5517.46	-570.78	28.82	1	-0.0224
1mm,90mmmin,350c	-12322.88401	4343.824451	-572.507837	36.15047022	1	-0.0202
1mm,3mmmin,350c	-28541.3	6994.38	-629.94	27.09	1	0.0223
2mm,3mmmin,350c	-9646.19	3059.84	-368.1	21.36	1	-0.0288
1mm,0.3mmmin,350c	-15432.00437	4217.640634	-384.4893501	20.94702348	1	-0.0282
2mm,0.3mmmin,350c	-4309.694794	1955.834829	-333.7163375	27.8043088	1	-0.0263
1mm,3mmmin,400c	-10065.7	2603.53	-291.05	16.6	1	-0.0336
2mm,3mmmin,400c	-4447.249191	1840.075512	-286.218986	21.35868393	1	-0.0311
1mm,3mmmin,450c	-6423.146357	2041.715023	-250.1031593	15.49580916	1	-0.0363
2mm,3mmmin,450c	-9474.238876	3432.494145	-448.2377049	26.54449649	1	-0.025
1mm,3mmmin,500c	-19951.84136	6619.971671	-824.3201133	50.50849858	1	-0.0154
2mm,3mmmin,500c	-3279.564607	1080.266854	-142.9494382	9.975421348	1	-0.0497

Table B.1: 1st stage poloynomial 0.13% C-steel

					b0	b1	b2	b3	b4	newton method	stability value
1mm,3mmmin,amb	8.5905	209.2652761	73.6607999	14.3539733	0.004793693	-0.12719333	1.30	-4.413394431	1	0.17	2.361
2mm,3mmmin,amb	5.0667	105.3373313	49.43051097	11.61683921	0.002761814	-0.093066577	1.10	-4.350828544	1	0.13	1.715
1mm,3mmmin,300c	4.3053	188.4429105	76.16329445	14.61680432	0.000672519	-0.036814017	0.69	-4.225098787	1	0.09	1.895
2mm,3mmmin,300c	4.4933	129.4979215	57.44941183	12.43953227	0.00140498	-0.059107116	0.86	-4.278645523	1	0.07	1.627
1mm,90mmmin,350c	9.8454	355.9159751	113.8587303	17.45052653	0.002852455	-0.095851437	1.10	-4.352500636	1	0.07	1.910
1mm,3mmmin,350c	-3.1595	-85.5895347	44.38290344	-10.98931469	0.000914114	-0.045091499	0.76	-4.245061718	1	0.08	1.556
2mm,3mmmin,350c	4.3398	92.69748966	46.00711812	11.01413558	0.002110678	-0.078534634	0.99	-4.317207105	1	0.07	1.515
1mm,0.3mmmin,350c	2.8896	60.52748894	31.3302428	9.691659036	0.001292575	-0.0511875	0.84	-4.273304785	1	0.13	2.082
2mm,0.3mmmin,350c	12.7552	354.6486758	111.9488036	17.25559393	0.006219538	-0.161319308	1.44	-4.45382212	1	0.14	2.068
1mm,3mmmin,400c	2.6190	43.47566898	25.61209278	7.698025165	0.001549818	-0.059479222	0.80	-4.258653646	1	0.06	1.376
2mm,3mmmin,400c	7.4753	159.6621073	66.54052084	13.30404766	0.004577815	-0.133519987	1.31	-4.413755882	1	0.08	1.641
1mm,3mmmin,450c	3.2549	50.43668867	29.55004249	8.756704235	0.002256808	-0.080288086	0.99	-4.317868364	1	0.10	1.449
2mm,3mmmin,450c	6.7552	179.3123223	75.69793598	14.49190459	0.002696206	-0.097424175	1.13	-4.362297615	1	0.07	1.608
1mm,3mmmin,500c	13.7232	693.1373687	174.2093547	21.54529412	3.04661E-07	-0.085162502	1.04	-4.331797529	1	0.12	2.489
2mm,3mmmin,500c	2.4838	24.7768386	17.64629294	6.627633297	0.032786973	-0.090217554	1.03	-4.329393375	2	0.07	1.289

Table B.3: Polynomial instability 0.13% C-steel

test2-al	x4	x3	x2	x1	c	Newton Method	a4	a3	a2	a1
50c-3mmmin	-3163.386728	1599.977117	-300.7093822	28.93363844	1	-0.0263	-0.001513475	-0.029105899	-0.207997673	-0.760954691
150c-3mmmin	-1792.336066	980.5942623	-197.2868852	18.96106557	1	-0.0363	-0.003112046	-0.046903929	-0.259962956	-0.68828668
amb-3mmmin	-2819.08046	1658.045977	-352	35.8183908	1	-0.0224	-0.00070974	-0.018635482	-0.17661952	-0.802331954
100c-3mmmin	-2829.52381	1410.380952	-257.1809524	23.4152381	1	-0.0306	-0.002480842	-0.040411104	-0.240813957	-0.716506286
100c-0.3mmmin	-2580	1239.419355	216.8602151	19.09892473	1	-0.088	-0.154721403	-0.844629587	1.679365505	-1.680705376
100c-30mmmin	-2483.295195	1511.784897	-331.2128146	34.18993135	1	-0.0234	-0.000744546	-0.019370355	-0.181358889	-0.800044394
amb-0.3mmmin	-2059.865952	1261.742627	-280.2412869	30.65147453	1	-0.0258	-0.000912678	-0.021668552	-0.18653981	-0.790808043
100c-90mmmin	-2317.286245	1279.442379	-255.7249071	24.7063197	1	-0.0298	-0.001827447	-0.033858641	-0.227093946	-0.736248327
200c-3mmmin	-548.2195122	270.5365854	-55.77804878	6.080487805	1	-0.0798	-0.022231361	-0.137478466	-0.355196846	-0.485222927
amb-30mmmin	-3090.786517	1673.505618	-334.4269663	33.66516854	1	-0.0235	-0.000942628	-0.021718547	-0.184687292	-0.791131461
amb-90mmmin	-2482.807018	1296.298246	-248.9298246	24.31578947	1	-0.0302	-0.002065241	-0.035704731	-0.227033957	-0.734336842

Table B.4: Polynomial coefficients for aluminium Alloy

test2-al				b0	b1	b2	b3	C	newton method	stability value
50c-3mmmin	17.37722668	502.7863939	137.4305211	0.008830295	-0.199265046	1.612398727	-4.505779803	0.008830295	0.1783	2.471113631
150c-3mmmin	11.66435372	221.1685758	83.5344317	0.010021037	-0.230723938	1.751384538	-4.547104018	0.010021037	0.0998	1.724247498
amb-3mmmin	31.5608342	1130.458293	248.8508655	0.012350974	-0.262432521	1.889317459	-4.58815135	0.012350974	0.2117	2.876035629
100c-3mmmin	12.33452325	288.8157986	97.06945573	0.007921912	-0.190059239	1.586247055	-4.4984517	0.007921912	0.1771	2.131187323
100c-0.3mmmin	0.568764233	10.86278527	-10.85412538	0.007015087	0.16070601	1.357130949	-4.480395099	0.007015087	0.4355	60.01450605
100c-30mmmin	31.42853082	1074.539311	243.5830524	0.013365278	-0.280520641	1.95972171	-4.608781791	0.013365278	0.2294	2.786570585
amb-0.3mmmin	28.26844524	866.4695294	204.3872252	0.014394856	-0.28697695	1.973657153	-4.61253628	0.014394856	0.2207	2.791271023
100c-90mmmin	16.30690436	402.8835924	124.2684317	0.010230208	-0.231372423	1.766744205	-4.552129622	0.010230208	0.194	2.227900574
200c-3mmmin	3.589523799	21.82605568	15.97728736	0.009267251	-0.214579348	1.582190684	-4.493482226	0.009267251	0.0801	1.245641809
amb-30mmmin	24.93029423	839.2825571	195.9280227	0.010568562	-0.227294605	1.732550531	-4.54144976	0.010568562	0.4319	-19.56411984
amb-90mmmin	14.6229908	355.5695659	109.9309758	0.009390899	-0.210316563	1.666591295	-4.522109949	0.009390899	0.1872	2.28338088

Table B.5: Ploynomial instability for aluminium alloy

test2-Br	x4	x3	x2	x1	c		a4	a3	a2	a1
80,3mmmin	-760.6485812	371.9052074	-65.35079514	6.886810103	1	-0.0723	-0.020784388	-0.140555276	-0.341607558	-0.49791637
160c,0.3mmmin	-2776.237085	901.3322458	-104.2822186	6.865959761	1	-0.0594	-0.034562276	-0.188905344	-0.367945209	-0.40783801
160c,3mmmin	-3833.246073	1194.34555	-133.1753927	7.964921466	1	-0.0529	-0.030018528	-0.176806005	-0.372679351	-0.421344346
160c,30mmmin	-5184.537915	1455.242891	-147.3755924	8.294135071	1	-0.0501	-0.032663368	-0.182998978	-0.369914211	-0.415536167
160c,90mmmin	-6699.196326	2073.880597	-225.9586682	11.98019518	1	-0.0402	-0.017495523	-0.134729255	-0.365158246	-0.481603846
amb,3mmmin	-2192.371134	779.1237113	-99.7371134	7.185824742	1	-0.0604	-0.029178424	-0.171679025	-0.363856948	-0.434023814

Table B.6: Polynomial coefficients for brass

Table B.7: Polynomial instability for brass

test2-Br				b0	b1	b2	b3	C	newton method	stability value
80,3mmmin	3.478572414	23.95626764	16.43577631	6.762540865	-0.180883004	1.552709683	-4.488931705	0.007739198	0.1882	1.506254639
160c,0.3mmmin	1.718636828	11.8000913	10.64586172	5.465651191	0.002112917	-0.077597983	1.011541475	-4.324659681	0.002112917	0.1752	1.233397426
160c,3mmmin	1.762244989	14.03614295	12.41497766	5.88989597	0.001816977	-0.071562248	0.969468688	-4.311575497	0.001816977	0.0739	1.229001117
160c,30mmmin	1.533828374	12.72177971	11.32504815	5.602575344	0.001406902	-0.058451751	0.870493058	-4.280689025	0.001406902	0.1073	1.303714113
160c,90mmmin	2.297730745	27.52726279	20.8715256	7.70078485	0.001639032	-0.069246744	0.962443873	-4.309571551	0.001639032	0.0537	1.25718246
amb,3mmmin	2.070022704	14.87482036	12.47006859	5.883766208	0.002821523	-0.094263261	1.111631242	-4.355379479	0.002821523	0.1327	1.338052696

test2-CS	x4	x3	x2	x1	c		a4	a3	a2	a1
300c,0.3mmmin	-4254.688525	2012.590164	-388.0918033	40.77245902	1	-0.0202	-0.000708391	-0.016588589	-0.158356979	-0.823603672
300c,30mmmin	-1077.328111	597.7806789	-180.1131419	27.86248912	1	-0.0296	-0.000827018	-0.015503045	-0.15780793	-0.824729678
300c,3mmmin	-1281.597633	811.9526627	-240.887574	37.0183432	1	-0.0232	-0.000371282	-0.010138989	-0.129655328	-0.858825562
450c,3mmmin	-7557.680813	2437.776449	-307.3042439	21.31978482	1	-0.0303	-0.006370288	-0.067814375	-0.282132953	-0.64598948
600c,3mmmin	-764.8703495	548.7936866	-142.9425028	15.13979707	1	-0.0442	-0.002919288	-0.047388822	-0.279258191	-0.66917903
amb,3mmmin	1383.540146	-650.4379562	87.00729927	0.968248175	1	-0.0191	0.00018413	0.004532168	0.031741133	-0.01849354
300c,30mmmin	-2278.235747	992.7195686	-199.0562404	24.04699538	1	-0.0318	-0.002329738	-0.031923312	-0.201293633	-0.764694453

Table B.8: Polynomial coefficients for carbon steel

Table B.9: Polynomial instability for carbon steel

test2-CS				b0	b1	b2	b3	C	newton method	stability value
300c,0.3mmmin	28.51531147	1162.639368	223.5444847	23.41726682	0.009347913	-0.192013131	1.510301461	-4.47302879	0.009347913	0.1458	3.009818475
300c,30mmmin	35.79125068	997.2333327	190.8156485	18.74572193	0.024934362	-0.360232661	1.831805146	-4.554873369	0.024934362	0.1236	2.569538384
300c,3mmmin	62.48623368	2313.136843	349.2100479	27.30807134	0.028104252	-0.404802161	2.088600582	-4.633547255	0.028104252	0.1404	3.198121399
450c,3mmmin	4.756456927	101.4066382	44.28888581	10.64541759	0.002688627	-0.084143309	1.008329643	-4.322556153	0.002688627	0.1125	1.769536795
600c,3mmmin	15.1406795	229.2268151	95.65970069	16.23300833	0.018486528	-0.393563174	2.339381522	-4.717498968	0.018486528	0.0766	1.541309707
amb,3mmmin	-103.7308968	-100.4372516	172.3844093	24.61391768	2.29497E-05	-0.125075048	1.473264924	-4.470125828	2.29497E-05	0.00016	1.000157144
300c,30mmmin	13.64960168	328.2319085	86.40182089	13.70253124	0.010116159	-0.18530105	1.394594458	-4.435740493	0.010116159	0.133	2.299791729

test2-St	x4	x3	x2	x1	c		a4	a3	a2	a1
amb,0.3mmmin	-152.0171215	96.35098983	-27.30337079	7.873461744	1	-0.0894	-0.009710522	-0.068844419	-0.218218369	-0.70388748
amb,3mmmin	-51.82990227	32.23331254	-12.0095654	5.180910792	1	-0.1336	-0.016512249	-0.076864236	-0.214358252	-0.692169682
amb,30mmmin	-24.15086299	22.02002983	-8.859791178	5.138077988	1	-0.114	-0.004078985	-0.032623643	-0.115141846	-0.585740891
amb,90mmmin	-67.23172628	43.04432348	-12.21384137	4.767884914	1	-0.1355	-0.022663733	-0.107086265	-0.224249181	-0.646048406
300c,3mmmin	-189.3975241	117.2957359	-32.09078404	8.212104539	1	-0.0843	-0.009564992	-0.07026919	-0.228052836	-0.692280413
300c,0.3mmmin	-118.8248652	81.12404201	-25.35992052	8.070678399	1	-0.0901	-0.007830807	-0.059336777	-0.205872088	-0.727168124
100c,3mmmin	-85.89543938	45.37422533	-13.20006356	5.021929128	1	-0.13	-0.024532596	-0.099687173	-0.223081074	-0.652850787
300c,30mmmin	-292.6453318	173.3793306	-41.80857311	8.905460951	1	-0.0758	-0.009660919	-0.075510081	-0.24021701	-0.67503394
450c,3mmmin	-469.2750678	256.9410569	-55.81300813	10.65955285	1	-0.0646	-0.008172549	-0.069267747	-0.232916613	-0.688607114

Table B.10: Polynomial coefficients for stainless steel

test2-St				b0	b1	b2	b3	C	newton method	stability value
anb,0.3mmmin	9.206508087	72.48708922	22.47236213	7.089672228	0.04521505	-0.411007673	2.0810573	-4.633816697	0.04521505	0.2702	2.224460131
anb,3mmmin	8.090963382	41.91855951	12.98177224	4.654982913	0.080665998	-0.563382146	2.097428285	-4.621905717	0.080665998	0.2583	1.861740671
anb,30mmmin	27.94813239	143.5996839	28.22806632	7.997981543	0.171342862	-0.94645315	3.102161638	-4.911769896	0.171342862	0.4006	2.43014474
anb,90mmmin	5.978715004	28.50582507	9.894626885	4.725005612	0.056043257	-0.434252834	2.102382605	-4.64023826	0.056043257	0.2929	1.935476138
300c,3mmmin	8.813389804	72.37647842	23.84245004	7.346497791	0.038079191	-0.382231357	2.027365424	-4.619309764	0.038079191	0.2556	2.152781172
300c,0.3mmmin	11.50583911	92.85992718	26.2900236	7.577351958	0.05950504	-0.494766136	2.261580909	-4.682719411	0.05950504	0.2866	2.338060491
100c,3mmmin	5.299072208	26.61156507	9.093251697	4.06345791	0.046823547	-0.365817516	1.738424538	-4.528249528	0.046823547	0.2402	1.787567137
300c,30mmmin	7.846044779	69.8726454	24.8648208	7.81603536	0.027013795	-0.316159518	1.92023075	-4.59245548	0.027013795	0.2511	2.181650851
450c,3mmmin	7.904510213	84.25854434	28.49987224	8.475659618	0.020583989	-0.260583989	1.761517361	-4.547527611	0.020583989	0.2399	2.338242238

Table B.11: Polynomial instability for stainless steel

test3-0.6mm	x4	x3	x2	x1	c	Newton Method		a4	a3	a2	a1
6-600c-0.3mmmin	-5578.571429	1962.755102	-244.7066327	12.75	1	-0.039		-0.012905696	-0.11642867	-0.372198788	-0.49725
7-300c-0.3mmmin	-907.5396825	531.25	-109.7867063	15.2906746	1	-0.0463		-0.004170514	-0.052728075	-0.235348665	-0.707958234
9-400c-0.3mmmin	-2057.037944	893.0232558	-136.7870257	12.74357405	1	-0.0469		-0.009952534	-0.092125805	-0.30087811	-0.597673623
10-500c-0.3mmmin	-1934.512326	843.8799571	-145.7234727	12.8681672	1	-0.0463		-0.008889871	-0.083757488	-0.312385951	-0.595796141
11-amb-0.3mmmin	-248.7863535	225.3747204	-77.52796421	15.4614094	1	-0.0501		-0.001567391	-0.028341209	-0.194595965	-0.774616611

Table B.12: 0.13% C-steel polynomial coefficients 0.6mm

test3-0.6mm				b0	b1	b2	b3	C	newton method	stability value
6-600c-0.3mmmin	3.021921515	38.52949932	28.83988529	9.021494937	0.002106274	-0.090016462	1.099380373	-4.351838303	0.002106274	0.0393	1.228956859
7-300c-0.3mmmin	11.10174897	169.7532311	56.43157225	12.64306376	0.015746611	-0.258792086	1.877093354	-4.585373852	0.015746611	0.2543	2.729845646
9-400c-0.3mmmin	4.712367685	60.05240655	30.23130663	9.256517433	0.005708973	-0.139189278	1.368889087	-4.434130668	0.005708973	0.1839	1.918826286
10-500c-0.3mmmin	5.208174487	67.01966012	35.13953652	9.421676317	0.006134966	-0.157308438	1.383999114	-4.436223613	0.006134966	0.091	1.467531494
11-amb-0.3mmmin	31.96393713	494.2075179	124.1527586	18.08176916	0.058127824	-0.685396668	3.02931457	-4.905896635	0.058127824	0.3095	2.75777918

Table B.13: Polynomial instability for 0.13% C-steel 0.6mm

test3-0.9mm	x4	x3	x2	x1	c		a4	a3	a2	a1
1-amb-0.3mmmin	-395.9900374	294.8069738	-83.48692403	13.29202989	1	-0.0536	-0.003268462	-0.045397519	-0.239854593	-0.712452802
2-600c-0.3mmmin	-2547.097844	805.4560531	-100.4262023	7.429519071	1	-0.0595	-0.03192372	-0.16966519	-0.355533863	-0.442056385
3-300c-0.3mmmin	-2727.334852	1133.257403	-177.2266515	16.95045558	1	-0.0389	-0.006245064	-0.066707915	-0.268181141	-0.659372722
4-400c-0.3mmmin	-910.6007067	416.2614841	-80.93992933	9.807773852	1	-0.0607	-0.012361829	-0.093096274	-0.29822236	-0.595331873
5-500c-0.3mmmin	-4909.261577	1941.426783	-266.6082603	13.85732165	1	-0.0373	-0.009502798	-0.10075057	-0.370929407	-0.516878098

Table B.14: 0.13% C-steel polynomial coefficients 0.9mm

test3-0.9mm				b0	b1	b2	b3	C	newton method	stability value
1-amb-0.3mmmin	16.39915124	217.9780084	73.38445476	13.88956688	0.03104126	-0.455228316	2.444273225	-4.744480785	0.03104126	0.2465	2.157204383
2-600c-0.3mmmin	1.863817884	13.84727051	11.13698104	5.314706129	0.002524253	-0.081772251	0.988102741	-4.316225015	0.002524253	0.0961	1.284125235
3-300c-0.3mmmin	6.228919722	105.5830271	42.94289975	10.68170307	0.005848367	-0.136178276	1.311536374	-4.415518249	0.005848367	0.1643	2.039618318
4-400c-0.3mmmin	4.91027645	48.15888097	24.12445193	7.530946358	0.009672487	-0.188543267	1.460271634	-4.457128444	0.009672487	0.1405	1.579880566
5-500c-0.3mmmin	3.925159703	54.39220055	39.033704	10.60220048	0.002618993	-0.111437094	1.240693435	-4.395462078	0.002618993	0.0362	1.235927735

Table B.15: Polynomial instability for 0.13% C-steel 0.9mm

test3-1.1mm	x4	x3	x2	x1	c		a4	a3	a2	a1
12-500c-0.3mmmin	-1098.151659	441.3744076	-83.38230648	6.011058452	1	-0.0697	-0.02591752	-0.149453291	-0.405078749	-0.418970774
13-600c-0.3mmmin	-1587.700535	698.9171123	-125.6136364	10.97326203	1	-0.0513	-0.010996084	-0.094357792	-0.330576151	-0.562928342
14-300c-0.3mmmin	-3042.503347	1515.19411	-272.6506024	20.61981258	1	-0.0322	-0.003270804	-0.050586646	-0.282695051	-0.663957965
15-400c-0.3mmmin	-3860.837272	1284.064821	-163.227549	13.00877785	1	-0.0437	-0.014080149	-0.107159643	-0.311714018	-0.568483592
16-amb-0.3mmmin	-196.5974843	166.3962264	-55.42893082	11.33773585	1	-0.064	-0.003298358	-0.043619772	-0.227036901	-0.725615094

Table B.16: 0.13% C-steel polynomial coefficients 1.1mm

test3-1.1mm				b0	b1	b2	b3	C	newton method	stability value
12-500c-0.3mmmin	2.689300569	16.16554292	15.62953387	5.766496698	0.004563175	-0.157333161	1.281704142	-4.40192482	0.004563175	0.0412	1.13382235
13-600c-0.3mmmin	4.66529718	51.19352842	30.0630796	8.581035876	0.006281576	-0.16514483	1.399738127	-4.44020714	0.006281576	0.0735	1.359118341
14-300c-0.3mmmin	9.844673568	202.9953239	86.42982896	15.46611863	0.006448576	-0.18600506	1.583640964	-4.49800902	0.006448576	0.0596	1.542832273
15-400c-0.3mmmin	3.103660377	40.37482838	22.13854569	7.610689671	0.003110408	-0.087924937	1.040039175	-4.332587139	0.003110408	0.1301	1.651165948
16-amb-0.3mmmin	19.403591145	219.9927944	68.83330101	13.22469129	0.052583256	-0.621552193	2.821081928	-4.846380242	0.052583256	0.273	2.257691262

Table B.17: Polynomial instability for 0.13% C-steel 1.1mm

test:3-1.3mm	x4	x3	x2	x1	c		a4	a3	a2	a1
17-300c-0.3mmmin	-1510.709838	779.5143213	-145.871731	15.1618929	1	-0.0433	-0.005310466	-0.063283106	-0.27349345	-0.656509963
20-400c-0.3mmmin	-2271.263345	917.1708185	-144.9466192	14.23309609	1	-0.0442	-0.008668752	-0.079198515	-0.283173513	-0.629102847
21-amb-0.3mmmin	-159.5159151	143.2891247	-51.07625995	11.73872679	1	-0.0636	-0.002609952	-0.036862482	-0.206601428	-0.746583024
22-500-0.3mmmin	-546.79	361.71	-97.5	12.64	1	-0.0539	-0.004615042	-0.056640465	-0.283257975	-0.681296

Table B.18: 0.13% C-steel polynomial coefficients 1.3mm

test3-1.3mm				b0	b1	b2	b3	C	newton method	stability value
17-300c-0.3mmmin	8.153709859	123.6256756	51.5008369	11.91667636	0.00937433	-0.203153079	1.644534663	-4.515992086	0.00937433	0.2009	2.018265845
20-400c-0.3mmmin	5.098773264	72.57132978	32.66600765	9.136092057	0.005826315	-0.133901837	1.275263426	-4.403815269	0.005826315	0.151	1.821246722
21-amb-0.3mmmin	24.36826637	286.0524213	79.15909813	14.1238174	0.067320723	-0.713980461	3.015019746	-4.898274787	0.067320723	0.3025	2.507813035
22-500-0.3mmmin	11.67920122	147.6251035	61.37712223	12.2730128	0.02128788	-0.379743594	2.162859599	-4.661515139	0.02128788	0.1047	1.604043599

Table B.19: Polynomial instability for 0.13% C-steel 1.3mm

test3-1.9mm	x4	x3	x2	x1	c		a4	a3	a2	a1
24-600c-0.3mmmin	-3069.197708	1246.131805	-212.7077364	17.14613181	1	-0.0371	-0.005814609	-0.063633485	-0.292773055	-0.63612149
25-400c-0.3mmmin	-1549.140049	666.7076167	-110.8538084	10.00614251	1	-0.0546	-0.013767696	-0.108520889	-0.330472939	-0.546335381
26-500c-0.3mmmin	-4868.257757	1778.997613	-255.8114558	20.00477327	1	-0.0328	-0.005634676	-0.062776471	-0.275212197	-0.656156563
??-300c-0.3mmmin	-520.24	336.26	-78.82	11.82	1	-0.0571	-0.005530293	-0.062601326	-0.256985516	-0.674922
??-amb-0.3mmmin	-1253.07	699.2	-138.71	14.22	1	-0.0453	-0.00527677	-0.064997406	-0.284645404	-0.644166

Table B.20: 0.13% C-steel polynomial coefficients 1.9mm

test3-1.9mm				b0	b1	b2	b3	C	newton method	stability value
24-600c-0.3mmmin	6.380480798	109.4005647	50.35128998	0.005260701	-0.144194557	1.287340709	-4.40601223	0.005260701	0.0715	1.513812928
25-400c-0.3mmmin	3.965805312	39.68241311	24.00350437	0.00581364	-0.149575734	1.362676447	-4.43037272	0.00581364	0.1164	1.429842724
26-500c-0.3mmmin	5.821097914	116.4497439	48.84259585	0.003903814	-0.109202863	1.148830768	-4.365427983	0.003903814	0.1218	1.784657846
??-300c-0.3mmmin	10.32494945	122.0409026	46.46869466	0.020798093	-0.325734276	2.090573581	-4.646355528	0.020798093	0.2619	2.282260096
??-amb-0.3mmmin	8.584797619	122.0758221	53.94311668	0.010550089	-0.23274039	1.784664863	-4.557989578	0.010550089	0.1277	1.676726472

Table B.21: Polynomial instability for 0.13% C-steel 1.9mm

test3-2.8mm	x4	x3	x2	x1	c		a4	a3	a2	a1
27-400c-0.3mmmin	-2572.147831	923.1387252	-120.0160686	9.202999464	1	-0.0536	-0.021230249	-0.142154738	-0.344801364	-0.493280771
28-600c-0.3mmmin	-4144.536424	1373.774834	-175.2152318	9.465231788	1	-0.0471	-0.020396685	-0.143541764	-0.388699222	-0.445812417
29-500c-0.3mmmin	-632.403496	225.1784414	-29.12672979	2.640932265	1	-0.1083	-0.086997764	-0.28603039	-0.34162421	-0.286012964
30-amb-0.3mmmin	-67.76083467	47.7046549	-14.56661316	3.802568218	1	-0.1422	-0.027706211	-0.137170129	-0.294549154	-0.540725201
31-300c-0.3mmmin	-3042.293578	1239.311927	-186.1605505	15.14724771	1	-0.0402	-0.007945209	-0.080511661	-0.300842896	-0.608919358

Table B.22: 0.13% C-steel polynomial coefficients 2.8mm

Table B.23: Polynomial instability for 0.13% C-steel 2.8mm

test3-2.8mm				b0	b1	b2	b3	C	newton method	stability value
27-400c-0.3mmmin	2.524699566	23.23480876	16.24104207	6.695858304	0.003189163	-0.096897672	1.123353879	-4.358898005	0.003189163	0.1421	1.484382144
28-600c-0.3mmmin	2.309198772	21.85710162	19.056698019	7.037504549	0.002042504	-0.086836176	1.036675588	-4.331466464	0.002042504	0.0364	1.171360611
29-500c-0.3mmmin	1.244859586	3.287589847	3.926815997	3.28779015	0.002594755	-0.09629041	1.114260213	-4.356067673	0.002594755	0.0531	1.086793757
30-anb-0.3mmmin	5.132423252	19.51638954	10.63115983	4.950880172	0.041359706	-0.486059458	2.327016463	-4.70401516	0.041359706	0.2136	1.471479276
31-300c-0.3mmmin	5.059652847	76.63981499	37.86469192	10.13335962	0.004650191	-0.127360604	1.283274027	-4.407361057	0.004650191	0.1554	1.734915086